Procreation of Energy Efficient Topologies for Data Transmission in Underwater Wireless Sensor Network

A Thesis

submitted in partial fulfillment of the requirements for the award of degree of

Doctor of Philosophy

by

Himanshu Jindal

Registration No. 901411009

under the guidance of

Dr. Sharad Saxena
Associate Professor

Dr. Singara Singh Kasana
Associate Professor

Computer Science and Engineering Department
Thapar Institute of Engineering and Technology
Patiala-147004, Punjab, India
February 2018

Certificate

I hereby certify that the work which is being presented in this thesis entitled **"Procreation of Energy Efficient Topologies for Data Transmission in Underwater Wireless Sensor Network"**, in partial fulfillment of the requirement for the award of degree of "Doctor of Philosophy" submitted in Computer Science and Engineering Department of Thapar Institute of Engineering and Technology, Patiala, is an authentic record of my own work carried out under the supervision of Dr. Sharad Saxena and Dr. Singara Singh Kasana. The work has referred research work of others which are duly listed in the reference section.

The matter presented in this thesis has not been submitted for the award of any other degree or to any other university.

Himanshu Jindal

(Himanshu Jindal)

Registration No. 901411009

This is to certify that the above statement made by the candidate is correct and true to the best of my knowledge.

(Dr. Sharad Saxena)
Associate Professor
Computer Science and
Engineering Department

(Dr. Singara Singh Kasana)
Associate Professor
Computer Science and
Engineering Department

Acknowledgement

I would like to express my sincere appreciation to my supervisors, **Dr. Sharad Saxena** and **Dr. Singara Singh Kasana**, Associate Professor, for being pillars of support and encouragement throughout my research work. Their experiences, strengths, tenderness and willfulness, have taught me valuable lessons of life, which are going to be of immense help in taking decisions for moving forward.

My sincere thanks are due to **Prof. O. P. Pandey**, Dean of Research/Scientific Projects, **Prof. R. K. Sharma**, Dean of Faculty Affairs, **Prof. Maneek Kumar**, Dean of Student Affairs, **Prof. S. S. Bhatia**, Dean of Academic Affairs and **Prof. Maninder Singh**, Head, Computer Science and Engineering Department, Thapar Institute of Engineering and Technology, Patiala, Punjab, India; for providing me the necessary administrative assistance in completion of the work. I am also thankful to my Ph.D. committee members, **Dr. Parteek Bhatia**, **Dr. Rajiv Kumar** and **Dr. Amit Kumar**, Thapar Institute of Engineering and Technology, Patiala for their constructive comments and regularly ensuring the progress of my research work. Lastly, I am thankful to all the **faculty** and **staff** members of the department for their kind support.

I offer my deepest gratitude to my loving parents, **Sh. Padmesh Kumar Jindal**, **Smt. Sunita Devi** and sisters **Mrs. Parul Sharma**, **Mrs. Swati Singla**, whose love and affectionate blessings have been a constant source of inspiration in making my vision a reality. I also acknowledge the cooperation and encouragement extended to me by my friends, especially **Ms. Monika Bharti**, **Mr. Amritpal Singh** and **Mr. Abhishek Khanna**.

The chain of gratitude would be definitely incomplete without thanking the **Almighty**, the prime mover, for inspiring and guiding me (a humble being) to complete this task successfully.

Patiala

February, 2018

Himanshu Jindal

(Himanshu Jindal)

ii

Abstract

Water, being an essential component for survival of flora and fauna and covers almost 71.4% area on the Earth. It undergoes various chemical, thermal and physical changes due to man-made and natural hazard which deteriorate the water quality. In order to monitor the quality of water with respect to its physical parameters such as Electrical Conductivity, pH, Temperature, Chloride and Dissolved Oxygen, a consistent monitoring methodology is required. For the purpose, the different sampling techniques were suggested earlier that focused on evaluating underwater quality through sample collection manually from various locations. These samples are further sent for laboratory testing which is time consuming process. The techniques face various challenges like manpower, continuous monitoring, high cost and complex installation. To address the challenges, Underwater Sensor Network *(UWSN)* came into existence that targets to gather data through the sensors as a wired or wireless network. These network exhibits some limitations such as acoustic communication, large number of sensors, low bandwidth, high latency, high bit error rate, limited energy and data storage. Due to these limitations, they suffer inefficient means for communication between sensors and surface station.

As an improvement, the Underwater Acoustic Sensor network *(UWASN)*, a networking methodology of *UWSN*, is used for communication. *UWASN* consists of variable number of sensors and autonomous vehicles, to perform collaborative monitoring tasks over targeted area. These network captures physical parameters and images using different kind of sensors and forward them to surface station through acoustical signals. The acoustic signals have less propagation speed in underwater due to water constraints like path loss, ambient noise, propagation delay, high bit error rates, fading and Doppler effect, therefore, affects the data transmission and produces impaired sensed data. Moreover, the battery power of sensors is limited and are prone to failure. In summary, to deal with water constraints and to perform efficient data monitoring in underwater, there is a need to design energy efficient sensor and topologies.

Therefore, in this work, a Multi-Parametric Sensor *(MPS)*, two topologies, *namely*, Multi-Parametric Sensor Topology *(MPST)*, Triangular Pyramidal Topology *(TPT)* and a technique for image transmission, are proposed. The two image refinement techniques *i.e.*,

Mosaicing and Ridgelet based Fusion, are applied. The *MPS* is an integration of different parametric sensors and a camera fabricated on Arduino board. It is used in *MPST* to measure physical parameters in river water. It minimizes energy consumption due to single hop communication. Its main features are energy efficient, in-expensive infrastructure, less manpower, longer sustainability and can cope with varying currents of water. *MPST* provides optimal coverage by minimizing the overlapping sensing areas and has assumed the area under anchored sensor as negligible. In *MPST* few of the sensors get displaced from its position due to currents of river that leads to increase in errors of localization and communication. Therefore, to improve its efficiency, *TPT* is proposed. As an extension to *MPST*, *TPT* provides full coverage of the targeted region considering the communication range under anchored sensor. It helps in detecting physical parameters' data in cost-effective manner and uses Dynamic Source Routing *(DSR)* protocol for data transmission.

In order to transmit captured data and images to surface station without negligible errors, a *Hybrid-OFDM* based image transmission technique is proposed. The technique uses various modulation schemes such as Phase Shift Keying for communication. The gathered images are blended and refined to produce big canvas using mosaicing technique. It helps to visualize wider area of targeted region. In order to improve pixel's intensities along edges and visual quality of panoramic images, Ridgelet based Fusion technique is proposed. The technique helps to overcome few issues like poor visibility, distortion, light scattering, wavelength attenuation due to water currents, varying colors with increase in depth, and refines images using fusion techniques. It provides better visual quality panoramic images having high pixel intensities, high content information and minimal erred pixels.

Contents

List of Figures

List of Tables

List of Algorithms

List of Symbols

Symbols	Meaning
d_a	Distance among Sensors
r_c	Sensing Range
ϑ	Ratio of Covered and Targeted Area
$\mathscr{A}^{\Delta}_{KLM}$	Uncovered Area
e	Edge of Triangular Pyramid
s	Slant of Triangular Pyramid
h	Height of Triangular Pyramid
a	Length of Side of Triangular Pyramid
H_t	Depth of River
I_A	Intensity at near Location
I_B	Intensity at far Location
T_l	Transmission Loss
S_l	Source Level
ν	Noise Constant
P_{w_a}	Power Consumption
A_l	Path Loss
f_{all}	Frequency
l	Spreading Factor
N_H	Number of Hops
T_x	Transmission Time
$E_{single_{total}}$	Energy Consumed
$E_{c_{total}}$	Total Energy Consumed
$P_{w_{single}}$	Power consumed in Single-hop
K_p	Number of Packets
A_p	Loss in Multi-path Propagation
β	Absorption Coefficient
D_s	Depth (in kms)
Nl	Ambient Noise

Nt	Turbulence Noise
Ns	Shipping Noise
Nw	Wave Noise
Nth	Thermal Noise
dp	Doppler Scaling Factor
c	Acoustic Signal Propagation Speed
$Dp_e(\upsilon,t)$	Doppler Effect
$amp_P(t)$	Amplitudes of Channel
υ_P	Delays
P_s	Propagation Speed
T_{i_1}, T_{i_2}	Signal Time
D_v	Directional Vector
ME_{err}	Mean Estimation Error
(X_i, Y_i)	Sensor's Position
(X_i', Y_i')	Localization Estimated Position of Sensor
R_T	Radius under Transmission Range
R_D	Radius under Detection Range
S_{BoS}	Bottom Sensors
S_{AS}	Anchored Sensors
Pr	Poisson Distribution
$F(r)$	Cumulative Distribution Function
λ	Density of Sensor
$f(r)$	Probability Density Function
$J_{S_{BoS}}, J_{S_{AS}}$	Energy Consumed at S_{BoS}, S_{AS}
En_{total}	Total Energy Consumption
SS_{DC}	Data Collector
N_c	Total Number of Sensor's Clusters
E_s	Energy of Sensor.
Dr_b	Bit Duration.
S_{AS_H}	Anchored Sensor as Head
σ	Standard Deviation
B	Input Image
h	Row Data
w	Column Data
$Basetx$	Bits or Symbol Data

$carrierct$	Total Size of Bits
fr	Frequency
$symblcarrier$	Carrier of Symbols
$symblframe$	Frame of Symbols
$framelen$	Length of Frame
$framedata$	Data of Frame
$Timetx$	Modulation Time
SNR	Channel Noise
$numframe$	Total Frame Count
$B1$	Received Image
$Loc(L,M,\varphi)$	Scale Space Construction
$G_f(L,M,\varphi)$	Gaussian Filtering
$Im(L,M)$	Input Image
$G_M(L,M)$	Magnitude of Gradient
$\Theta(L,M)$	Orientation
$matchInd$	Modeling Image
xp	Parameter Vector
$ndgrid$	Stitching Image
T	Transformation
F_{avg}	Fusion by Average Technique
$I_{A_{ij}}$, $I_{B_{ij}}$	Images of Same Location
F_{max}	Fusion by Maximum Technique
F_{min}	Fusion by Minimum Technique
$I_{intensity}$	Intensity
υ_1, υ_2	Intermediate Variables in Cartesian Coordinate System
η	Fraction of Gray Image to low Resolution Intensity
M_{Ev}	Matrix of Eigen Vectors
C_{VM}	Covariance Matrix
D_{g_m}	Diagonal Non-zero Elements
$\psi_{a,b,\theta}$	Ridgelet *2D* function
b	Translation Parameter
a	Dilatation Parameter
θ	Direction Parameter
Rts	Radon Transform
rs	Ridgelet Coefficients

M_a	Finite Field
M_a^2	Distinguished Lattice
$R_{i,j}$	Collection of Points
$L_{p,q}$	Set of Pixels
$f_r(y)$	Bivariate Function
E_0, E_1	Low and High pass Filters
μ	Mean
C	Covariance of Image
$I_{In_{i,j}}$	Input Fused Image
$I_{F_{i,j}}$	Resultant Fused Image

List of Abbreviations

Abbreviations	Description
16PSK	16-bit Phase Shift Keying
256PSK	256-bit Phase Shift Keying
3DUL	Three-Dimensional Underwater Localization
3DUT	3-Dimensional Underwater Target Tracking
AoA	Angle of Arrival
AODV	Ad-Hoc on Demand Vector
AS	Anchored Sensor
ASCII	American Standard Code for Information Interchange
ASSL	Autonomic System Specification Language
AUV	Autonomous Underwater Vehicles
BAN	Body Area Network
BER	Bit Error Rate
BoS	Bottom Sensors
BPSK	Binary Phase Shift Keying
BT-FIDA	Backtracking based Installation Field Deployment Algorithm
CCOR	Congestion Control
CDF	Cumulative Density Function
CDMA	Collision Detection Multiple Access
CH	Cluster Head
Cl	Chloride
CLAHE	Contrast Limited Adaptive Histogram Equalization
DBMS	Database Management Systems
DCA	Distributed Coverage Algorithm
DCP	Dark Channel Prior
DisSenT	DistriNet Sensor Network Toolkit
DO	Dissolved Oxygen
DOC	Dissolved Organic Carbon
DoG	Difference of Gaussian

DSN	Destination Sequence Number
DSR	Dynamic Source Routing
DTN	Delay/Disruption Tolerant Network
DWT	Discrete Wavelet Transform
EC	Electrical Conductivity
EIMS	Environmental Information Management Systems
FDOM	Flurescent Dissolved Organic Matter
FFT	Fast Fourier Transform
FIA	Future Internet Architecture
FOV	Field of View
FRAT	Finite Radon Transform
FRIT	Finite Ridgelet Transform
GIS	Geographical Information System
GMRE	Greedy Maximum Residual Energy
GP	Gaussian Process
GPS	Global Positioning System
GUI	Graphical User Interface
HDR	High Dynamic Range
HSI	Hue Saturation Intensity
Hybrid-OFDM	Hybrid-Orthogonal Frequency Division Modulation
IDE	Integrated Development Environment
IFFT	Inverse Fast Fourier Transform
IHS	Intensity Hue Saturation
ISI	Inter-Symbol Interference
LAN	Local Area Networks
LOS	Loss of Signals
MCCP	Minimum-Cost Clustering Protocol
MILP	Mixed Integer Linear Programming
MPS	Multi-Parametric Sensors
MPST	Multi-Parametric Sensors' Topology
MSE	Mean Squared Error
NN	Neural Network
OLSR	Optimized Link State Routing
PCA	Principal Component Analysis
PDF	Probability Density Function

PSK	Phase Shift Keying
PSNR	Peak Signal to Noise Ratio
QAM	Quadrature Amplitude Modulation
QOSTFC	Quasi-Orthogonal Space-Time-Frequency Codes
QPSK	Quadrature Phase Shift Keying
RANSAC	Random Consensus Algorithm
RERR	Route Error
RF	Radio Frequency
RM	Random Movement
RREP	Route Reply Message
RREQ	Route Request Message
RSS	Received Signal Strength
RTRM	Real-Time Remote Monitoring
SEMM	Sensor Energy Management Method
SIFT	Scale Invariant Feature Transform
SNR	Signal to Noise Ratio
SSIM	Structural Similarity Index Metrics
SURF	Speeded Up Robust Feature
S-TDMA	Spatial Time Division Multiple Access
TDMA	Time Division Multiple Access
TDoA	Time Difference of Arrival
TDS	Total Dissolved Solids
ToA	Time of Arrival
TPT	Triangular Pyramidal Topology
UV-VIS	UltraViolet-Visible
UWASN	Underwater Acoustic Sensor Network
WMN	Wireless Mesh Network
WOAG	*WSN* OpenAPI Gateway
WoT	Web-of-Things
WPAN	Wireless Personal Area Network
WSN	Wireless Sensor Network

Chapter 1

Introduction

With the advancement in the communication technology and deployment strategies, Wireless Sensor Network (*WSN*) has emerged as a promising domain. *WSN* is composed of spatially distributed autonomous devices, *i.e.*, intelligent sensors, to measure physical or environmental conditions. A sensor has various components such as a radio transceiver with an internal antenna, micro-controller and electronic circuit(s) (Orumwense et al. (2016)). With the advances in *WSN* and their pervasive deployment for information gathering, various networks on land, underground, underwater and multimedia have been described. Among them, Underwater Acoustic Sensor Network (*UWASN*) is required for regular water quality monitoring, surveillance and navigation purposes. It is self-configurable, service oriented wireless communication network that aims to transmit monitored data to the base station through angular acoustic waves. For the purpose, it uses various sensors for collaborative monitoring over a deployed region. The future *UWASN* needs to have proficient communication capabilities to sustain in the underwater for longer periods with sleep or awake scheme.

1.1 Wireless Sensor Network

The sensor is a physical device that may vary in sizes, property and functionality in accordance to the application (Climent et al. (2012); Fonseca et al. (2015)). For example, temperature and ultrasonic sensors are used for measuring room temperature and finding obstacles, respectively. The basic structure of a sensor is shown in Figure 1.1. Each sensor has main

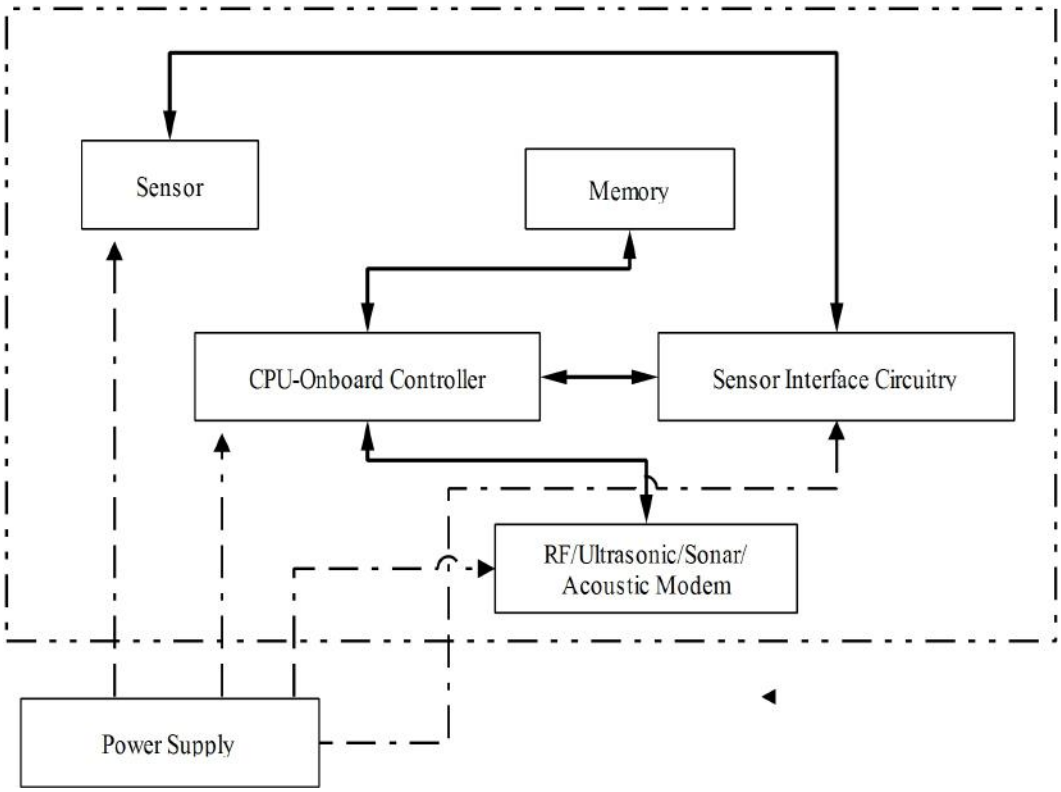

Figure 1.1: Sensor Architecture

controller unit, *i.e.*, *CPU* which is inter-linked with sensor interface circuitry and on-board storage for storing the sensed data. This data is further transmitted to the surface station *via* waves like Radio Frequency (*RF*), ultrasonic and sonar. Each sensor is protected with Poly Vinyl Chloride (*PVC*) housing (Sozer et al. (2000)) and is equipped with battery operable components before it is deployed in the hostile environment (Fiorelli et al. (2006); Proakis et al. (2001)). It is due to the battery dissipation issue that affects the lifetime of the sensor while processing sensed data. To meet the issue, various scheduling techniques like sleep or wakeup, Time Division Multiple Access *(TDMA)*, Collision Detection Multiple Access *(CDMA)* schemes, *etc.*, are suggested (Lloret (2013)). These techniques enable sensors to transmit data to the surface station efficiently.

WSN is a collection of sensors deployed over some geographical area for sensing and monitoring the physical activities like climate, humidity, fluctuations, *etc*. A typical architecture of *WSN* is shown in Figure 1.2 (Lloret (2013)). It is capable of interacting with the environment by processing the sensed data. The sensors collaboratively interact among each other to send the buffered data as it is not possible for single sensor to process the data.

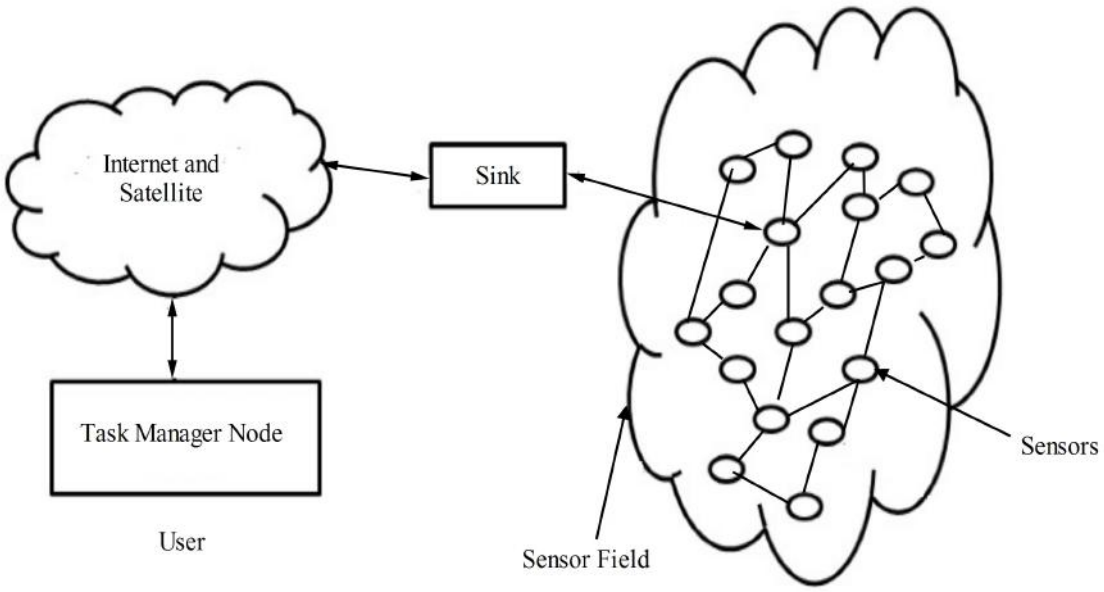

Figure 1.2: Sensor Network scattered in a Field

1.1.1 Types of *WSN*

On the basis of deployment, *WSN* is categorized into following types (Climent et al. (2012)).

i. **Terrestrial *WSN*:** It is created with hundreds to thousands of inexpensive wireless sensors deployed in a given area *via* an ad-hoc or a pre-planned manner. Another important consideration is the reliable communication in a dense environment where each sensor must be able to effectively communicate data back to the base station.

ii. **Underground *WSN*:** To monitor underground conditions, a network composed of number of sensors are buried underground or in a cave, mine. Sink nodes are located above ground to relay information from the sensors to the surface station. An underground *WSN* is more expensive than a terrestrial *WSN* with respect to equipment, deployment and maintenance.

iii. **Multimedia *WSN*:** It is used for monitoring and tracking of events like audio, moving text, video, *etc*. The network consists of a number of low cost sensors equipped with cameras, microphones and interconnects among each other over a wireless connection for data retrieval.

iv. **Underwater *WSN*:** In this type of network, sensors are deployed underwater along with autonomous underwater vehicles to gather data for exploration. In comparison to terrestrial *WSN*, a sparse deployment of sensors is positioned underwater and underwater wireless communications are performed using ultrasonic, sonar and acoustic waves.

Among these types of *WSN*, work proposed in this thesis has focused on *UWASN*, a networking methodology based on underwater *WSN*.

1.2 Underwater Acoustic Sensor Network

Underwater *WSN* enable sensors to explore and predict the sea environment. *UWASN* is an enabling technology of underwater *WSN*, used for monitoring and surveillance applications. It is self-organized network that enable sensors to adapt underwater environment and to perform collaborative monitoring *via* acoustic links over the deployed area (Akyildiz (2007)). It was initially deployed to explore hostile environment during the *World War II* in *1945* to analyze the unknown hindrances. During that period, issues such as limited bandwidth, propagation delay, noise, sensing and subsequent transmission have resulted in to unstable communication. Therefore, *UWASN* needs to be investigated throughly with respect to various application areas in order to eliminate these issues. The various application areas of *UWASN* are savor networks, tremors monitoring, prevention of disaster, undersea explorations, reinforced navigation, distributed surveillance scattering and monitoring accessories, environment (Chryssostomidis (1991); Bellingham (2003)).

1.2.1 Communication Methodology

The communication methodology for underwater is through optical, radio, electromagnetic and acoustics waves. The electromagnetic waves are used at very low level as they propagate to short distances. The acoustics waves are used to provide high speed communication among the sensors and to carry digital data through the channel which in turn provide better communication. Optical and radio waves are used when there is a wire communication whereas heavy cables are used for wired construction underwater. The communication in

underwater is done through single hoping and multiple hoping (Catipovic (1990); Akyildiz et al. (2002)).

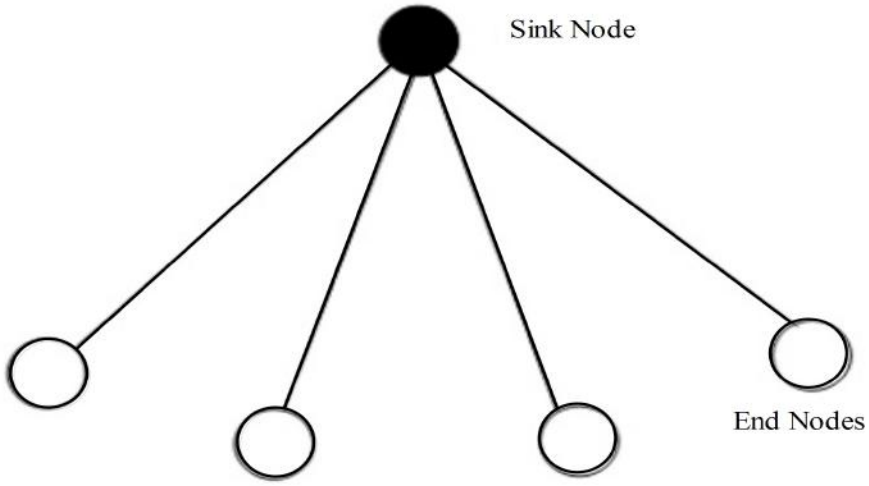

Figure 1.3: Single Hoping

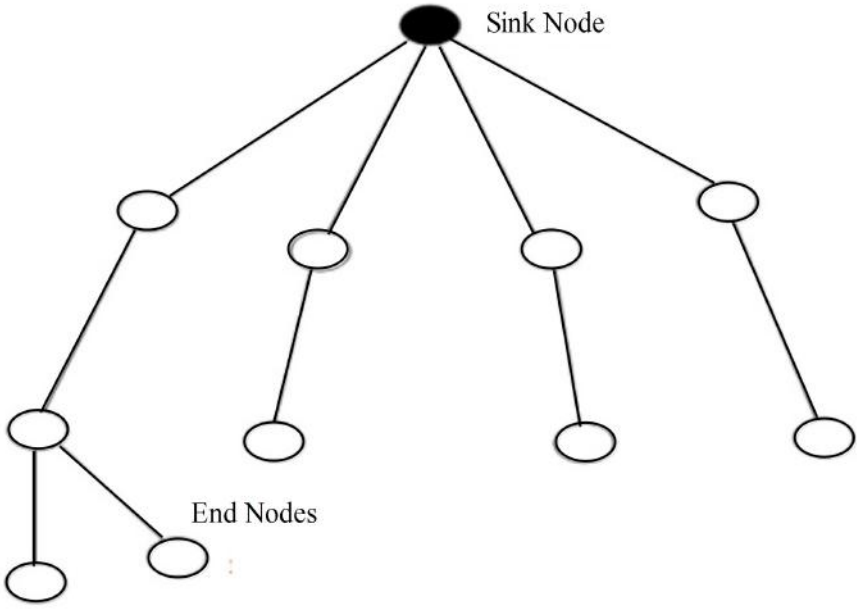

Figure 1.4: Multiple Hoping

In former, there is only one hop between destination and host. In latter, there are multiple hops or nodes between the host and destination which are used for underwater communication.

1.2.2 Factors Affecting Communication in *UWASN*

The factors like path loss, noise, multi-path, Doppler spread, propagation delay affect acoustic communication with changing physical parameters' variability of the channel. They bound the available bandwidth of the acoustic channel where bandwidth relies on both range and frequency. Long-range systems with bandwidth upto few *KHz* run over several tens of kilometers (*km*) whereas a short-range system have more than a hundred *KHz* bandwidth working over tens of meters and has low bit rates. The acoustic communication links are categorized on the basis of their range and direction in which sound waves travel as vertical and horizontal. With respect to time dissipation, multi-path delay spreads, delay variance and their propagation characteristics differ consistently (Proakis et al. (2001); Freitag et al. (2001); Brekhovskikh and Lysanov (2003)). These factors are described below.

i. **Path loss:** The transfer of acoustic energy into heat results into path loss or attenuation that increases with distance and frequency. Path loss is determined by the depth of water. It gets affected by dispersion, refraction, and diffraction.

ii. **Geometric Spreading:** The expansion of the wavefronts results in to scattering of energy produced by sound and is affected with the propagation distance but is independent of frequency. The two types of geometric spreading are sphere-shaped and cylinder-shaped.

iii. **Noise:** The noise is produced by different sources at different frequencies that affects the communication. It is classified into two types, *i.e.*, *man-made* and *ambient noise*. The former is caused by machine and shipping activities whereas the latter is related to hydraulics, unstable and natural phenomena.

iv. **Multi-path:** The degradation of the acoustic communication is due to multi-path extension. The link configuration is generated by multi-path geometry where vertical channels are distinguished by little time dispersion and horizontal channels have extreme long multi-path spreads, whose value rely on the water depth.

v. **High delay and delay variance:** The propagation speed is the amount of time taken to transmit data from source to destination. It depends on the medium of communication.

It is five orders of magnitude lower than in radio channel in *UWASN*. This results into large propagation delay which is a measured by ratio of distance of communication medium to propagation speed. Hence, this large propagation delay can reduce the system's throughput.

vi. **Doppler spread:** Doppler spread causes a degradation in the performance of digital communications, *i.e.*, transmissions at a high data rate cause many adjacent symbols to interfere at surface station. It generates two effects *i.e.*, a simple frequency translation and a continuous spreading of frequencies, which constitutes a non-shifted acoustic signal. While the former is easily compensated at surface station, the effect of the latter is harder to compensate.

1.2.3 Topological Challenges in *UWASN*

The design of underwater communication differs from terrestrial network with respect to its cost, energy consumption, deployment, data gathering and storage capacity. The various challenges that come across in underwater communications providing a design for *UWASN* are described below (Glegg et al. (2000); Jurdak et al. (2004)).

i. **Cost:** The underwater sensors are costlier as compared with terrestrial nodes. It is due to the complexity of underwater' transceivers and the hardware protection which is needed in extreme environment.

ii. **Power:** As there is use of *RF* waves in underwater through various physical architectures or designs, the high power is needed for underwater communications.

iii. **Deployment:** With respect to deployment of sensor network in underwater, it is sparser as compared with terrestrial sensor network which are densely deployed.

iv. **Correlation Geographically:** The terrestrial sensors correlate geographically easily and is difficult in *UWASN* because there is a greater distance among sensors.

v. **Memory:** The sensors having larger capacities for data caching are needed in underwater as compared to terrestrial sensors, where limited storage capacity is required.

In order to deploy *UWASN* that sustain for longer period and gathers maximum data of the environment, various strategies are adopted. These are discussed with its pros and cons in the next subsection.

1.2.4 Deployment Strategies

UWASN provides communication coverage as the sensors establish multi-hop routing and sending data of the supervised area to the surface station. The sensors sense the region in a sphere due to its omni-directional nature. The three approaches that have been widely used for *UWASN* are described below (Jindal et al. (2014)).

i. **Two Dimensional Deployment**: The sensors which act as Cluster Head, are anchored at the bottom and are connected to the Underwater Gateways (*UW-Gateways*) by means of wireless acoustic links in Two Dimensional *(2D)* deployment. *UW-Gateways* are network devices that communicate by sending the data from bottom to the surface station. For the purpose, they are equipped with two acoustic transceivers known as vertical and horizontal transceiver. The former is used by the *UW-gateways* to send forth the details to surface station. The latter is used for communication to: (i) send data from *UW-gateway* to sensors, and (ii) collect the supervised details, *i.e.*, from sensors to *UW-gateway*, as shown in Figure 1.5. When dealing with various underwater applications, the long range vertical transceivers are required. As there are multiple parallel communication links with deployed *UW-gateways*, the outside terminal is equipped with a detection device having acoustic signals and a long-range *RF* for transferring data to the onshore sink (*OS-sink*) or to a surface sink (*S-sink*). In case of shallow water, sensors deployed at the bottom can communicate directly with the surface buoy (Sozer et al. (2000)).

ii. **Three Dimensional Deployment**: The Three Dimensional *(3D)* deployment is used for performing the synergistic experiment of underwater *3D* environment. Here, the sensors float at a certain depth for observing a process and are tied with a floating buoy. It is docked at bottom as shown in Figure 1.6 (Jindal and Sharma (2011)). There is an electronically controlled engine embedded on the chip board that regulates the depth

of sensors by altering the wire's length.

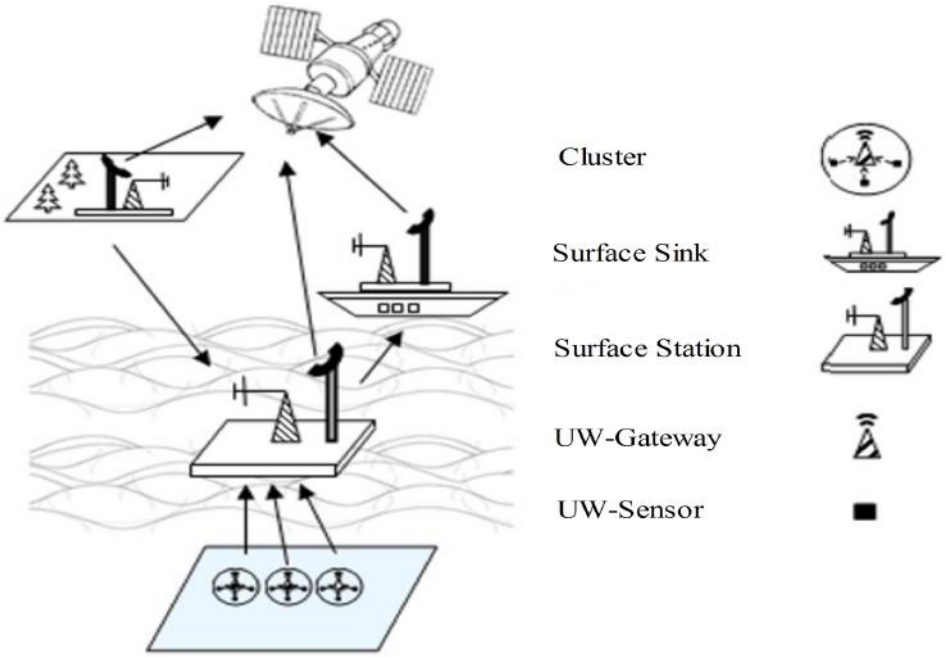

Figure 1.5: *2D* Deployment

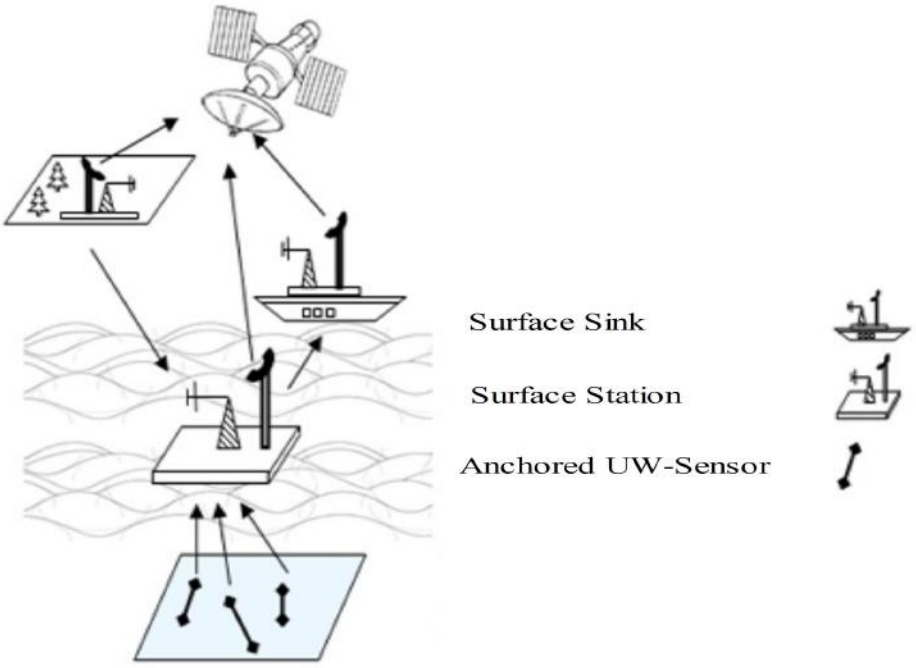

Figure 1.6: *3D* Deployment

iii. ***3D* deployment with Autonomous Underwater Vehicles**: The Autonomous Underwater Vehicles (*AUV*) work without wires and their movement is controlled by user.

The integration of *UWASN* with *AUV* provides a network circuitry coordination algorithms as explained below.

- **Adaptive Sampling:** This includes control strategies to command the mobile vehicles to places where their data will be most useful. For example, the density of sensors can be adaptively increased in a given area when a higher sampling rate is needed for a given monitored phenomenon.
- **Self-configuration**: This includes control procedures to automatically detect connectivity holes due to sensor's failures or channel impairment, and request the intervention of an *AUV*. Furthermore, *AUV*s can either be used for installation and maintenance of the sensor network infrastructure or to deploy new sensors.

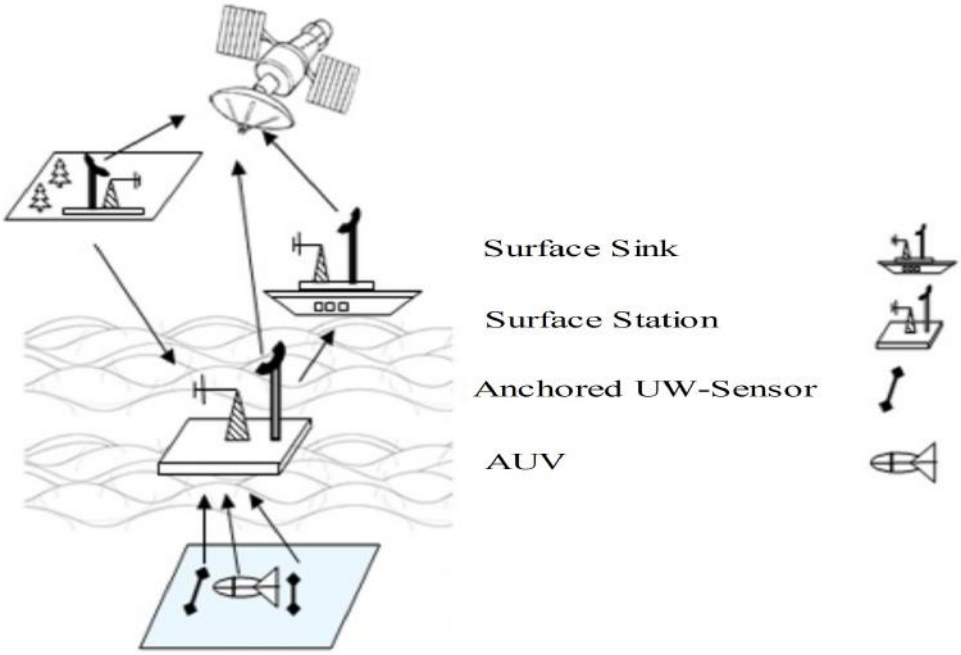

Figure 1.7: *AUV* deployment in *3D*

The comparison among various deployment strategies are summarized in Table 1.1. It is observed that there is a major concern of communication among devices in *UWASN*, if *2D* deployment schema is considered. But it is quite possible for getting information of whole area in *3D* as well as in *3D* with autonomous vehicles schemes but maintenance and complexity are the issues in these schemes. Therefore, there is a need to regulate and maintain

Table 1.1: Comparison among Deployment Strategies in *UWASN*

Techniques $\longrightarrow$ **Properties**	***2D* Deployment**	***3D* Deployment**	***3D* Deployment with *AUV***
Battery Consumption	Less consumption	More consumption	More consumption
Failure	Less prone to failure	More prone to failure	More prone to failure
Cost	Cheap	Costly	Very costly
Complexity	Less complex	Complex	More complex
Sensor's Deployment	Anchored sensors	Floating sensors	Floating sensors
Bandwidth	Less bandwidth ,*i.e.*, < 1	More bandwidth ,*i.e.*, 2-5	Large bandwidth ,*i.e.*, ~ 10
Range	Long range upto 100 kms	Less range upto 10 kms	Less range upto 10 kms
Hoping technique	Horizontal and vertical multi-hop	Vertical multi-hop	Vertical multi-hop
Communication	Radio waves are used in vertical and horizontal communication	Acoustic communication is vertical	Acoustic vertical communication
Area coverage	Not full area coverage	Coverage of entire area	Coverage of entire area
Reliability	Less reliable	More reliable	More reliable
Nodes Displacement	Fixed number of nodes	Random nodes are displaced at the bottom	Random nodes are displaced using a grid

deployments if *3D* or *3D* with autonomous schemes are used for acoustic communications. Thus, an optimized designing of communication strategy should be adopted which is adaptable to the characteristics of *UWASN* for monitoring, recording of data in underwater set up.

1.3 Image Transmission in *UWASN*

UWASN is used to capture images in underwater for getting information and it comes out to be beneficial as the images provide significant data for analysis (Jindal et al. (2017d)). *UWASN* retrieve, process, store, correlate, and merge image streams originated from hetero-

geneous sources in real-time. The captured images are further transmitted to surface station for analysis process. But during transmission, the lifetime of sensor network is decreased quickly due to limited battery, storage capacity and computational power constraints. Also, the surface station gathers, filters and aggregates data sent by sensors in order to extract useful information. But the extraction does not provide complete information as the data loss occur due to Doppler spread, path loss and propagation delay, during transmission.

Various measures are adopted to improve image transmission methodology and different refinement techniques are implemented to improve the quality of image having reliable information. The main motive of image transmission is to develop panoramic images that will be generated from sequence of captured images. The image transmission and refinement takes place in following steps:

i. **Capturing:** The image is captured using sensors.

ii. **Composition:** The lightening and temperature are adjusted to clear the image.

iii. **Removing Halos:** The shadows and blurriness are removed from captured images.

iv. **Detail:** The local contrast enhancement of blurred images is performed.

v. **Framing:** The enhanced images are straightened to produce panoramic image.

vi. **Refinements:** The refinement technique is implemented to enhance panoramic image using various color combinations.

vii. **Output:** The panoramic images are blended for better results.

1.4 Thesis Organization

The thesis has been organized as per following chapters.

Chapter 1: Introduction

This chapter discusses the basics related to *WSN*, *UWASN*, its communication methodologies and emerging key challenges that influence acoustic communications. It focuses on topology designing constraints and various deployment strategies towards maximum coverage of

deployed region. The image transmission and refinement process in *UWASN* has also been discussed.

Chapter 2: Literature Review

The comprehensive survey of work done in the area of *UWASN* is carried out in this chapter; highlighting the various deployment strategies, protocols, techniques, topologies for communication, and panoramic image refinement techniques based on edge preservation, enhancement and mosaicing. The various energy harvesting mechanism used for providing energy to devices underwater have also been suggested.

Chapter 3: Research Methodology

The chapter presents the extensive study of the specifications, data transmission and refinement techniques. It highlights the various sensors calibrated on circuitry board, techniques that are used to sustain Multi-Parametric Sensors *(MPS)* underwater for longer periods, techniques for finding *MPS*'s relative position for communication and refining techniques that are applied on gathered underwater images for better visualization. The methodology also outlines the thesis contributions.

Chapter 4: Multi-Parametric Sensors' Topology

This chapter proposes Multi-Parametric Sensors' Topology (*MPST*) for river water quality monitoring. It helps to check physical parameters of river water through *MPS*. It proves to be energy efficient, sustainable, cost-effective and reduces acoustical path loss as compared with existing sampling technique.

Chapter 5: Triangular Pyramidal Topology: An Extension to Multi-Parametric Sensors' Topology

With extending the topological factors with respect to coverage, connectivity and communication, Triangular Pyramidal Topology (*TPT*), an extension to *MPST* is proposed in this chapter that provides optimized monitoring covering large area. It consumes minimum power while monitoring and is sustainable in underwater for longer periods. It uses Dy-

namic Source Routing (*DSR*) protocol for routing data to surface station and proves to be self-configuring and extensible technique for monitoring river water.

Chapter 6: Hybrid-OFDM based Panoramic Image Transmission and Refinement using Mosaicing

A Panoramic Image Transmission and Refinement Technique is proposed in this chapter. It uses *Hybrid-OFDM* for transmitting captured underwater pipeline images without any loss in pixels. The technique uses mosaicing algorithm for producing panoramic images that helps to rectify the joints and corroded areas of pipe, and to prevent leakages by taking suitable measures.

Chapter 7: Ridgelet based Fusion Technique for Panoramic Image Refinement

This chapter proposes a technique to refine panoramic underwater images using Ridgelet. It fuses together two or more images of same location to produce good quality image. The proposed technique generates images that are rich in edge preservation, color, free from line discontinuities and are smooth along edges. It enhances the visualization quality of images and is a better technique for panoramic image refinement.

Chapter 8: Conclusion and Future Scope

The chapter concludes the thesis outcome and provides an insight into the future scope of the work.

Chapter 2

Literature Review

2.1 Introduction

The chapter highlights the most comprehensive contributions in the field of *UWASN* with respect to underwater data communication and image refinement. The former, *i.e.*, data communication includes deployment strategies, protocols and network topologies. The latter covers different techniques for image refinement such as edge preservation, enhancement and mosaicing. A general, comprehensive and structured overview of existing techniques are described. The literature overview is shown in Figure 2.1.

2.2 Underwater Data Transmission Techniques

Due to hostile environment of underwater, human reach is quite difficult. Therefore, sensors are deployed in underwater to help sensing and transmitting data to surface station for further processing. For the purpose, the prior requirement is to understand distinct deployment strategies and protocols for sensors. This will help to ease in communication and computation processes. This section has provided a structured literature survey of the existing research contributions with respect to communication techniques, systems, models, algorithms based on real time simulations, test beds, and implementations of protocols on underwater sensors.

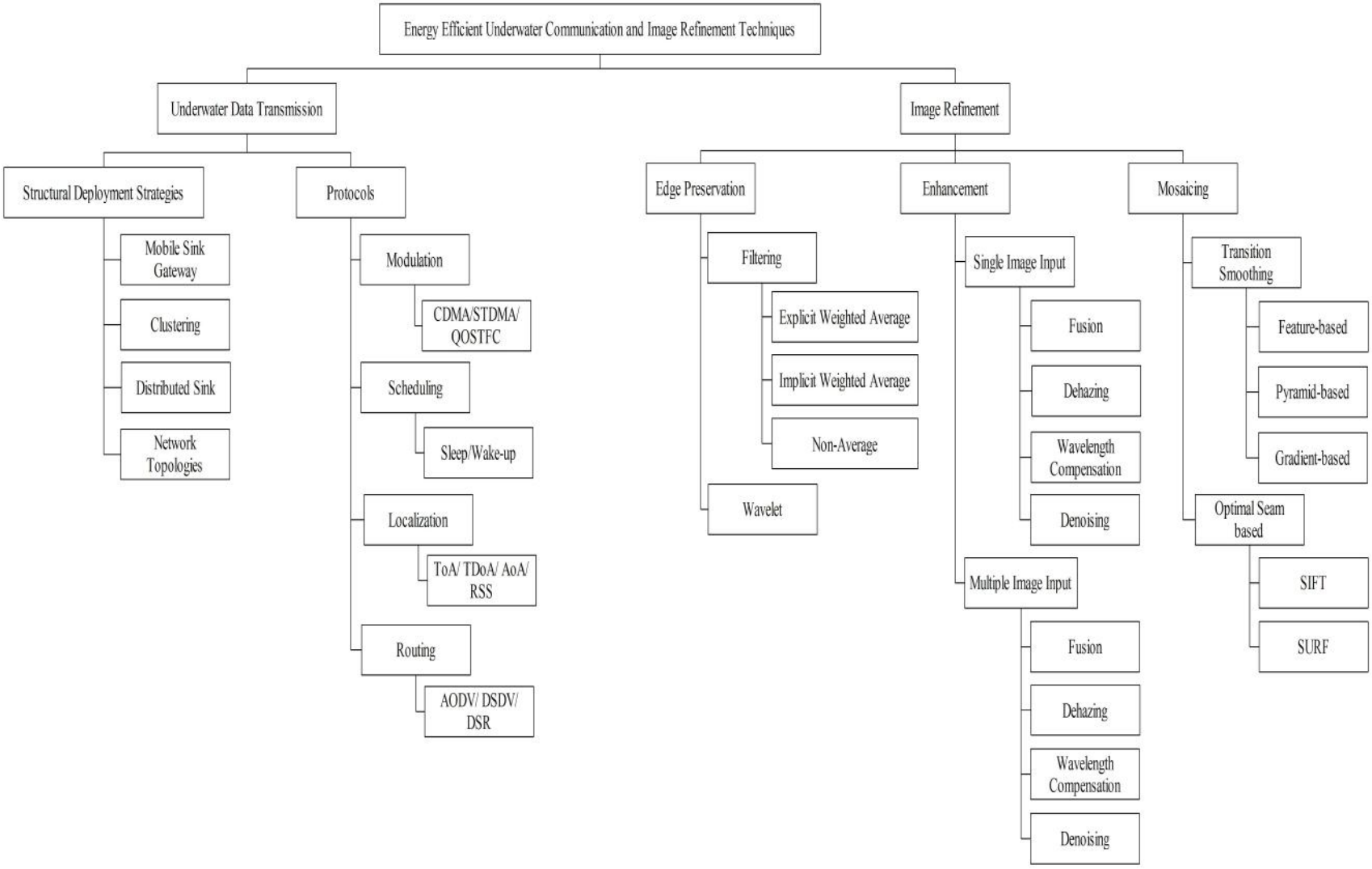

Figure 2.1: Overview of Literature for Energy Efficient Communication and Refinement Techniques

2.2.1 Structural Deployment Strategies

The deployment strategies for data transmission are broadly classified in to methodologies, *namely*, mobile sink gateway, clustering, distributed sink and network topologies. These are discussed.

i. **Mobile Sink Gateway based Techniques:** In mobile sink gateway based techniques, a mobile sensor act as an interface to transmit data among various surface stations and helps to preserve the energy of the idle sensors deployed at the bottom surface. For example, a network system for detecting underwater pipeline leakage has been designed by Tu and Chen (1999). The system helps in taking suitable actions against pipeline leakages. The system has its limitations that it detects limited portion of pipeline. To this improvement, Wu et al. (2007), have presented a modular *WSN* design that provide access to host for detecting leakages in wide area networks. The design allows the gateway to be deployed in heterogeneous network environment and enables remote upgrading. It faces few limitations that the continuous updating of design slows the process of deployment and measurement. To improve the techniques of measurement and prolonging the lifetime of *WSN*, three schemes have been postulated by Basagni et al. (2008). These schemes exploit the mobility of the network sink. For determining sink movements, *firstly*, Mixed Integer Linear Programming *(MILP)* analytical model is described. It helps in maximizing network's lifetime. The *second* scheme *namely*, Greedy Maximum Residual Energy *(GMRE)* controls distributed and localized sink movements and heuristically moves the sink from its current location to a new site. The *third* scheme, *i.e.*, Random Movement *(RM)* moves the uncontrolled sink randomly throughout the network. These schemes are compared using *NS-2* simulations and is observed that moving the sink increases network's lifetime. In order to implement these schemes on real environment, it is improved with a technique based on continuous phase distributions and Kronecker algebra (Bruneo et al. (2010)). It helps in reducing power consumption of sensors. The technique provide effectiveness in figuring wider network context with complex topology, redundant nodes, and unreliable links. To analyze sensor's failure, a mobile gateway is designed that supports Zig-

bee and blue-tooth (Angove et al. (2011)). It facilitates interaction with conventional mobile devices using wireless communication (*see* Figure 2.2) (Angove et al. (2011)).

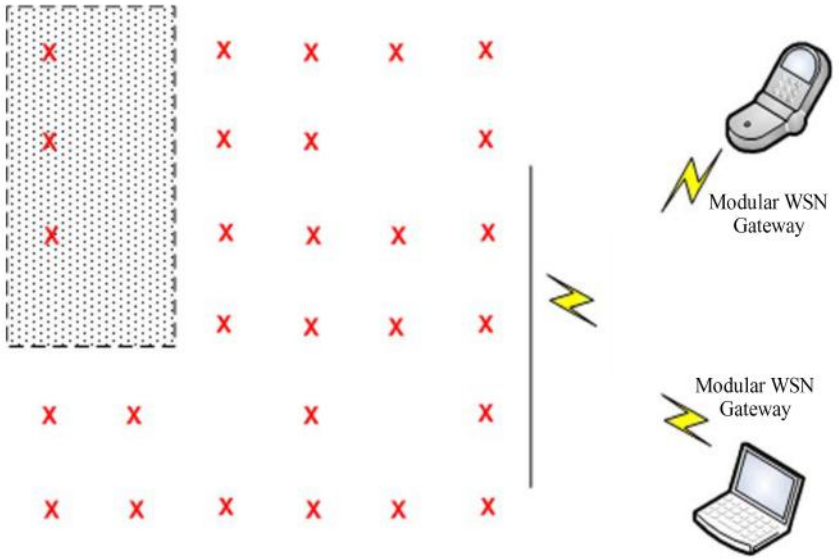

Figure 2.2: Using the Mobile Gateway to Access *WSN*

This mobile gateway is further extended for monitoring river water using a satellite *namely*, EnviSat RA-2. The satellite helps in analyzing echoes over inland water (Berry et al. (2012)). This satellite provides successful measurement of smaller water surfaces at 1800 *Hz*. It enables monitoring of smaller river systems. The satellite has its disadvantages that it provide delayed monitoring during rainfall.

Few authors have presented a name-based Future Internet Architecture *(FIA)*, such as Mobility First for *IoT* service platform (Li et al. (2013); Al-Radaei and Mishra (2013)). The architecture is ubiquitous and scalable with increasing number of smart phone users. It delivers a temperature sensor data from an Android phone directly to multiple applications. To utilize maximum resources and to deploy multiple sensors, Karvonen et al. (2014), have postulated a hierarchical architecture for *WSN*. It consumes less power by utilizing a wake-up radio signaling. The results supports the power efficiency using wake up schemes and is further used for estimating event frequency and channel conditions. Also, Morón et al. (2014), have presented health tele-monitoring system for evaluating and characterizing medical Wireless Personal

Area Network *(WPAN)* using smartphones and blue-tooth communication. The smartphone provides information gateway for gathering data from sensors and retransmits it to base station *via* Wi-Fi signal. It has its limitations while integrating with central server using cloud computing because smartphone does not provide proper gateway for gathering information. Another design, *i.e.*, handheld smartphone based *pH* sensor has been demonstrated for monitoring river water quality (Dutta et al. (2015)). It evaluates its *pH* level using bromocresol, green, chlorophenol red dyes' wavelength absorption condition. It provides reliable data but is not advantageous to deeper depth of rivers. To improve the mechanism of collecting data, a self-organizing *WSN* for remote water quality monitoring has been designed (Chung and Yoo (2015)). It helps in measuring physical parameters of water such as turbidity, *DO*, *pH*, conductivity, depth and temperature; for analyzing water quality variation in river areas. The data is stored in buffer for frequent time duration and is further transmitted to neighboring node for sending data to base station. The design has various challenges related to depth of water and multi-hop schemes.

ii. **Clustering based Techniques:** In clustering, bottom sensors are grouped together to relay data to surface station and consume more energy. In order to preserve energy, one sensor among bottom sensors is chosen as cluster head for data transmission. As an example, a cluster-centric cost-based optimization technique has been proposed for minimizing energy consumption and to increase lifetime of network (Wang et al. (2007)). The authors have also suggested Minimum-Cost Clustering Protocol *(MCCP)* for selecting potential clusters in order to reduce data-traffic during communication. This protocol is implemented in various systems for efficient transmission. Yang et al. (2008), have demonstrated an on-line water quality monitoring and management system that uses chemical oxygen demand sensor with an artificial neural network technology and a virtual instrument. It is observed from gathered information that the system provides an effective technique to water quality control for environmental protection. In order to improve the technique with automatic detection, O'Connor et al. (2011); Tripathi and Mishra, have postulated a visual sensor for off-line river monitoring. This sensor provides an estimation of extreme events at the site with longer

sustainability and involves little maintenance. It sends timely alarms to take preventive measurements. It has its limitations to pick water colors due to change of lightening in water. To this improvement, Lee et al. (2015), have suggested optical UltraViolet-Visible *(UV-Vis)* and Fluorescent Dissolved Organic Matter *(FDOM)* sensors to monitor turbidity levels in forested watersheds. These sensors are tested in both laboratory experiments and in situ monitoring in a forest stream of Korea during storm events. The results have shown the increase of turbidity concentrations in streams. These sensors face few limitations that these are very sensitive and are affected due to attenuation of light (Kumari et al. (2015)). To its improvement, few authors have considered nutrient enrichment on coastal hypoxia, harmful algal blooms, its impacts to human health and suggested the use of nutrient sensors for studying its adverse effects (Pellerin et al. (2016)). It is suggested that for minimizing risk to humans or underlying drivers, accurate and timely nutrients should be provided (Islam et al. (2017)).

iii. **Distributed Sink based Techniques:** To compute the accuracy while communicating data from bottom sensors to the surface station, techniques based on distributed sink come in to existence in which sensors are added dynamically which can act as sink node or bottom sensors for better communication. As an illustration, the key benefits of implementing and integrating a multi-layered sensor network architecture, *namely*, Environmental Information Management Systems *(EIMSs)*, for environmental data gathering have been summarized (Pokorny (2006)). The system has its limitations of retaining the data quality of processed information as shown in Figure 2.3 (Pokorny (2006)).

The system requires more sophisticated techniques for metadata processing. To retain the data quality and metadata processing, various developments in *WSN* have been studied that are used for analytical measurements (Diamond et al. (2008b)). The authors have also inhibited the integration of *WSN* with sensors and analytical devices. The various issues have come across with these integration techniques and suggest it is possible to construct a solution according to the platform and application's requirements. To analyze sensor's position more efficiently, a context model has been

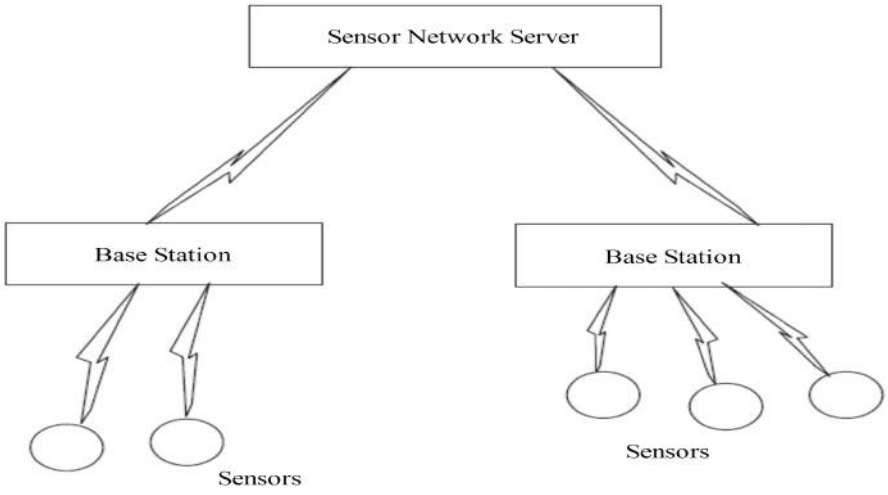

Figure 2.3: Environmental Information Management Systems

introduced that support dynamic interoperability and decision making processes (Ballari et al. (2009)). It focuses on capturing and reasoning various contexts using contextualizing and bridge rules. In order to maintain interoperability among sensors, a distributed node deployment technique is proposed by Akkaya and Newell (2009). The technique provides maximum coverage of deployed region and helps to connect new sensors in communication range. The results show that the technique outperforms well with expense to very little extra cost to each sensor in terms of messaging and transmission distance. Few researchers have proposed Neural Network *(NN)* based technique for evaluating rainfall radar images and in-situ depth measurements to predict freshwater levels of rainfall (O'Connor et al. (2012)). The technique is a low cost solution with limited data requirements to capture the dynamics of a river catchment. For providing storage and maximum monitoring data, Backtracking based Installation Field Deployment Algorithm *(BT-FIDA)* is suggested by Khalfallah et al. (2013); Prodan et al. (2014). It helps in minimizing geographical field installations along river. Its simulation results into good performance and full coverage of area but is hard to cover vast areas of Amazon rivers. In order to minimize the energy consumption, Sensor Energy Management Method *(SEMM)* has been proposed for environmental monitoring at the Amazonian Basin (Vieira et al. (2015)). The lifetime of sensors using this method is increased to 20% when compared with conventional technique. But

it faces the issue of maintainability and continuous route updating for coverage of long geographical location.

iv. **Network Topologies:** The communication is the process of transmitting sensed data to surface station with the use of sensors. These sensors are deployed in a defined manner in order to cover maximum area. The topology plays an essential role for communication as it covers maximum area with deployment of minimum number of sensors. In order to design a topology various practical or predicted designs are demonstrated. For example, various network topologies that have focused on data transfer capabilities with respect to its battery consumption, bandwidth, channel impedance, are surveyed by few authors (Sozer et al. (2000)). Also, Li et al. (2001), have discussed network topologies based on proximity graphs *namely*, Gabriel, Yao and relative neighborhood graph. The authors have suggested to maintain sparse spanner to preserve energy efficient route among sensors. It faces few limitations that these graphs don't have constant degrees of power stretch factor. Watfa and Commuri (2006a); Watfa and Commuri (2006b), have considered coverage and deployment problems in *3D* environment underwater and various techniques are implemented to compute minimum sensors deployed for full coverage of region. But due to the energy constraints of sensors in underwater, the suggested techniques fail to provide analyzed coverage area for longer period. Zhang et al. (2010), have designed low connectivity and full coverage patterns for *WSN*. The patterns optimally use minimum number of sensors and provide maximum exploration in *3D* environment. To improve the coverage pattern, Ammari and Das (2010), have postulated Reuleaux tetrahedron model to characterize k-coverage of *3D* field that consider the corresponding minimum sensor spatial density (*see* Figure 2.4) (Ammari and Das (2010)).

The model can sustain a large number of sensor failures. Even, Bai et al. (2009), have designed 14 and 6 connectivity set of patterns for full coverage of area. The design provides its optimality for *3D WSN* over sophisticated practical settings of flow or drift models in water. For wide network reliability, Three-Dimensional Underwater Localization *(3DUL)* has been introduced for achieving network with robust *3D* localization.

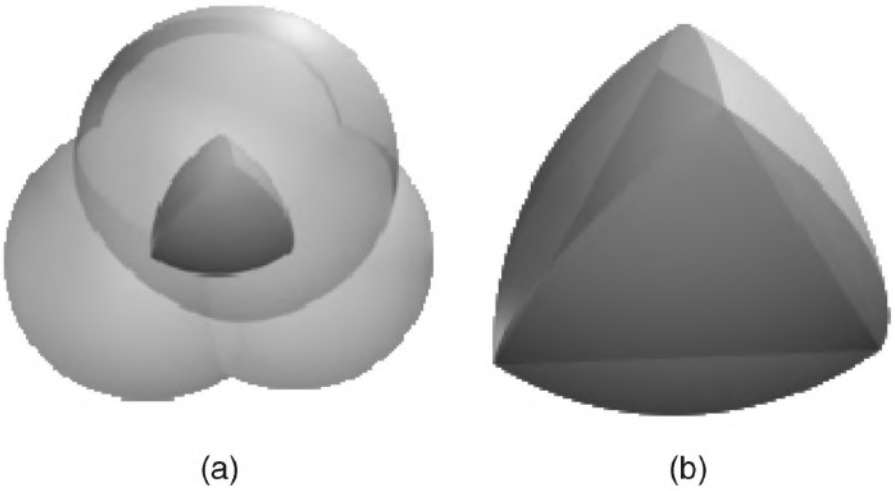

Figure 2.4: K-Coverage (a) Intersection (b) Tetrahedron

It uses a distributed and iterative technique that provides high accuracy in underwater localization and is used for *AUV* (Isik and Akan (2009)). It faces few limitations with coverage and connectivity *via AUV*. Few authors have proposed target tracking technique *namely*, *3D* Underwater Target tracking *(3DUT)* to check targets in underwater with minimum energy consumption (Isbitiren and Akan (2011)). For energy efficient tracking, it works on target-movement-based duty-cycle mechanism as shown in Figure 2.5 (Isbitiren and Akan (2011)). The proposed has its disadvantages of consuming more energy in tracking continuously. In order to cover maximum area with lesser nodes, another technique *namely*, Kelvin's conjecture, is postulated by Alam and Haas (2015); Isabona and Srivastava (2017). The authors dynamically put redundant sensors into sleep mode to increase network lifetime. It has been observed that truncated octahedral tessellation of *3D* space provide full coverage.

v. **Energy Harvesting based Techniques:** A common challenge faced by above said techniques (mobile sink, clustering, distributed sink and network topologies), is related to power dissipation of the sensors. The batteries of the sensors are energy constrained and cannot be recharged easily. Therefore, in order to preserve the energy of the sensors, few of the researchers have provided the different topologies and communication techniques in real-time and multi-modal network to gather information. The strategies are worked upon with energy efficient sensors to sustain the topology

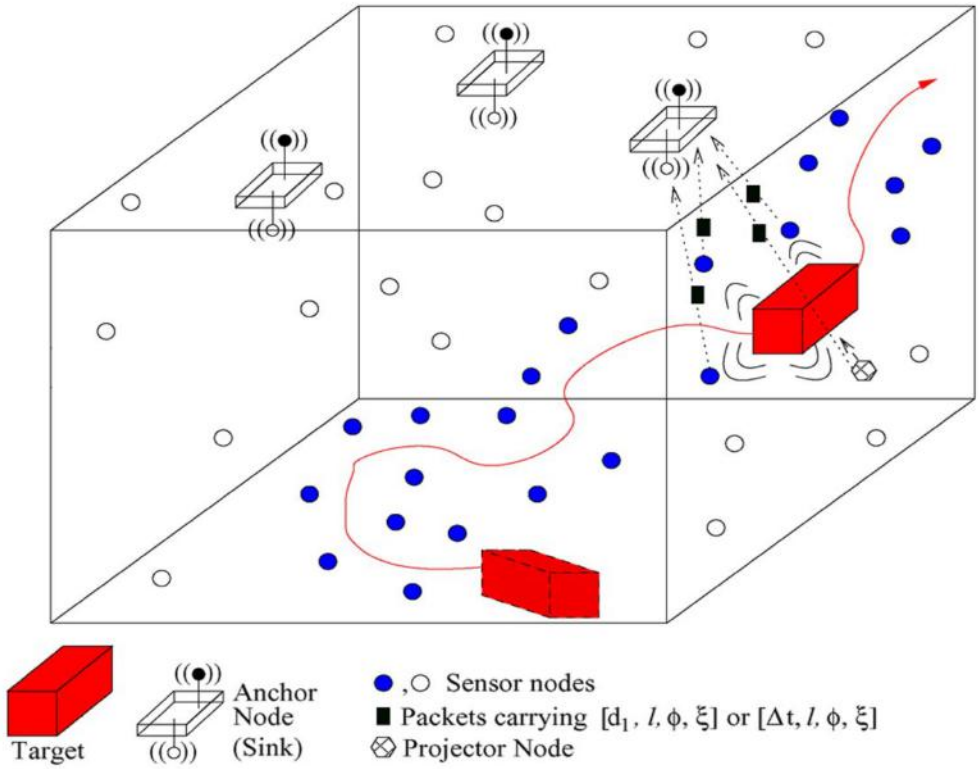

Figure 2.5: Network Model for *3DUT*

in underwater for longer periods. For the purpose, Glasgow et al. (2004), have presented Real-Time Remote Monitoring *(RTRM)* and sensing technologies for statistical and mechanistic monitoring of water quality trends. These technologies are used by federal, state regulatory agencies, industries and academic laboratories for detection of environmental threats leading to fish kill events and potential human health impacts. To its modification, a technique is suggested by Bruggen and Braeken (2006), which explores the usage of wastewater after recycling it. The technique is intended for optimizing water consuming processes aiming at zero discharge of wastewater. The technique is beneficial for removal of particles, fibres and suspended solids but a zero discharge of wastewater is not entirely obtained. Few researchers have highlighted the benefits of using mote-based, chemo-/bio sensors for pervasive sensing and self-sustaining the sensed data. The authors have suggested the use of these sensors for event detection of hostile environment that varies its deployment from few months to five years (Diamond et al. (2008a)). These sensors have few disadvantages with re-

spect to its cost of deployment. Therefore to minimize the deployment cost, a cheap, unmanned, fully automated in-sewer gas monitoring system, *namely*, *SewerSnort*, is proposed by Kim et al. (2009). It helps in measuring flow levels, detecting leaks and monitoring exceptional dumps. It has its disadvantages that the system has slower data rate transfer to surface station. To its improvement, a low-power, low-cost, 802.15.4 and 802.11 compatible *WSN* gateway is presented by Zennaro and Bagula (2009). It is designed for sites having limited infrastructure with frequent power shortages and network unreliability. Another technique *namely*, Autonomic System Specification Language *(ASSL)* has been demonstrated for developing intelligent sensors autonomously with self-management capabilities (Vassev et al. (2010)). The technique lacks in developing automatic detection to alternating sensors. These techniques are improved by developing a tool *namely*, Geographical Information System *(GIS)* for planning and managing the reuse of agricultural drainage water for irrigation in Nile Delta (Shaban et al. (2010)). It is used to draw thematic maps based on the entire Nile Delta. The tool provides cost-effective pollution control measures. Few authors have presented remote real-time environmental monitoring framework that uses web services for data collection, sending monitored data through seamless integration of wired and wireless system (Yang et al. (2010a)). The monitoring system is being integrated into the Texas Environmental Observatory infrastructure for long-term operation. The process works well with 100 sensors which are hard to deploy and has high maintenance. In order to realize large scale deployment of sensors, DistriNet Sensor Network Toolkit *(DisSenT)* software is demonstrated by Ueyama et al. (2010). The *DisSenT* provides efficient runtime reconfiguration component, lightweight management framework and declarative quality-aware deployment framework. The software has its disadvantage of understanding its working and providing the dependent platform which is practically very costly to implement. To its improvement, **?**, have proposed water quality monitoring system that includes floating grid method for extracting patterns of motion trajectories of live fish. It determines the frequency of pattern changes *via* neural network mechanism. It efficiently distinguish motion trajectories and is used as a precautionary warning system for aquatic farms, drinking water treatment plants, and

other related industries. Also, Lee et al. (2012), have postulated Wireless Mesh Network *(WMN)* for Four Major River Restoration Project in South Korea that contributes to solve flood damages and water shortages. *WMN* provides monitored data through voice and video, with reliability to cover few kilometers. It proves to be powerful solution but is costly, unable to take timely preventive measurements and its propagation is exploited by Loss of Signals *(LOS)*, providing low quality monitored data. Moreover, it fails to provide data at changing geographical conditions like weather, forests and rock walls. A scalable metadata management system for Web-of-Things (*WoT*) has been designed by Fortuna et al. (2012). It is found that the techniques can be prototyped and middle-ware technique is more convenient for web applications. The system has its disadvantages that it does not provide data access mechanisms and does not work with *XML* syntaxes for storage, accessing the data. Few authors have discussed the use of senors for small agricultural streams, road construction site, construction works and urban road system. It is found that the sensors are easy to install and helps in detecting physical parameters without the usage of manpower (Skarbovik and Roseth (2015)). It is suggested to lower the cost of sensors with respect to its deployment strategy. To deal with delayed packets upon transmission, Velasquez-Villada and Donoso (2016), have postulated Delay/Disruption Tolerant Network *(DTN)*-based solution for retrieving data on the spot. The solution is suitable to carry large amount of data with high delivery rate and delay. Also, it guarantees to deliver approximately 99 % data to surface station using Distributed Forwarding Algorithm which uses the concept of multi-hop for data communication. It has its limitations that it degrades the life of sensors. To use multiple sensors, Kamenar et al. (2016), have designed energy harvesting devices, *namely*, hydro-generator, piezoelectric eel and piezoelectric beam for providing continuous energy to sensor nodes for framework of EU FP7 project "*GOLDFISH*" (*see* Figure 2.6) (Kamenar et al. (2016)).

These devices are employed as a power source for pollution monitoring in river streams. It is found that these devices benefit in collecting data from sensors but are not suited at large scale due to its deployment cost and continuous charging of these devices *via* wired media.

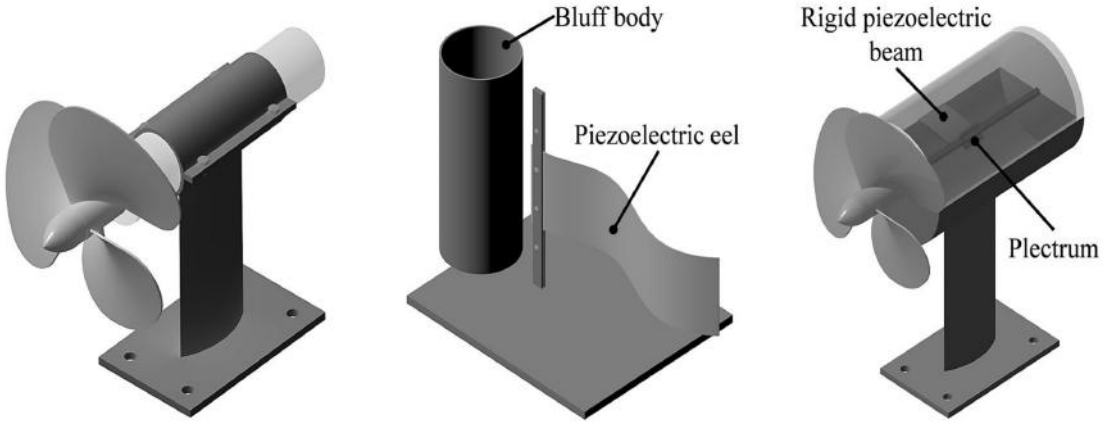

Figure 2.6: Energy Harvesting Concepts: Hydro-generator (left), Piezoelectric eel (center) and Piezoelectric beam (right)

2.2.2 Techniques based on Protocols

With respect to data transmission underwater, efficient communication protocols among the sink nodes and surface stations are needed. It is due to the fact that high attenuation and scattering affects the acoustic communication. For example, Pompili and Akyildiz (2009), have presented an overview of solutions for medium access control, routing, transport-layer, and cross-layer networking protocols. These protocols are well suited for real world monitoring in underwater with its efficient communication capabilities to sense and transmit data over a long range distances. Moreover, these protocols help user to remotely control devices or autonomous robots for controlling their motion and sensing capabilities. King et al. (2010), have summarized various issues related to communication, development, deployment and testing of protocols for underwater *WSN*. It is reviewed that communication due to acoustic waves is difficult in underwater due to reflection, refraction, deployment, testing based simulations and real environments that are expensive in nature. With respect to protocols for communication, Yadav and Yadav (2016), have surveyed and examined various energy efficient protocols with issues on activities mainly data collection, clustering and routing. The protocols should fulfill the aspects like minimizing total energy spent in network, minimizing number of data transmission time and maximizing number of alive sensor over time or balancing energy dissipation among sensors. For the purpose, different protocols are being implemented by the researchers based on modulation, scheduling, localization and routing

to provide faster transmission and to avoid collisions among the data traffic that minimizes the congestion on the sensors. Protocols based techniques are subdivided into modulation, localization, routing; and are discussed.

i. **Modulation Techniques:** Modulation fastens the transmission through the conversion of data into bits and symbols using encoding schemes. For example, Sozer et al. (2000), have suggested that Collision Detection Multiple Access (*CDMA*) provides the most robust method for underwater network environment. Quasi-Orthogonal Space-Time-Frequency Codes *(QOSTFCs)* have been examined by Tran et al. (2007), to increase data rates and error performance in STFC Multiband *OFDM* Ultra Wideband *(MB-OFDM UWB)* communications systems. It increases the transmission power, and reduces higher decoding complexity at surface sink to analyze the monitored data. To efficiently transmit data to surface station, an optical fair scheduling in Spatial Time Division Multiple Access *(STDMA)* network is presented by Luque-Nieto et al. (2016). It provides optimal frame determination for sending data. The technique has increased throughput and performance with limited number of sensors (*say*, up to 12) but its performance is degraded with increase in the number of sensors, *i.e.*, 20, 30, 50, 80, *etc*.

ii. **Localization Techniques:** Localization helps to monitor and update the position of sensors continuously that enhance the communication of the deployed sensors. In order to provide efficiency, localization technique is suggested for constructing spanner which has constant degree and power stretch factor. Few authors have evaluated various localization techniques for determining the location of each sensor in underwater and evaluated its performance on test beds on the basis of its range and depth (Chandrasekhar et al. (2006)). Different measurement techniques on the basis of range are suggested. These include Received Signal Strength *(RSS)*, Angle of Arrival *(AoA)*, Time of Arrival *(ToA)* and Time Difference of Arrival *(TDoA)*. The *RSS* does not work with acoustical interferences such as tidal noise, Doppler effect, ambient noise, *etc*. *AoA* requires directional transmission incurring extra cost and *TDoA* provides no feasibility with Radio Frequency (*RF*) signals in underwater. It is suggested that *ToA* is

most suitable as it helps in measuring arrival time in localization process (Lee et al. (2008b)). The performance of technique is analyzed through simulations by considering factors like initial reference, its position, sensor's communication range and total number of sensors. The technique has its limitations that it evaluates the positioning of limited sensors.

iii. **Routing Protocols:** In routing, the routing-table keeps on updating the position of the sensors which further helps in finding the shortest route through single-hop or multi-hop techniques. It benefits in preserving the energy of the sensors and does not let collision to occur. Many researchers have enlightened the sensitivity in deployment and communication *via* routing protocols with respect to energy consumption, data gathering and route updating process. For example, Catipovic (1990); Kilfoyle and Baggeroer (2000), have addressed various limitations for using underwater acoustic telemetry. The complex computations have decreased the reliability of telemetry systems where video image transmission is used. The data rate is slower ranging from 1 to 500 kbps and its performance varies due to its dependency on channel phase, bandwidth and impulse response fluctuation rate. Xie and Gibson (2001), have demonstrated a network layer protocol for *UWASN*. It provides network control and management mechanisms with respect to response, self-configure, adaptable and scalable networks. The technique has its limitations due to its increased average node density consuming more energy. The use of *WSN* for ecological experiments have been studied by Suri et al. (2006); Doss et al. (2006). It is suggested that the lifetime of *WSN* are optimized by implementing low-level energy routing protocol and are used for applications in remote, hospital environments. To decrease cost, manpower and increasing the efficiency of data transmission various routing protocols are suggested. These protocols help in transmitting data by selecting the shortest route among source and surface station. In order to deal with data gathering, Pompili et al. (2006), have suggested a two-phase resilient routing which provide guaranteed survivability of the network to sensor and link failures. Few authors have designed new set of routing protocols considering factors like transmission mediums, energy consumption in terrestrial and underwater *WSN*. The protocols fail to provide the performance on the basis of sen-

sor's localization. The reactive and proactive protocols *namely*, Ad-Hoc on Demand Vector *(AODV)*, Destination Sequenced Distance Vector Routing *(DSDV)*, Optimized Link State Routing *(OLSR)*, respectively, are appropriate for dynamic environment but cause large signaling overhead resulting into sensor failures (Huang et al. (2009); Horng et al. (2010)). Therefore, Dynamic Source Routing *(DSR)* based on fuzzy logic inference system is proposed. It estimates distance, angles among neighboring sensors and remaining energy among sensors; before forwarding a packet to destination. This protocol consumes less energy. To provide continuous route updating, Banik et al. (2015), have provided a technique for optimally design water quality monitoring stations in sewer networks of Massa Lubrense. The technique is based on information theory. It is formulated as multi-objective optimization technique. The various constraints like geographical convenience, accessibility, safety, *etc.*, are assessed for computing joint entropy and total correlation for suggested technique. Therefore, to improve its performance, Ding et al. (2016), have postulated Optimizing Routing Algorithm based on Congestion Control *(CCOR)* that succinctly maintains energy efficiency and congestion control. The suggested technique decreases the packet loss rate and can alleviate congestion effectively by maintaining high energy efficiency, though with a relatively high delay under heavy traffic load (Alajeely et al. (2017)).

In summary, the key aspects to underwater communication is efficient protocols that are implemented with deployment strategies having longer sustainability. The topologies must have the properties for dynamically adding up of new sensors in order to gather data efficiently covering larger area. The underwater communication through sensors are beneficial in monitoring and surveillance applications. For deep analysis, the data gathering and refinement process is simulated through imaging sensors. These sensors help in capturing the data of surrounding and further transmitting it to surface station. To visualize wider area, various techniques of panoramic image refinement are suggested by researchers. These techniques are discussed in next section.

2.3 Panoramic Image Refinement Techniques

To monitor the biological and geological environments, quality of captured image through sensors plays a pivotal role. It is due to the fact, poor visibility of the acquired image may degrade the exploration process in underwater (Yuh and West (2001); Lebart et al. (2003)). In order to eliminate the issue of poor visibility, image refinement techniques are suggested by researchers. These techniques are categorized into edge preservation, enhancement and mosaicing. Each technique with its detailed description and literature survey is discussed.

2.3.1 Edge Preservation Techniques

Edge preservation is a technique to smooth panoramic images by retaining the edges. For example, Perona and Malik (1990), have worked on realizing semantically meaningful edges using a diffusion process. The process is time consuming. In order to provide smooth edges in less time, neighborhood filtering is considered which averages pixels with a similar gray level value belonging to the spatial neighborhood. It is currently named as Bilateral filter, given by Smith and Brady (1997); Tomasi and Manduchi (1998). It has various advantages *i.e.*, non-iterative and simple formulation. It depends on few parameters (spatial domain and intensity range kernels) and is an efficient scheme. It smooths edges reasonably very fast on large images in real time environment with dedicated graphics hardware. Edge-preservation techniques are further classified as filtering and wavelet. Each one of them is discussed.

i. **Filtering based Edge Preservation Techniques:** Filtering transforms the pixel intensity value to reveal certain image characteristics such as noise reduction, colorization, edge preservation, detail enhancement, texture editing, haze or rain removal, *etc*. For the purpose, the number of techniques exist, *namely*, explicit weighted average, implicit weighted average and non-average filters described as under.

   - **Explicit Weighted- Average Filters:** It is the simplest and most intuitive filtering technique for preserving edges during smoothing. It computes the median in the filter's support rather than computing the mean. Although this filter is effective in many cases such as noise removal and extraction of detail at a fine spatial

scale, it is noticed that it may have artifacts in High Dynamic Range *(HDR)* compression (Durand and Dorsey (2002)). These artifacts are generated from the pixels around the edge that have an unstable Gaussian Weighted Sum. Hence, the results may exhibit unwanted profiles around the edges. The fast implementation of explicit weighted average filter is a challenging problem. In order to address this challenge, the bilateral filter is generalized to joint bilateral filter, where the weights are computed from another guidance image rather than the filter input (Petschnigg et al. (2004)). The technique is favored specifically when the image that is to be filtered is not reliable to provide the information about the edges. The reason behind it is that when a pixel on an edge has few similar pixels around it, the Gaussian weighted average becomes stable. For real-time implementation, a bilateral filter involves histogram based approximation due to its computation efficiency and memory concern (Tseng et al. (2011)).

- **Implicit Weighted Average Filters:** It optimizes a quadratic cost function and solve a linear system, which is equivalent to implicitly filtering an image by an inverse matrix. The affinities of this matrix are Gaussian functions of the color similarities in colorization and image segmentation (Levin et al. (2004a); Grady (2006)). Another technique *namely*, weighted least squares filter adjusts the matrix affinities according to the image gradients and produces halo-free edge-preserving smoothing, suggested by Farbman et al. (2008). Although this technique often generates high quality results but is time consuming. To produce results in less time, the implicit weighted average filters are considered. It takes at least a few seconds to process a one megapixel image either by preconditioning or by multi-grid (Farbman et al. (2008)).

- **Non-average Filters:** It helps to smooth Edge-preservation more efficiently through the median filter, named as edge-aware operator. It is a special case of local histogram filters. For example, the Total-Variation *(TV)* filter optimizes an L1-regularized cost function, and are shown equivalent to iterative median filtering (Rudin et al. (1992)). The L1 cost function can also be optimized *via* half-quadratic split alternating between a quadratic model and soft shrinkage (Wang

et al. (2008)). But it is noticed that non-average filters are computationally expensive and complex.

ii. **Wavelet based Edge Preservation Techniques:** Wavelet smooths the edge by considering the pixel values. It is highly feasible to generate good quality images. Wavelets are well-established edge-preservation technique due to their sparseness and de-correlation properties. In the preservation context, the de-correlation property of the Discrete Wavelet Transform *(DWT)* suggests processing the coefficients independently of each other, while the sparseness property leads to the use of thresholding and shrinkage techniques. *DWT* aims at removing, or attenuating, those coefficients that are small compared with the noise level. To this end, a variational technique in a deterministic wavelet setting is considered, consisting in the minimization of a function. This technique is further extended for two-dimensional discrete dyadic transform, in which the two components of the *DWT* are proportional to the two components of the gradient smoothed at that scale (Mallat and Zhong (1992)). This allows to use penalty term to obtain new non-linear wavelet estimators. For the particular choice of the penalty function in smoothing the edges, a simple iterative technique is provided by Charbonnier et al. (1997). It is shown that the iterative technique turns out to be a simplified version of the half-quadratic regularization technique from which it inherits all the convergence properties. A number of techniques have been proposed for edge preservation using *DWT* that include stochastic, variational, and non-linear diffusion filtering. It is proved by Chambolle et al. (1998), that the variational formulation in the Besov space leads to the wavelet shrinkage. Few authors have described that hard and soft thresholding wavelet estimators correspond to the lower and upper envelopes of a class of penalized least-squares estimators (Antoniadis and Fan (2001)). Few authors have considered the correspondence between wavelet shrinkage, non-linear diffusion and derive new wavelet shrinkage functions from existing diffusivity functions (Mrázek et al. (2003)). Some of the researchers have provided the relations between soft wavelet shrinkage and total variation edge-preservation. These relations are analyzed by Steidl et al. (2004); Mittal and Kumar (2006), for their equivalence. The purpose of developing wavelet based edge preservation is to exploit the interplay be-

tween non-linear diffusion filtering and variational techniques in the wavelet domain.

2.3.2 Enhancement Techniques

Enhancement is a technique to improve the poor quality of acquired images which is affected by the dark pixels (haze). The haze is produced when the light is absorbed, *i.e.*, reflected by water surface and scattered due to water particles. It results into change in color due to random attenuation and scattering at different wavelengths. The color distortion affects the processing of underwater panoramic images and produces the poor quality images. To improvise, the researchers, from decades, are trying to enhance the quality of underwater panoramic image with the removal of effects due to light scattering, distortion and color change. The input for image quality enhancement is carried out in two ways, *i.e.*, *single* and *multiple* and are discussed.

i. **Single Image Input based Enhancement:** For single input, Hou et al. (2007), have tried to reduce blurring effect by combining point spread and modulation transfer functions. A technique to estimate hazy scenes on minimal input is suggested by Fattal (2008). The technique is dependent on local transmission and produces an implicit graphical model by considering extrapolated reliable pixels. The technique has its limitations of removing blurriness to less extent due to its dependency on transmission. Even, He et al. (2011) have proposed dehazing technique *namely*, Dark Channel Prior *(DCP)* based on a key observation. The technique uses matting Laplacian to remove haze by considering dark pixels of the images. Its disadvantage is the production of poor quality images if the sunlight is bright and thus, fails to recover true scene radiance of distant objects. To produce good quality images and recovering scene radiance, Ancuti et al. (2012), have introduced a technique for enhancing underwater images and videos. The authors have used image fusion technique for color correction and contrast enhancement. The suggested technique aims to increase the visibility of distant objects and helps in reconstructing clear images in turbid water. To overcome the limitations of blurriness or low contrast, Chiang and Chen have postulated systematic underwater image enhancement technique that uses dehazing and contrast

enhancement algorithms (Chiang and Chen (2012)). The technique helps in restoring natural appearance, visibility, and color in order to extract valuable information. But, it has few shortcomings that it does not help in removing noise from the image and has not considered objects that are farther from the source. For removing noise and to overcome the limitations of *DCP*, another technique *namely*, guided image filtering is proposed by He et al. (2013). It considers foggy images as reference and remove haze by smoothing their edges using bilateral filtering. The produced output has better perseverance and quality. However, it has its limitations of producing halos near edges that lead to incomplete haze removal.

ii. **Multiple Image Input based Enhancement:** For multiple input, Schechner and Averbuch, have suggested adaptive filtering technique to improve the visibility of distant objects. It helps in removing noise from images by regularizing the pixels using polarization. The technique has its limitations in underwater due to depth-illumination and varying colors with depth. Various color correction techniques are suggested to estimate underwater environmental parameters. The estimates are found by performing color registration with light attenuation (Yamashita et al. (2007)), suggesting histogram technique for additive colors *(RGB)* and Hue Saturation Intensity *(HSI)* color spaces, in order to manage luminance distribution (Iqbal et al. (2007)). With the span of time, image refinement and enhancement techniques are integrated with fusion to improve the quality of images. From the existing techniques, wavelet and fusion such as Intensity Hue Saturation *(IHS)* and Principal Component Analysis *(PCA)* are widely used for refinement. Few authors have suggested wavelet based technique that combine the coefficients of images produced by different fusion. The technique uses window based consistency verification process to validate the output image. The quality of produced images are satisfactory but the process is time consuming and images got blurred along the edges (Yang et al. (2010b)). To improve it, He *et al*. have suggested a fusion technique based on *IHS* and *PCA*. The technique combines the fusion schemes to preserve the spatial information and produce good quality images. It has its limitations that the resultant images are produced in low spatial resolution (He et al. (2010)). To this improvement, Treibitz and Schechner (2012), have postulated multi-directional

illumination fusion for enhancing underwater images. The technique is limited in the sense that it does not remove the background scattering and thus, distant objects are less visible. Also, a post-processing technique of enhancing underwater images using laser lightening and bilateral filtering is proposed by Ouyang et al. (2012). The technique involves cost and regular maintenance of laser equipment that makes it insufficient to sustain for longer periods. In 2014, few authors have reviewed various fusion techniques and suggested that wavelet based fusion is an efficient technique but it has its disadvantages of preserving edge information (Sahu and Sahu (2014)). To improve the disadvantages of edge preservance, a *PCA* and *DWT* based technique is introduced. *PCA* is used to retain important characteristics of images by considering significant eigen values. The technique helps in minimizing color distortion but face challenges in preserving original colors of input images. Moreover, the technique produces blur images due to noise (Ansar and VR (2014)). To overcome the limitations of blurriness, a technique based on *DWT* and *IHS* is proposed. *IHS* is used to provide information of high activity region and is further processed using *DWT*. The technique outperforms well in providing good quality images but produces image with less color distortion and blurriness along edges (Bhavana and Krishnappa (2015)). Li et al. (2017), have studied various pixel level image fusion techniques and suggested that image fusion with other refinement techniques provide promising results, but various challenges still need to be studied in terms of edge preservation, resolution, noise and computational complexity.

Based on the existing techniques, following Table 2.1 is summarized that discusses pros and cons for various techniques, techniques suggested for image enhancements.

Table 2.1: Summary of Existing Techniques for Enhancement

Authors	**techniques**	**Strength**	**Weaknesses**
Schechner and Averbuch	Adaptive Filtering	•Improves the visibility of distant objects •Removes noise from images using polarization	•Errors in color correction due to depth illumination
Fattal (2008)	Dehazing	•Estimates hazy scenes •Produces an implicit graphical model	•Removes blurriness to less extent •Dependency on transmission
He et al. (2010)	Fusion	•Preserves the spatial information •Produce good quality images	•Images are produced in low spatial resolution
Yang et al. (2010b)	Wavelets	•Considers coefficients of images •Produce good quality images	•Time consuming •Blurriness along the edges
He et al. (2011)	Dark Channel Prior	•Removes haze •Uses matting Laplacian	•Time consuming process •Fails to recover true scene radiance of distant objects
Chiang and Chen (2012)	Dehazing and contrast enhancement	•Restores natural appearance, visibility, and color •Extracts valuable information	•Methodology to remove noise is not considered •Objects farther from source are not accounted

Treibitz and Schechner (2012)	Multi-directional Illumination Fusion	•Combines fusion techniques •Enhances underwater images	•The background scattering is not removed to extent •Distant objects are not visible clearly
Ouyang et al. (2012)	Laser lightening and Bilateral Filtering	•Enhances underwater images	•Due to high cost and maintenance, difficult to sustain for longer periods
Ancuti et al. (2012)	Fusion	•Increases visibility of distant objects •Reconstructs clear images in turbid water	•Method does not provide detailed information •Blurred images are produced
He et al. (2013)	Guided Image Filtering	•Removes haze by smoothing their edges •Better perseverance and quality of images produced	•Generates halos near edges •Incomplete haze removal
Ansar and VR (2014)	*PCA* and *DWT*	•Retains important characteristics of images •Minimizes color distortion	•The feature to preserve original colors is missing •Produces blurred images due to noise
Bhavana and Krishnappa (2015)	*DWT* and *IHS*	•Provide information of high activity region •Provide good quality images	•Images are produced with less color distortion •Blurriness along edges

2.3.3 Mosaicing Techniques

Mosaicing is the alignment of multiple overlapping images into a large composition which represents a part of a *3D* scene (Capel (2004)). It is a special case of scene reconstruction where the images are related by planar homography only. Using mosaicing it is possible to extend the Field of View *(FOV)* of a camera by preserving the original resolution and without introducing undesirable lens deformation (Bevilacqua and Azzari (2007)). There have been a variety of new additions to the classic applications of image mosaicing that primarily aim to augment the *FOV*.

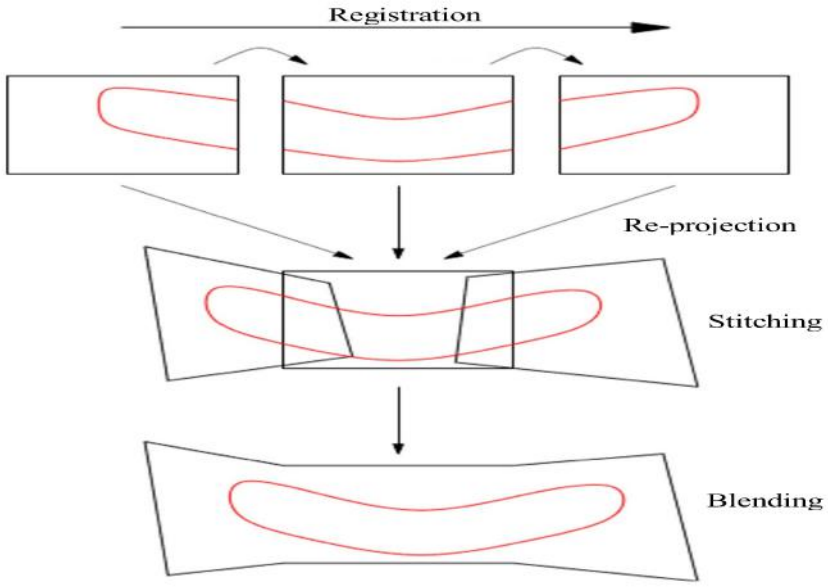

Figure 2.7: Steps of Mosaicing

As shown in Figure 2.7, mosaicing involves various steps *i.e.*, registration, re-projection, stitching, and blending (Capel (2004)). Registration refers to the establishment of geometric correspondence between a pair of images depicting the same scene. In order to register a set of images, it is required to estimate the geometric transformations which align the images with respect to a reference image within that set. The set may consist of two or more images taken of a single scene at different times, from different viewpoints or by different sensors. The most general case of the transformation is the eight degree of freedom planar homography. The next step, following the registration, is re-projection which refers to the alignment of the images into a common coordinate system using the computed geometric

transformations. The goal of the stitching step is to overlay the aligned images on a larger canvas by merging pixel values of the overlapping portions and retaining pixels where no overlap occurs. Errors propagated *via* geometric and photometric misalignments often result in undesirable object discontinuities and seam visibility in the vicinity of the boundary among panoramic images. Thus, a blending technique needs to be used during or after the stitching step in order to minimize the discontinuities in the global appearance of the mosaic. The aforementioned registration step has been conceived to work with images with a single color band. Different techniques have been used by various mosaicing to deal with multiple color bands. For example, one of the color bands of the input *RGB* images are taken into consideration for obtaining the transformation parameters (Behrens et al. (2010)). On the other hand, the *RGB* images are first converted to gray scale and then transformation parameters are obtained by Park et al. (2012). In either case, after finding the optimal transformation parameters, all the color bands are processed and combined together during the re-projection step in order to produce color mosaic panoramic images. It is categorized into two types, *namely*, transition smoothing and optimal seam based, described as under.

i. **Transition Smoothing based Mosaicing:** The technique attempts to minimize the visibility of seams by smoothing the common overlapping regions of the combined images. The information of the overlapping region among two panoramic images of same area are fused in such a way that the boundaries of the images become imperceptible. Even though a totally indistinguishable transition is achieved, the content and coherency of the overlapping region is not guaranteed. It is due to the fact that the information is fused without taking into account the content of the scene (Belan and Yuzhakov (2013)). Thus, transition smoothing techniques generate mosaic with blurry transitions in the boundary regions. The popular techniques which use transition smoothing for their blending operation include feature, pyramid, and gradient-based and are discussed.

   - **Feature-based Transition Smoothing:** It performs smoothing operation by taking an average value of each pixel in the overlapping region. However, the simple average technique fails when exposure differences, misalignments, and presence

of moving object are present in the input panoramic images. A superior technique is to use weighted averaging along with a distance map. The pixels near the center of an image are weighted heavily and those near the edges are weighted lightly. Frequently, it is difficult in practice to achieve a balance between smoothing low-frequency exposure differences and preserving sharp enough transitions to prevent blurring. Furthermore, these techniques suffer from ghosting artifacts. Li et al. (2008); Jain et al. (2012) have used alterations of the above mentioned technique for finding the weights of images in the overlapping region. The weight is measured by computing the distance of the overlapping pixels from the borders of the left and the right images.

- **Pyramid-based Transition Smoothing:** In an attempt to perform smoothing in a more robust way, pyramid-based techniques convert the input panoramic images into band-pass pyramids. The mask image associated with each source image is then created automatically using grassfire transform (Xiong and Turkowski (1998)). This mask image is converted into a low-pass pyramid by using a Gaussian kernel as suggested by Szeliski (2006). The resultant blurred and subsampled masks are treated as weights to perform pre-level featuring. The final mosaic panoramic image is generated using interpolation. Techniques used in the above technique achieve reasonable balance between smoothing that generates low frequency components and preserves sharp transitions to prevent blurring (Pandey and Pati (2013)). Edge duplication is also eliminated noticeably using these techniques. However, double contouring and ghosting effects become proper when the registration error is significant.

- **Gradient-based Transition Smoothing:** It helps in smoothing mosaic image regions by mixing the gradient of panoramic images. It generates visually more pleasant results compared to the other two techniques (feature- and gradient-based). However, working exclusively in the gradient domain requires higher computational resources to deal with large data sets. For best performance, the alignment of images through registration needs to be almost perfect. Few authors have developed a technique called Gradient Domain Image Stitching *(GIST)*

(Levin et al. (2004b)). This technique is based on minimizing a cost function that evaluates the dissimilarity measure between the derivatives of the mosaic and the derivatives of the source images. Another technique in the same is based on inferring a mosaic by optimization over image gradients. A gradient domain object moving and region filling technique is suggested by Xiong (2009), to eliminate the visible artifacts arising from moving objects in the scene. Also, assigning low resolution offset based technique map to each source image followed by Poisson's blending (Szeliski et al. (2011)).

ii. **Optimal seam based Mosaicing:** Optimal seam based mosaicing attempts to minimize the visibility of seams by joining the boundaries between panoramic images. It targets to allocate the optimal location of a seam line by looking into the overlapping region between a pair of images. The seam line is placed in a way that it minimizes the photometric differences between the two sides of the line. It is further classified into two types, *namely*, Scale Invariant Feature Transform *(SIFT)* and Speeded Up Robust Feature *(SURF)*, described here.

- **SIFT:** *SIFT* technique is a low-level feature detection technique which detects distinctive features (also called key-points) from images. *SIFT* descriptor is invariant to translations, rotations and scaling transformations in the image domain and robust to moderate perspective transformations, illumination variations. *SIFT*'s operation is based on five major steps: scale-space construction, scale-space extrema detection, key-point localization, orientation assignment, and defining keypoint descriptors. Several researchers have made variations to the above mentioned *SIFT*-based mosaicing technique in order to further improve its performance. For example, the author exploited a deformation vector propagation technique in the gradient domain to reduce the intensity discrepancy between the mosaiced images (Yao (2008)). Similarly, a bundle adjustment technique along with a modified Random Consensus *(RANSAC)* algorithm capable of developing a probabilistic model is used to eliminate registration error and make the matching process more accurate (Li et al. (2008)). Also, few authors

have proposed switching between Kanade Lucas Tomasi *(KLT)* tracker and *SIFT* matching to find the correspondences between successive frames depending on their amount of overlapping (Nemra and Aouf (2009)).

- **SURF:** *SURF* technique is a scale and rotation invariant local feature detector. Like *SIFT*, this technique is also based on scale space theory. *SURF*-based mosaicing techniques are faster than *SIFT*. However, it perform poor mosaicing under certain variations (particularly color, illumination, some affine transformation). The process of determining the *SURF* descriptors has been modified by some authors. For example, few authors have proposed dividing the *SURF* descriptor window into eight sub-regions while assigning descriptor vector (Rong et al. (2009)). This technique increases the matching speed at the cost of increased number of false matches. However, the authors show that the use of *RANSAC* guarantees the elimination of most of those incorrect matches. It is suggested that *SURF* uses Hessian matrix of the integral image to estimate local maxima across different scale spaces (Yang et al. (2011)). Often, multiple low-level feature extraction techniques are used together in image mosaicing in order to use their respective benefits. Joshi (2013), have proposed a mosaicing technique which uses both Harris corner detector and *SURF* detector for extracting distinctive features from source images.

In summary, the key aspects to refinement techniques are to provide good quality panoramic images that are rich in intensity, visualization having reliable information.

2.4 Gaps Identified

Based on the literature survey, following gaps are identified.

i. **Topology Instability:** The topology for *UWASN* refers to the sensors' deployment wherein sensors provide full coverage of the targeted area. The deployed sensors experience high bit error rates and temporary losses of connectivity due to impaired communication, multi-path and fading. Moreover, sensors are prone to failures because of fouling, corrosion and affects the overall performance of the topology (Xiao

(2009)). In summary, topology deployment in underwater is an eminent challenge due to (i) multi-path and fading in underwater channel, (ii) maintain data integrity due to connectivity issues among sensors and (iii) physical damage to sensors with varying climatic changes.

ii. **Erroneous in Localization:** Underwater acoustic channels are characterized by harsh physical layer environments influenced by transmission loss, noise, multi-path, Doppler spread, high propagation delay that leads to stringent bandwidth limitation. This limitation hinders in finding the actual position of sensors in underwater (Lloret (2013)). The technique of finding the correct position of sensor takes into consideration its mobility as major concern parameter in distributed environment. Therefore, there is requirement for strategy that can work for discovering the location of sensors.

iii. **Image Refinement Issue:** Due to factors such as distortion, light scattering, noise and wavelength attenuation, the captured panoramic images from the hostile environment of the underwater are observed to have poor visibility (He et al. (2011)). Hence, there is scope for improving the quality of the panoramic images with respect to (i) reduce noise and haze, (ii) retain positive values along edges, (iii) remove checkerboard artifacts along edges, (iv) give anti-aliasing in images, and (v) enhance visibility.

iv. **Data Transmission:** The data is transmitted through the routing protocols which causes a large signaling overhead to establish routes for the first time. Since, network is modified each time due to sensor failures, updated topology information needs to be propagated to all connected sensors. This way, each sensor is able to establish an updated path for data transmission which is a time consuming process resulting into power degradation of sensors (Pompili et al. (2006)). Therefore, the issue is to design an efficient routing protocol for faster data transmission and to conserve energy of sensors.

v. **Energy Consumption Issue:** Energy consumption determines the lifetime of a *UWASN* as sensors use battery power as an energy source. Energy is consumed in three operations, *i.e.*, sensing task, communicating information, and processing the

data. As, the battery-life is limited and the sensors are placed in a hostile environment, therefore, replacing the battery is impractical (Climent et al. (2012)). So, the issue is to minimize the energy consumption.

vi. **Failure of Sensor:** Sensors are prone to failure because of unattended environment. A sensor may fail due to hardware, software problem. If any of the sensor fails, the working protocol should handle this type of failure (Sehgal et al. (2011)). The issue is to have a backup plan for fault tolerance in a way to replace the failed sensor without disturbing the topology deployed.

2.5 Problem Formulation

With the exhaustive survey on *UWASN*, it has been found that *UWASN* is promising field of research and definitely will be a major step forward towards monitoring, surveillance applications. The main focus for deploying sensors in *UWASN* is to know its hostile environment with its vital assets like natural resources, minerals, gas, petroleum, *etc*. These assets promote economy of most countries, therefore, it is required to maintain and protect them. The protection of these assets from unknown hindrances, *i.e.*, intentional and non-intentional attacks, needs special consideration. Moreover, with the deployment of sensors, the monitored data should be sent to surface station in an efficient manner to take timely preventive measurements.

But, the energy efficient transmission in *UWASN* is still a key challenge as the sensors are adhered with water constraints like Doppler effect, path loss, noise, propagation delay, *etc*. The dynamic deployment of sensors and sleep/wake-up protocols need to be implemented to mitigate the effects of water and to sustain the deployment for longer periods. Further, these sensors need to be equipped with storage capacity in order to retain data for some time and must have capability to communicate sensed data to either smartphone or *PC via* bluetooth in short time interval. This strategy will not hamper in computation of gathered data at surface station. It has been observed that most of the prior work has focused on sensing data, ignoring the performance of the deployment. Also, existed work fails to provide maximum coverage of monitored data. Further, image transmission and refinement over *UWASN* needs

more attention, specifically in harsh environments where survival of sensor for a long time is quite impossible.

The researchers have provided deployment strategies, routing protocols for communication and image transmission methodologies. But, their major limitations are less sustainability in water, prone to failure of sensor, corrupted data, covering smaller area of monitoring through captured images. These gaps are needed to be addressed for efficient communication in underwater. Further, the gathered image-data needs to be verified in order to check region and the image should provide complete information of the area. Various image refinement techniques need to be improved to enhance the quality of image with respect to its visual inspection. Even, efficient communication technique should be adopted with single-hop strategy among designed topology that provide longer sustainability with maximum coverage of area. Such topology should be dynamically processed with routing. This technique can be considered to enable pollution monitoring and surveillance for longer period.

2.6 Objectives

The objectives of this work are-

i. To study and analyze the existing techniques for underwater data communication and panoramic image refinement.

ii. To procreate energy efficient topology for data transmission to the surface station.

iii. To propose a technique for panoramic image refinement.

iv. To validate results by comparing with existing techniques.

Chapter 3

Research Methodology

3.1 Introduction

The chapter details the methodology to address the research objectives of the thesis. The objectives of the study are to procreate energy efficient topologies for efficient data communication and refinement of underwater images. For the purpose, the methodology is classified into three categories, *i.e.*, requirement specification, data transmission and image refinement techniques. The requirement specification includes the exhaustive study of economic, sustainable sensors with respect to their hardware, software configuration and their calibration for gathering under-water data. The data transmission includes techniques based on sleep-/wakeup, localization, modulation for sending textual and image data in form of bits. The image refinement specify techniques used for refining panoramic images gathered at surface station.

To address the research objectives through the usage of classified categories as shown in Figure 3.1, the different sustainable sensors are calibrated as *(MPS)* on Arduino board and is encased in stainless conceal with respect to its requirement specification. For the efficient data transmission through *MPS*, three techniques, *namely*, asynchronous sleep/wakeup, *ToA* based localization and *OFDM* are implemented for *MPS* sustainability for longer period, finding their relative position for communication and image data transmission with less erred pixels, respectively. Finally, Ridgelet transform is used for refining panoramic images to obtain better visual quality with minimal erred pixels.

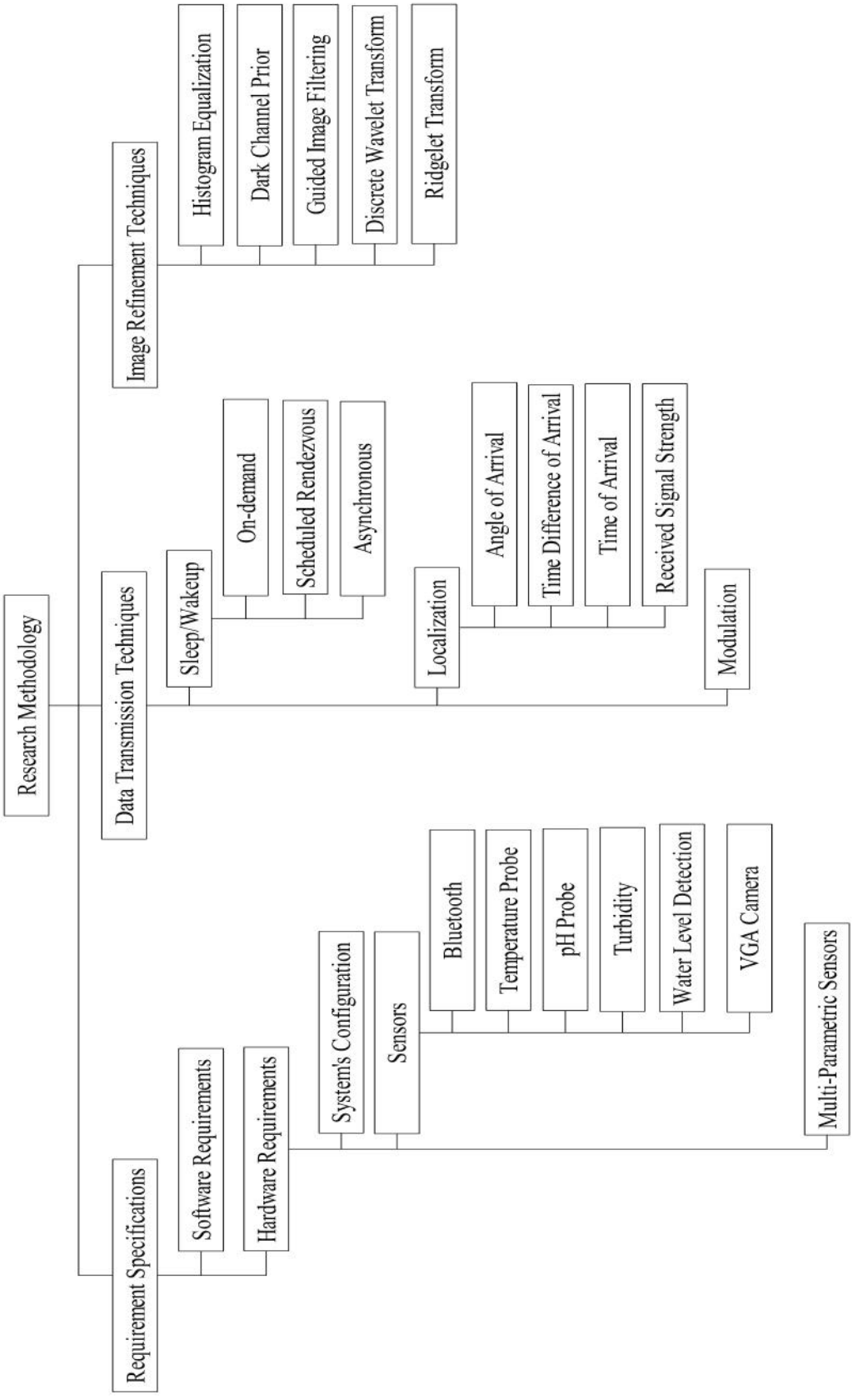

Figure 3.1: Classification of Research Methodology

3.2 Requirement Specifications

To address the objectives stated for the thesis, the foremost requirement is to understand required specifications with respect to hardware and software. For the same, the specifications are described.

3.2.1 Software Requirements

The subsection details the software requirements with respect to *UWASN*, that consists of various numbers of floating and anchored sensors to be deployed over an unexplored area. The pre-requiste for the deployment of sensors is to plan the budget and eminent power depletion with respect to hardware meant for acoustical underwater communication. To meet the requirements, the researchers have suggested some techniques such as analytical, practical implementations and computer simulations. The analytical technique or sampling is a method that is used to determine the concentration of a chemical compound or chemical element. This method requires manpower and takes three to four hours in processing the data. It has the disadvantage that it often causes *UWASN* to be unsuitable or inaccurate due to network constraints, complexity and consumes more time in processing data. The practical implementations is at its infancy stage having low deployment cost, less diversity and application dependency of sensors. The computer simulations allows rapid evaluation, optimization, adjustments of algorithms and protocols, hence, making it as most widely adopted method for analyzing *UWASN*. For the simulation of *UWASN*, the prior requirement is to have a physical environment and energy models.

In order to provide appropriate physical environment to addrress the research objectives, used simulators are described.

i. **Network Simulator-2:** Network Simulator-2 *(NS-2)* is a tool which provides substantial support for simulation of *TCP* and *UDP*, traffic source behavior, router queue management mechanism, routing algorithms and multicast protocols over wired and wireless networks (Issariyakul and Hossain (2012)). It is written in two key languages, *i.e.*, C++ and Object-oriented Tool Command Language *(OTcl)*. C++ defines the inter-

nal mechanism (*i.e.*, a backend) of the simulation objects and *OTcl* sets up simulation by assembling, configuring the objects and scheduling discrete events. The compiled C++ objects are made available to the *OTcl* interpreter having in-built C++ objects can be controlled from the *OTcl* level.

ii. **MAThworks LABoratory:** MAThworks LABoratory *(MATLAB)* development environment is used for simulation and result analysis (Chapman (2015)). It is an interactive developmental and research programming platform, designed specifically for matrix processing. It provides high-performance language for technical computation, visualization, and programming. It provides an easy-to-use environment where problems and solutions are expressed in familiar mathematical notation.

iii. **Arduino Integrated Development Environment:** The Arduino Integrated Development Environment *(IDE)* is a cross-platform application (for Windows, macOS and Linux) (Banzi and Shiloh (2014)). It is used to write and upload programs to the Arduino board. The source code for the *IDE* is released under the GNU's Not Unix *(GNU)* General Public License, version 2. The Arduino *IDE* supports the languages C and C++ using special rules of code structuring. The Arduino *IDE* supplies a software library from the wiring project, which provides many common input and output procedures.

Since, the simulators as an application program need an operating system, therefore, to support the simulators, .NET Framework 3.5 Software Development Kit *(SDK)* is installed on Microsoft Windows 8 (64-bit) operating system.

3.2.2 Hardware Requirements

The sub-section is broadly classified into two categories, *i.e.*, system's configuration and sensor's description. These are discussed.

i. **System's Configuration:** The minimum configuration of the system required for the thesis, is described.

Processor: *2.5-GHz* Intel Pentium-class processor.

Memory: *4 GB* of RAM, *8 GB* recommended.

Hard Disk: *20 GB* of hard disk space required, 6 GB additional hard disk space required for installation.

Display: *1024* $\times$ *768* or higher-resolution display with 24 bits colors.

ii. **Sensors' and Circuitry Board Description:** A sensor is a device that detects and responds to some type of input from the physical environment. The specific input could be light, heat, motion, moisture and pressure. The output is generally a signal that is converted to human-readable display at the sensor location or transmitted electronically over a network for reading or further processing. The various types of sensors with circuitry board, used in the thesis are described (Banzi and Shiloh (2014)).

- **Arduino Uno:** Arduino Uno is a micro-controller circuitry board based on the ATmega328. It has 20 digital input or output pins (of which 6 can be used as *PWM* outputs and 6 can be used as analog inputs), a 16 MHz resonator, a *USB* connection, a power jack, an In-Circuit System Programming *(ICSP)* header, and a reset button. It has the feasibility to simply connect with computer using *USB* cable and codes are directly installed on the board using Arduino *IDE*. The board is shown in Figure 3.2.

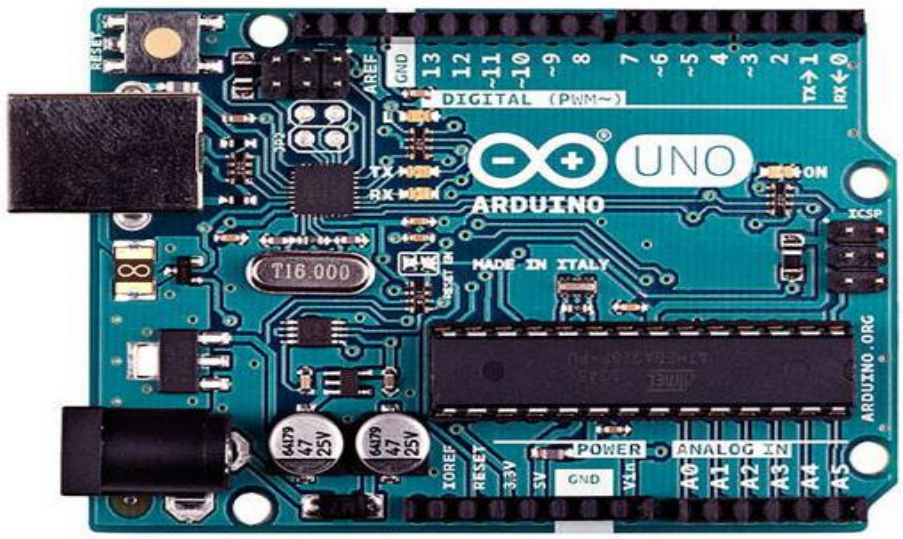

Figure 3.2: Arduino Uno Board

- **Arduino Mega 2560:** The Arduino Mega 2560 is a micro-controller circuitry board based on the ATmega2560. It has 54 digital input or output pins (of which 15 can be used as *PWM* outputs), 16 analog inputs, 4 *UART*s (hardware serial ports), a 16 MHz crystal oscillator, a *USB* connection, a power jack, an *ICSP* header, and a reset button. It has the same working as of Arduino Uno micro-controller board (*see* Figure 3.3).

Figure 3.3: Arduino Mega 2560 Board

- **Breadboard:** A breadboard is a solderless device for temporary prototype with electronics and test circuit designs. The breadboard has strips of metal underneath the board and connect the holes on the top of the board as shown in Figure 3.4. Most of the electronic components in electronic circuits can be interconnected by inserting their leads or terminals into the holes and then making connections through wires.

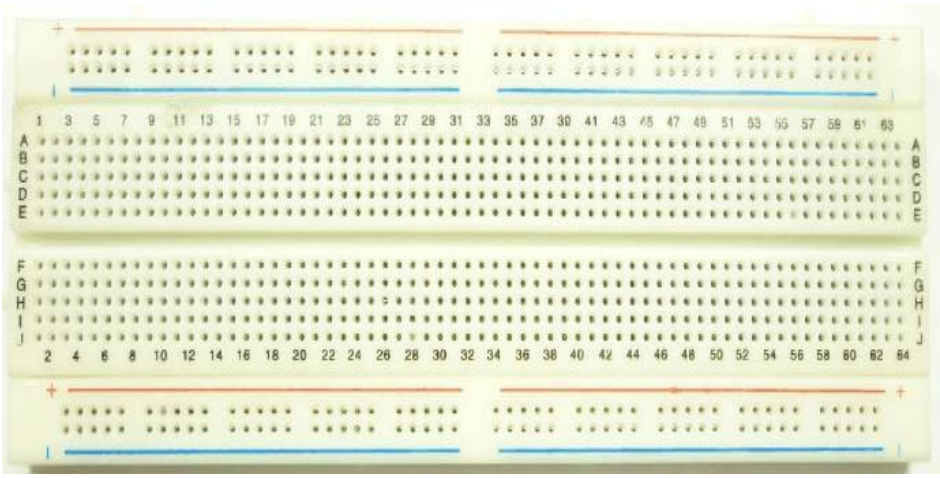

Figure 3.4: Breadboard

- **Jumper Wires:** Jumper wires have connector pins at each end, allowing them to connect two points with each other without soldering. They are typically used with breadboards and other prototyping tools in order to make it easy to change a circuit as per requirement. The set of jumper wires are shown in Figure 3.5.

Figure 3.5: Jumper Wires

- **Bluetooth Module:** The Bluetooth module (version HC-05) is a Master/Slave module (*see* Figure 3.6). By default, the factory setting is Slave. The role of the module (Master or Slave) is configured using *AT Commands*. The Slave module cannot initiate a connection to another Bluetooth device, but it accepts connections. Master module can initiate a connection to other devices. Bluetooth module is used for a serial port replacement to establish connection between Multi-point Control Unit *(MCU)* and Geographical Positioning System *(GPS)* or *PC*.

Figure 3.6: Bluetooth Module (version HC-05)

- **Temperature Probe:** The temperature probe is a precision integrated-circuit with a voltage output, that is, linearly proportional to the Centigrade temperature. The device does not require any external calibration or trimming to provide accuracies over a full -55°C to 150°C temperature range. The temperature probe is shown in Figure 3.7.

Figure 3.7: Temperature Probe

- **pH Probe:** The *pH* probe is used to measure hydrogen ion concentration dissolved in any type of liquids. The total *pH* scale ranges from 1 to 14, with 7 considered to be neutral. *pH* less than 7 is said to be acidic in nature and solutions with a *pH* greater than 7 are basic or alkaline. It has built-in simple, convenient and practical connections to easily work with Arduino controllers. It has a Light Emitting Diode (*LED*) which works as power indicator, a *BNC* connector and *pH*-2.0 sensor interface. It can be connected with Arduino controller by plugging the *PH2.0* interface into the analog input port of Arduino. The probe is shown in Figure 3.8.

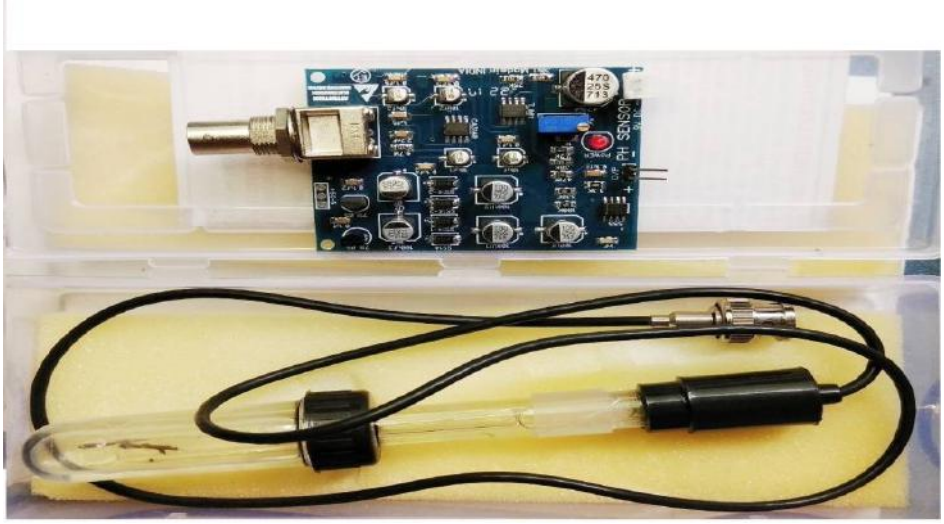

Figure 3.8: *pH* Probe

- **Turbidity Sensor:** Turbidity sensor (see Figure 3.9) is used to test the water quality by measuring the levels of turbidity. It uses light to detect suspended particles in water by measuring the light transmittance and scattering rate, which changes with the amount of total suspended solids *(TSS)* or Total Dissolved Solids *(TDS)* in water. As the *TSS* or *TDS* increases, the liquid turbidity level increases. It provides analog and digital signal output modes. The threshold is adjustable when the output of the sensor is set in digital signal mode.

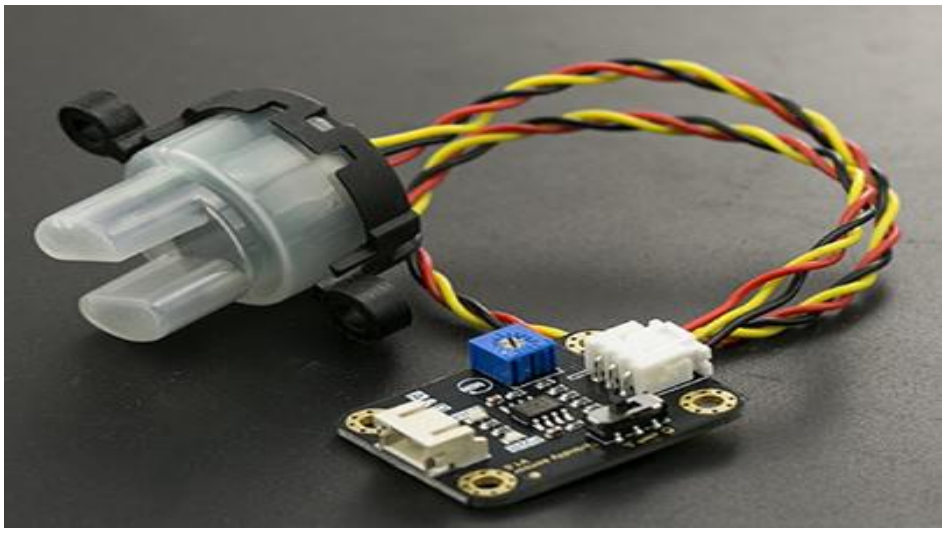

Figure 3.9: Turbidity Sensor

- **Water Level Detection Sensor:** The sensor is the analog type that produces analog output signals according to the water pressure. The water level detection sensor has operating voltage of DC 3-5V and current less than *20mA*. It is an easy to use and cost-effective with high level or drop recognition sensor by having a series of parallel wires. These wires measure droplets or water volume in order to determine the water level. The sensor is shown in Figure 3.10.

Figure 3.10: Water Level Sensor

- **Camera Module:** The camera module (version OV7670) used in thesis work, is a small image sensor having low operating voltage and it provides all functions of a single chip of Video Graphic Array (*VGA*) camera and image processor.

The sensor can output the whole frame, sampling, and various resolution of 8 bits of data through Serial Camera Control Bus *(SCCB)*. The *VGA* image can be captured up to a maximum of 30 frames per second. It provide features to control the image quality, data format and transmission mode of an image. The module is shown in Figure 3.11.

Figure 3.11: Camera Module

The various probes and sensor modules are fabricated on Arduino Uno/Arduino Mega 2560 micro-controller and is placed underwater to measure physical parameters, *i.e.*, Electrical Conductivity, *pH*, Temperature, Chloride, and Dissolved Oxygen of river water.

iii. **Multi-Parametric Sensors:** *MPS* is comprised of Arduino board powered with rechargeable batteries, an external Radio Frequency (*RF*) connector to receive signals, a Bluetooth to send or receive signals acoustically *via* angular communications, and an expansion connector to increase memory size. The maximum bit rate achieved is 16 bits/second. Different types of sensors *namely*, Electrical Conductivity, *pH*, Temperature, Chloride, and Dissolved Oxygen are fabricated on Arduino board and are controlled by user (*see* Figure 3.12(a)). In order to protect sensor's vulnerability to

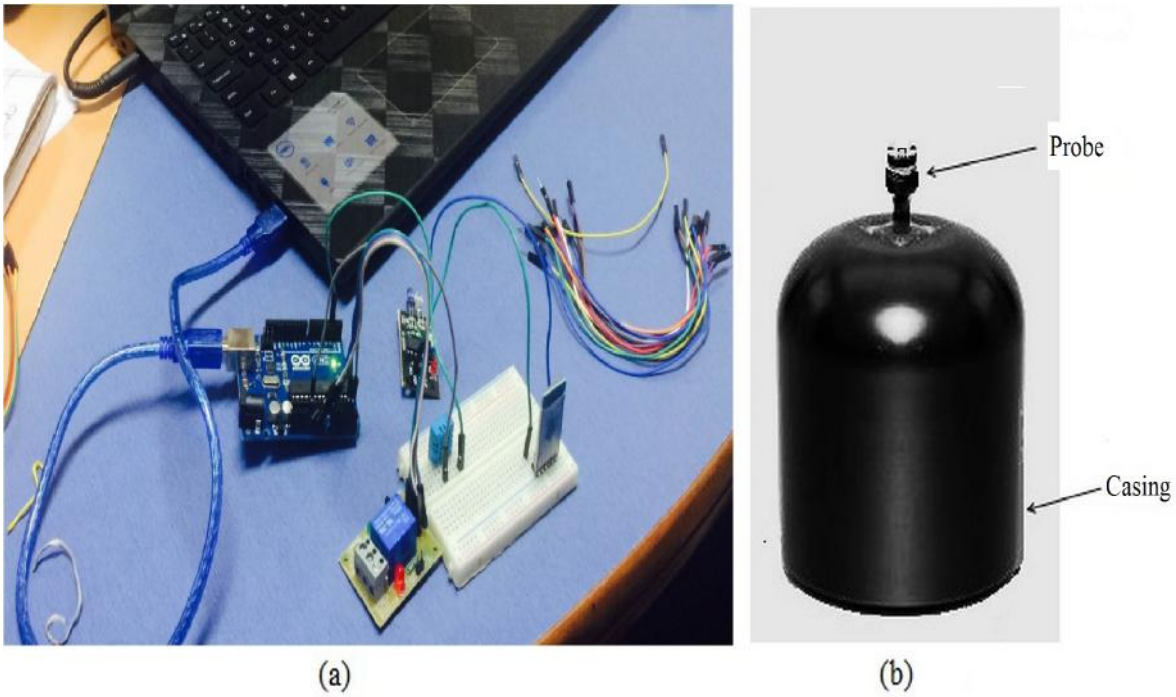

Figure 3.12: Multi-parameter: (a) Sensors Embedded with Arduino and (b) *MPS* in Casing

withstand against enormous water pressure, it is placed inside a casing of stainless conceals (used for housing) as shown in Figure 3.12(b). The probe is a sensor attached to Arduino board to optimize translated phenomena and enhancing sensor's performance. It is placed outside the casing for sensing water's parameters. The specifications of the *MPS* are shown in Table 3.1.

Table 3.1: Specifications of Multi-Parametric Sensor

S. No.	Parameters	Specifications
1	Chip Board	Arduino
2	Frequency Range	25 KHz
3	Communication Method	Bluetooth
4	Transmission Process	Angular
5	Memory	800 KB
6	Packet Size	532 bytes
7	Packet with error ratio (1/1000)	5 (packets)
8	Batteries (Panasonic Eneloop Pro Ni-MH)	1880 and 2550 mAh

3.3 Techniques for Data Transmission

With respect to underwater data transmission, efficient communication protocols among the sink nodes and surface stations are needed. It is due to the fact that high attenuation and scattering affect the acoustic communication. For the purpose, different protocols are being implemented by the researchers based on sleep/wakeup, localization and modulation to provide faster transmission, to avoid collisions among the data traffic that minimizes the congestion on the sensors. The techniques, (*i.e.*, sleep/wakeup and localization) are used to send textual data in form of bits to the surface station whereas modulation is used to send image data in form of bits. These techniques are discussed.

i. **Sleep/Wakeup Techniques:** The Sleep/Wakeup based techniques permit a greater flexibility as they can be tailored to the application needs. It is classified in three broad categories, according to the sensors' switching mode: on-demand, scheduled rendezvous, and asynchronous schemes (Giuseppe et al. (2009)). The sensors must coordinate their wakeup periods with the sink nodes in order to make communication feasible and efficient. The schemes with their detailed description are described.

   - **On-demand:** On-demand scheme is based on the idea that a sensor should be awaken when it has to receive a packet from a neighboring sensor. It minimizes the energy consumption and, thus, makes on-demand schemes particularly suitable for sensor network applications with a very low duty cycle. On-demand sleep/wakeup scheme is aimed at reducing energy consumption in the monitoring state while ensuring a limited latency for transitioning in the transfer state.
   - **Scheduled Rendezvous:** Scheduled rendezvous scheme requires all the neighboring sensors to wake up at the same time. Typically, sensors wake up periodically to check for potential communication. Then, they return to sleep mode until the next rendezvous time. The major advantage of the scheme is that when a sensor is awake, it is guaranteed that all its neighbors are awake. It allows sending broadcast messages to all neighbors. On the flip side, scheduled rendezvous scheme requires sensors to be synchronized in order to wake-up at the same time.

- **Asynchronous:** Asynchronous scheme avoids the tight synchronization among sensors. It allows each sensor to wakeup independently of the others by guaranteeing that neighbors always have overlapped active periods within a specified number of cycles. Asynchronous wakeup was introduced with reference to IEEE 802.11 ad-hoc networks. The basic IEEE 802.11 Power Saving Mode *(PSM)* is suggested for single hop ad-hoc network and thus, it is not suitable for multi hop ad-hoc networks. In this scheme, alternative method is implemented that an asynchronous sensor finds its communication counterpart (*i.e.*, the receiver) active when it wakes up, and is forcing the receiver to listen periodically. The receiver wakes up periodically and listens for a short time to discover any potential asynchronous sender. If it does not detect any activity, it returns to sleep, otherwise remains active for receiving packets.

Among the categories, asynchronous sleep/wakeup is implemented on *MPS* for efficient communication and to retain them for longer periods.

ii. **Localization Techniques:** The localization permits to optimize sensor's position based on the specific sleep/wakeup pattern used for power management. The factors like network architecture, sensor density in an area, number of anchor sensors, geometric shape of the measurement area, sensor time synchronization, and signaling bandwidth among sensors, affect the accuracy of the localization of sensors' position. However, it is the type of measurement and the corresponding precision that determines the accuracy of localization. Thus, localization based measurement techniques are broadly classified into Angle of Arrival *(AOA)*, Time Difference of Arrival *(TDoA)*, Time of Arrival *(ToA)* and Radio Signal Strength *(RSS)* based measurements (Singh et al. (2015)). Each measurement techniques are discussed.

- **Angle of Arrival Measurement:** The *AOA* measurement is obtained from two methodologies, *i.e.*, one from the receiver antenna's amplitude response and another from the receiver antenna's phase response. These methodologies calculate the angle at which the signal arrives from the anchored sensor to the unknown sensor. Then, the region where the unknown sensor is located, is a line having

a certain angle from the anchored sensor. In *AOA* measurement, at least two anchored sensors are needed to calculate the position. The localization error could be large if there is a small error in measurement. The accuracy is dependent on the directionality of the antenna and measurements are affected by multi-path. It has the limitation that it requires directional transmission incurring extra cost and proves to be inefficient method.

- **Time Difference of Arrival Measurement:** *TDoA* measures the difference between the arrival times of a transmitting signal at two separate receivers (anchored sensors) respectively, assuming the locations of the two receivers are known and they are perfectly synchronized. This type of measurement requires three receivers to uniquely locate the transmitter (base sensor's) location. The accuracy is affected by synchronization error and multi-path. The accuracy for finding transmitter's location is improved when the distance between receivers are increased because it increases the difference between the times of arrival at receivers. It has the shortcoming that it does not provide feasibility with *RF* signals underwater.
- **Time of Arrival Measurement:** *ToA* is based on measuring the propagation time of a signal. It computes the range measurement in a distributed way among individual sensors. *TOA* measurement requires precise time synchronization between sender (base sensor) and receiver. It uses a radio signal to synchronize the clocks of the sender and the receiver, *i.e.*, transmitting a radio signal at the same time an acoustic signal is transmitted. Accurate range measurements are carried if sensors have well synchronized clocks. Once the measurement is done among neighboring sensors, each sensor's relative position is computed using clock timings.
- **Received Signal Strength Measurement:** The distance between two sensors are obtained using *RSS* measurement. Most sensors have capability to measure the *RSS*. On the basis of measurement, sensor's position and distance from neighboring sensors are estimated. RSS has the disadvantage that it does not work with acoustical interferences such as tidal noise, Doppler effect and ambient noise,

etc.

Among the techniques, *ToA* is found to be most suitable as it helps in measuring arrival time in localization process. Therefore, it is designed for *MPS* based topological deployment to collect temporal and spatial parameters underwater.

iii. **Modulation Techniques:** Modulation is a process through which audio, video, image or text information is added to an electrical or optical carrier signal to be transmitted over a telecommunication or electronic medium. Modulation enables the transfer of information on an electrical signal to a receiving device that demodulates the signal to extract the blended information. It fastens the transmission through the conversion of data into bits and symbols using Orthogonal Frequency Division Multiplexing *(OFDM)* techniques (Sklar (2001)). *OFDM* is based on multi-carrier modulation and it divides the available bandwidth into closely spaced orthogonal sub-bands. Modulation is a process of transmitting acoustic signals in the form of bits. Each orthogonal sub-band carries a signal that is to be transmitted. *OFDM* works well with fluctuating frequencies, which mitigates the problem of frequency by converting fading channel into small flat fading channels, *i.e.*, single carrier to multi-carrier. Each sub-band is further divided into bit streams, which are mapped using modulation schemes such as Phase Shift Keying *(PSK)*, Binary Phase Shift Keying *(BPSK)*, Quadrature Phase Shift Keying *(QPSK)*, 16-bit Phase Shift Keying *(16PSK)* and 256-bit Phase Shift Keying *(256PSK)*. *PSK* conveys data by changing the phase of modulating signal and is widely used in wireless Local Area Networks *(LAN)* and blue-tooth communications. It considers finite number of phases with uniquely assigned binary numbers. The simplest form of *PSK* is *BPSK*, which takes into account two phases separated by 180°. *QPSK* is another part of *PSK* that considers equi-spaced four points around a circled pixel. The 16-bit and 256-bit *PSK*s take values equi-spaced in a circled pixel collectively.

OFDM solves the problem of Inter-Symbol Interference *(ISI)* that is caused due to lack of carriers, larger delay time, and no spacing to separate the carriers. It combines low rate signals to high data rate communication carrier diminishing interference problems. Since, the information is in the form of bits, therefore, symbols (for information) are

used to construct *OFDM* data and is further converted into time domain using Inverse Fast Fourier Transform *(IFFT)*. The data are modulated in time signals in parallel, for available frequency. At the time of modulation, frames are generated by segmenting the symbols that are received at the receiver end. A cyclic extension is added with each symbol to diminish *ISI*, which considers 25% of previous symbol data added in a next symbol. Thus, the demodulator ease in providing the correct information to the receiver for the entire symbol period, up to the length of cyclic extension as shown in Figure 3.13 below.

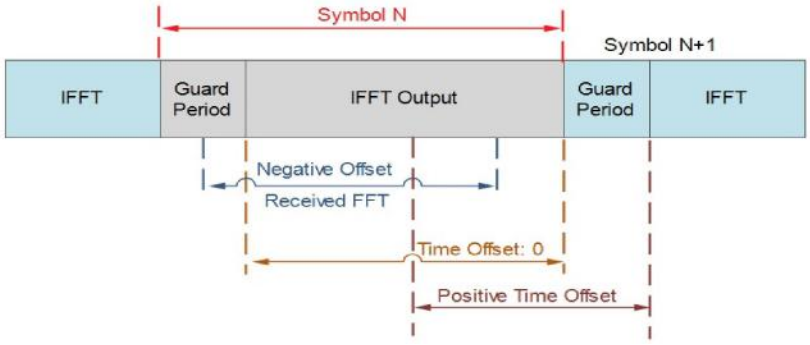

Figure 3.13: Cyclic Extension

Here, the guard period is the duration for uncertainty that is captured by the receiver from the starting point of the symbol period. The process of capturing is provided by Fast Fourier Transform *(FFT)* giving correct information. The effectiveness of cyclic extension is illustrated using Figure 3.14.

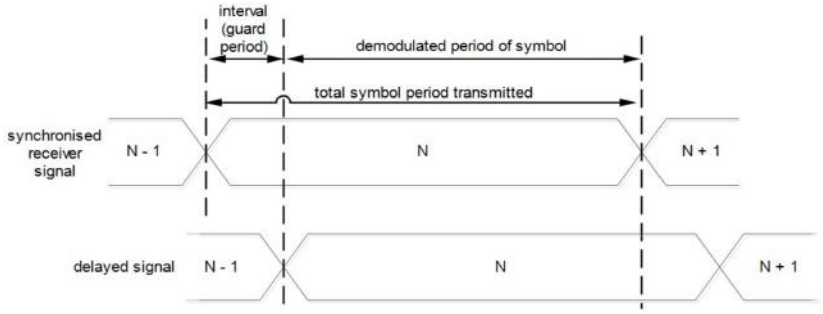

Figure 3.14: Efficiency of Cyclic Prefix

Figure 3.14 indicates that guard interval helps in demodulating signal in cyclic extension and thus provides complete information to surface station.

Spectral bandwidth and Inverse Fast Fourier Transform *(IFFT)* limit the size of the number of carriers who describe the complexity of the system, and its relation is defined as: $total\ carriers \leq \left(\frac{ifft-size}{2}\right) - 2$ (Ballari et al. (2009)). The modulation method has loss in pixels' names as Bit Error Rate *(BER)*. If the frequency (phase shift) is higher, then there is a large symbol with high bit errors. It results into transmission of less symbols and thus, the decoding is at higher risk for incorrect data at receiver side, providing higher peak to signal ratio of *OFDM* symbols. Thus, *OFDM* has high tolerance of power due to limitations of transmission. *OFDM* should maintain the orthogonality of carriers. The two signals are orthogonal if integral of product of the two acoustic signal is *zero* over a time period.

The methodology of *OFDM* is used in the thesis for image transmission to surface station using *MPS*.

3.4 Image Refinement Techniques

The image refinement is used to smooth panoramic images by retaining the edges, reveals image characteristics (such as noise reduction, colorization, edge preservation, detail enhancement, texture editing, haze or rain removal, *etc*). It smooths the edge by considering the pixel values to generate good quality panoramic images. Few of the image refinement techniques are discussed.

i. **Histogram Equalization:** Histogram Equalization *(HE)* method flattens the histogram and stretches the dynamic range of intensity values by using the cumulative density function (Yadav et al. (2014)). It usually enhances the contrast of an image, particularly when the usable information of an image is characterized by close contrast values. Through this arrangement, the intensity or power is scattered on the histogram. Histogram leveling achieves higher contrast by adequately spreading out the most regular force values. *HE* faces few limitations that it transforms the histogram of the input image into a uniform histogram by distributing the entire range of gray levels uniformly over the histogram of an image, with a mean value that is in the middle of gray level range. This results in significant change in the view of the enhanced image.

Moreover, it highlights the borders and edges between different objects, but may reduce the local details of these objects, and thus, it is not adequate for image refinement underwater.

ii. **Dark Channel Prior:** Dark Channel Prior *(DCP)* is a technique to remove haze from an image (He et al. (2011)). It is a type of statistics to generate outdoor haze free images. It emphasizes on the key observation that outdoor images have some pixels with very low intensity. This implies that pixels are very dark and difficult to see with human eye. The technique helps to estimate the thickness of the haze and generate a good quality haze free image. The technique uses matting Laplacian to remove haze by considering dark pixels of the images. It produces high quality depth map that gives the good estimation of transmission. *DCP* has its disadvantage of producing poor quality images if the sunlight is bright and thus, fails to recover true scene radiance of distant objects.

iii. **Guided Image Filtering:** It computes the filtering output by considering the content of a guidance image (input image) (He et al. (2013)). The guided filter is used as an edge-preserving smoothing operator. It has better behaviors near edges. Moreover, the guided filter has a fast and non-approximate linear time algorithm, regardless of the kernel size and the intensity range. It considers foggy images as reference and remove haze by smoothing their edges using bilateral filtering. The produced output has better perseverance and quality. It has a disadvantage that it produces halos near edges which results into incomplete haze removal.

iv. **Discrete Wavelet Transform:** *DWT* is an implementation of the wavelet transform using a discrete set of the wavelet scales on an image and translations, obeying some defined rules prescribed as per the given format (Andreopoulos and van der Schaar (2008)). It can be executed as per the available values of the image that are further be divided into four sub-bands on the basis of low and high filters, *say LL, HL, LH* and *HH* where *'L'* is for low filter and *'H'* is for high filter. The *LH, HL* and *HH* sub-bands are quite uninformative. The low-pass filter is a kind of a predictor, *i.e.*, it tells about the average value of a group of pixels. The high-pass filter stores the errors

that got created by low-pass predictors. *LH* and *HL* stores the errors that is used to get to average values of column-errors across rows, or vice versa, whereas *HH* stores *LH*'s and *HL*'s errors. *DWT* faces few shortcomings that it does not decompose high frequency bands producing blurriness, distortion and aliasing in images. Moreover, it produces some halo effects along the edges due to loss of pixels with some distortions. The first and second level *DWT* are shown in Figure 3.15

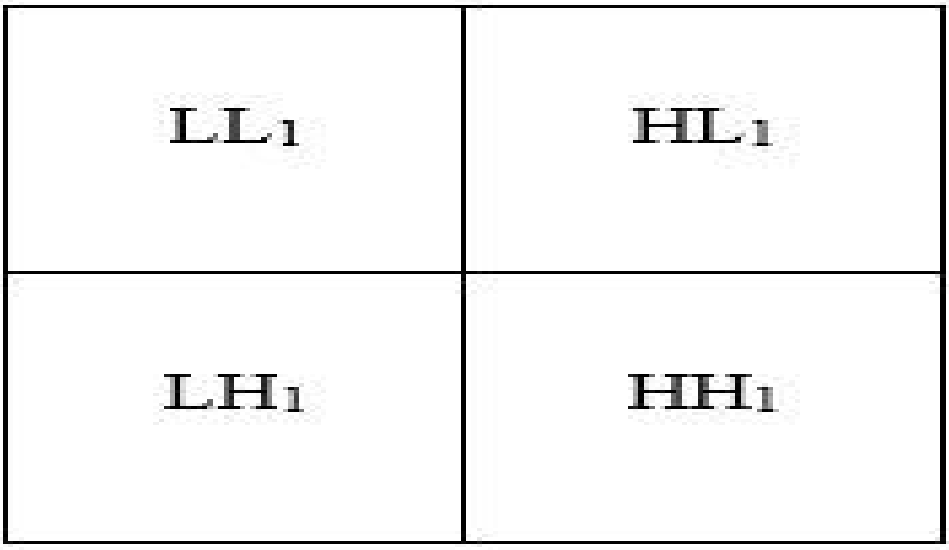

(a)

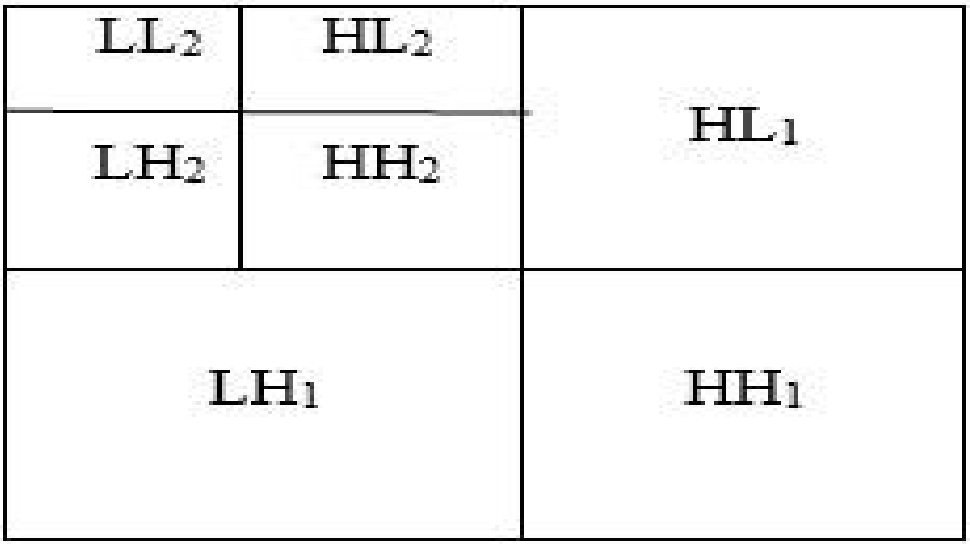

(b)

Figure 3.15: *DWT* Decompositions at (a) First Level (b) Second Level

v. **Ridgelet Transform:** The substantial foundation for Ridgelet analysis is documented by Candes (1998). The continuous Ridgelet transform of image $s \epsilon L^2(\mathbb{R}^2)$ is defined as the scalar product of s with a function $\psi_{a,b,\theta}$, the Ridgelet *2D* function defined from a wavelet *1D* function ψ as given in Eq. 3.1.

$$\psi_{a,b,\theta}(x) = a^{-1/2} \times \psi\left(\frac{x_1 \times cos\theta + x_2 \times sin\theta - b}{a}\right) \tag{3.1}$$

with $x = (x_1, x_2) \epsilon \mathbb{R}^2$, $b \epsilon \mathbb{R}$ is the translation parameter, $a \epsilon \mathbb{R}$ is the dilatation parameter and $\theta \epsilon [0, 2\pi]$ is the direction parameter. The function $\psi_{a,b,\theta}$ is oriented at the angle θ and is constant along lines $x_1 \times cos\theta + x_2 \times sin\theta$.

The transverse to these ridges is a wavelet function. A basic tool for calculating Ridgelet coefficients is to view Ridgelet analysis as a wavelet analysis in the Radon domain. The Radon transform, *Rts* is obtained by applying the *1D* inverse Fourier transform to the *2D* Fourier transform restricted to radial lines going through the origin. This is the projection-slice formula that is used in image reconstruction from projection techniques. The Ridgelet coefficients, *rs* of *s* are given by the *1D* wavelet transform to the projections of the Radon transform where the direction y is constant and t is varying, as given by Eq. 3.2.

$$rs(\theta, a, b) = \int_{\mathbb{R}} \psi_{a,b}(t) \times Rts(\theta, t) dt \tag{3.2}$$

Among the techniques, Ridgelet transform is found to be most suitable technique for panoramic image refinement as it helps to improve pixel's intensities along edges in panoramic image. It helps to overcome issues such as poor visibility, distortion, light scattering, wavelength attenuation, varying colors with increase in depth, and refines images using fusion techniques. It provides better visual quality panoramic images having high pixel intensities, high content information and minimal erred pixels.

3.5 Thesis Contributions

The contributions of the thesis are-

i. An *MPS* is designed to check physical parameters such as Electrical Conductivity, *pH*, Temperature, Chloride and Dissolved Oxygen, of river water.

ii. Two topologies, *namely*, *MPST* and *TPT* are proposed for monitoring the quality of river water. *MPST* helps in sensing results in less time and is an efficient topology for monitoring. *TPT* provides best throughput, maximum packet delivery with no packet loss using *DSR* protocol.

iii. *Hybrid-OFDM* technique is proposed which uses various modulation schemes to transmit sensed images to surface station without any error. Mosaicing technique is used to refine gathered images and to produce good quality panoramic image. To preserve pixel's intensities along edges, Ridgelet based Fusion Technique *(RBFT)* is proposed. *RBFT* refines panoramic images and smooths them by color approximations using fusion approaches.

Chapter 4

Multi-Parametric Sensors' Topology

4.1 Introduction

Water, being an essential ingredient for the survival on Earth's surface; needs to be monitored regularly for its quality. The water quality is defined in terms of variations in physical parameters such as Electrical Conductivity, pH, Temperature, Chloride and Dissolved Oxygen for both coastal and inland marine locations. These parameters have undergone drastic changes due to increased inflow of wastes from industries, domestic, villages, algal blooms and environmental pollution. Hence, it has resulted in to water quality degradation with respect to physical parameters. Thus, there is a requirement of timely preventive measures for regular monitoring and maintenance of the water quality.

The existing sampling technique of monitoring involves high cost, time, labor intensive, on the site sampling, data collection, transportation to laboratories for analysis, and finally subsequent evaluation. This type of monitoring retains sample for a longer time and uses chemical for laboratory testing. Hence, it fails to produce accurate information. In short, the sampling based monitoring is more time consuming, requires man-power and is not cost-effective. To overcome these limitations, *MPST* is proposed[1]. It uses economical sensors and is sustainable in river water for 10-15 days through usage of sleep, wake-up schedule of communication. The topology measures the quality on the basis of physical parameters as

[1]The contents are published in Jindal, H., Saxena, S. and Kasana, S. S. (2017), "A sustainable multi-parametric sensors network topology for river water quality monitoring", *Wireless Networks*, pp. 1-25, https://doi.org/10.1007/s11276-017-1532-z

water pollutants. The measured data from the sensors is transmitted to surface station using localization and communication algorithm. These algorithms are proposed and discussed in subsequent sections. The data is processed at surface station to examine water's quality. The topology enables a user to make immediate measurements without sampling and is inter-operable, consumes less power, produces results in short span of time.

4.2 Proposed Multi-parametric Sensors' Topology

The *MPS* (described in Chapter 3) is used underwater as topology, *namely*, Multi-parametric Sensors' Topology *(MPST)* for gathering physical parameters of water. *MPST* consists of sensors deployed in a pyramidal manner of which, the base is triangular; and it makes the grid as a polyhedron type for sending maximum data. It considers sensors *namely*, low powered and high powered, differentiated on the basis of battery usage. The former uses 1880 mAh batteries and is deployed at the bottom. These are also known as Bottom Sensors *(BoS)*. The latter uses 2550 mAh batteries and are placed at a certain height above the surface level. They are also called as Anchored Sensor *(AS)*. The *BoS* collect information and transmit it up to the *AS via* angular acoustic signals. The *AS* is tied with nylon wires to make it float at certain height through a floater and is within range of bottom sensors. The data collected at *AS* is transmitted to the surface station for further processing. The proposed topology is shown in Figure 4.1.

The geometric setting for the topology has enabled to deploy minimal sensors and can be modified on the basis of area required to be sensed. With its deployment it targets to cover almost 10 square meters in diameter, according to the sensing range of *MPS*. Each deployed sensor has the same range of sensing *say*, r_c and the distance among sensors is d_a; which forms the sides of an equilateral triangle for getting full coverage of the region *say*, ϑ, where ϑ defines the ratio of covered and targeted area to get optimal coverage and thus minimizing the overlapping areas as shown in Figure 4.2. The uncovered area is $\mathscr{A}^{\Delta}_{KLM}$ and is assumed to be zero in order to minimize the sensed region load. With the topology, it is guaranteed to have a targeted sensing coverage with the minimal number of sensors. Theorem 3.1 is postulated for the deployment of *MPST*.

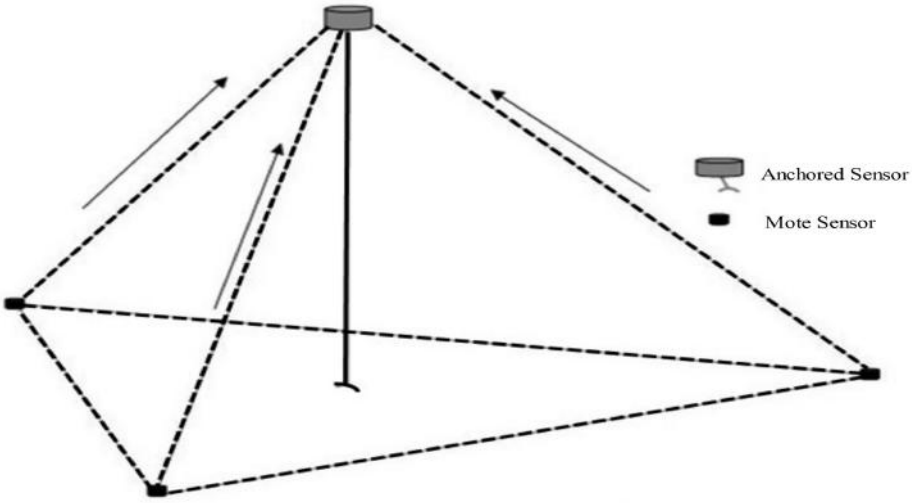

Figure 4.1: Pyramidal *MPST*

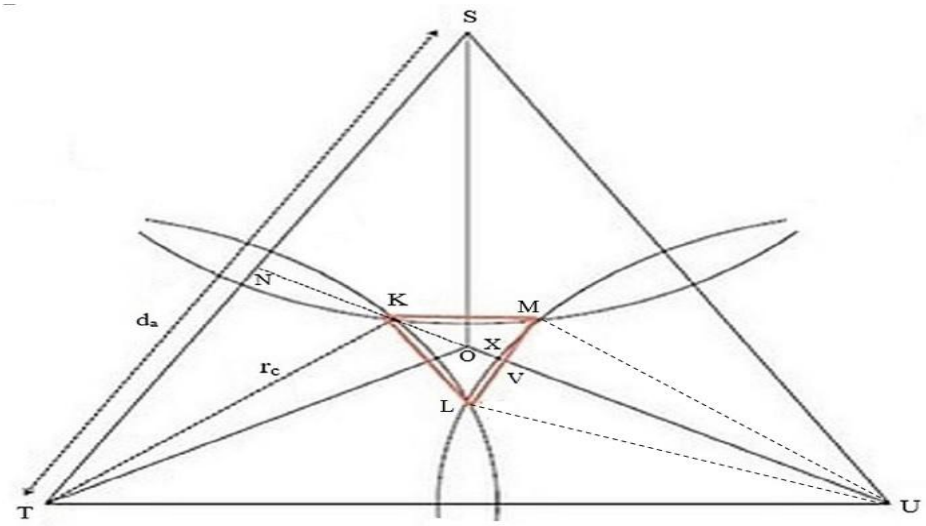

Figure 4.2: Top View of *MPST*

Theorem 3.1. The triangular pyramidal grid has sensing range $\vartheta(d_a/r_c)$, *i.e.*, which is described as the ratio of covered and targeted area given by Eq. 4.1.

$$\vartheta\left(\frac{d_a}{r_c}\right) = \begin{cases} \frac{\mathscr{A}_{STU}-\mathscr{A}_{KLM}}{\mathscr{A}_{STU}} = 1 - \frac{\mathscr{A}_{KLM}}{\frac{\sqrt{3}}{4}d_a^2}, \frac{d_a}{r_c} \in [0,2] \\ \frac{3\frac{\pi r_c^2}{6}}{\frac{\sqrt{3}}{4}d_a^2} = \frac{2\pi}{\sqrt{3}}\left(\frac{d_a}{r_c}\right)^{-2}, \frac{d_a}{r_c} \in (2,\infty) \end{cases} \tag{4.1}$$

where

$$\mathscr{A}_{KLM} = \frac{\sqrt{3}}{4} \times \left(\frac{d_a}{2} - \sqrt{3 \times r_c^2 - \frac{3}{4} \times d_a^2} \right)^2 - 3 \times r_c^2 \times arcsin\left(\frac{LM}{2 \times r_c} \right) + \frac{3}{4} \times LM \times \sqrt{4 \times r_c^2 - LM^2} \tag{4.2}$$

and

$$LM = \frac{d_a}{2} - \sqrt{3 \times r_c^2 - \frac{3}{4} \times d_a^2} \tag{4.3}$$

Proof. To prove the sensing range, two cases are considered. First case is the trivial case for $\frac{d_a}{r_c} \epsilon [0,2]$ which describes the area covered by sensors' communication range and second case is non-trivial for $\frac{d_a}{r_c} \epsilon (2,\infty)$ which considers the area below anchored sensor to be null. Figure 4.2 shows the top view of the topology in which $TK = r_c$ and $TN = d_a/2$. As the triangle *STU* is equilateral, $NO = (\sqrt{3}/6) \times d_a$. Also, $KN = \sqrt{r_c^2 - d_a^2/4}$, holding Eq. 4.4 as

$$KO = NO - KN = (\sqrt{3}/6) \times d_a - \sqrt{r_c^2 - d_a^2/4} \tag{4.4}$$

Since, triangle *STU* is equilateral, therefore, triangle *KLM* is also equilateral. As, $KO = (\sqrt{3}/3) \times LM$, therefore *LM* is given by Eq. 4.5,

$$LM = d_a/2 - \sqrt{3 \times r_c^2 - (3/4) \times d_a^2} \tag{4.5}$$

This implies that the area of the triangle *KLM* is deduced as in Eq. 4.6, *i.e.*,

$$\mathscr{A}_{KLM}^{\Delta} = (\sqrt{3}/4) \times LM^2 \tag{4.6}$$

For expressing the sensing range $\vartheta(d_a/r_c)$, there is a need for computing the area $\mathscr{A}_{KLM}$ of uncovered part *KLM* within the circles having centers at *S, T,* and *U* with radius r_c. This is calculated using Eq. 4.7.

$$\mathscr{A}_{KLM} = \mathscr{A}_{KLM}^{\Delta} - 3 \times \mathscr{A}_{LXMV} \tag{4.7}$$

The $\mathscr{A}_{LXMV}$ is computed as the difference among areas of region *LXMU* and triangle *LMU* as shown in Eq. 4.8, *i.e.*,

$$\begin{aligned}\mathscr{A}_{LXMV} &= \mathscr{A}_{LXMU} - \mathscr{A}^{\Delta}_{LMU} \\ &= r_c^2 \times arcsin(LM/2r_c) - (LM/4) \times \sqrt{4 \times r_c^2 - LM^2}\end{aligned} \tag{4.8}$$

Thus, $\mathscr{A}_{KLM}$ is given by Eq. 4.9,

$$\begin{aligned}\mathscr{A}_{KLM} = \frac{\sqrt{3}}{4} \times \left(\frac{d_a}{2} - \sqrt{3 \times r_c^2 - \frac{3}{4} \times d_a^2}\right)^2 \\ - 3 \times r_c^2 \times arcsin\left(\frac{LM}{2 \times r_c}\right) + \frac{3}{4} \times LM \times \sqrt{4 \times r_c^2 - LM^2}\end{aligned} \tag{4.9}$$

where $LM = d_a/2 - \sqrt{3 \times r_c^2 - (3/4) \times d_a^2}$, providing Eq. 4.1 for the first case. For the second case, there is no overlapping, thus the covered area ϑ is calculated directly. For calculating and sending data with angular movement to the upward position, the edge and slant height are calculated as in Eqs. 4.10 and 4.11:

$$e = \sqrt{h^2 + \frac{1}{3} \times a^2} \tag{4.10}$$

$$s = \sqrt{h^2 + \frac{1}{12} \times a^2} \tag{4.11}$$

where e, s, h, and a are edge, slant height, height and length of the side, respectively, of *MPST*. Thus, Eq. 4.1 is used to compute the sensing coverage area.

MPST intends to achieve an efficient perception of appropriate deployment area for river monitoring such that destined location and communication coverage is obtained; providing timely alarms to use purification process properly. It is extended at a vividly large scale to get maximum overall coverage of the area. The extended topology is in the form of hexagonal tetrahedron having 7 *BoS* and 6 *AS* (*see* Figure 4.3(a)). The *BoS* are placed in order to get coverage of almost 20 square meters in diameter, according to the sensing range. The *AS* are deployed at a height of 6 meters from the *BoS*. The data thus collected is in redundant form

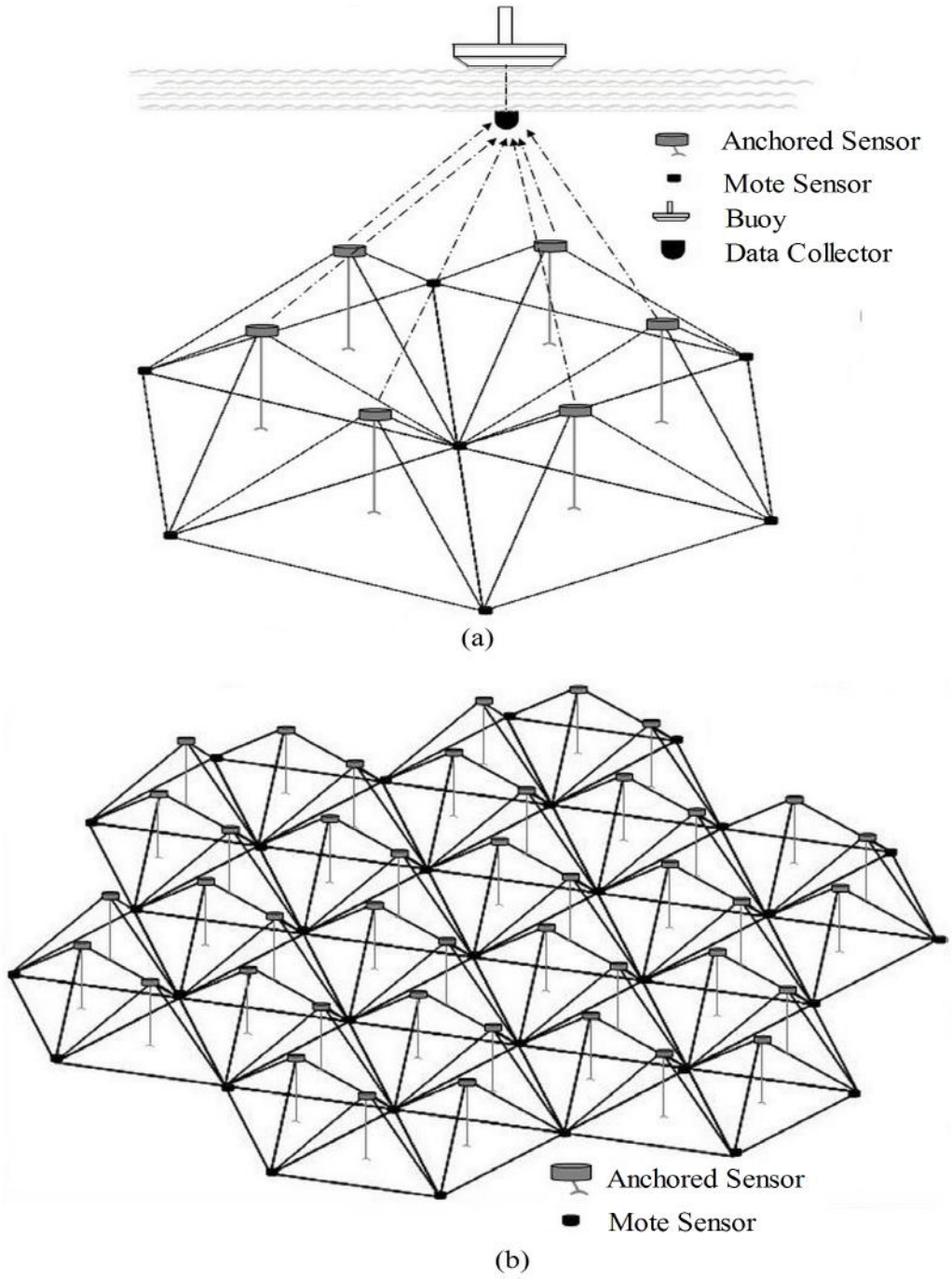

Figure 4.3: *MPST* Deployment (a) Strategy 1 (b) Strategy 2

and is used as accuracy to get the finest information in underwater. The topology can further be extended to explore various regions of interest at river level and giving an alarm for any unusual activity (*see* Figure 4.3(b)). The consequences like cylindrical spreading, acoustic path loss, energy consumption and water current are discussed in subsequent sections.

4.2.1 Cylindrical Spreading

The acoustic waves at river surface with upper and lower boundaries are assumed to be distributed uniformly like surface of cylinder with radius r_c equivalent to sensing range, at height H_t (equivalent to depth of river). These waves are spread gradually in cylindrical form and radiate horizontally far from the source (*see* Figure 4.4) (Chaitanya et al. (2011)).

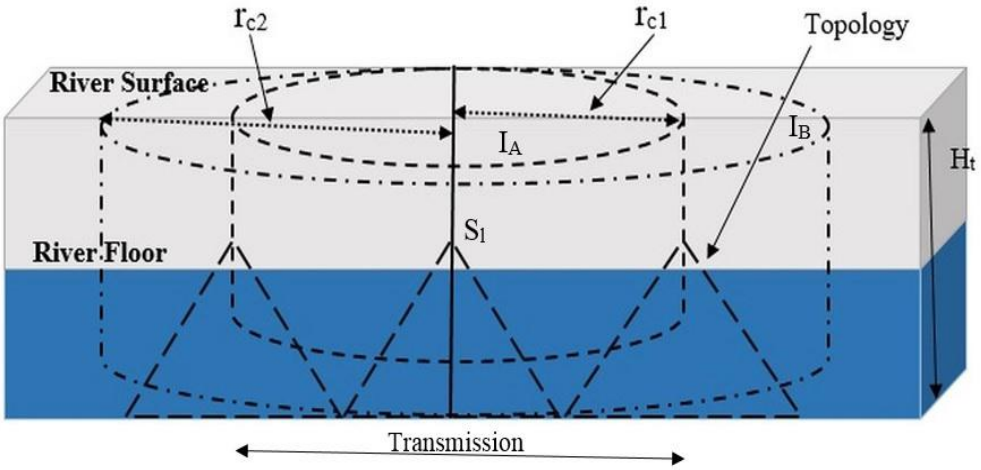

Figure 4.4: Cylindrical Spreading of Acoustic Wave

Let I_A and I_B are the intensities at near and far location to a source pint, respectively, then Transmission Loss, T_l (in dB) is given by Eq. 4.12.

$$T_l = 10 \times log_{10}\left(\frac{I_A}{I_B}\right) = 10 \times log_{10}(I_A) - 10 \times log_{10}(I_B) \tag{4.12}$$

Here, the Source level, S_l is described using Eq. 4.13.

$$S_l = 10 \times log_{10}\left(\frac{I_A}{I_{A_{new}}}\right) = 10 \times log_{10}\left(\frac{I_A}{\nu \times P_{w_a}}\right) \tag{4.13}$$

where, ν is the noise constant, and P_{w_a} is the power consumption.
Initially, P_{w_a} and ν are assumed to be 1. Thus, Eq. 4.13 is deduced to Eq. 4.14,

$$S_l = 10 \times log_{10}(I_A) \tag{4.14}$$

Therefore, the relation among T_l and S_l is found by replacing value of S_l in Eq. 4.12 and is

shown in Eq. 4.15.

$$T_l = S_l - 10 \times log_{10}(I_B) \tag{4.15}$$

Eq. 4.15 is used to find transmission loss in *MPST*.

4.2.2 Acoustic Path Loss

The path loss is defined as the rate at which acoustic waves propagate with respect to frequency and distance among sensors or surface station in underwater (Chaitanya et al. (2011)). It is affected due to refraction, reflection, diffraction, spreading loss and absorption loss. Moreover, it considers a spreading factor, l, described as the ratio of power in dominant path to the power in scattered path, *i.e.*,

$$l = \frac{power\ in\ dominant\ path}{power\ in\ scattered\ path} \tag{4.16}$$

The value of l is *zero*, if the communication is Rayleigh and is *infinite*, if communication is Gaussian. In order to have less probability for dwindling of acoustic wave two different spreads, *namely*, cylindrical, sphere with values 2 and 1, respectively, are defined.

Among them, cylindrical spread is considered for data transmission in *MPST*. It is due to its tendency to consider spreading and absorption loss factors and is independent from refraction, reflection and diffraction. It is given by Eq. 4.17.

$$A_l(d_a, f_{all}) = d_a^l \times a(f_{all})^l \tag{4.17}$$

where, A_l is acoustic path loss, d_a is distance among sensors, f_{all} is frequency in *KHz* and $a(f_{all})$ is absorption loss with changing frequencies. Taking logarithmic on both sides of Eq. 4.17 gives Eq. 4.18. This equation is used to compute acoustical path loss.

$$10 \times log_{10}(A_l(d_a, f_{all})) = 10 \times l \times log_{10}(d_a) + l \times 10 \times log_{10}(a(f_{all})) \tag{4.18}$$

where, $10 \times l \times log_{10}(d_a)$ is spreading loss, $l \times 10 \times log_{10}\ (a(f_{all}))$ is absorption loss and l has value 2 (for cylindrical spreading).

Thorpe's formula is used to calculate absorption loss and is given in Eq. 4.19 (Thorp (1967)).

$$10 \times log_{10}(a(f_{all})) = 0.10 \times \left(\frac{f_{all}^2}{f_{all}^2+1}\right) + 45 \times \left(\frac{f_{all}^2}{f_{all}^2+4100}\right) + 0.275 \times 10^{-3} \times f_{all}^2 + 0.003 \tag{4.19}$$

The absorption loss is computed in dB/km and the frequency in KHz.

4.2.3 Energy Consumption

It is defined as the consumption of power while transmitting sensed data among sensors. The energy consumption is analyzed with transmitting data in single-hop, in which *BoS* send data directly to *AS* and further to surface station.

As the acoustic signals propagate in cylindrical manner, it leads to path loss (Sehgal et al. (2011)). Considering two points, say r_{c_1} and r_{c_2} as shown in Figure 4.4, where power is measured using Eqs. 4.20 and 4.21.

$$P_{w_a} = 2 \times \pi r_{c_1} H_t I_A \tag{4.20}$$

$$P_{w_b} = 2 \times \pi r_{c_2} H_t I_B \tag{4.21}$$

where, H_t is cylinder's height (depth of surface). As, P_{w_a} and P_{w_b} are considered to be full at an instance. Therefore,

$$P_{w_a} = P_{w_b} \tag{4.22}$$

The acoustic signal radiates horizontally away from source. Then, its intensity decreases and is given as inverse of power range for cylindrical spread, *i.e.*, $I_B = I_A \left(\frac{r_{c_1}}{r_{c_2}}\right)$. For $r_{c_1} = 1$, T_l is given by Eq. 4.23.

$$T_l = 10 \times log_{10}\left(\frac{I_A}{I_B}\right) = 10 \times log_{10}(r_{c_2}) \tag{4.23}$$

Let's suppose that *BoS* are located at distance $N_H d_a$ from *AS* that aim to send K_p pack-

ets. Here, power level $P_{w_{single}}$ and energy consumed $E_{single_{total}}$ are given by Eqs. 4.24, 4.25, respectively, as:

$$P_{w_{single}} = 2\pi r_{c_1} H_t I_A \tag{4.24}$$

and

$$\begin{aligned} E_{single_{total}} &= P_{N_H d_a} T_x K_p + P_{(N_H-1)d_a} T_x K_p + ... + P_{d_a} T_x K_p \\ &= T_x K_p \Sigma_{i=1}^{N_H} P_{i.d_a} \end{aligned} \tag{4.25}$$

where, N_H is number of hops, T_x is transmission time of one packet.

T_l in cylindrical spreading and attenuation is denoted using Eq. 4.26 (Ainslie and McColm (1998)).

$$T_l = 10 \times log_{10}(r_c) + \beta \times r_c \times 10^{-3} + A_p \tag{4.26}$$

where, r_c is the range, β is coefficient of absorption and A_p is loss accounting multi-path propagation. β is calculated using model described by Ainslie and McColm (1998) and is calculated using Eq. 4.27.

$$\begin{aligned} \beta = 0.10 \times \frac{f_A \times f_{all}^2}{f_A^2 + f_{all}^2} \times e^{\frac{pH-8}{0.5}} + 0.5 \times \left(\frac{Temp}{43} + 1\right)\left(\frac{Cl}{35}\right) \\ \frac{f_B \times f_{all}^2}{f_B^2 + f_{all}^2} \times e^{-\frac{D_s}{6}} + 0.049 \times 10^{-3} \times f_{all}^2 \times e^{-\left(\frac{Temp}{27} + \frac{D_s}{17}\right)} \end{aligned} \tag{4.27}$$

where, pH tells the acidic nature of river, $Temp$ is temperature in °C, D_s is depth (in kms) and Cl is chloride in mg/l. f_A and f_B is obtained using Eqs. 4.28, 4.29, respectively.

$$f_A = 0.78 \times \sqrt{\frac{Cl}{35}} \times e^{\frac{Temp}{26}} \tag{4.28}$$

$$f_B = 42 \times e^{\frac{Temp}{17}} \tag{4.29}$$

Using Eq. 4.15, the Eq. 4.30 is deduced as-

$$I_A = 10^{\frac{S_l - T_l}{10}} = 10^{\frac{S_l - 10 \times log_{10}(r_c) + \beta \times r_c \times 10^{-3} + A_p}{10}} \tag{4.30}$$

The power consumption in single hop is estimated by Eq. 4.20 and is computed using Eq. 4.31.

$$\begin{aligned} P_{w_{single}} &= 2 \times \pi \times r_c \times H \times I_A \\ &= 2 \times \pi \times r_c \times H \times 10^{\frac{S_l - 10 \times log_{10}(r_c) + \beta \times r_c \times 10^{-3} + A_p}{10}} \end{aligned} \tag{4.31}$$

Eqs. 4.25 and 4.31 are used to find energy consumption in single hop for *MPST*.

The above discussed effects are confined to the available bandwidth of acoustic channel that affects *MPST*'s range and frequency. The long range systems with few *KHz* bandwidth is operated up to few kilometers whereas short range systems with 100 *KHz* bandwidth operate at few meters, hence low bit rates.

4.2.4 Water Current Consequence on *MPST*

During high currents in water, the deployed sensors get affected with number of factors like ambient noise, propagation delay and Doppler effect. These factors deteriorate the performance of sensors, hence, need to be resolved. The deployment of *MPST* consider sensors network to be self-organizing and are distributed randomly across the deployed area. Initially, the sensors *(BoS)* are dropped into the river from surface buoy and communicate among themselves once they settle down on bottom surface. The *AS* with floater is kept at certain height and is in the range of *BoS*. The *BoS*'s location is unaware and *AS* keep information for *BoS* position.The *BoS* are assumed to be variable in 3-Dimensional river. Since, the acoustic signals experience these factors due to parameters like temperature, salinity, and altitude. Therefore, their effects need to understand with regard to *MPST* so that they can be minimized. Each of them is discussed below.

i. **Ambient Noise:** It is the background sound noise that is generated from various sources at a given location. It considers four sources of noise, *i.e.*, turbulence, ship-

ping, waves and thermal (Wenz (1962);King et al. (2010)). It is measured by Eq. 4.32.

$$Nl = Nt(f) + Ns(f) + Nw(f) + Nth(f) \tag{4.32}$$

where, Nl is Ambient noise, f is frequency, Nt is turbulence noise, Ns is shipping noise (with s_n as factor of shipping with value lies between 0 and 1), Nw is wave noise (w is wind speed in m/s), and Nth is thermal noise.

These sources are having continuous spectrum and Gaussian statistics. The values of each noise sources is obtained from following Eqs. 4.33, 4.34, 4.35, and 4.36.

$$10 \times log_{10}(Nt(f)) = 17 - 30 \times log_{10}(f) \tag{4.33}$$

$$10 \times log_{10}(Ns(f)) = 40 + 20(s_n - 0.5) + 26 \times log_{10}(f) - 60 \times log_{10}(f + 0.03) \tag{4.34}$$

$$10 \times log_{10}(Nw(f)) = 50 + 7.5 \times w^{\frac{1}{2}} + 20 \times log_{10}(f) - 40 \times log_{10}(f + 0.4) \tag{4.35}$$

$$10 \times log_{10}(Nth(f)) = -15 + 20 \times log_{10}(f) \tag{4.36}$$

Eqs. 4.32 - 4.36 are used to analyze noise effects on *MPST*.

ii. **Propagation Delay:** It is described as the amount of time taken by acoustic signal to travel among *AS*, *BoS* and surface station. The speed of sound in water is 1500 m/s which is lower than the speed of electromagnetic waves in air. This observes propagation delays (seconds) in underwater with difficulty for sending complete information to surface station and coherence time (time duration of channel impulse response) is less, *i.e.*, 100 milliseconds (Sozer et al. (2000)).

iii. **Doppler Effect:** It is defined as change in frequency of signals when speed among transmitter and receiver is relative. At the time of nearby *BoS* and *AS*, the signal of successor considers the effect on it *(BoS)* from previous point (hop) and thus, it *(BoS)* again send signal with more frequency to *AS* or surface station. The underwater

communications deal with non-negligible Doppler effect that are caused due to relative motion of signal among *AS, BoS* (Xiao (2009)). The Doppler scaling factor is shown by Eq. 4.37.

$$dp = \frac{v \times r}{c} \tag{4.37}$$

where, $v \times r$ is relative velocity, c is acoustic signal propagation speed.
The Doppler effect of underwater channel is given by Eq. 4.38.

$$Dp_e(\upsilon,t) = \sigma_P \times amp_P(t) \times \delta(t - \upsilon_P + dp \times t) \tag{4.38}$$

where, σ_P and $amp_P(t)$ are variance and amplitudes of channel, respectively and υ_P are the delays. In an open air, the Doppler effect due to electro-magnetic waves is 10^{-7}, but in underwater it can reach to 10^{-4}. This is due to the lower velocity of acoustic signals. There are many Doppler shifts in underwater channels due to wide-band signals.

Although these factors support performance up-gradation with respect to *MPST*, but they raise a critical issue related to positioning disturbance of sensors *(AS, BoS)*. The positioning disturbance leads to problem in communication among deployed sensors. The technique of finding the correct position of sensor takes into consideration its mobility as major concern parameter in distributed environment. Therefore, there is requirement for strategy that can work for maintaining and discovering the location of sensors locally. One possible solution is *localization strategy*. It uses different measurement techniques that include Received Signal Strength *(RSS)*, Angle of Arrival *(AoA)*, Time of Arrival *(ToA)* and Time Difference of Arrival *(TDoA)* (Chandrasekhar et al. (2006)). *RSS* does not work with acoustical interferences such as tidal noise, Doppler effect and ambient noise, *etc*. *AoA* requires directional transmission incurring extra cost and *TDoA* provides no feasibility with *RF* signals in underwater. Out of these, *ToA* is most suitable as it helps in measuring arrival time in localization process (Lee et al. (2008b)). Therefore, *ToA* based localization algorithm is designed for *MPST* deployment to discover sensor's location. Considering 3-Dimensional deployment of *MPS* and its coordinates as (X,Y,Z). The localization algorithm is discussed with its four

phases *namely*, deployment, distance estimation, neighboring sensor selection and position estimation (Bisht et al. (2011); Naik and Nene (2012)). These phases are explained below.

i. **Sensor Deployment:** For *AS*, a flag $F1$ is initialized to *one* and for *BoS*, $F1$ is initialized to *zero*. The characteristics of *MPS* are Sensor-ID, Network-ID, F1, list of neighboring sensors, and sensors' position, (X,Y,Z), where Z is the depth at which sensor is placed. Sensor-ID is a unique number to identify a sensor. Network-ID tells the network of sensor, $F1$ stores the status of sensor. If it is *one*, then it is *AS* and if it is *zero*, then it is *BoS*, whose location is yet to be found.

ii. **Distance Estimation:** For finding position of unknown sensors *(BoS)*, the distance among *AS*s and *BoS* are estimated using *ToA* technique. *ToA* uses propagation time of signal to estimate distance. To measure propagation time, it needs precise time synchronization among sensors. If acoustic signal is sent at time interval of T_{i_1} and is received at other sensor at time T_{i_2}, then the distance among *BoS* is given by Eq. 4.39.

$$d_a = P_s \times (T_{i_1} - T_{i_2}) \tag{4.39}$$

Here, P_s is speed of propagation (1500 m/s).
Using the process, all neighboring *AS* and *BoS* lists are found in communication range.

iii. **Neighboring Sensor Selection:** There is need of minimum three reference points to find coordinates of *BoS* which provide point of intersection. The list of neighboring sensors has information of nearby sensors; and the distance among them. The communication range of sensor represents a sphere as sensor's sensing range and sends data in omni-direction (Foley et al. (2013); PadmaPriya (2015)). Hence, the intersection of two spheres will provide circle in plane as shown in Figure 4.5.

Thus, the selected *BoS* gives three overlapping spheres that intersect at one point, taking Figure 4.2 as an assumption. Considering the equations of three spheres, the intersection is given by Eqs. 4.40, 4.41, and 4.42.

$$(X - X_1)^2 + (Y - Y_1)^2 + (Z - Z_1)^2 = r_1^2 \tag{4.40}$$

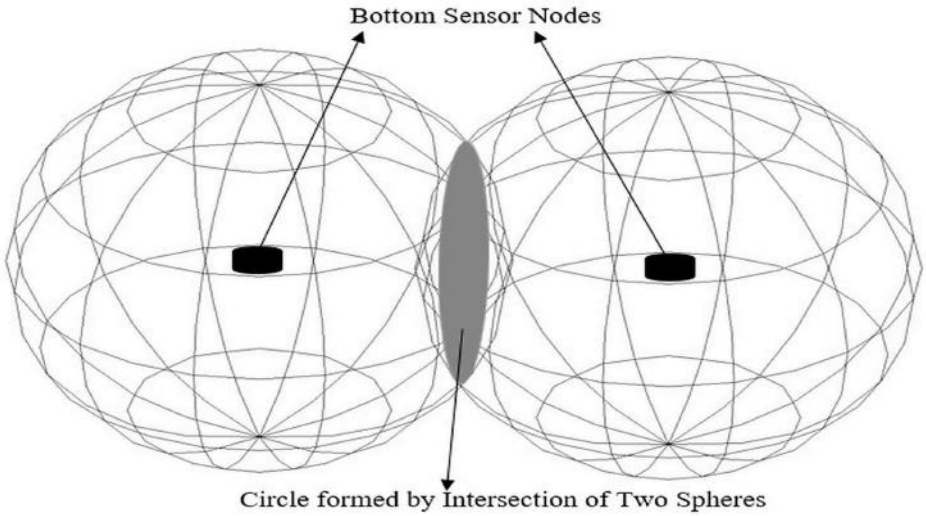

Figure 4.5: Intersection of Spheres

$$(X-X_2)^2+(Y-Y_2)^2+(Z-Z_2)^2=r_2^2 \tag{4.41}$$

$$(X-X_3)^2+(Y-Y_3)^2+(Z-Z_3)^2=r_3^2 \tag{4.42}$$

where, (X_1,Y_1,Z_1), (X_2,Y_2,Z_2) and (X_3,Y_3,Z_3) are coordinates of three reference points and (X,Y,Z) is coordinate of unknown sensor. Taking any equation from above and subtracting from other two, will provide those other two equations into linear equation in three variables and is given by Eq. 4.43.

$$\mathbb{A}_i \times X + \mathbb{B}_i \times Y + \mathbb{C}_i \times Z = ed_i \tag{4.43}$$

where, *ed* gives the intersecting reference point, i = 1,2,3 and the equation provides intersecting circle in plane. The possibilities of intersection of planes are shown in Figure 4.6.

To find whether the three planes in Eq. 4.43, meet at single point which would tell the reference (neighboring) sensor, it must satisfy following two conditions.

i. The first two planes should not be parallel to each other.

ii. The line formed by the intersection of the first two planes should not be parallel to the third plane.

To find the intersection of two planes, consider their vectors as $<a_1, b_1, c_1> = n_1$, $<a_2, b_2, c_2> = n_2$ and $<a_3, b_3, c_3> = n_3$; which are normal (perpendicular) to planes $\mathbb{A}_1 \times X + \mathbb{B}_1 \times$

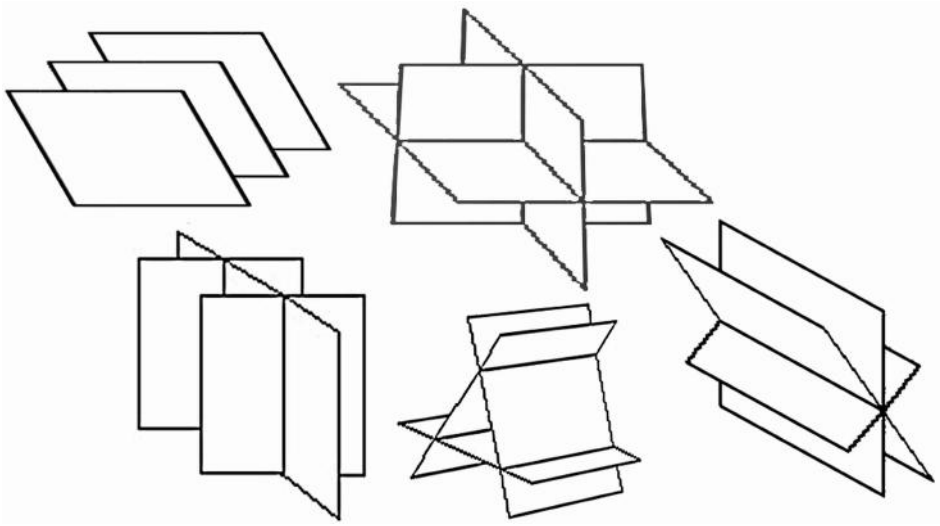

Figure 4.6: Possibilities for Intersection of Planes

$Y + \mathbb{C}_1 \times Z = ed_1$, $\mathbb{A}_2 \times X + \mathbb{B}_2 \times Y + \mathbb{C}_2 \times Z = ed_2$ and $\mathbb{A}_3 \times X + \mathbb{B}_3 \times Y + \mathbb{C}_3 \times Z = ed_3$, respectively. From geometric reasoning, it is concluded that the planes are either parallel or intersecting in only straight line. If normal vectors n_1 and n_2 are parallel then its cross product is zero, *i.e.*, $n_1 \times n_2 = 0$. If planes are intersecting then $n_1 \times n_2 > 0$, always. Since, the intersecting line is perpendicular to plane, therefore, its cross product provide a perpendicular vector adjacent to these planes and is parallel towards the planes' intersection. It is given by Eq. 4.44.

$$< a_1, b_1, c_1 > \times < a_2, b_2, c_2 > = < a_{12}, b_{12}, c_{12} > = D_v \tag{4.44}$$

where D_v is directional vector (formed by intersection of planes).

iv. **Estimating Position:** Using pressure sensors, the depth and position of unknown sensors *(BoS or AS)* are identified by modifying the Eq. 4.43 giving Eq. 4.45.

$$\mathbb{A}_i \times X + \mathbb{B}_i \times Y = fd_i \tag{4.45}$$

where, $fd_i = ed_i + \mathbb{C}_i \times Z$.

Using the above Eqs. 4.40, 4.41, 4.42, and 4.45, the values of unknown sensors are

estimated, *i.e.*, (X,Y,Z). It does not consider distances among known sensors and thus reducing their computational overhead.

The localization algorithm is distributed and decentralized in nature. It is suggested for locating the sensors *(BoS and AS)* which are moved apart due to high currents of river. With the deployment, if any movement or part is moved from the prescribed location then it's location error is to be checked. On the basis of these phases, the working of the localization algorithm is given as under (*see* Algorithm 4.1).

Algorithm 4.1 Localization Algorithm

Require: Bottom Sensor *(BoS)*, Anchored Sensor *(AS)*, Time of Arrival *(ToA)*, Distance Estimation (D_e), and Propagation Time (P_s), number of sensors (n), threshold

begin
for ($AS_i = 1..6$) **do**
  for ($BoS_j = 1..3$) **do**
    if ($range(BoS_j) == true$) **then**
      $D_e \longleftarrow P_s(T_1(BoS_j) - T_2(AS_i))$ // Distance Estimation
      if ($D_e \leq$ threshold) **then**
        store $list_A \longleftarrow BoS_j$ // storing BoS_j
      end if
    end if
  end for
  for ($BoS_j = 1..3$) **do**
    if ($AS_i ==$ 'selected' & & $list_A(BoS_j(data)) == true$) **then**
      send $position(BoS_j)$ to AS_i
      $communicate(AS_i, BoS_j)$ //calling Algorithm 4.2
    end if
  end for
end for
end

In this algorithm, the process begins with initializing a loop for *AS*. It checks for *BoS* in range. The distance is estimated to provide the difference among the positions of *BoS* and *AS* within communication range using *ToA* technique. A condition is checked whether estimated distance is lesss then threshold or not and stores *BoS*s positions in array list, $list_A$. If *AS* is selected and list has data for position of *BoS* then *BoS*s position is send to *AS*. The process then start communicating among the sensors (*BoS* and *AS*) which are in communication range.

The location error is computed using mean estimation error and is given by Eq. 4.46. Mean Estimation Error, ME_{err} defines the efficiency of localization algorithm.

$$ME_{err} = \frac{\Sigma_{i=1}^{73} \sqrt{\left(\left(X_i - X_i'\right)^2 + \left(Y_i - Y_i'\right)^2 + \left(Z_i - Z_i'\right)^2 \right)}}{73} \tag{4.46}$$

where, (X_i, Y_i) is sensor's position and (X_i', Y_i') is localization estimated position of sensor; with maximum total number of sensors to be 73.

4.2.5 Communication in Topology

For communication, the *MPST* is having six pyramidal clusters, namely (A-F), seven Bottom Sensors, $BoS_{(1-7)}$ and six Anchored Sensors, $AS_{(i-vi)}$, as shown in Figure 4.7. Its working comprises of two primary states, *namely*, *communication* and *clustering*. The former helps to establish a communication avenue among BoS_i(i = 1..7) and $AS_i \forall$ i = 1..6, namely, (i-vi), which gathers the necessary data from the clusters, (A to F). The *AS* act as Cluster Head (CH[i] $\forall$ i = 1..6) and forwards the sensed evidences to the data collector. The latter is authoritative for construction of clusters and selecting complementary *AS* from it. With *AS*, data is received from all *BoS* and then the sensors are checked for threshold value in order to find its workable state. If it is persistent, the cycle is repeated again for collecting data. Here, the following assumptions are considered for *clustering* and *communication* process.

i. All *ASs* are in floating mode and are tied with bottom surface using nylon wires.

ii. The surface station is present at the top, at one end of the network.

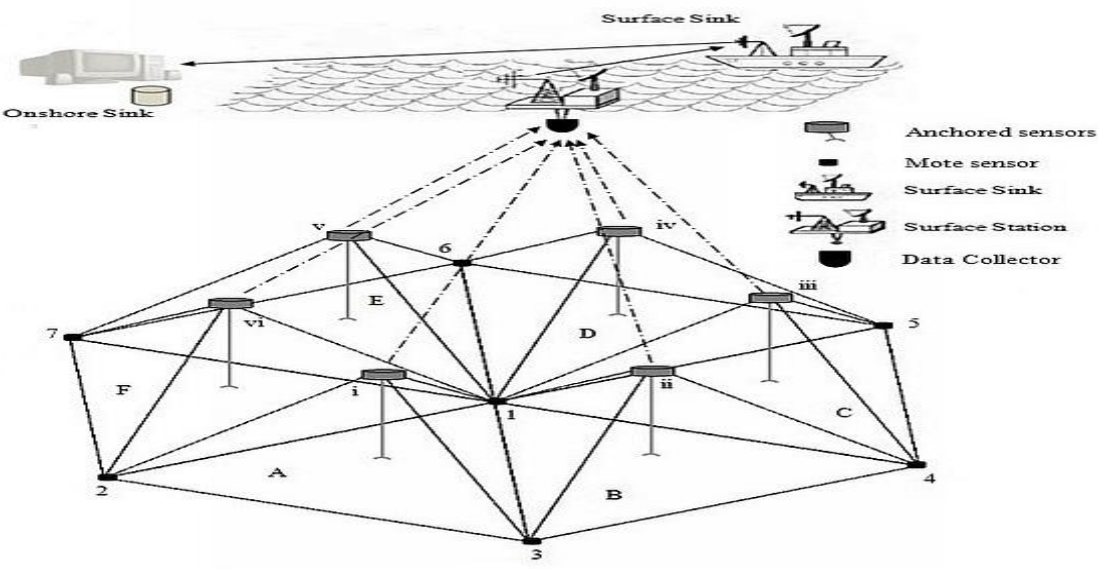

Figure 4.7: Labeled Topology

iii. The sensor's location is stored at surface station.

iv. All the sensors are homogeneous, but they are having different factors like failure, congestion, and the energy level.

Using these assumptions, communication algorithm is designed for data *sensing* at *BoS* and *sending* it to both *AS* and surface station using acoustic signals. The procedure is discussed in Algorithm 4.2.

In this algorithm, a counter is initialized to 0 and its *clustering* process begins. Initially, all sensors are in sleep mode and the process checks for sensors in range for clustering using Eq. 4.1. If *BoS* are active in clusters, then *AS* will get activated to receive data from *BoS*. Once *clustering* is done, both *BoS* and *AS* will go back to sleep mode and will remain as sleep or awake, till all clusters' processes are executed at least once. As it completes with execution, *communication* phase will initiate to check memory size and remaining energy in the sensors. If the values are less than threshold value (*e.g.* threshold value for memory size = 700 KB (maximum) and energy left = 5 Joules), then values for all sensors are reset by incrementing the counter. If the value is more than threshold value then, it will begin *clustering* process again. Finally, if counter reaches to last node, then it calculates memory size for all packets, sends the data from *AS* to the surface station and then all sensors are sent back to the sleep mode.

Algorithm 4.2 Clustering and Communication Algorithm

Require: Sensor (S), Cluster (C), Bottom Sensor (BoS), Anchored Sensor (AS), Memory Size (M_s), Data Collector (DC) and Counter (Ctr), number of packets (P_i), Data Size (DS), Buffer (B), Memory of Sensor (Ms) and Acknowledgment (ack = $HIGH/LOW$), Energy (E)

initialize $n \longleftarrow 0, Ctr \longleftarrow 0$

//initiation of clustering process

for (i = 1..n) **do**

$S_i \longleftarrow$ sleep //at start, all sensors are in sleep mode

end for

for ($C_i = 1..n$) **do** // activating bottom and anchored sensors in a cluster simultaneously

for ($S_i <= \vartheta(d_a/r_c)$) **do** //checking sensor in range given by Eq. 4.1

if ($BoS_i == 1$ && $BoS_i == active$) **then**

$AS_i \longleftarrow active$ // anchored sensor got activated

receive data

$AS_i \longleftarrow sleep$ //anchored sensor go in sleep mode

BoS_i++

end if

end for

end for

//communication process begins

if ($E! = 0$ && $B! = 0$) **then**

$S_i \longleftarrow threshold$ //check for energy left and buffer size

if ($threshold == 0$) **then**

$C_i \longleftarrow reset$ //cluster is reset

$process \longleftarrow halt$

else

$C_i \longleftarrow repeat$ //clustering is repeated

end if

end if

for ($AS_i = 1..n$) **do**
  $P_i \longleftarrow AS_i$ // packets are sent by AS
  calculate DS //calculating data packet size
  if ($B <= Ms$) **then**
    $data \longleftarrow store$
    $continue$
    if ($Ctr == 0$ && $AS_i \longleftarrow data$) **then**
      $DC \longleftarrow data$
      Ctr++
      if ($DC \longleftarrow data$ && $Ctr == n$) **then**
        process data1
        $ack \longleftarrow DC$ // DC sends acknowledgment to AS
        if ($ack == HIGH$) **then**
          $S_i \longleftarrow sleep$ // sensors go in sleep mode
          $Ms \longleftarrow reset$ // memory size is resetted
        end if
      end if
    end if
  end if
end for

4.3 *MPST* Testing and Result Analysis

MPST is first simulated and analyzed on *MATLAB* to find the sensing coverage and effects of various constraints on the deployment defined in sections 4.2.1-4.2.4 on sensors. The simulated results are discussed in trailing subsections.

4.3.1 Sensing Coverage

In order to compute the sensing coverage with deployment of minimum number of sensors and to cover maximum area, Eq. 4.1 from Theorem 3.1 is simulated for both of its cases. The

first case describes the ratio of sensor distance and sensing range varying between $(d_a/r_c) = [0,2]$ and second case has ratio, $(d_a/r_c) = (2,\infty)$. Here, the ideal case is considered in which the velocity of river current does not change with depth. The results are shown in Figure 4.8. It is depicted that the first case is providing the full coverage area and is constant throughout

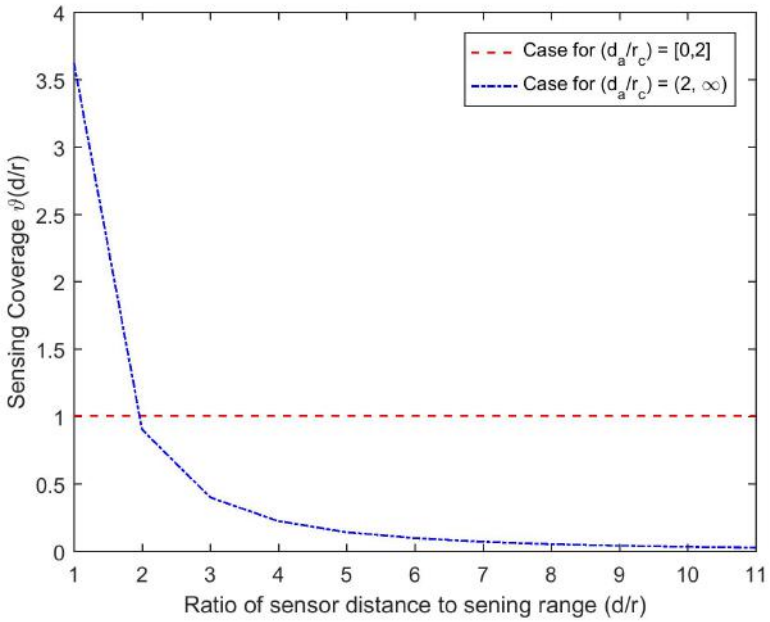

Figure 4.8: *MPST* Deployment: Sensing Coverage

with its sensing ratio of covered and targeted region. This implies that with increase in number of sensors the maximum coverage is optimally reached considering the scenario of first case, *i.e.*, $\vartheta = 1$. For the second case, it is observed that with increase in number of sensors, the coverage ratio is decreasing monotonically due to collisions among sensing regions. Thus, the target sensing region is achieved through first case of $(d_a/r_c) = [0,2]$.

4.3.2 Acoustic Path loss Analysis

To analyze path loss, initially, it is required to generate values for varying frequency and distances with spreading factor, $l = 2$ using Eq. 4.18 for cylindrical spread. The generated values are stored in tabular form (*see* Table 4.1), for path loss at different frequencies as *10 Hz, 100 Hz, 1 KHz, 10 KHz, 20 KHz, 25 KHz* and *50 KHz* with respect to changing distances in meters as 100, 500, 1000, 2000, 5000, 7500 and 10,000. From the table,

the path loss is ranging from -34.6 to -34.5dB, -10.4 to -10.3 dB, 0.005 to 0.7 dB, 10.50 to 22.30 dB, 24.50 to 65.5 dB, 30.5 to 91.5 dB and 36.20 to 209.20 dB for frequencies, $f = (10Hz, 100Hz, 1KHz, 10KHz, 20KHz, 25KHz)$, respectively. Thus, it is observed that

Table 4.1: Path Loss Trends in Underwater at l=2

Distance	**Path Loss (dB)**						
	f = 10 Hz	**f = 100 Hz**	**f = 1 KHz**	**f = 10 KHz**	**f = 20 KHz**	**f = 25 KHz**	**f = 50 KHz**
100 m	-34.5385	-10.3968	0.0069	10.5159	24.5550	30.8340	36.2855
500 m	-34.5373	-10.3951	0.0345	10.9907	26.2085	33.2759	43.2723
1 Km	-34.5358	-10.3930	0.0690	11.5842	28.2754	36.3284	52.0059
2 Km	-34.5328	-10.3888	0.1380	12.7713	32.4092	42.4332	69.4730
5 Km	-34.5237	-10.3762	0.3450	16.3324	44.8108	60.7476	121.8744
7.5 Km	-34.5162	-10.3657	0.5175	19.2999	55.1453	76.0096	165.5422
10 Km	-34.5087	-10.3552	0.6900	22.2675	65.4799	91.2716	209.2100

path loss is less, *i.e.*, approximately 66 dB (for low frequencies) and is varying with distance between 1 to 10 kms whereas it is more than 200 dB for higher frequencies of more than *20 KHz*. It is evident from Figure 4.9 that path loss is more at higher frequencies with more depth. Thus, it depicts that path loss is dependent on frequency and distance and is increasing with rise in frequency ranges at larger distances. There is a loss of almost 200 dB with frequency and distance of *50 KHz* and 10 km, respectively. This loss is comparatively higher with respect to other frequencies and distances. This scenario of path loss highlights the hostility environment of underwater and thus, signifies the importance of using low frequencies.

4.3.3 Energy Consumption Analysis

In order to analyze the energy consumption of *MPST*, the concept for single-hop need be understand which highlights the sensor's dependency for sending data. Single hop means there is only one hop between destination and host. For the analysis, various nodes with network count as 13, 24, 34, 44, 54, 64 and 73 having inter-node distance d_a = 35, 80, 145,

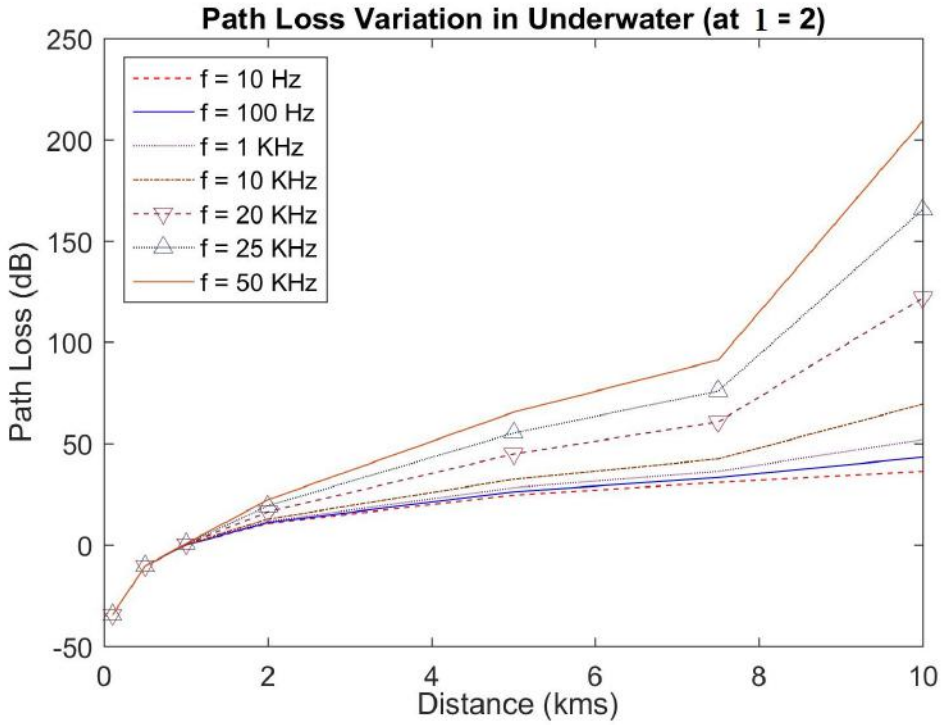

Figure 4.9: Acoustical Path Loss Variations

190, 225, 280, 350 (meters) are considered. The frequency is set at *25 KHz*, Chloride is 35 mg/l, *pH* is 7.8 and temperature is 27 °C. The network transmits 1000 packets and scenario is at depth 75 m. These values are used to evaluate values of inter-node distances and energy consumption for single-hoping using Eqs. 4.25, 4.31 and are shown in Figure 4.10. It is depicted that energy consumption increases gradually with increase in number of sensors in the network. The scenario provides better and accurate result of energy consumption with varying inter-node distances. This indicates that T_l grows exponentially with inter-node distance among sensors leading to higher energy costs for more sensors. This suggests the use of single-hop communication in *MPST* with deployment of minimal number of sensors, in order to conserve energy and to sustain it for longer period.

4.3.4 Ambient Noise Analysis

For analyzing the *Nl* for *MPST*, initially, it is required to compute values for varying frequencies and noise components using Eqs. 4.33, 4.34, 4.35, and 4.36. The generated values are stored in tabular form (*see* Table 4.2) for *Nl* at different frequencies *10 Hz, 50 Hz, 100*

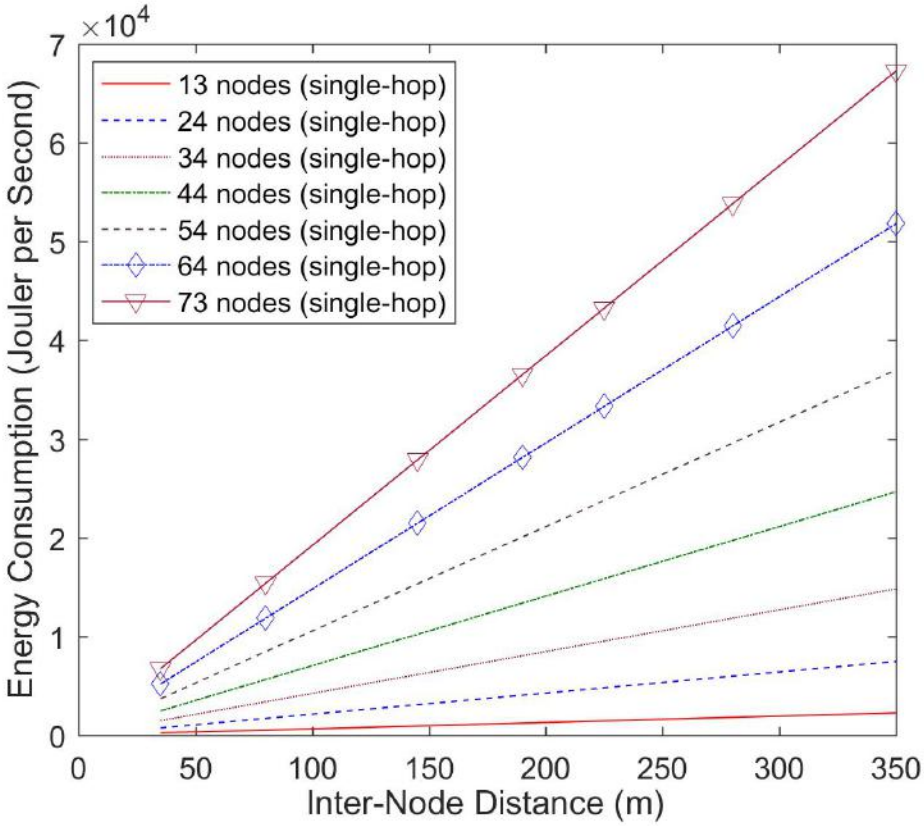

Figure 4.10: Energy Consumption in Single-Hop

Hz, 500 Hz, 1 KHz, 10 KHz, 20 KHz, 25 KHz, 30 KHz and *50 KHz* with respect to changing noise. From Table 4.2, it is observed that with change in frequencies, the minimum value for Nt is -100.3607 dB at $f = 50KHz$ and maximum is 155.1551 dB at $f = 10Hz$. Ns is ranging between -2846.5 to -0.0865 in dB. The minimum value for Nw is -25.3329 at $f = 10Hz$ and maximum value is 181.2735 at $f = 50KHz$. Nth is varying from -107.1034 dB to 63.2405 dB for frequency ranging from *10 Hz* to *50 KHz*. It is observed that the Nt affects only low frequencies regions (upto *10 KHz*), Ns dominates in frequency range of $10 - 100Hz$. Nw is affected in frequency ranging from $100Hz - 100KHz$ and Nth works and affected if range is high, *i.e.*, more than $100KHz$.

Table 4.2: Noise Trends

Components	Ambient Noise (dB)									
	f = 10 Hz	**f = 50 Hz**	**f = 100 Hz**	**f = 500 Hz**	**f = 1 KHz**	**f = 10 KHz**	**f = 20 KHz**	**f = 25 KHz**	**f = 30 KHz**	**f = 50 KHz**
Turbulence Noise	155.1551	106.8720	86.0776	37.7944	17.0000	-52.0776	-72.8720	-79.5663	-85.0359	-100.360
Shipping Noise	-0.0865	-0.0451	-28.1	-8.2	-18.2	-496.3	-1076.3	-1368.5	-1661.8	-2846.5
Wave Noise	-25.3329	13.8024	32.9957	69.6781	87.5000	137.1309	154.2852	161.8117	168.3355	181.2735
Thermal Noise	-107.1034	-74.9146	-61.0517	-28.8629	-15.0000	31.0517	44.9146	49.3775	53.0239	63.2405

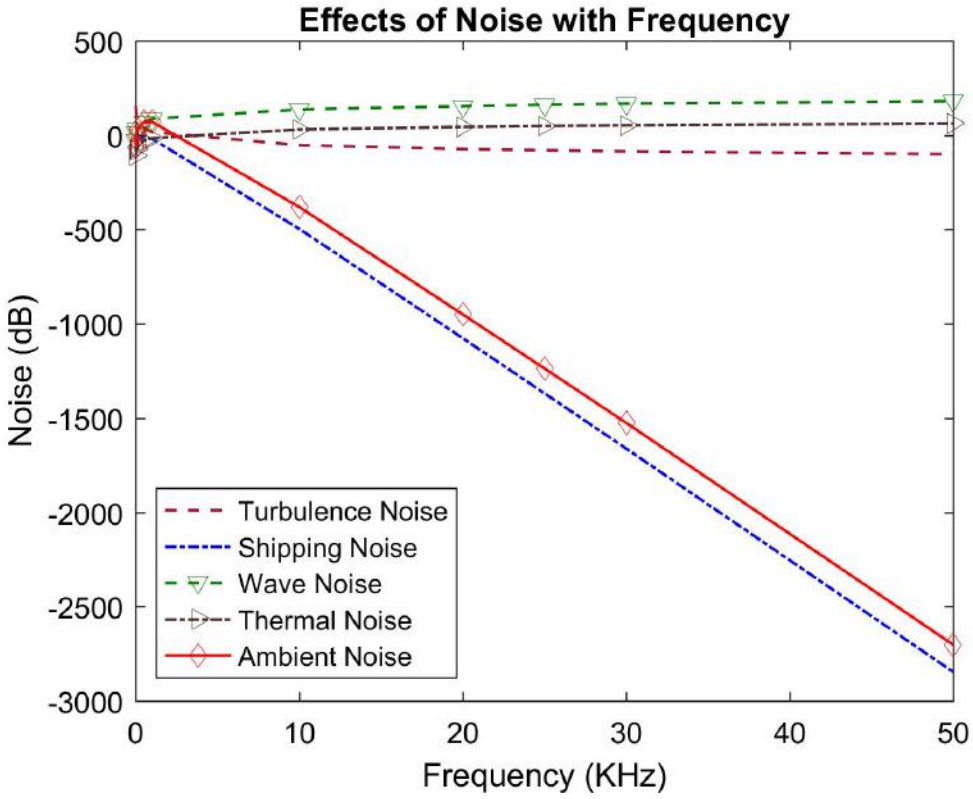

Figure 4.11: Noise Variations

Figure 4.11 illustrates the effects of noise with variations in frequencies and it is found that Nt, Nw and Nth have adverse effects on ambient with increase in frequencies. Nl got negative at higher frequencies and highly affected with lesser values of Ns (using Eq. 4.32). This suggests that noise is suitable at lower frequencies and there is data loss but at higher frequencies the noise effects are lowered with other factors present in underwater channel.

4.3.5 Localization Error Measurements

The values of average mean error for estimating position of sensors on its deployment, are calculated using Eq. 4.46. Various simulations are derived using $AS = 4$ and $BoS = 13, 24, 34, 44, 54, 64, 73$, in a region of 500×500 and are shown in Figure 4.12.

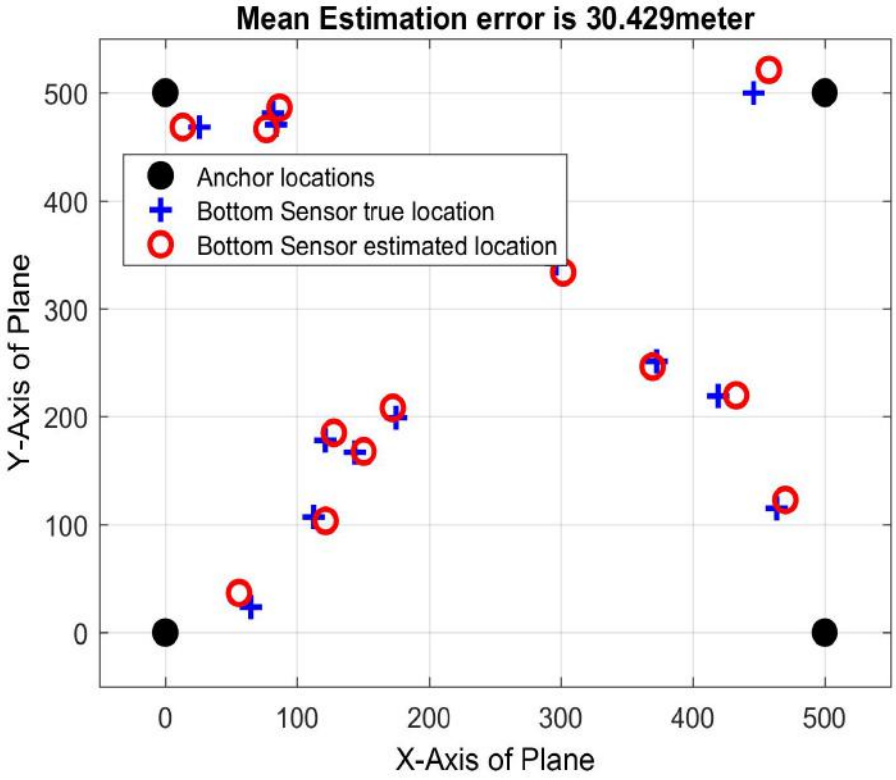
Mean Estimation error is 30.429meter
Anchor locations
Bottom Sensor true location
Bottom Sensor estimated location
Y-Axis of Plane
X-Axis of Plane
0
100
200
300
400
500

(a)

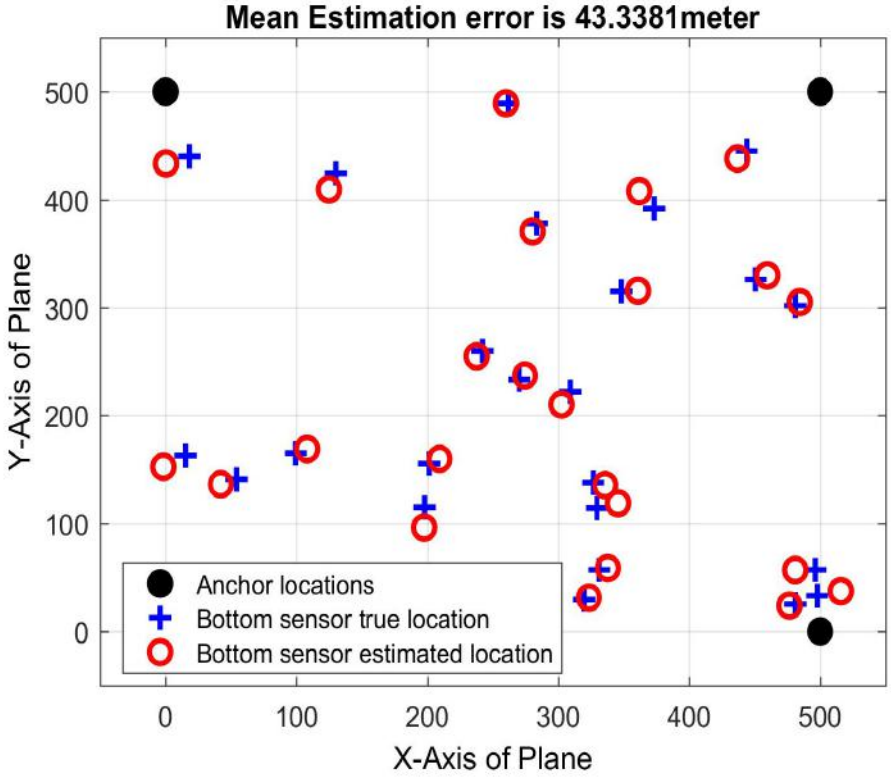
Mean Estimation error is 43.3381meter
Anchor locations
Bottom sensor true location
Bottom sensor estimated location
Y-Axis of Plane
X-Axis of Plane
0
100
200
300
400
500

(b)

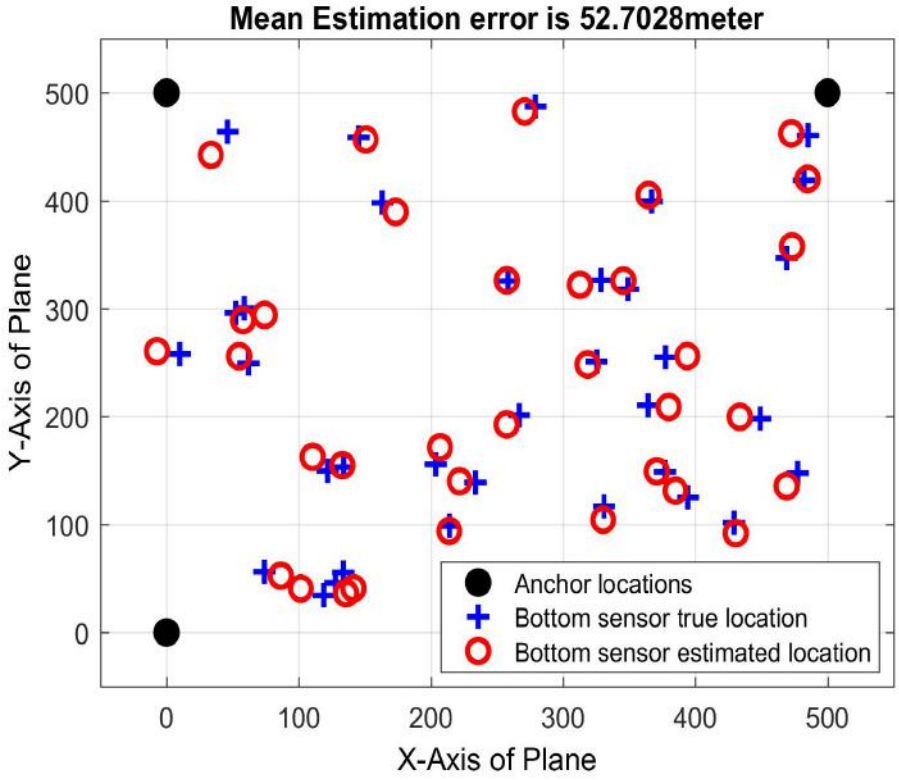
Mean Estimation error is 52.7028meter
Y-Axis of Plane
X-Axis of Plane
0
100
200
300
400
500
Anchor locations
Bottom sensor true location
Bottom sensor estimated location

(c)

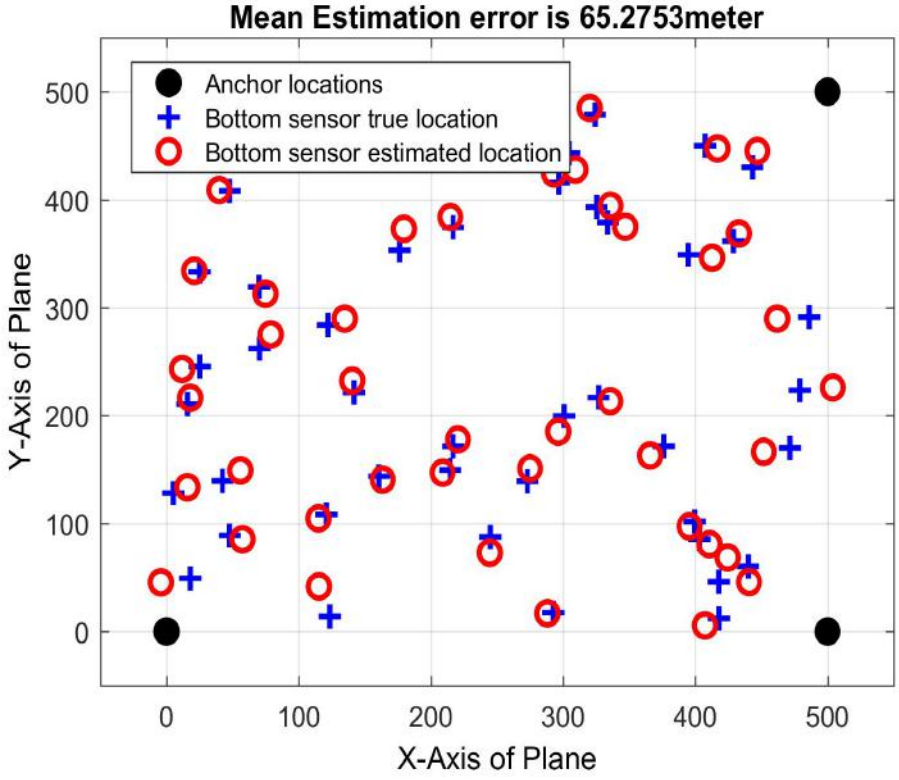
Mean Estimation error is 65.2753meter
Y-Axis of Plane
X-Axis of Plane
0
100
200
300
400
500
Anchor locations
Bottom sensor true location
Bottom sensor estimated location

(d)

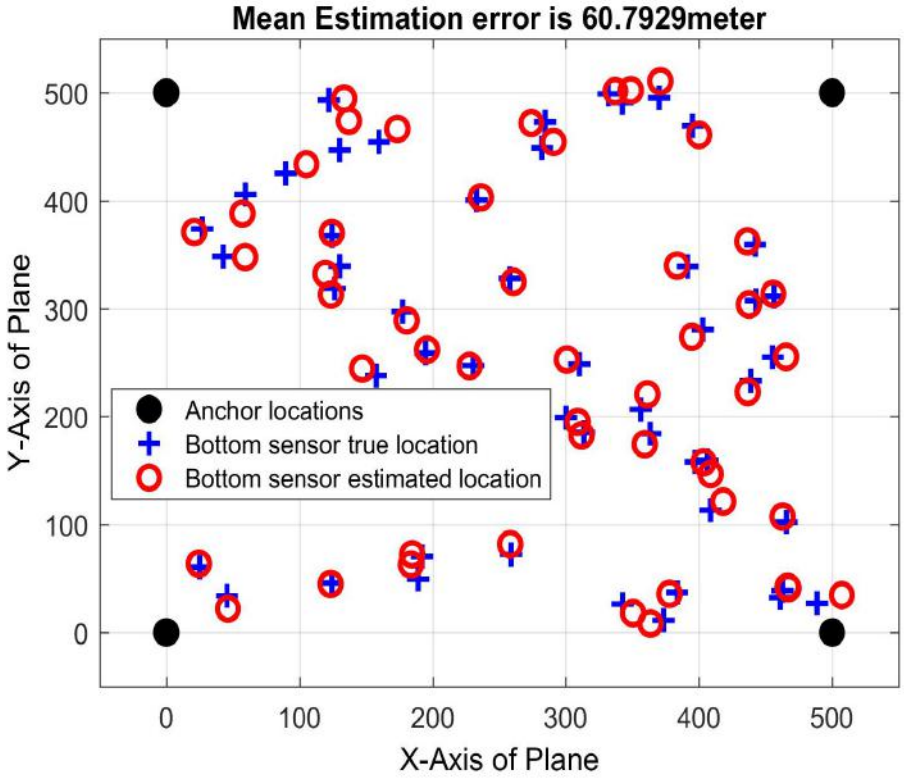
Mean Estimation error is 60.7929meter
Anchor locations
Bottom sensor true location
Bottom sensor estimated location
Y-Axis of Plane
X-Axis of Plane
0
100
200
300
400
500

(e)

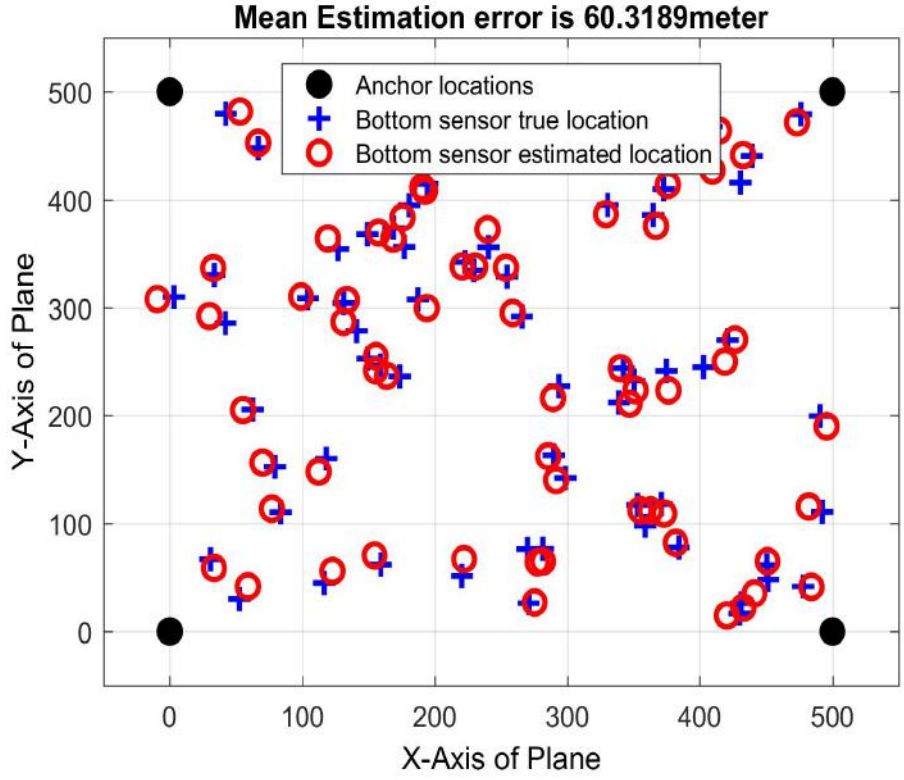
Mean Estimation error is 60.3189meter
Anchor locations
Bottom sensor true location
Bottom sensor estimated location
Y-Axis of Plane
X-Axis of Plane
0
100
200
300
400
500

(f)

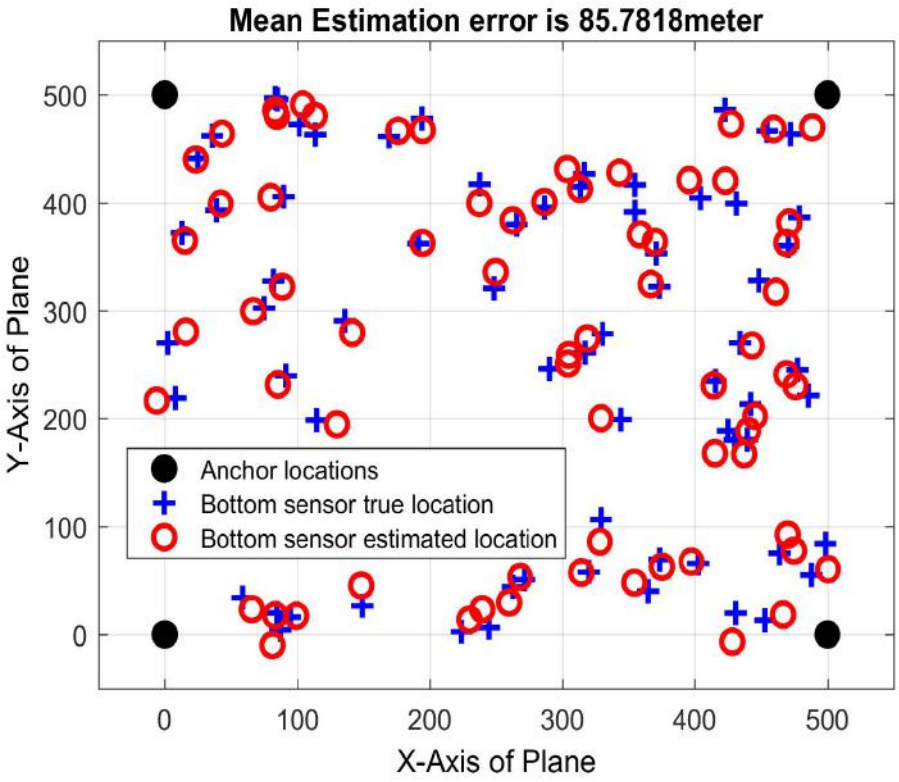

(g)

Figure 4.12: Simulations of Mean Estimation Error (a)13 sensors (b) 24 sensors (c) 34 sensors (d) 44 sensors (e) 54 sensors (f) 64 sensors (g) 73 sensors

From the simulation results, it is observed that sensor network with sizes = 13, 24, 34, 44, 54, 65, 73 nodes, the mean estimation error calculated are 30.429, 43.3381, 52.7028, 65.2753, 60.7929, 60.3189, and 85.7818 (in meters), respectively. Their average is shown in Figure 4.13, which tells the increase in errors of localization. It is concluded that with the increase in number of sensors, there is an increase in the value of error succinctly. Also, it leads to falsification of sensors' location.

4.3.6 Discussion on Topology Deployment

For *MPST* deployment in river, it requires decision making for its design and implementation with respect to its initial installation requirements, which depends on various trade-offs. The outcomes of decisions might not be satisfactory. Therefore, it is essential to define system's deployment and maintenance strategy for decision making to minimize the cost

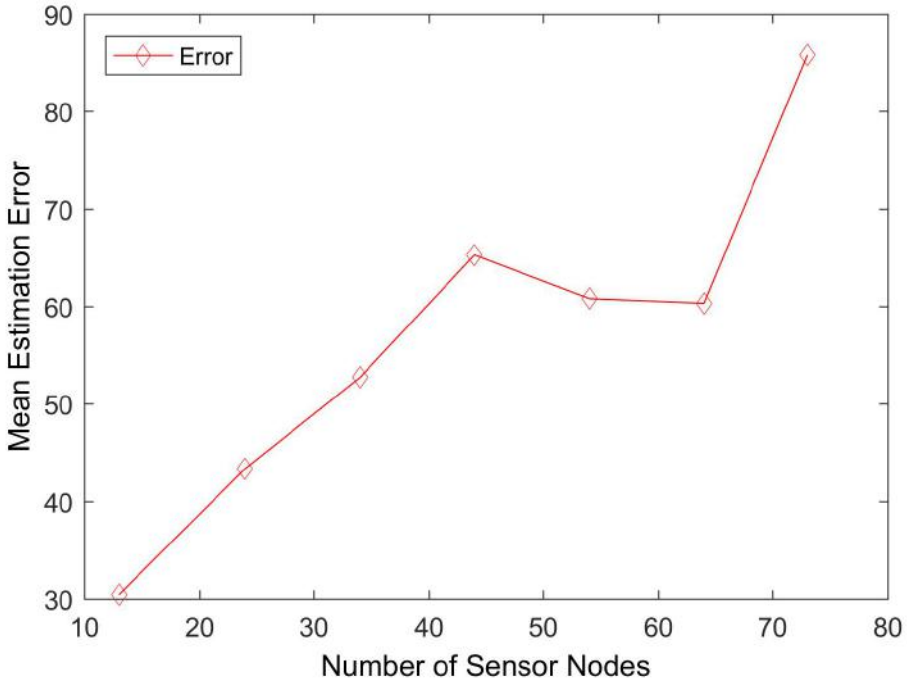

Figure 4.13: Mean Estimation Error

and preserving proper function of topology. The analysis is discussed below.

i. **Low cost:** The design specifications for *MPS* costs approximately 20,000 INR to sense physical and chemical parameters. The estimated cost is found viable for budgetary constrained projects.

ii. **Ease in deployment:** It has simpler infrastructure that weighs 1 kg approximately, hence, is easier to be deployed.

iii. **Insulation:** The design of *MPS* guarantees insulation and corrosion proofing.

iv. **Ease of access:** The infrastructure is fully assembled which includes replacing batteries, blue-tooth, calibration of sensors and replacing few wires or casing leakages. It provides maintenance at a very low cost (5,000 INR) approximately.

v. **Ease in adding up new sensors:** It provides ease in adding new sensors to the deployment without much efforts.

vi. **Good stability:** It is quite stable and sustainable for shallow river water.

4.3.7 Study Area

Ludhiana city, being major industrial city, situated on the bank of river Sutlej. The river is a major source of potable and irrigation water for villages located in southern districts of Punjab. The direct or indirect discharged effluents like domestic sewage produced from various industrial units set up results in to deterioration of the water quality. Therefore, it needs to be monitored regularly and take preventive measures. *MPST* is tested in Sutlej river at Bassi near Nurpur Bedi, Ludhiana, India (*see* Figure 4.14).

Figure 4.14: Study Area

4.3.8 Measurements

For the real-time measurements, the data is collected from destined location (*see* Section 4.3.7) using *MPST* and is tested regularly for half an hour duration at different day-timings for three months. The communication range among sensors lies between 20 square meters. The various parameters of sensors for deployment are shown in Table 4.3. The *LABVIEW* software is used for collecting data and is checked thoroughly giving out good results in short span of time (*see* Figure 4.15). The data value includes Electrical Conductivity *(EC)*, *pH*, Temperature, Chloride, and Dissolved Oxygen *(DO)*. *MPST* is initially tested for 15 days and is withdrawn to replace batteries due to battery drain. After replacing the batteries, it is deployed again. The collected underwater parameters are shown in Table 4.4, measured

Table 4.3: Sensor' Parameter

Parameters	**Values**
Frequency Range	25 KHz
Number of Sensor Nodes	13
Maximum Transmission Distance (single-hop)	d_a = 35 m
Minimum Cluster Head candidate range	70 %
Maximum Cluster Head candidate range	90 %
Packet with error ratio (1/1000)	10
Batteries (Panasonic Eneloop Pro Ni-MH)	1880 and 2550 mAh

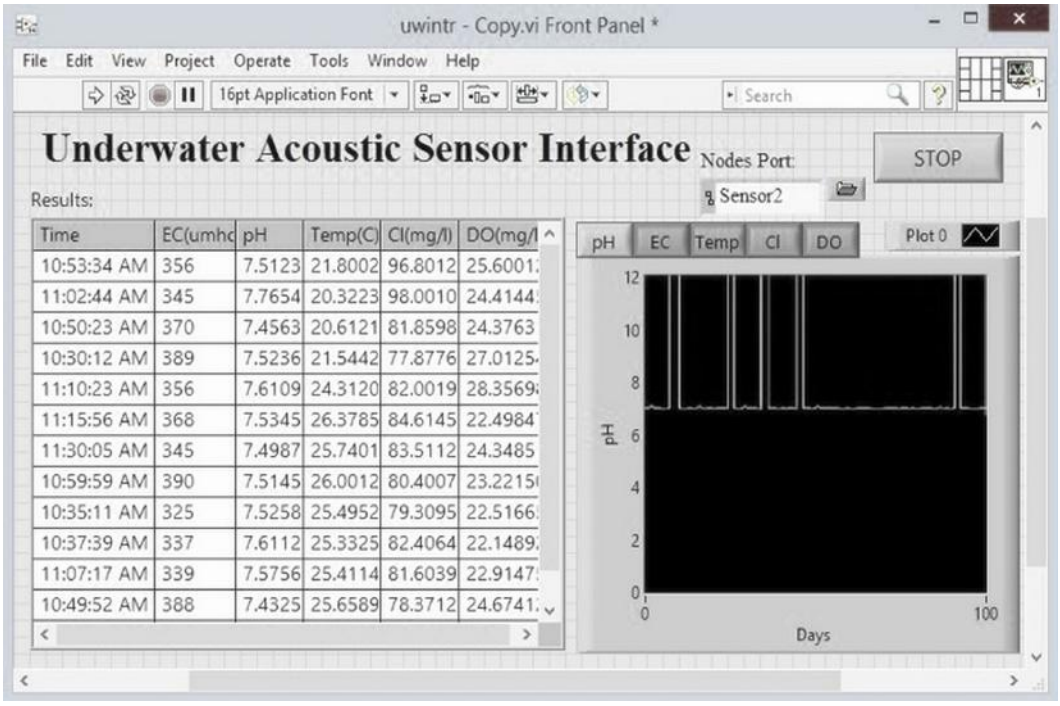

Figure 4.15: Data Collection *LABVIEW*

values are shown in Tables 4.5 - 4.9, and the results are shown in Figures 4.16 - 4.20.

Table 4.4: Water Quality Parameters

Parameter	**Nominal Range**	**Computational Formula**	**Effects/ Reasons**
Electrical Conductivity (mg/l)	400-550	$EC(mg/l) = \frac{TDS\ (ppm)}{0.64}$	The increased level of *EC* would be critical for aquatic animals because they have specific tolerance ranges. It depends on the climatic conditions and pollutants which increases during or after rainfall as the Total Dissolved Solids *(TDS)* of water increase under such weather conditions. It is calculated by the estimation of *TDS* in water which is measured in ppm or in mg/l. As the *EC* is used to measure capacity of water for conducting electrical currents, it is related to dissolved salts in water.
pH	6.5-7.2	$pH = -\log[H_3O^+]$	The *pH* factor calculates the acidity or alkalinity of water. If it decreases, acidity in the water increases. It affects various chemical and biological processes in the water.
Temperature (°C)	26-28	$\Delta T = \frac{Q}{mc}$	The temperature has a vital effect on the activities and growth of organic beings within the water. The rise in temperature increases the chemical reaction and hence affects organic beings. The amount of heat released or absorbed gives rise to changes in the temperature.
Chloride (mg/l)	80-90	$NaCl + H_2O \longrightarrow Na^+ + Cl^- + H_2O$	The chloride tells about the alkaline nature of water. The high chloride concentration in fresh water is toxic to aquatic organisms and is a threat to survival, growth and reproduction of the species.
Dissolved Oxygen (mg/l)	7-9	*DO* = Amount of Titrant Used (mL)	*DO* is necessary for many forms of life residing underwater, which includes flora and fauna of water. The aquatic animals require *DO* for respiration and phytoplankton needs *DO* for respiration; when there is no light for photosynthesis processes. The *DO* concentration is calculated using the amount of Titrant added.

Table 4.5: Observations for Electrical Conductivity (mg/l) (April, May, June 2016)

Days	April	May	June	Days	April	May	June	Days	April	May	June
1	456	460	495	12	488	417	581	23	398	523	589
2	471	476	508	13	495	425	575	24	380	528	523
3	490	488	513	14	474	437	569	25	364	531	525
4	440	470	524	15	422	453	564	26	350	525	541
5	418	455	537	16	467	459	558	27	376	514	553
6	400	430	542	17	487	471	553	28	403	510	567
7	445	412	549	18	495	490	520	29	427	506	579
8	480	410	555	19	460	505	510	30	445	500	534
9	425	408	563	20	430	512	533	31	-	491	-
10	437	415	572	21	410	520	545				
11	455	416	577	22	402	521	564				

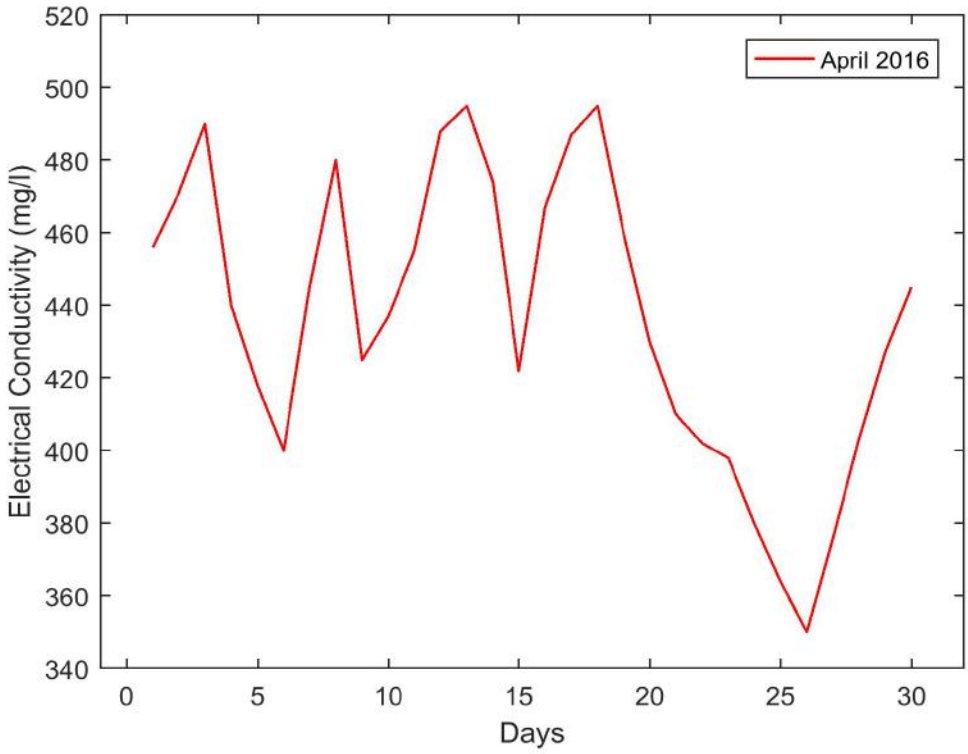

(a)

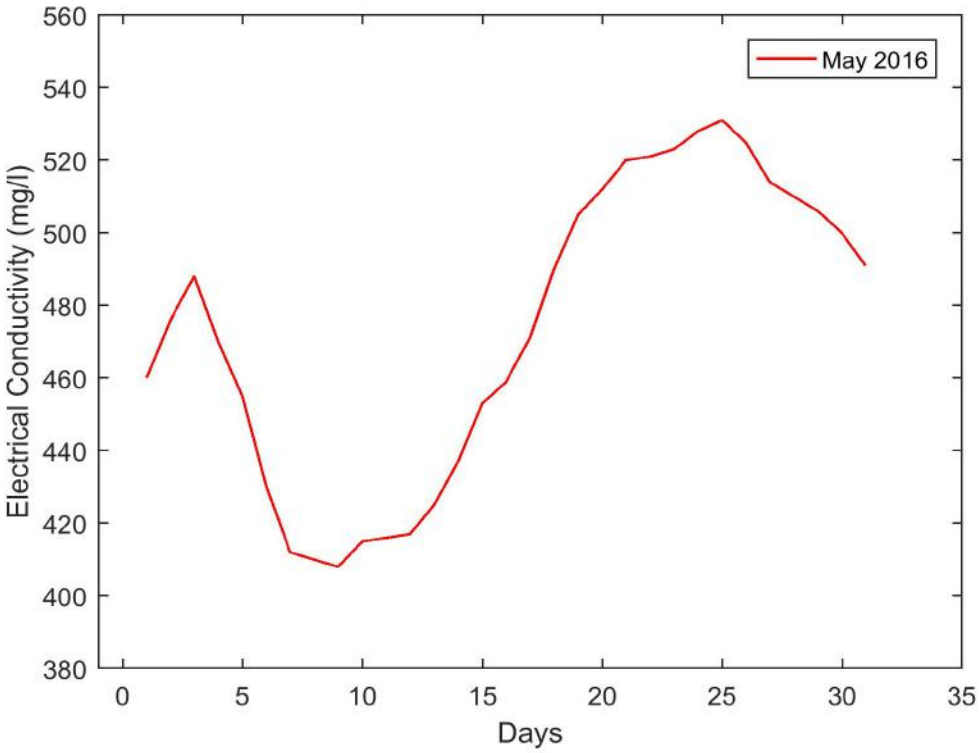

(b)

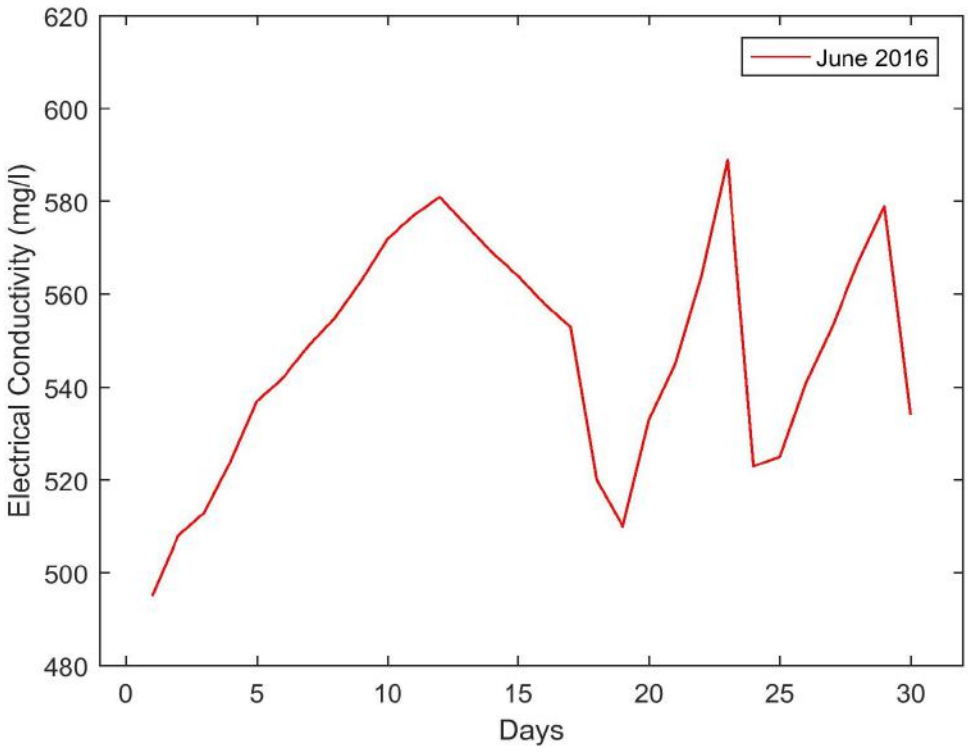

(c)

Figure 4.16: Observation Graphs of Electrical Conductivity (a) April 2016 (b) May 2016 (c) June 2016

Table 4.6: *pH* Data (April, May, June 2016)

Days	April	May	June	Days	April	May	June	Days	April	May	June
1	7.5	7.5	7.4	12	7.5	7.5	7.3	23	7.6	7.7	7.4
2	7.7	7.5	7.2	13	7.4	7.4	7.5	24	7.8	7.5	7.3
3	7.4	7.3	7.6	14	7.3	7.3	7.6	25	7.7	7.6	7.4
4	7.5	7.4	7.7	15	7.6	7.5	7.5	26	7.4	7.5	7.3
5	7.6	7.5	7.6	16	7.8	7.6	7.4	27	7.5	7.5	7.4
6	7.4	7.4	7.6	17	7.7	7.4	7.5	28	7.4	7.4	7.5
7	7.5	7.5	7.7	18	7.6	7.5	7.3	29	7.4	7.6	7.4
8	7.4	7.6	7.4	19	7.5	7.5	7.4	30	7.3	7.5	7.5
9	7.5	7.7	7.5	20	7.4	7.6	7.6	31	-	7.3	-
10	7.5	7.6	7.4	21	7.4	7.4	7.6				
11	7.6	7.6	7.5	22	7.5	7.6	7.5				

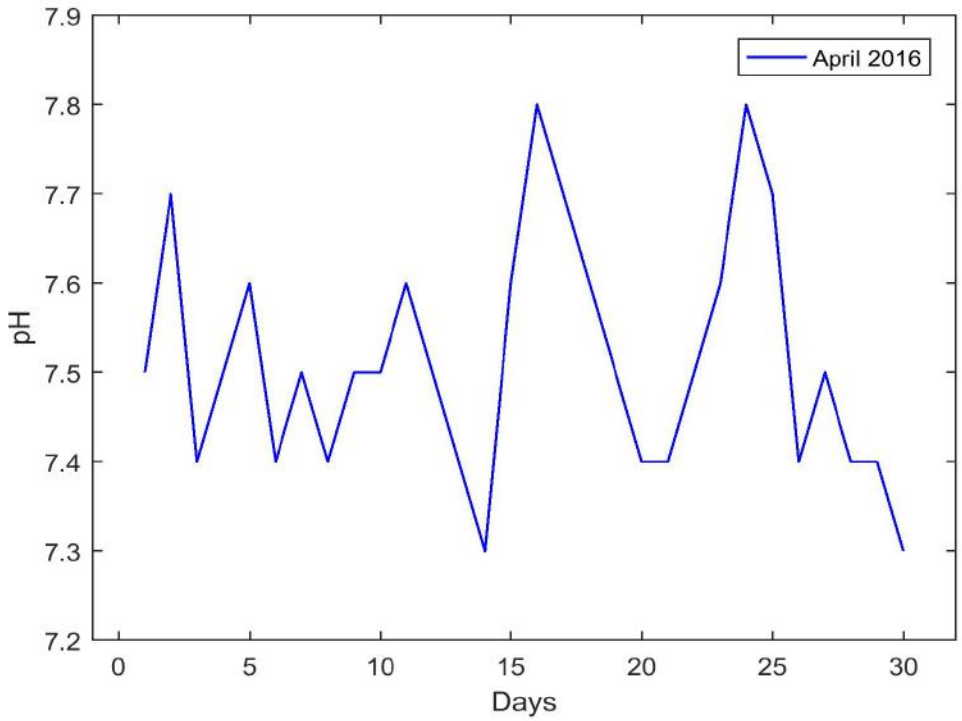

(a)

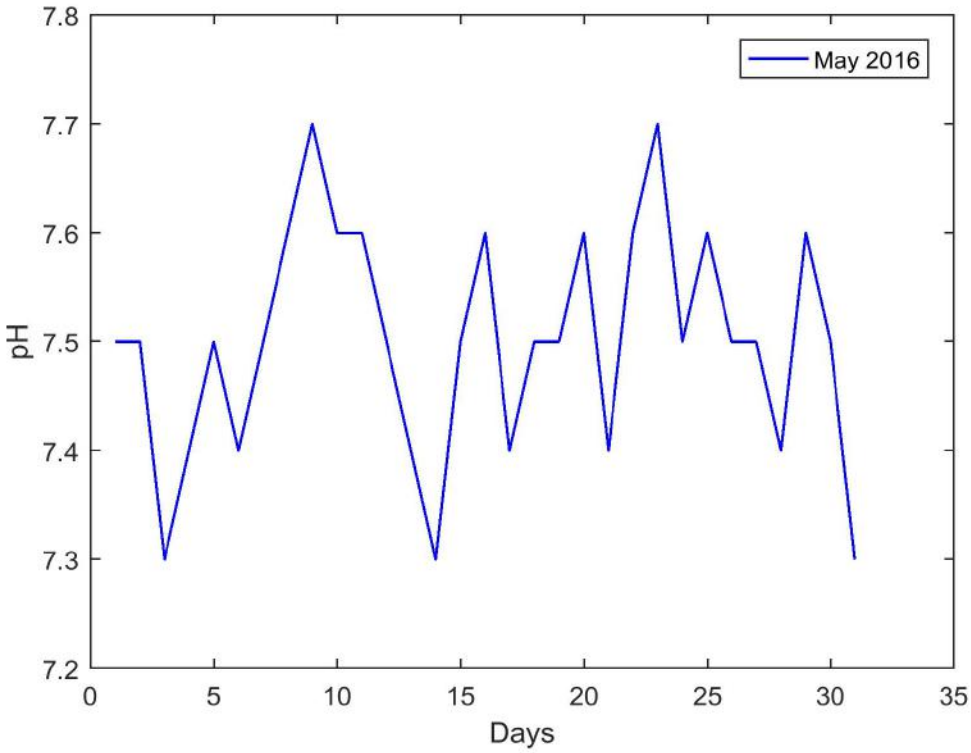

(b)

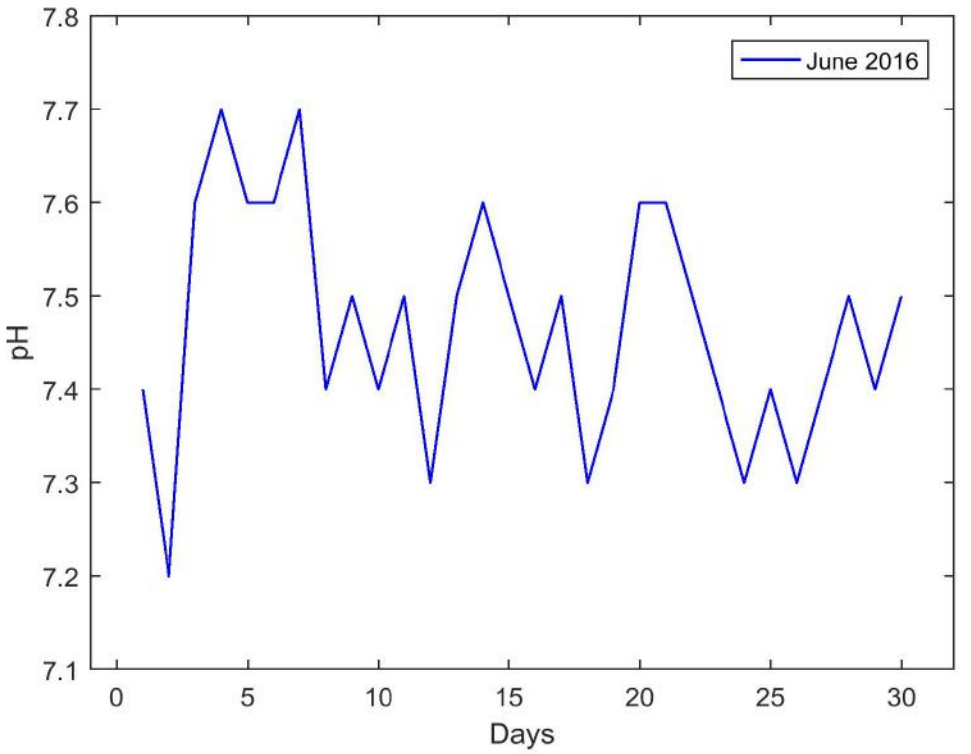

(c)

Figure 4.17: Observations for *pH* (a) April 2016 (b) May 2016 (c) June 2016

Table 4.7: Measurements for Temperature (°C) (April, May, June 2016)

Days	April	May	June	Days	April	May	June	Days	April	May	June
1	21.8	26.4	27.7	12	25.6	26.7	28.7	23	25.9	26.5	28.8
2	22.3	26.5	27.6	13	25.5	26.6	28.5	24	26.2	26.6	28.5
3	22.9	26.6	27.5	14	26.4	26.6	28.6	25	26.3	26.9	28.6
4	23.5	26.6	27.6	15	26.3	26.5	28.5	26	26.1	27.2	28.4
5	24.3	26.5	27.8	16	26.4	26.7	28.8	27	26.2	27.4	28.5
6	26.3	26.4	27.5	17	25.2	26.5	28.8	28	26.3	27.2	28.4
7	25.7	26.5	27.8	18	25.4	26.8	28.9	29	26.4	27.3	28.6
8	26.0	26.6	27.9	19	25.6	26.7	28.7	30	26.4	27.5	28.7
9	25.4	26.4	28.3	20	25.6	26.8	28.6	31	-	27.6	-
10	25.3	26.7	28.6	21	25.7	26.9	28.4				
11	25.4	26.4	28.5	22	25.9	26.7	28.6				

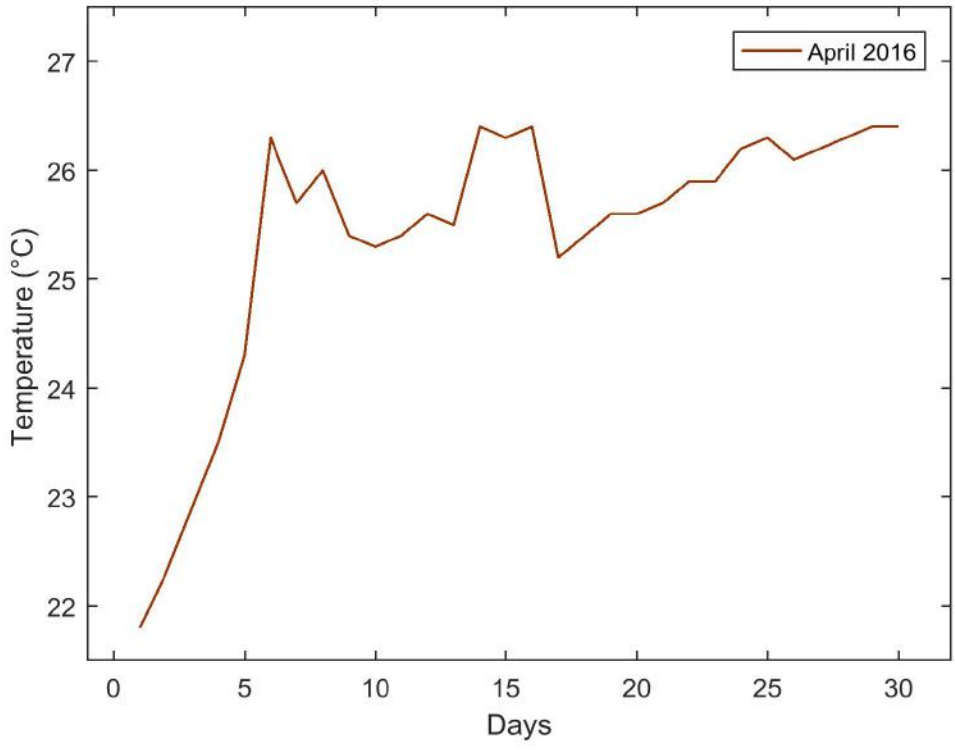

(a)

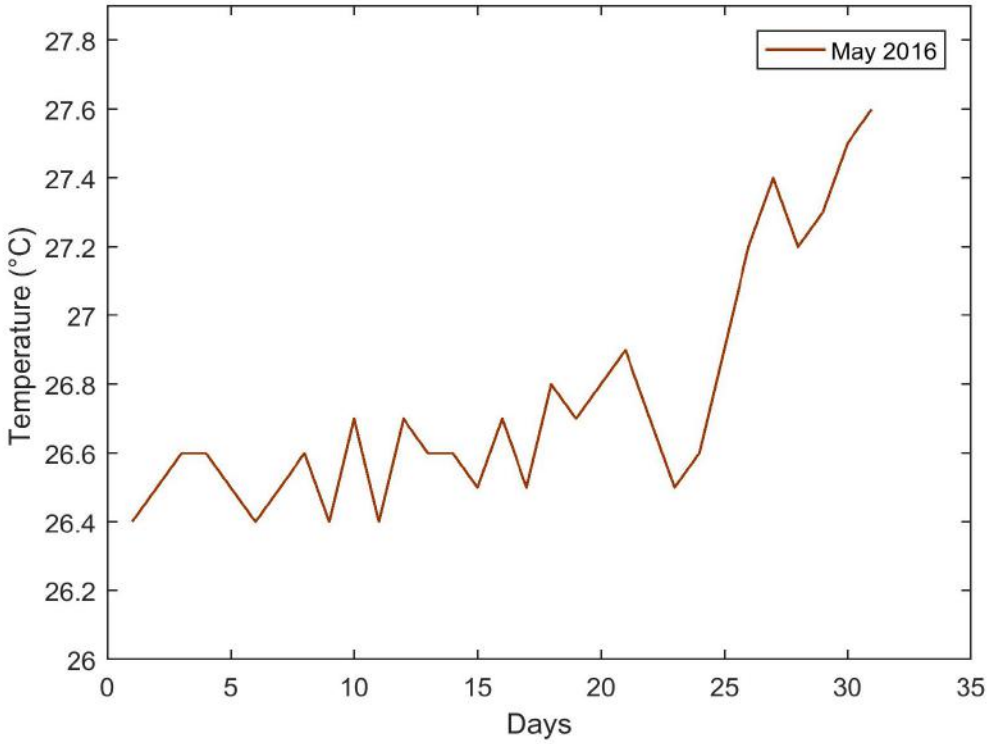

(b)

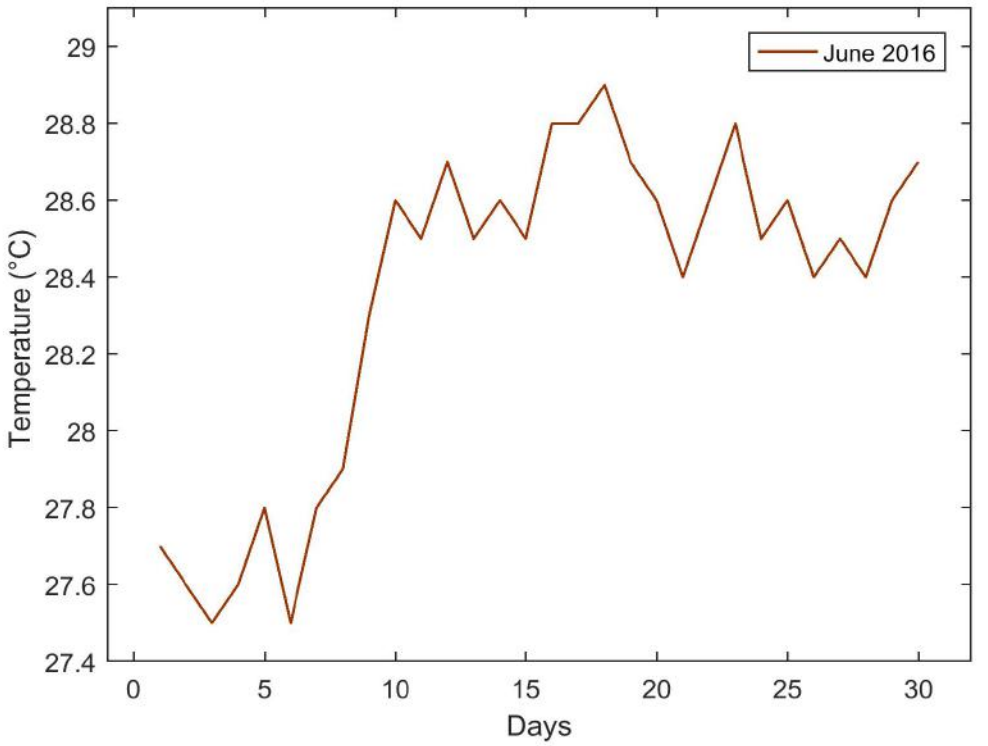

(c)

Figure 4.18: Temperature Observations (a) April 2016 (b) May 2016 (c) June 2016

Table 4.8: Chloride Data (mg/l) (April, May, June 2016)

Days	April	May	June	Days	April	May	June	Days	April	May	June
1	96.8	86.8	88.4	12	78.3	82.8	82.5	23	79.3	93.6	87.8
2	98.0	81.8	86.8	13	76.9	83.5	82.2	24	79.7	94.8	86.4
3	81.8	78.8	86.4	14	75.3	84.7	80.5	25	80.4	95.9	85.7
4	77.8	76.9	85.9	15	74.9	85.7	81.4	26	81.6	96.1	85.1
5	82.0	77.5	85.3	16	74.2	86.9	83.8	27	82.5	94.4	84.3
6	84.6	74.4	84.3	17	76.4	87.9	84.2	28	84.8	93.7	83.8
7	83.5	73.9	84.2	18	73.9	88.6	85.3	29	85.6	92.5	83.5
8	80.4	75.7	83.6	19	72.8	88.9	85.7	30	86.8	91.7	82.7
9	79.3	76.8	83.1	20	71.7	90.2	85.6	31	-	90.3	-
10	82.4	79.3	82.8	21	73.8	91.7	86.8				
11	81.6	80.4	82.9	22	77.9	92.1	87.3				

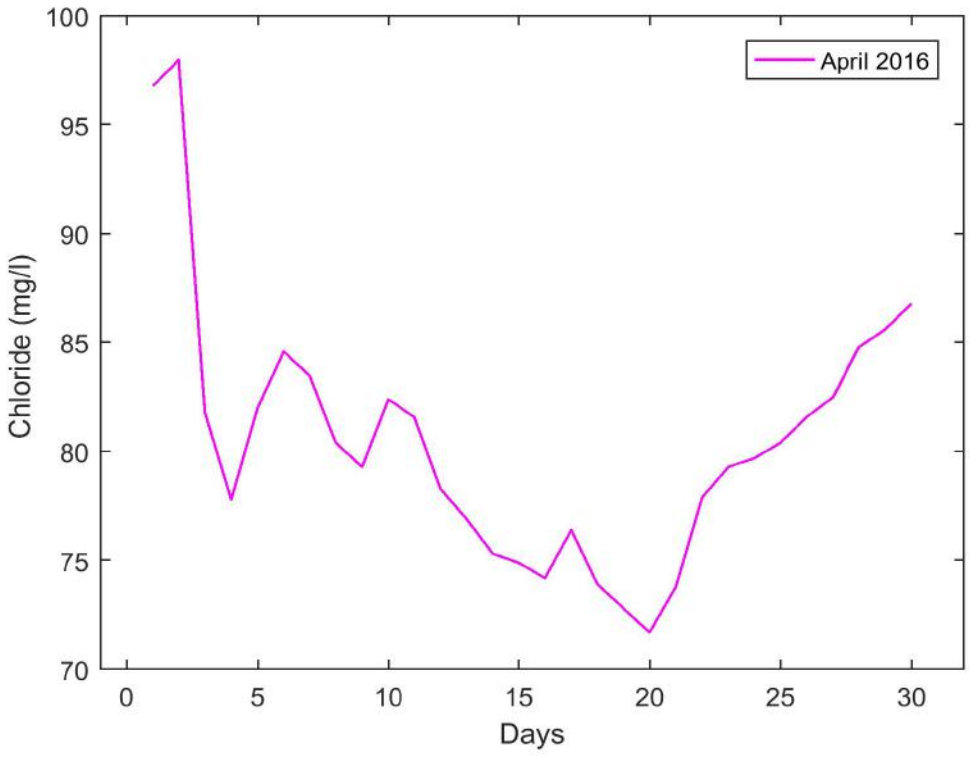

(a)

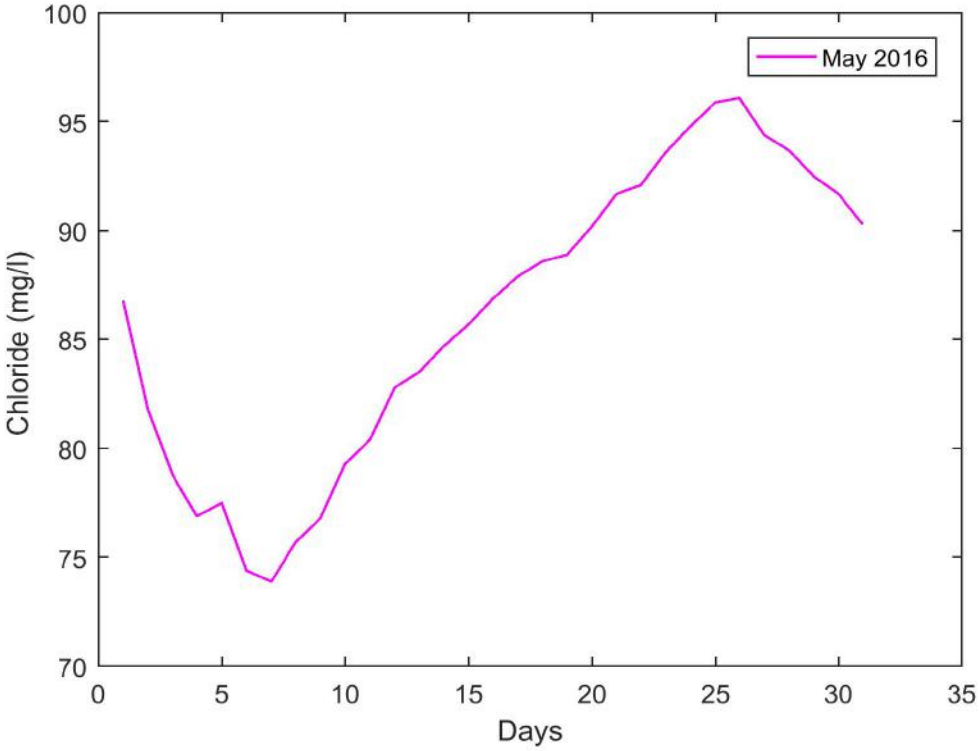

(b)

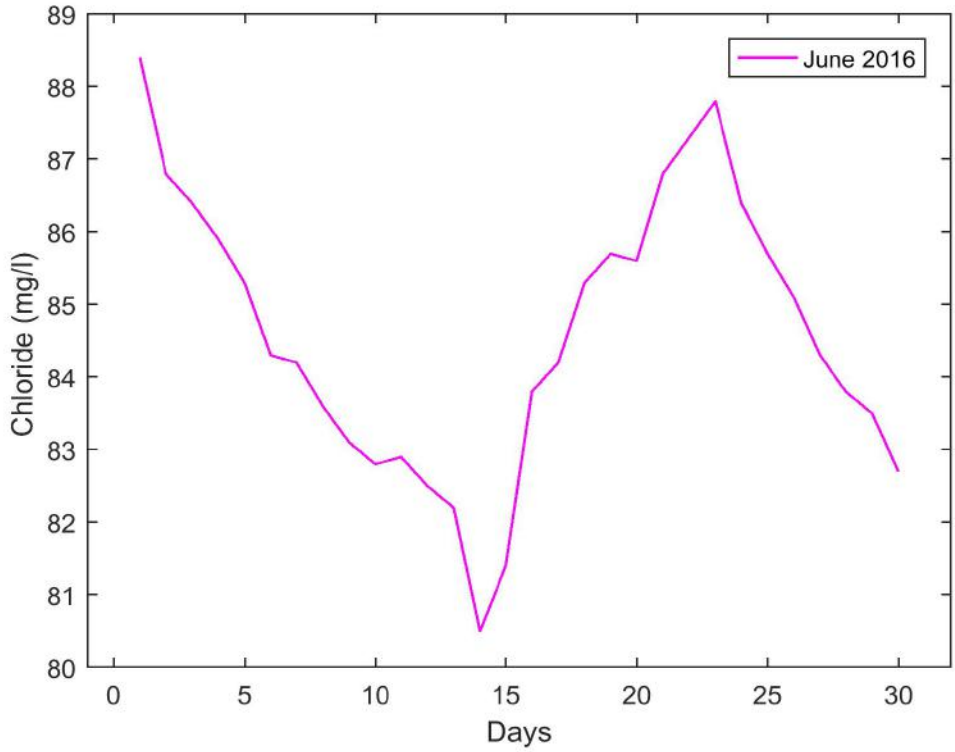

(c)

Figure 4.19: Observation Graphs of Chloride (a) April 2016 (b) May 2016 (c) June 2016

Table 4.9: Observations for Dissolved Oxygen (mg/l) (April, May, June 2016)

Days	April	May	June	Days	April	May	June	Days	April	May	June
1	8.6	8.0	7.5	12	8.1	7.7	7.3	23	8.0	7.9	7.3
2	9.4	7.9	7.5	13	8.1	7.8	7.2	24	7.7	7.8	7.4
3	9.3	7.8	7.4	14	8.0	7.6	7.2	25	7.9	7.8	7.3
4	9.0	7.8	7.5	15	8.1	7.8	7.4	26	7.8	7.6	7.2
5	8.3	7.9	7.2	16	8.0	7.6	7.2	27	7.7	7.5	7.3
6	8.0	7.9	7.6	17	7.9	7.6	7.3	28	7.7	7.5	7.2
7	8.1	7.9	7.5	18	7.8	7.7	7.3	29	7.8	7.6	7.2
8	8.0	7.8	7.3	19	8.2	7.6	7.2	30	7.6	7.5	7.3
9	8.1	7.7	7.3	20	8.2	7.7	7.1	31	-	7.4	-
10	8.2	7.8	7.2	21	8.0	7.4	7.2				
11	8.1	7.6	7.3	22	7.8	7.5	7.4				

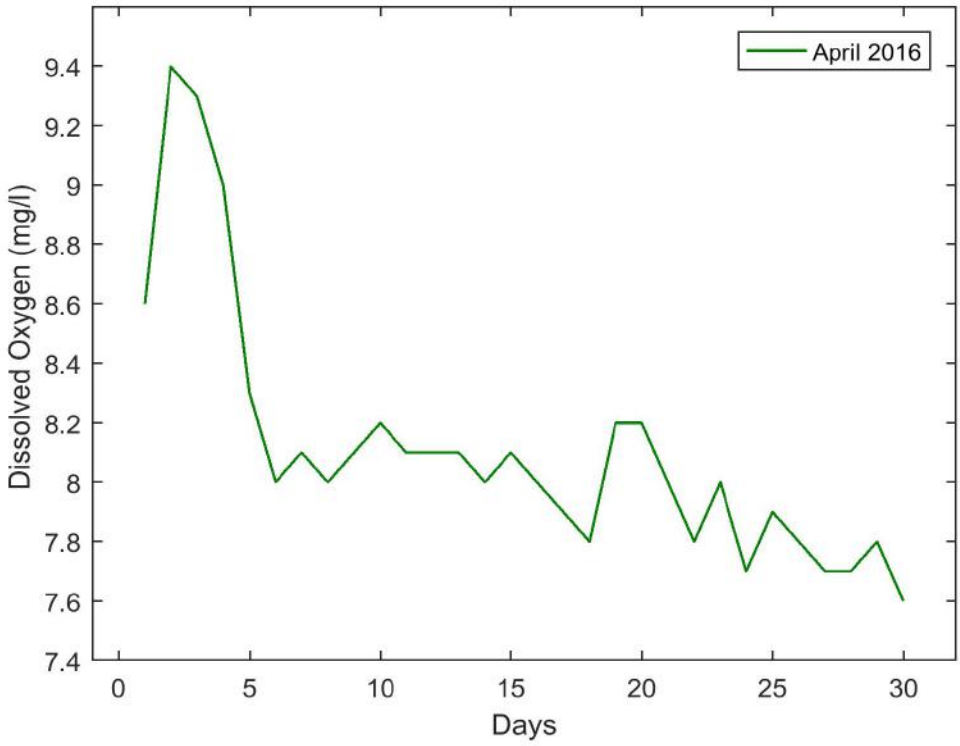

(a)

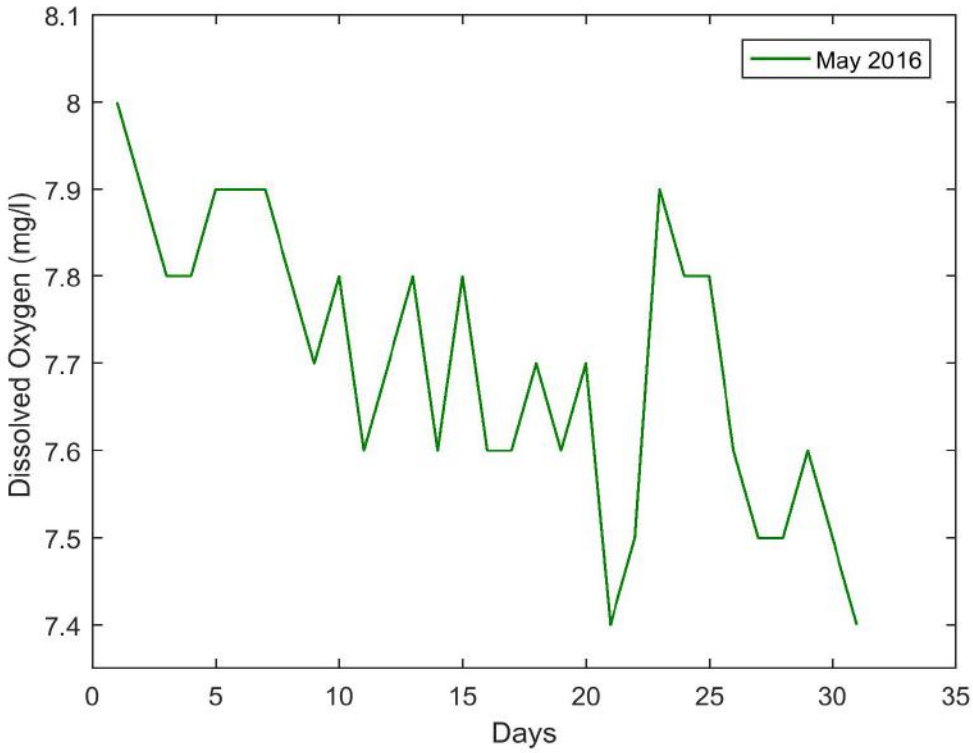

(b)

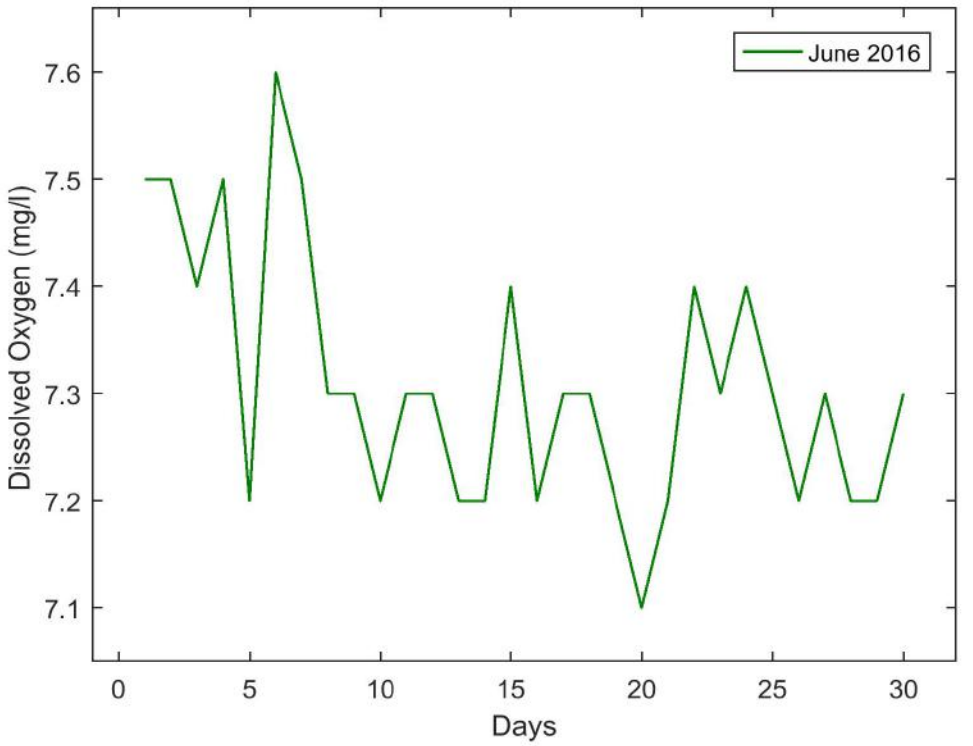

(c)

Figure 4.20: Graphs for Dissolved Oxygen (a) April 2016 (b) May 2016 (c) June 2016

From the data collected (Tables 4.5 - 4.9) and subsequent observation graphs (*see* Figures 4.16 - 4.20), the following conclusions are drawn for the months of April, May and June, 2016.

During the month of April, 2016, *EC* is ranging between $345 - 500$ (mg/l), *i.e.*, there is no fear of contamination. The value of *pH* is varying between $7.2 - 7.8$ depicts its level is up to mark and inclined towards the lower part of acidic nature. The temperature varies between $21 - 27$ (°C) that is normal and is best suited for amphibians. The chloride is recorded between $70 - 100$ (mg/l) that reflects the decrease in salinity of water and is well suited for drinking purpose. *DO* is sensed between $7.5 - 10$ (mg/l), hence, best soluble for flora and fauna. The graph shows the decrease in *DO* due to the effluents added in the river.

For the month of May, 2016, *EC* is ranging between $400 - 540$ (mg/l) due to more industrial disposal and rainfall results into contamination. *pH* is varying from $7.2 - 7.8$ within the intermediate level and is varying maximum between $7.3 - 7.6$; and is under nominal aquatic conditions. The change in temperature lies between $25 - 28$ (°C) and is due to change in climatic conditions. The increase in salinity of water is due to variation in chloride that range between $70 - 105$ (mg/l) and hence, is not fit for drinking purposes. The sudden decrease in the level of *DO* sensed between $7.4 - 8$ (mg/l) represents the fear for living organisms.

During the month of June, 2016, the increase in rainfall and discharges of effluents raise contamination level with change in *EC* ranging between $490 - 590$ (mg/l), causing the river water not fit for drinking purposes. The rise in acidic nature is observed with *pH* range increasing high, *i.e.*, $7.2 - 7.7$. The acidic nature is prone to living of aquatic animals and for drinking purposes. The temperature has increased from $27 - 29$ (°C) and affects photosynthetic process. The chloride noted, is ranging between $80 - 90$ (mg/l) and is suitable for drinking. The drastic decrease in *DO*'s value is observed between $7.1 - 7.6$ (mg/l) due to increase in temperature, and hence, making it unsuitable for flora and fauna.

4.3.9 Comparison with Sampling Technique

To show the effectiveness of *MPST*, it is compared with one of the existing sampling based monitoring system (Jindal and Sharma (2011)) on the basis of data analysis. The data in system is collected manually through the sampling technique from random locations of river and

is send to various laboratories for validation. In this sampling technique, various challenges like manpower, continuous monitoring, expensive and time consuming, are faced. Moreover, it often generates invalid results due to addition of chemicals during laboratory testing. On the other hand, *MPST* enables a user to measure data on the site, using *MPS*. The measured data is collected and analyzed on nearby surface station and thus, enable timely preventive measures. The topology provides results in a short span of time; giving accurate assumption for using chemicals and is indeed trustworthy and an economical process of monitoring river water. In order to check contamination, the physical parameters' data are collected and compared for both techniques as shown in Table 4.10 and Figure 4.21.

Table 4.10: Comparison of Physical Parameters

Parameters	**Months**	**Sampling Technique**	***MPST***
Electrical Conductivity (mg/l)	April 2016	512.56	436.33
	May 2016	530.45	473.48
	June 2016	589.36	547.26
pH	April 2016	7.8	7.51
	May 2016	7.9	7.5
	June 2016	7.95	7.47
Temperature (°C)	April 2016	26	25.41
	May 2016	28	26.75
	June 2016	24	28.34
Chloride (mg/l)	April 2016	91	80.5
	May 2016	94	86.07
	June 2016	88	84.61
Dissolved Oxygen (mg/l)	April 2016	7.9	8.11
	May 2016	8.2	7.7
	June 2016	7.15	7.31

In Table 4.10, the average of observed values (without added chemical or effluents) for the month of April, May and June, 2016 with respect to parameters like *EC*, *pH*, temperature, chloride and *DO*, respectively; is computed using both sampling technique and proposed *MPST*. The generated outcome with respect to computed values for each parameter

are described as follows.

The observed values of *EC* for the month of April, May and June (2016) are 512.56, 530.45, and 589.36 (mg/l), respectively, for sampling technique whereas 436.33, 473.48, and 547.37 (mg/l), respectively, for *MPST*. The results show that more contamination is seen for all three months with former technique whereas less contamination is observed with latter in June only.

With sampling technique, value for *pH* is observed as 7.8, 7.9 and 7.97 for the month of April, May and June (2016), respectively, which suggests more acidic nature of water for the entire duration. In *MPST*, the values are 7.51, 7.5 and 7.47, which confirms water to be normal and is not acidic in nature.

The variations in the observations of temperature with values 26, 28 and 24 (°C) are noted for April, May and June (2016), respectively. These variations suggest rise in temperature for month of April and May whereas decrease in June (yet to be noted increased temperature due to summer season). On the other hand, for *MPST*, slight increase in temperature values for each month, is observed. The values are 25.41, 26.75 and 28.34 (°C) for April, May and June, respectively. It interprets that the topology has given the correct results as temperature is expected to rise only due to summer season with no rainfall.

In case of sampling technique, chloride is noted as 91, 94, 88 (mg/l) and for *MPST*, it is 80.5, 86.07 and 84.61 (mg/l), for the month of April, May and June (2016), respectively. The results from former technique is not correct as value for chloride can not rise consecutively due to normal temperature and *pH*. On the other side, *MPST* is providing accurate results as it is giving normal range for chloride.

DO plays an important role for the survival of aquatic life. With observed values as 7.9, 8.2, 7.15 and 8.11, 7.7, 7.31 for sampling and *MPST*, respectively, for the months of April, May and June (2016). It depicts that values are fluctuating for both techniques. The former technique tells alternative fall and rise in the value whereas latter shows continuous decrease in the value due to the increase in temperature.

On the basis of these values for both sampling technique and proposed topology, the results are plotted in Figure 4.21 and are discussed subsequently.

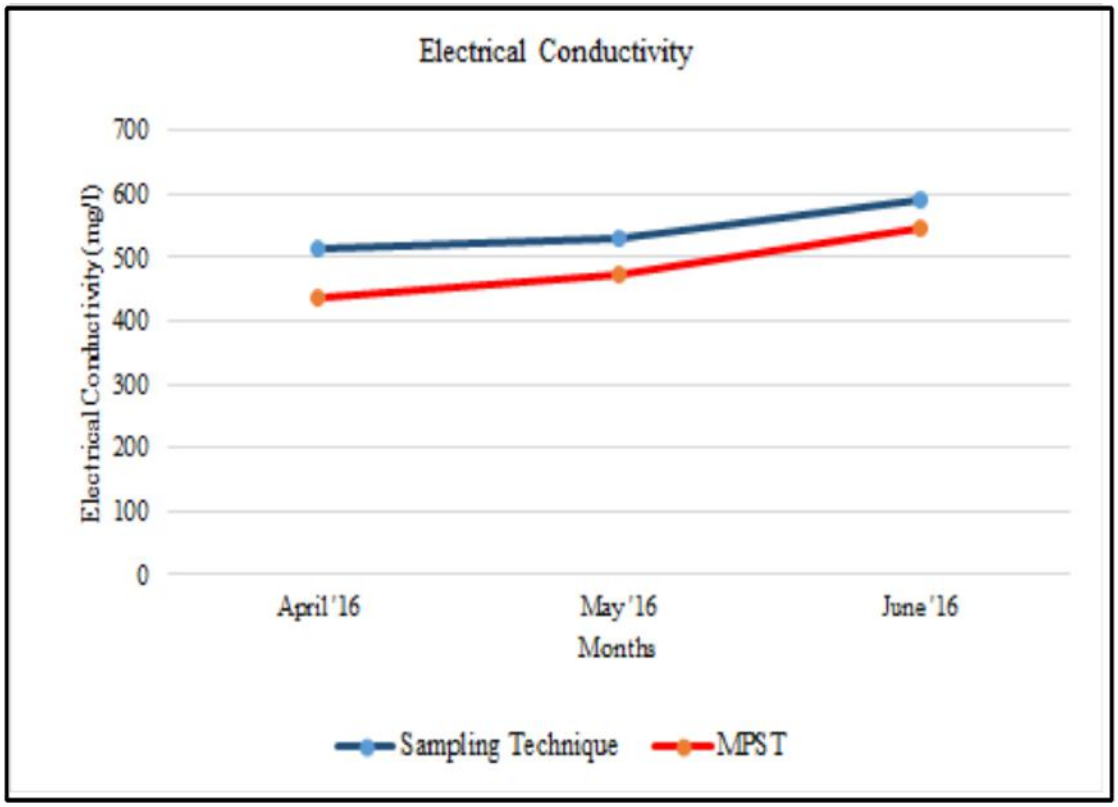
Electrical Conductivity
700
600
500
400
300
200
100
0
Electrical Conductivity (mg/l)
April '16
May '16
June '16
Months
Sampling Technique
MPST

(a)

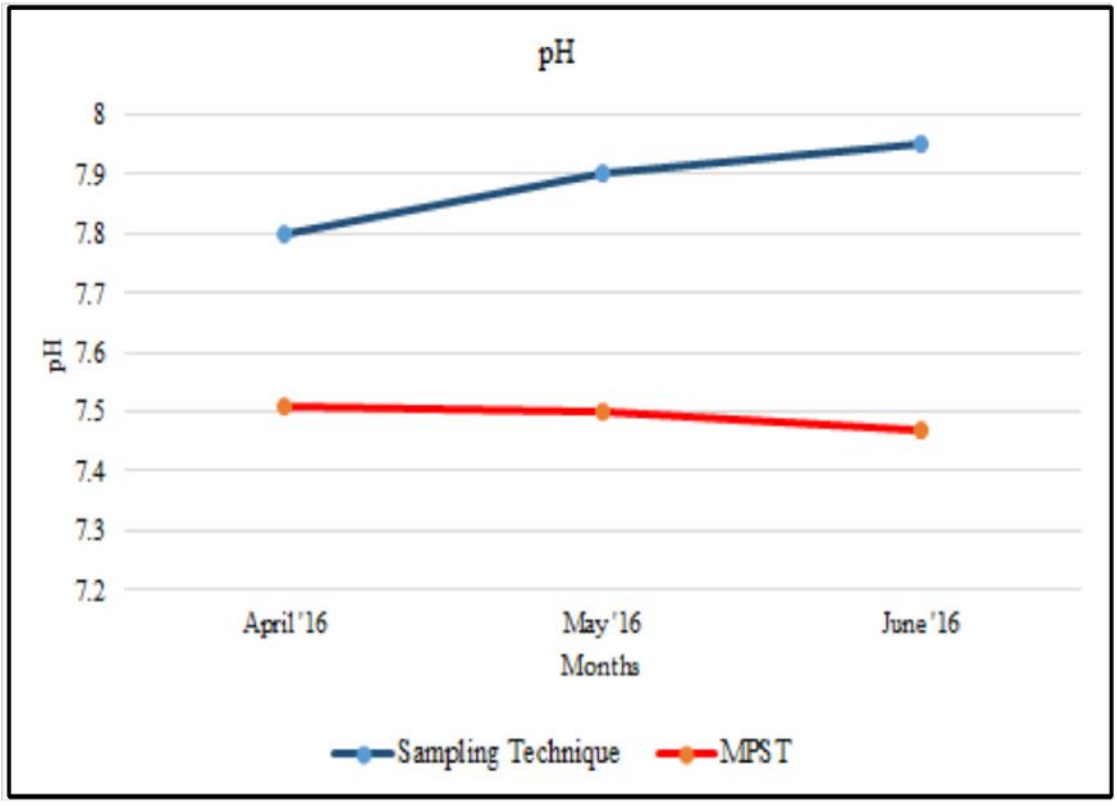
pH
8
7.9
7.8
7.7
7.6
7.5
7.4
7.3
7.2
pH
April '16
May '16
June '16
Months
Sampling Technique
MPST

(b)

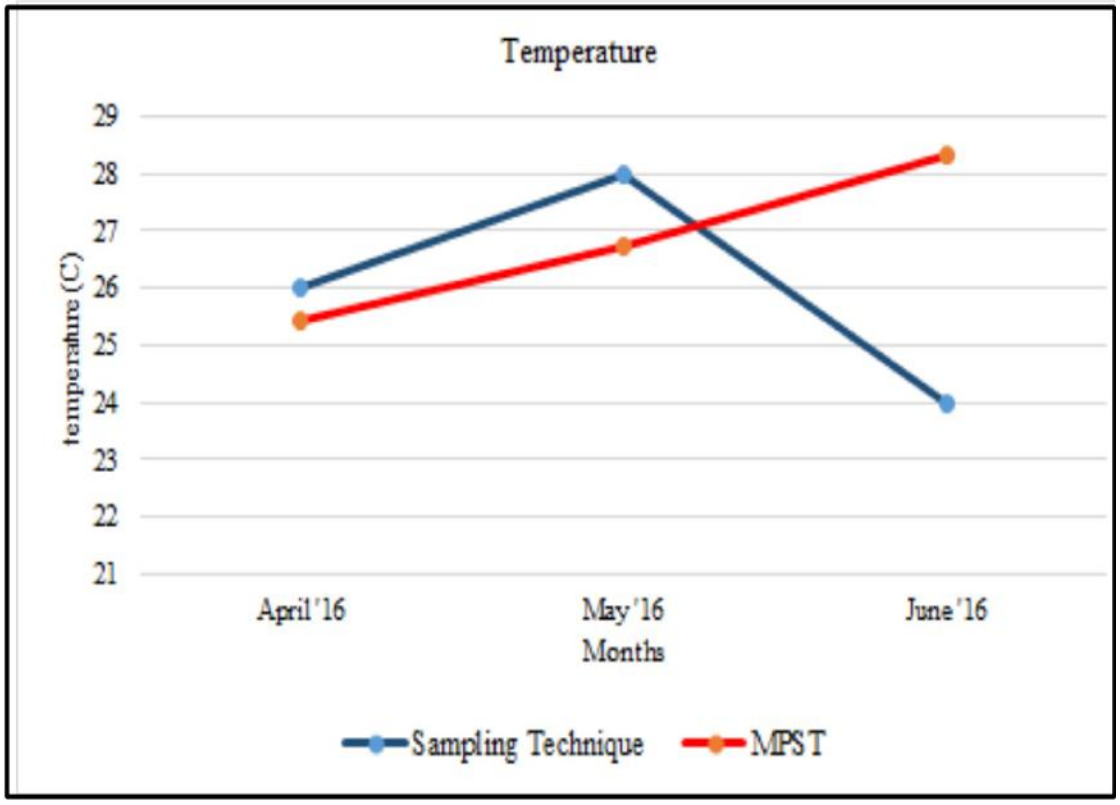
Temperature
29
28
27
26
25
24
23
22
21
temperature (C)
April '16
May '16
June '16
Months
Sampling Technique
MPST

(c)

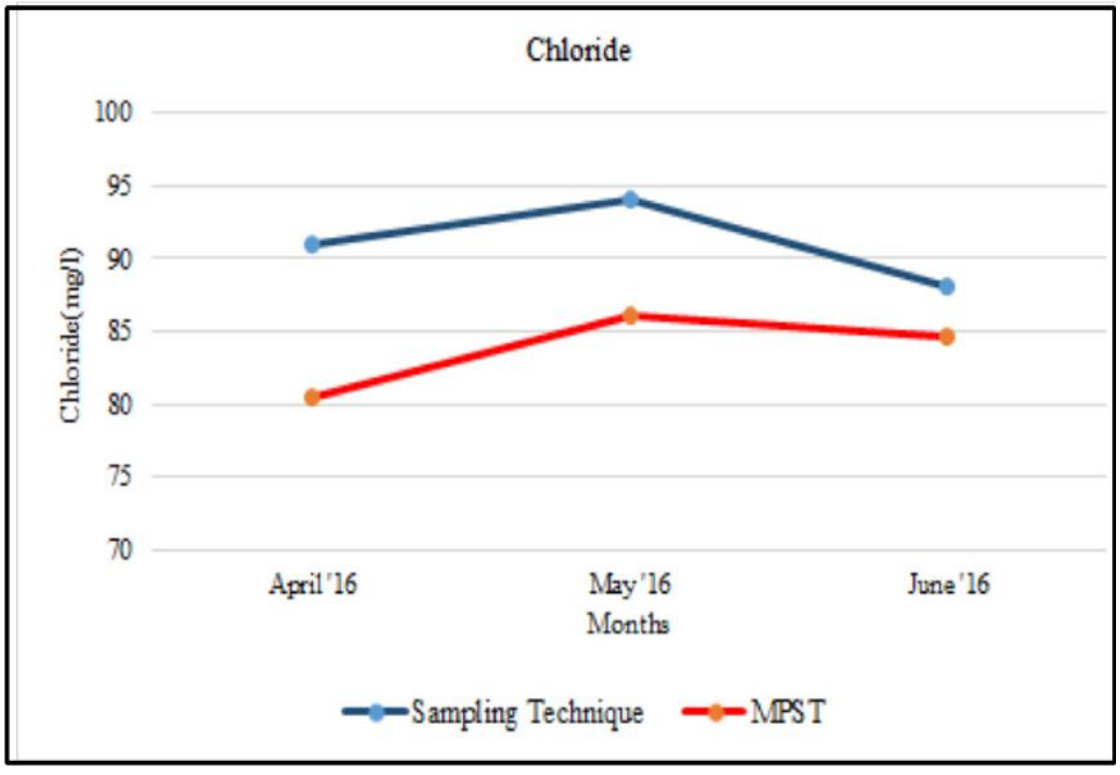
Chloride
100
95
90
85
80
75
70
Chloride(mg/l)
April '16
May '16
June '16
Months
Sampling Technique
MPST

(d)

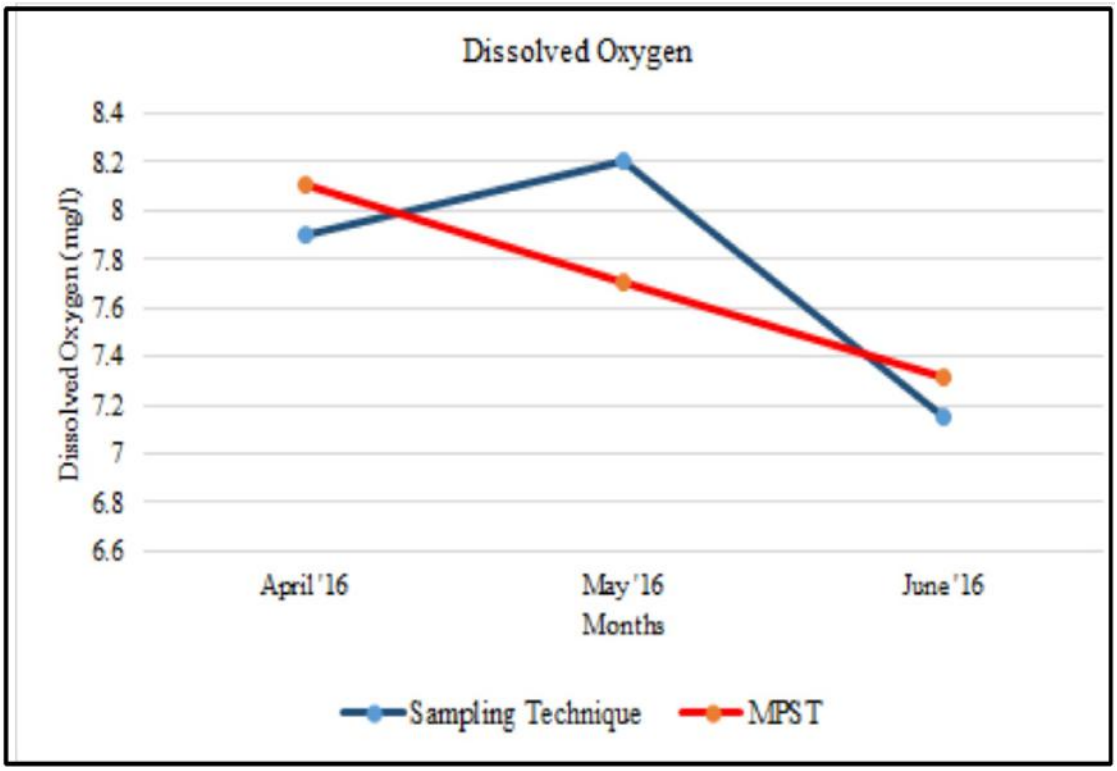

(e)

Figure 4.21: Comparison of Observed Data of Three Months (a) Electrical Conductivity (b) *pH* (c) Temperature (d) Chloride (e) Dissolved Oxygen

Unlike sampling technique, the correct values for *EC* is provided by *MPST* which confirms no contamination in water (*see* Figure 4.21(a)). The similar results are observed for *pH*, *i.e.*, Figure 4.21(b) shows that the sampling technique gives acidic nature of water whereas *MPST* gives non-acidic nature. Figure 4.21(c) represents temperature, where *MPST* provides slight increase in temperature due to summer season. The Figure 4.21(d) provides more alkalinity in water for sampling technique and is harmful for flora and fauna, whereas the normal range of alkalinity is shown by *MPST*. It tells the water quality to be fine with no adverse effects on flora and fauna. Figure 4.21(e) provides *DO* observations that suggests, in sampling technique, water is deficient for oxygen in the month of June. On other hand, *MPST* shows increased volume of oxygen that supports the growth for flora and fauna.

From the above discussions, it is concluded that *MPST* provides proper estimation of using chemicals in river water to remove pollutants. Thus, it is found to be indeed a trustworthy and an economical topology.

4.4 Conclusion

MPST uses economical sensors that through its deployment helps in sensing physical parameters of river water to evaluate its quality. The topology works well at frequency of *25 KHz*, minimizes energy consumption due to single-hop communication and is less affected by noise. The topology enables regular and instant monitoring without any human intervention. On comparison with sampling technique, it is found that *MPST* provides 11.1, 5.20, 5.19, 8.69 and 6.4 (in %) more accurate measurements for physical parameters such as *EC*, *pH*, Temperature, Chloride and *DO*, respectively. Thus, it is an efficient topology for monitoring quality of river water covering large area.

Chapter 5

Triangular Pyramidal Topology: An Extension to Multi-Parametric Sensors' Topology

5.1 Introduction

For evaluating the water's quality with respect to physical parameters, *MPST* is deployed in *3D* environment of river water (discussed in Chapter 3). It covers 20 square meters area considering the sensing range of *MPS*. The deployment has not accounted the coverage area under *AS* and is assumed to be nil to provide maximum coverage. Moreover, *MPST* transmits the sensed data to surface station using localization and communication algorithm and is not tested for existing communication protocols like *AODV*, *DSDV* and *DSR*. Also, the surface station has to continuously update the position of *BoS* by estimating the distance among *BoS* and *AS*. Due to high currents of river, few of the sensors get displaced from its position that leads to increase in errors of localization and communication[1]. Thus, the deployment of *MPST* faces few challenges with respect to coverage, connectivity, communication and efficiency.

In order to address these challenges, *TPT*, an extension to *MPST*, is proposed. It has

[1]The contents are published in Jindal, H., Saxena, S. and Kasana, S. S. (2017), "Triangular Pyramidal Topology to Measure Temporal and Spatial Variations in Shallow River Water using Ad-hoc Sensors Network", *Ad Hoc and Sensor Wireless Networks*, Vol. 39, No. 1-4, pp. 1-35.

considered the area under *AS* and provides maximum coverage of destined location with respect to communication range of *MPS*. The topology is tested for routing protocols for data transmission to surface station. It enables the delivery of maximum sensed data and thus, optimum stationed coverage area is achieved. It is proficient, extensible and beneficial topology for monitoring river water.

5.2 Triangular Pyramidal Topology

TPT considers *MPS* having interface circuitry with inbuilt external *RF* adapter for transmitting or receiving acoustic signals in omni-directional manner (Jindal et al. (2017c); Xiong et al. (2015)). For the deployment of *TPT*, *MPS*s communication range is considered that includes transmission, detection and interferences ranges for sensing (only transmission range is accounted for *MPST*). These ranges are described as under (*see* Figure 5.1).

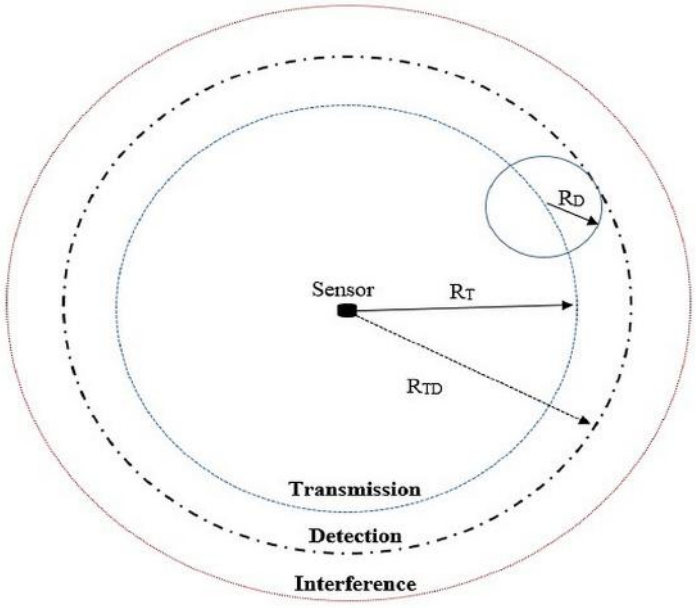

Figure 5.1: *MPS* Range for Communication

i. **Transmission Range -** This range is the actual sensing range of *MPS*. In this range, the sensor communicates with neighboring sensors easily. The range is specified under radius R_T in Figure 5.1. Here, the sensor acts as both sender and receiver for sharing the data with less packet loss.

ii. **Detection Range -** This range is responsible for carrying communication partially due to overlapping of two or more sensing ranges. This range comes under the radius (R_D) where communication is possible but it faces more data packet losses due to the noise of the environment (that include noise caused by shipping, man-made or natural). The sensor has maximum communication range up to detection range forming complete sensing radius as R_{TD}. The data communicated in this range succinctly decreases by 25-30 %.

iii. **Interference Range -** This range does not establish communication due to high traffic and less bandwidth. This range is heavily affected by the background noise with maximum data loss. Even, the receiver would not detect any signals.

These ranges are considered for designing *TPT* and a deployment strategy is adopted to cover maximum area of deployed region. On the basis of the coverage and sensed area, two Axioms are postulated, described as under.

Axiom 1: The uncovered area, *XYZ* is considered as zero for minimizing the load on sensing area (*see* Figure 5.2).

To present the scenario, Theorem 4.1 is postulated to achieve the maximum coverage with the proposed topology.

Theorem 4.1. The triangular pyramidal grid has sensing range $\vartheta(d_a/r_c)$ which is described as the ratio of covered and targeted area and covers $\mathbb{A}_{PQR}$ excluding $\mathbb{A}_{XYZ}$, as shown in Eq. 5.1.

$$\vartheta\left(\frac{d}{r}\right) = \begin{cases} \frac{\mathbb{A}_{PQR}-\mathbb{A}_{XYZ}}{\mathbb{A}_{PQR}} = 1 - \frac{\mathbb{A}_{XYZ}}{\frac{\sqrt{3}}{4}\times d_a^2}, \frac{d_a}{r_c} \epsilon [0,2] \\ \frac{3\times\left(\frac{\pi r^2}{6}\right)}{\frac{\sqrt{3}}{4}\times d_a^2} = \frac{2\times\pi}{\sqrt{3}}\left(\frac{d_a}{r_c}\right)^{-2}, \frac{d_a}{r_c} \epsilon (2,\infty) \end{cases} \tag{5.1}$$

where

$$\mathbb{A}_{PQR} = \frac{\sqrt{3}}{4}\times d_a^2 \tag{5.2}$$

$$\mathbb{A}_{XYZ} = \frac{\sqrt{3}}{4} \times \left(\frac{d_a}{2} - \sqrt{3 \times r_c^2 - \frac{3}{4} \times d_a^2} \right)^2 - 3 \times r_c^2 \times arcsin\left(\frac{YZ}{2 \times r_c} \right) + \frac{3}{4} \times YZ \times \sqrt{4 \times r_c^2 - YZ^2} \tag{5.3}$$

and

$$YZ = \frac{d_a}{2} - \sqrt{3 \times r_c^2 - \frac{3}{4} \times d_a^2} \tag{5.4}$$

Proof: To prove the sensing range, two cases are considered. First case is the trivial case for $\frac{d_a}{r_c} \epsilon [0,2]$ which describes the area covered by sensors' communication range and second case is non-trivial for $\frac{d_a}{r_c} \epsilon (2,\infty)$ which assumes the area below *AS* to be null. These cases are already solved in previous Chapter 3 in Section 3.2.2.

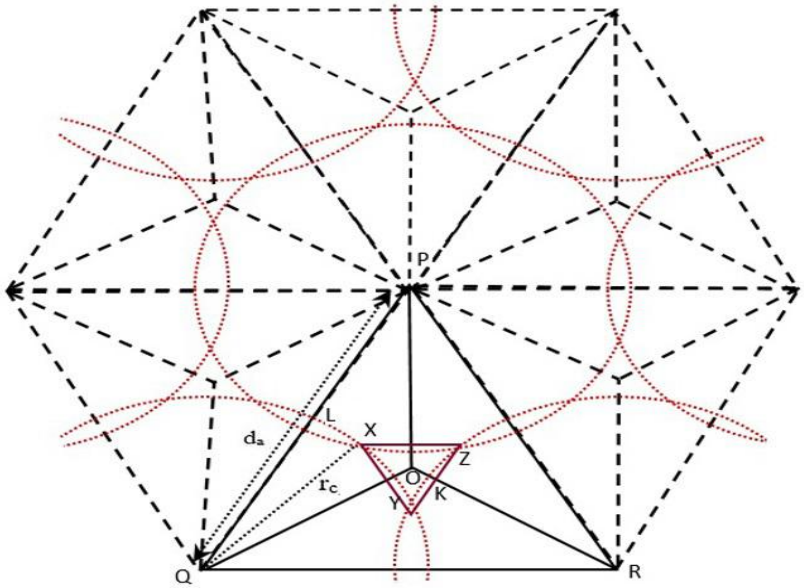

Figure 5.2: *TPT* under Transmission Range

Axiom 2: Considering the region, *XYZ* to be non-zero and is covered under detection range with less packet loss. To achieve this, Theorem 4.2 is postulated with *TPT*.

Theorem 4.2. The triangular pyramidal grid has sensing range $\vartheta(d_a/r_c)$ to cover the whole

region of targeted area, *i.e.*, $\mathbb{A}_{XYZ}$ as shown in Eq. 5.5.

$$\vartheta\left(\frac{d_a}{r_c}\right) = \frac{\partial En_{total}}{\partial R_D}, covering\ whole\ region \tag{5.5}$$

Proof: To present the scenario, let the sensors in *TPT* has ranges as transmission and detection, say, R_D and R_{TD}, respectively. The region $\mathbb{A}_{XYZ}$ to be sensed is covered by R_{TD} as shown in Figure 5.3.

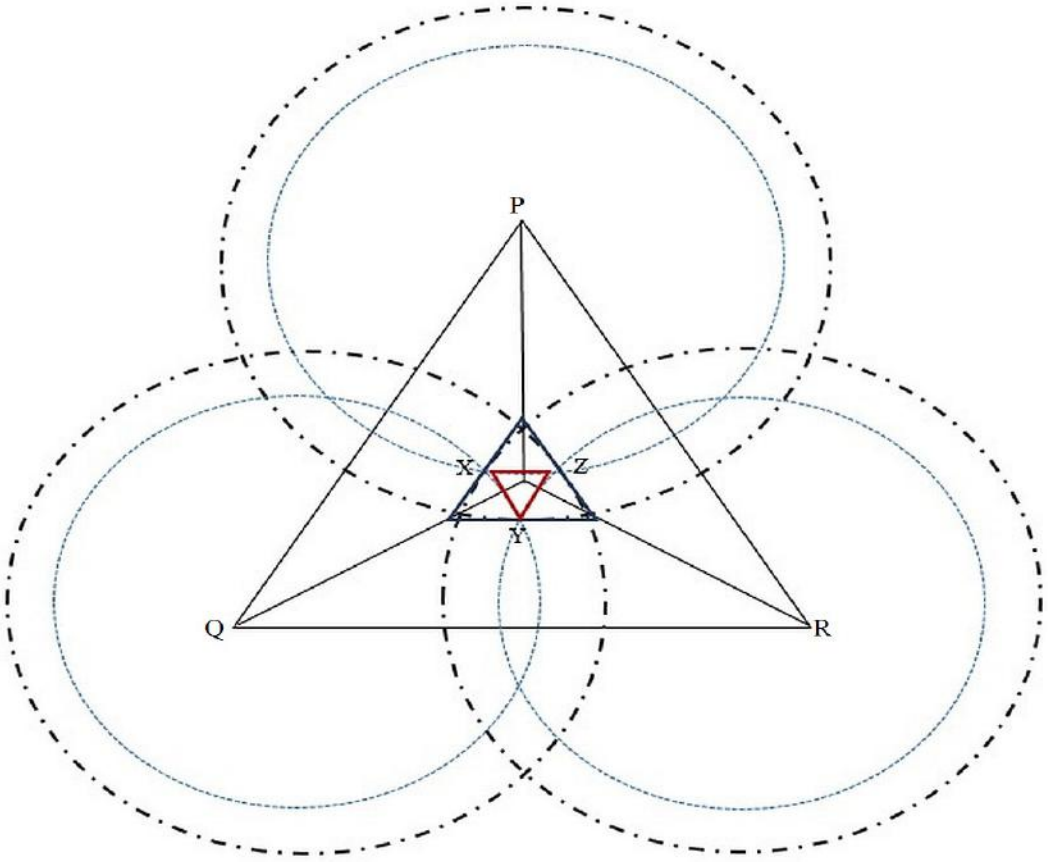

Figure 5.3: Scenario for Sensing considering Detection Range

The bottom sensors *(S_{BoS})* are deployed at the surface and their location follow 2-Dimensional Poisson Distribution (Pr). Considering, N number of S_{BoS} in area $\mathbb{A}_{PQR}$, Pr is described in Eq. 5.6.

$$Pr(S_{BoS_N}) = \frac{(\lambda \times \mathbb{A}_{PQR})^{S_{BoS_N}} \times exp^{-\lambda \times \mathbb{A}_{PQR}}}{S_{BoS_N}!} \tag{5.6}$$

where, λ is density of sensor. As sensors are uniformly distributed and independent in $\mathbb{A}_{PQR}$, it communicates directly with Anchored Sensor *(S_{AS})* which act as Head, *say*, S_{AS_H}, *via* single hoping. Then, the distance r_c from S_{BoS} to S_{AS} has its Cumulative Distribution Function (cdf), $F(r)$ given by Eq. 5.7.

$$F(r) = Pr(R_D \leq r_c) = \frac{\pi \times r_c^2}{\pi \times R_D^2} = \frac{r_c^2}{R_D^2} \tag{5.7}$$

The Probability Density Function *(pdf)* of r_c, $f(r)$ is given by Eq. 5.8.

$$f(r) = \frac{2 \times r_c}{R_D^2} \tag{5.8}$$

The total energy consumption covering the whole region as shown in Figure 5.3 is given by Eq. 5.9 (Xiao (2009)).

$$\begin{aligned} En_{total} &= 2 \times N_c \times E_s + N_c \times Dr_b \times S_{AS_H} \times J_{S_{BoS}} \\ &\quad + N_c \times \vartheta \left(E_s + Dr_b \times S_{AS_H} \times J_{S_{AS}}\right) \end{aligned} \tag{5.9}$$

where, N_c is total number of sensor's clusters, E_s is energy of sensor, Dr_b is bit duration, S_{AS_H} is Anchored Sensor as Head, $J_{S_{BoS}}$ and $J_{S_{AS}}$ are the energy consumption at S_{BoS} and S_{AS} and are given as -

$$J_{S_{BoS}} = E_s \left[r_c \times exp^{\alpha(f_s) \times r_c} \right] \tag{5.10}$$

$$J_{S_{AS}} = E_s \left[d_a \times exp^{\alpha(f_s) \times d_a} \right] \tag{5.11}$$

and

$$\alpha(f_s) = (1.27 \times exp - 5)R_D^2 + (6.5 \times exp - 6)R_D + (0.68 \times exp - 5) \tag{5.12}$$

Then, the total energy consumption for deployment of S_{BoS} and S_{AS} using *pdf* for region under radius R_{TD}, is given by Eqs. 5.13, 5.14 (referring Eqs. 5.7, 5.8 and Figure 5.1).

$$\begin{aligned} J_{S_{BoS}} &= \int_0^{R_D} r_c \times exp^{\alpha(f_s)\times r_c} \times \frac{2\times r_c}{R_D^2} dr_c \\ &= \frac{2\times r_c}{R_D^2}\left[\frac{exp^{\alpha(f_s)\times r_c}}{\alpha(f_s)^3} \times \left(\alpha(f_s)^2 \times r_c^2 - 2\times\alpha(f_s)\times r_c + 2\right)\right]_0^{R_D} \\ &= \frac{2\times exp^{\alpha(f_s)\times R_D}}{\alpha(f_s)^3}\left(\alpha(f_s)^2 - \frac{2\times\alpha(f_s)}{R_D} + \frac{2}{R_D^2}\right) - \frac{4}{\alpha(f_s)^3\times R_D^2} \end{aligned} \tag{5.13}$$

$$\begin{aligned} J_{S_{AS}} &= \int_0^{R_{TD}-R_D} r_c \times exp^{\alpha(f_s)\times r_c} \times \frac{2\times r_c}{R_{TD}^2} dr_c \\ &= \frac{2\times r_c}{R_{TD}^2}\left[\frac{exp^{\alpha(f_s)\times r_c}}{\alpha(f_s)^3} \times \left(\alpha(f_s)^2 \times r_c^2 - 2\times\alpha(f_s)\times r_c + 2\right)\right]_0^{R_{TD}-R_D} \\ &= \frac{2\times exp^{\alpha(f_s)\times(R_{TD}-R_D)}}{\alpha(f_s)^3\times R_{TD}^2}\left(\alpha(f_s)^2(R_{TD}-R_D)^2 - 2\times\alpha(f_s)\right)(R_{TD}-R_D) \\ &+ 2 - \frac{4}{\alpha(f_s)^3\times R_{TD}^2} \end{aligned} \tag{5.14}$$

Taking partial derivative of Eq. 5.9 and putting second part as zero, the consumption within range of R_{TD} is given by Eq. 5.15.

$$\begin{aligned} \frac{\partial En_{total}}{\partial R_D} &= \frac{8 + 2.exp^{\alpha.R_D}\left(-4 + 4.\alpha.R_D - 2.\alpha^2.R_D^2 + \alpha^3.R_D^3\right)}{\alpha^3.R_D^3} \\ &+ \vartheta\Big(\frac{1}{\alpha^3.R_{TD}^2}\big(exp^{-\alpha.R_D}\big(-4.exp^{\alpha.R_D} + 2.exp^{\alpha.R_{TD}} \\ &(\alpha^2.R_D + \alpha(2 - 2.\alpha.R_{TD} + \alpha.R_D))\big)\big) \\ &- \frac{1}{\alpha^2.R_{TD}^2} \\ &\big(exp^{-\alpha.R_D}\big(-4.exp^{\alpha.R_D} + 2.exp^{\alpha.R_{TD}}\big(2 + \alpha.R_{TD}\big(-2 + \alpha.R_{TD} \\ &+ \alpha.R_D(2 - 2.\alpha.R_{TD} + \alpha.R_D)\big)\big)\big)\big)\Big) \end{aligned} \tag{5.15}$$

Eq. 5.15 is used to cover the whole region covering the area $\mathbb{A}_{XYZ}$ and is assumed to be zero in the previous case (*see* Section 4.2).

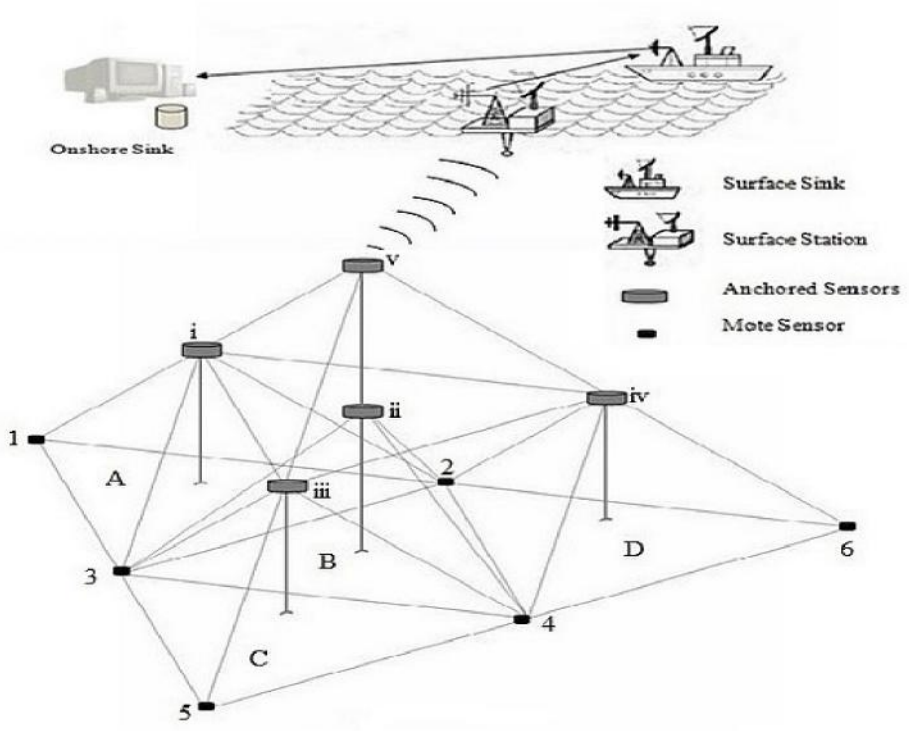

(a)

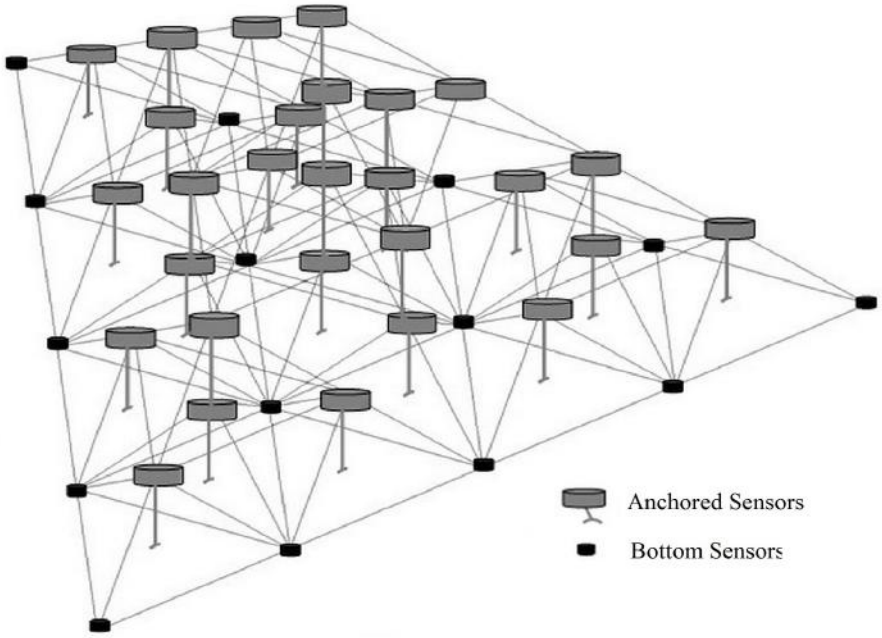

(b)

Figure 5.4: *TPT* Deployment (a) Vertical View (Data Collection) (b) Topology at Large Scale

The topology can be extended on a large scale vertically (*see* Figures 5.4) to investigate regions of interest in shallow rivers, lakes and ponds.

5.2.1 Communication Process

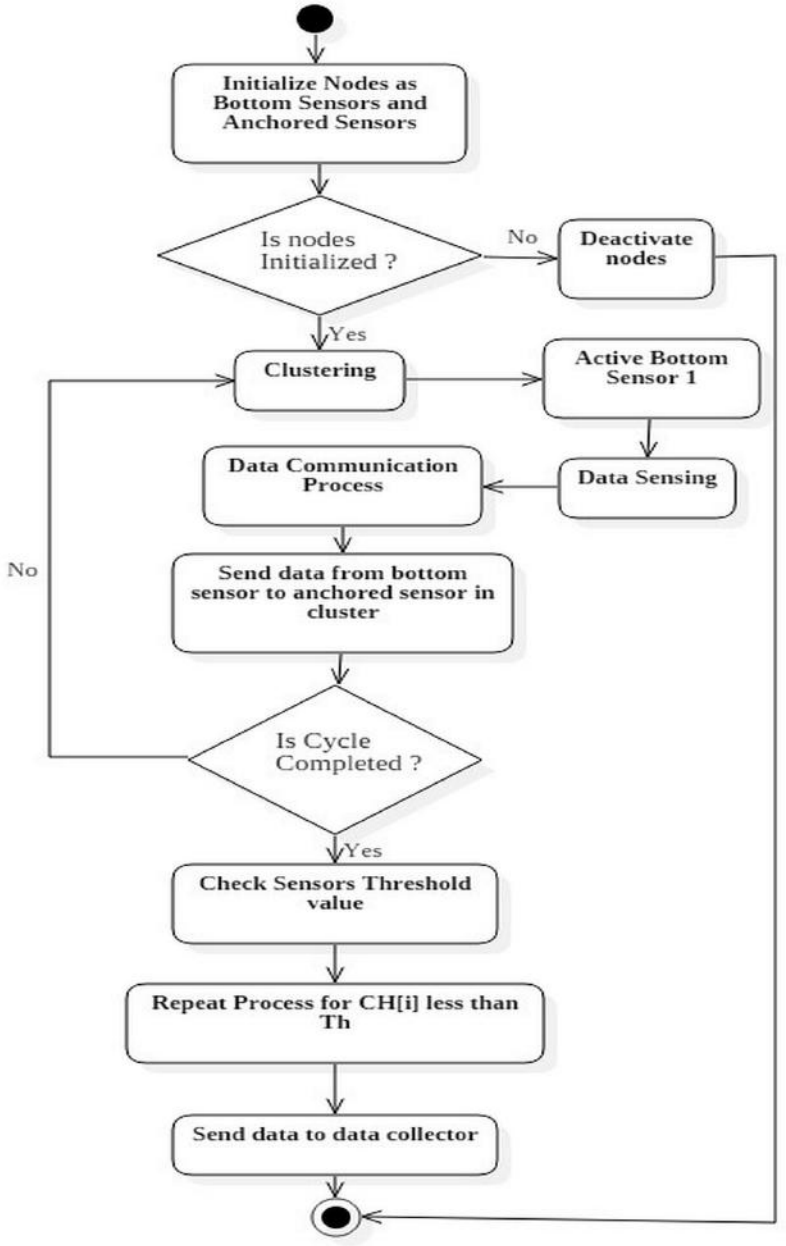

Figure 5.5: Communication Process

TPT is tested as its vertical expansion having 4 pyramidal clusters, namely (A-D),

$S_{BoS_{(1-6)}}$ and $S_{AS_{(i-v)}}$ for which data collection technique is shown in Figure 5.4(a). The topology works in two stages *i.e.*, *clustering* and *communication* (*see* Figure 5.5). The process is initialized with establishing connection among Bottom Sensors, S_{BoS_i}(i = 1..6) and Anchored Sensors, ($S_{AS_i} \forall$ i = 1..5) *namely*, (i-v). S_{AS} acts as Cluster Head (CH[i] $\forall$ i = 1..4), *namely*, (A to D), that collects data from S_{BoS} and further sends it to surface station. At an instance, the nodes initialization are checked and are disabled on the basis of its initial states. If the nodes have been initialized then cluster process is started for activating S_{BoS}, sensing physical parameters and selecting rightful S_{AS} to send gathered data. The transmission of data within the clusters are performed using angular acoustics. S_{AS} collects all data from S_{BoS} and its energy is checked with respect to threshold value. The process is repeated again to sense more data if sensor's (S_{AS} and S_{BoS}) energy is retained, otherwise all sensors goes in sleep mode and process ends. The descriptive working is explained in Algorithm 5.1.

The algorithm starts with allocating j to 1, p to *zero*. The loop at an instance, investigates sensors to be in sleep mode and for each cluster, it activates them. After activation, the process of clustering and communication acts for sending data to S_{AS} by S_{BoS}. Afterwards, the process checks the energy consumption of each sensor. If the consumed energy is less than threshold then the process is repeated for clustering and sensing physical parameters. Further, the data is transmitted to surface station using data collector (SS_{DC}), which sends the acknowledgment in return for confirming the reception of data. At last, all sensors goes in sleep mode after receiving acknowledgment and the process ends.

5.2.2 Routing and Simulation

For *TPT*, the three routing protocols like *AODV*, *DSDV* and *DSR* are initially simulated with sensors-count set as 11, 19, 27, 35, 43, 51 and 57 in *NS-2*, to find the best protocol for real-time testing. The *AODV* and *DSDV* are appropriate for dynamic environment but cause large signaling overhead resulting into sensor failures (Alsaghier and Mishra (2014)). *DSR* helps in estimating distance, angles among neighboring sensors and remaining energy among sensors; before forwarding a packet to destination. *DSR* consumes less energy. Moreover, these protocols help to eliminate factors like path loss, noise, multi-path, variance, *etc* (Prodan et al. (2014)). These protocols are used because these are capable for prolonged working

Algorithm 5.1 Communication Process Algorithm

Require: Bottom Sensor (S_{BoS}), Anchored Sensor (S_{AS}), Cluster (clust), Sensor (S), counter, threshold (th), Data Collector (SS_{DC}) and Acknowledgment (ack)

begin
initialize $p \longleftarrow 0, j \longleftarrow 1$
//initiation of clustering process
while $(j \leq p)$ **do**
  $S_j \longleftarrow 0$ //all sensors are in sleep mode
  while $(clust_j = 1..p)$ **do** // activating sensors
    activate $S_{AS_j} \forall S_{BoS_j}$ // activating all S_{AS} in range of S_{BoS}
    receive $\longleftarrow$ data //data is recieved
    increment $clust_j$ //selecting next cluster
  end while
  increment j
end while
//communication process begins
for $(S_j = 1..p)$ **do**
  if $(S_j(energy) \leq th)$ **then**
    $clust_j = repeat$
  else
    return
  end if
end for
while $(S_{AS_j} \leq p)$ **do**
  send data to S_{AS_j}
  $SS_{DC} \longleftarrow data(S_{AS_j})$ //sending data from S_{AS_j} to SS_{DC}
  send ack $\longleftarrow SS_{DC}$ //SS_{DC} sends acknowledgement
end while
while $(j \leq p)$ **do**
  if $(SS_{DC} \longleftarrow data \;\&\&\; ack == true)$ **then**
    $S_j \longleftarrow sleep$ //all sensors go in sleep mode
  end if
end while
end

with dynamically adding up of new sensors within the network. The execution of the protocols are as under.

i. ***AODV:*** The protocol maintains route information as soon as it is requested by nearby nodes. Its main feature is storage of a Destination Sequence Number *(DSN)* for every routing entry, which is generated by destination node itself with the routing information. S_{AS} in *TPT* generates *DSN* for having data information from S_{BoS}. The protocol helps in providing best path with greatest sequence number by performing two functions: route discovery and route maintenance. In the former function, the S_{BoS} sends a Route Request Message *(RREQ)* to other S_{BoSs} (for communication). If the neighboring S_{BoS} have information about S_{AS}, then it forwards the request to the connected S_{BoS} unless S_{AS} is found. The intermediate S_{BoSs}, which stores information for the S_{AS} send Route Reply Message *(RREP)* to S_{BoS_1}. The path is recorded in the routing table and the route is identified. Hence, it starts the communication between S_{BoS_1} and S_{AS_1}. In case, the link of next hop breaks, then it reports Route Error *(RERR)*. For latter function, it generally has table for *RERR* and *HELLO* messages (used for establishing communication with neighboring S_{BoS}). The process continues till all S_{BoS_i}(i = 1..6) in range, sends data to all ($S_{AS_i} \forall$ i = 1..5). The process of *AODV* is described by the Algorithm 5.2.

   The algorithm initializes message counter to *zero* and requests for connection establishment if message contains value of *RREQ* and then update the path between S_{AS} and S_{BoS}. If the selected sensor is S_{AS}, then process sends *RREP* to S_{BoS}. When the new sensors are added in the route path, the *RREQ* is sent to S_{AS} and path values are updated. The process goes on till all S_{BoS} send data to S_{AS} and S_{BoS} get acknowledgment as reply. The route table are updated and the process stops.

ii. ***DSDV:*** The protocol helps in maintaining the route table with a condition that each node updates *RREQ* and *RREP* messages of neighboring nodes to achieve multihoping. Each routing table contains all possible paths to reach S_{AS} in *TPT* and thus data packets are transmitted through the channel. The protocol maintains three attributes, *i.e.*, avoid loops, resolving count for infinity problems, and to reduce high

Algorithm 5.2 *AODV* Process for *TPT*

Require: Anchored Sensor *(S_{AS})*, Bottom Sensor *(S_{BoS})*, Message (msg), Route Request Messgae *(RREQ)*, Route Reply Message *(RREP)*, Route Error *(RERR)*, NodeRemove (N_r = HIGH/LOW)

start
initialize $msg \longleftarrow 0$
if ($msg == RREQ$) **then** // requesting for establishing connections nad sending packets
  $update \longleftarrow route$ //at source node *(S_{BoS})*
  send information about destination *(S_{AS})* to source *(S_{BoS})*
  if ($node == S_{AS}$) **then** //destination
    send $RREP \longleftarrow S_{BoS_i}$ //all S_{BoS} sends route reply to S_{AS}
  else
    if (new nodes added $\longleftarrow route$) **then**
      send $RREP \longleftarrow S_{BoS_i}$ //all S_{BoS} sends route reply to S_{AS}
    else
      send $RREQ \longleftarrow S_{BoS_i}$ //all S_{BoS} asks for route request to S_{AS}
    end if
  end if
end if
if ($msg == RREP$) **then**
  $update \longleftarrow$ route table //route table have sequence numbers
  if ($node == S_{BoS}$) **then** //source
    send packets $\longleftarrow S_{AS}$ // sending packets to S_{AS}
  else
    send $RREP \longleftarrow$ neighboring nodes //asking to establish connection and send packets
  end if
end if
if ($msg == RREP$) **then** //error packets
  affected nodes $\longleftarrow remove$ //affected nodes are removed
  if ($N_r == HIGH$) **then**
    forwards $RERR \longleftarrow$ neighbouring nodes //nodes send route error
    $update \longleftarrow$ route table //route table is updated
  else
    $route \longleftarrow reset$ //route is resetted
  end if
end if
end

routing overhead. Any path towards S_{AS} having highest *DSN* replaces identical path with smaller *DSN* in routing table maintained by one S_{BoS} and does not bothers about the number of hops to reach S_{AS}. At this point, each S_{BoS} instantly updates and advertises change in routing table in order to avoid S_{BoS} failure but waits for certain amount of time to advertise those changes (called as settling time). Thus, each S_{BoS} has route table with destination address *(S_{AS})*, with last and average settling time. *DSDV* does not support multi-casting routing. The process is discussed in Algorithm 5.3.

DSDV begins with the search of the neighbors of active sensor. If S_{AS} as neighbor is found, then it sends the sensed data and checks for its buffer size to sense more data. Once, the buffer size is full, it discards the packets, else, new packets are formed which are updated in buffer. The packets are broadcasted to S_{AS} by giving sequence number to each packet. If the packets are received by the S_{AS}, then it sends acknowledgment to S_{BoS} and checks for number of hops for routing the packet. It calculates the total time spent in sending the acknowledgment between hops and packets. Finally, it updates the time counter with average time for both the hops in routing path. The process ends with updating the routes between S_{BoS} and S_{AS}.

iii. ***DSR:*** Like *AODV*, it also has an on-demand feature which is not table driven. In this protocol, the S_{BoS_1} in *TPT* usually stores the complete hoping information towards the S_{AS_1} which is further stored in route cache (continuously updated). As *DSR* allows the network to be self-organizing and self-configuring, thus, it is adhere to any hostile environments. The protocol does not require any periodic packets for its routing and supports load balancing. Each and every route guarantees to be independent from all the loops such that source *(S_{BoS})* avoids similar hops for the chosen paths. Algorithm 5.4 discusses the *DSR*'s working.

In Algorithm 5.4, the process maintains a list of routes at source (S_{BoS}) and destination (S_{AS}). Initially, the sensor sends a *RREQ*. It validates *RREQ* by checking route record list. If the list has the address of S_{AS}, then its address is recorded in S_{BoS} and packets are sent. The acknowledged *RREP* is forwarded to both S_{AS} and S_{BoS}. The route record

Algorithm 5.3 *DSDV* Technique for *TPT*

Require: Anchored Sensor *(S_{AS})*, Bottom Sensor *(S_{BoS})*, Source (S), Destination (D), Buffer (Bf = 0/1), Route Request Message *(RREQ)*, acknowledgment *(ACK)*, Settling Time(S_T)

start
if ($S.nexthop() != active$) **then** //S_{BoS} is checking neighboring nodes
  $S_{AS} \longleftarrow$ Deliver packet from S *(S_{BoS})* //packets from S_{BoS} are delivered to S_{AS}
else
  if ($S.Bf == 1$) **then** //buffer is full
    $packet \longleftarrow discard$ //packets are discarded
  else
    $packet \longleftarrow S.Bf$ packets are send to buffer
    $update \longleftarrow S.Bf$ // update buffer
    S.broadcast(*RREQ*, 1, D *(S_{AS})*, S *(S_{BoS})*) // sending packets
  end if
end if
if ($S.nextneighbour \longleftarrow$ route to D) **then**
  $S.recieve \longleftarrow ACK$ //acknowledgement is recievied
  Update time = 1
else
  if ($S \longleftarrow ACK$) **then**
    if ($ACK.hops <= MaxHops \;\&\&\; ACK.hops >= MinHops$) **then**
      Update time $\longleftarrow$ ACK.UpdateTime //calculating time among nodes
    end if
  end if
  calculate $\longleftarrow S_T$ //settling time is calculated
end if
end

and neighboring S_{BoS} list are compared for updated routing information and packets are sent by updated S_{BoS} to S_{AS}. The process ends with updating route records in S_{BoS}.

The simulation parameters are shown in Table 5.1. The simulation results are analyzed on the basis of various performance metrics (Energy Consumption, Packet Delivery Ratio, Throughput and Routing Overhead) for assessing network's performance. The comparison of protocols is shown in Figure 5.6.

Algorithm 5.4 *DSR* Algorithm for *TPT*

Require: Anchored Sensor *(S_{AS})*, Bottom Sensor *(S_{BoS})*, Route Request Messgae *(RREQ)*, Route Reply Message *(RREP)*

start
initialize $node \longleftarrow RREQ$ //route request send by S_{BoS}
if $(RREQ == valid)$ **then**
  if ($S_{AS}.address \longleftarrow$ route record) **then** //address of S_{AS} is stored in route record of S_{BoS}
    discard $\longleftarrow$ route record //route record is discared
  else
    if $(S_{AS}.address == target.address)$ **then**
      send $\longleftarrow$ *RREP* //acknowledging
      send $\longleftarrow$ packet from S_{BoS} //sending data
    else
      compare(neighbouring S_{BoS} list, route record)
    end if
  end if
else
  discard $\longleftarrow$ packet //packets are discarded
end if
update $\longleftarrow$ route record //update addresses of S_{BoS}
end

Table 5.1: Simulation Parameters

Attributes	**Values**
Simulator	Network Simulator
Simulation time	100 ms
Simulation Area	1100 $\times$ 1100 m
Number of nodes	11, 19, 27, 35, 43, 51, 57
Routing Protocols	AODV, DSDV, DSR
Traffic Type	UDP

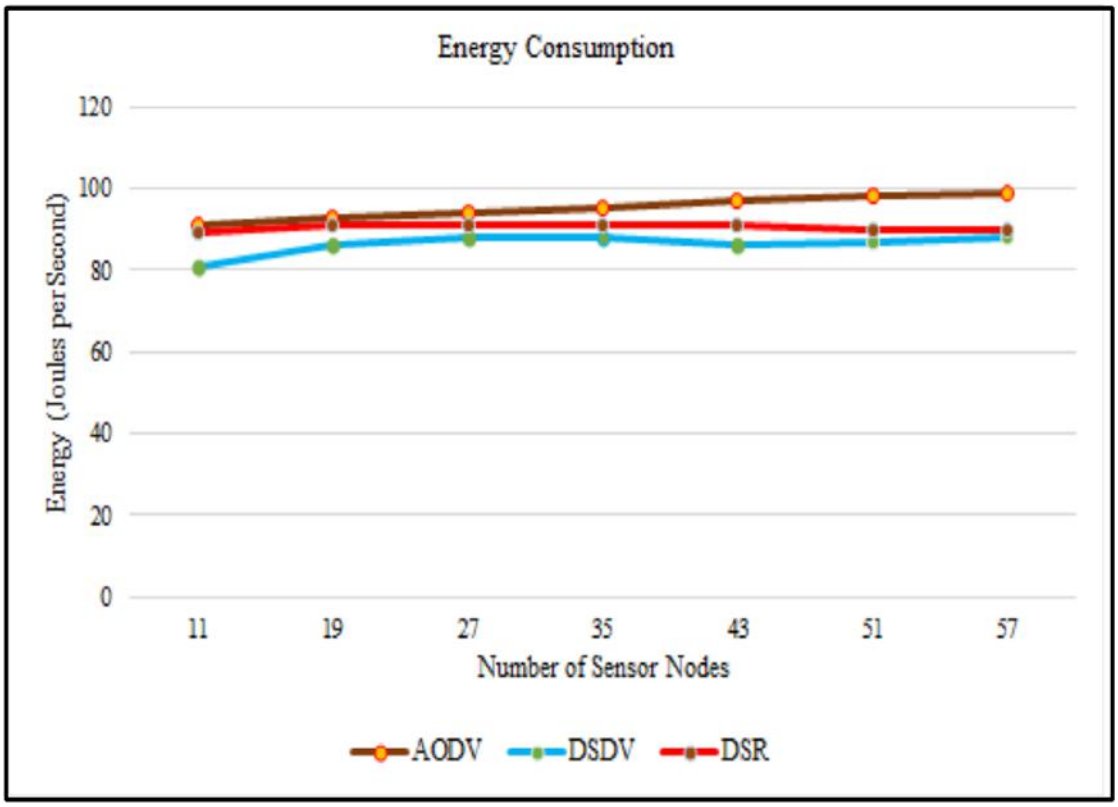
Energy Consumption
120
100
80
60
40
20
0
Energy (Joules per Second)
11
19
27
35
43
51
57
Number of Sensor Nodes
AODV
DSDV
DSR

(a)

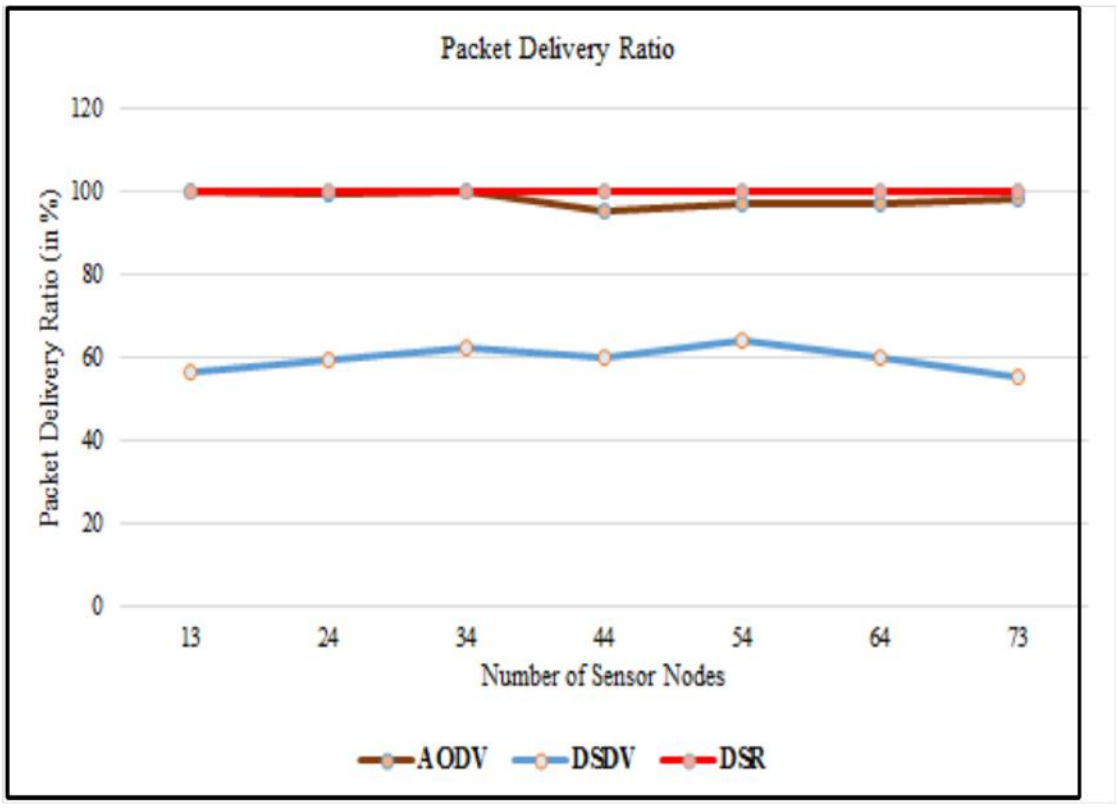
Packet Delivery Ratio
120
100
80
60
40
20
0
Packet Delivery Ratio (in %)
13
24
34
44
54
64
73
Number of Sensor Nodes
AODV
DSDV
DSR

(b)

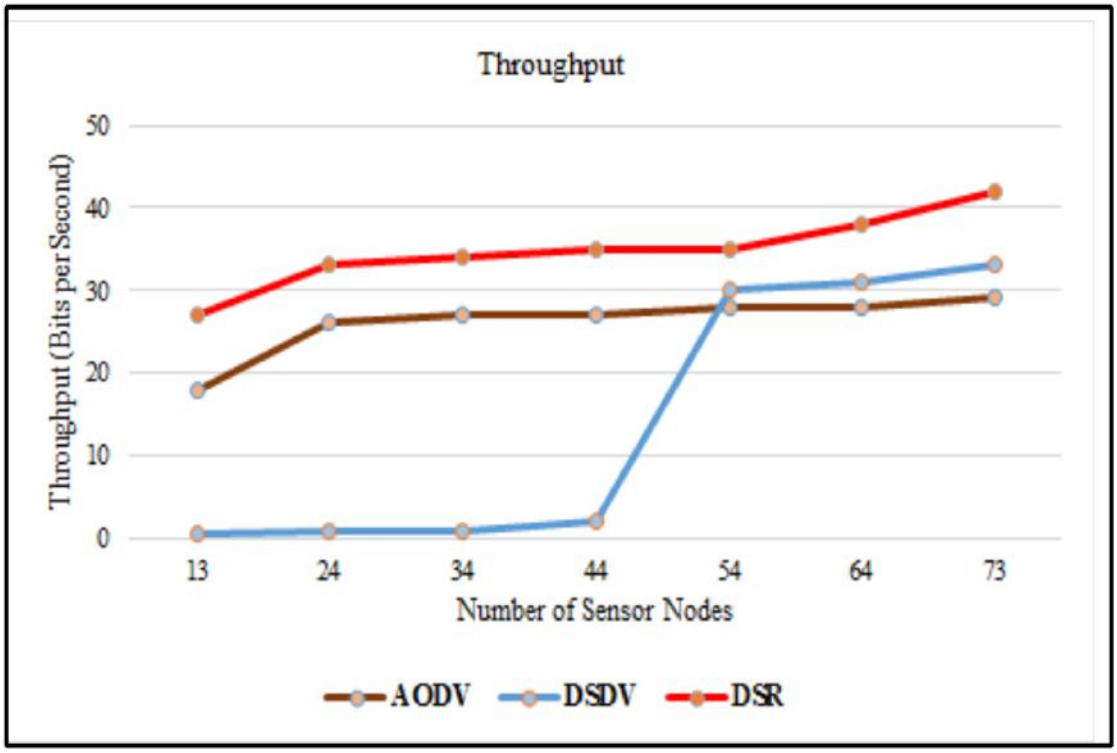

(c)

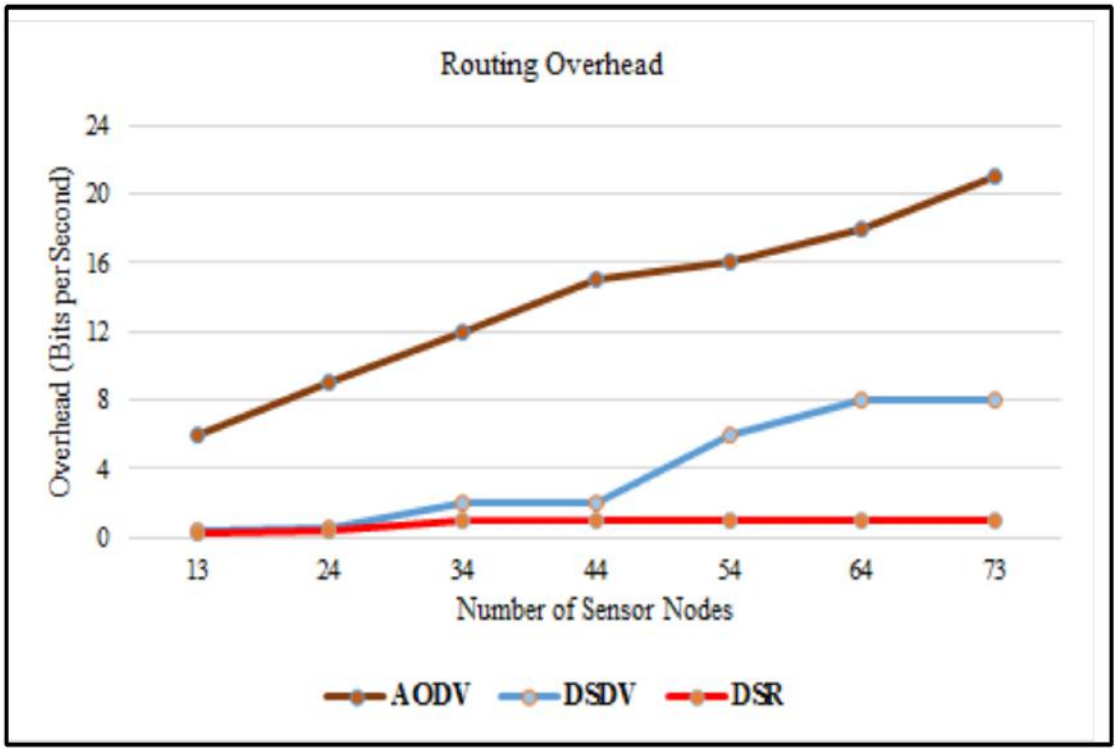

(d)

Figure 5.6: Comparison of Routing Protocols on Performance Metrics (a) Energy Consumption (b) Packet Delivery Ratio (c) Throughput (d) Routing Overhead

i. **Energy Consumption** Since energy consumption determines the energy level for both sensor and network, therefore, the energy of a node is considered to be full initially. Figure 5.6(a) depicts that energy consumption is increasing in case of *AODV* as soon as the number of sensors are increasing; *DSDV* consumes less energy and is changing consistently whereas *DSR* provides average consumption and is constant throughout. In regard to energy efficiency, *DSR* is well suited technique for *TPT*.

ii. **Packet Delivery Ratio** It indicates the number of packets' percentage delivered in unit time. From Figure 5.6(b), it is observed that *DSDV* is providing lowest packet delivery ratio with more packet losses within the path. The packet loss is due to attenuation and underwater currents. The *AODV* and *DSR* outperform well guaranteeing approximately 99 % delivery of packets and are independent of increasing number of sensors.

iii. **Throughput** It measures the total number of packets delivered successfully to destination. The graph in Figure 5.6(c) shows that the throughput of *DSDV* is degraded and is not satisfactory; whereas in comparison *AODV* performs well and *DSR* is providing best throughput with maximum data delivery to the surface station.

iv. **Routing Overhead** It is used to identify number of routed packets transmitted within the network and it is the overhead on the sensors which are accepting packets from its neighboring sensors. Figure 5.6(d) shows that there is maximum overhead of packets over *AODV* as it calls the neighboring sensors at once to route path for communicating data. The *DSDV* and *DSR* perform better than *AODV* and provide the best output and delivery with less overhead within the routing path.

From the results of simulation, it is observed that *DSR* is best routing for *TPT* providing best throughput, maximum packet delivery to surface station with no packet loss.

5.3 Experimental Results and Discussion

TPT is tested in Ganges River of Sutlej, Doraha, situated in Ludhiana region of India. The data is collected at different timings.

5.3.1 Study Area

The city of Ludhiana has wide industrial set-up located to nearby intensive irrigated plain at the banks of Sutlej river (*see* Figure 5.7). It has markets of agricultural products and manufacturing products that includes textile, leather goods, woods and sports products. The

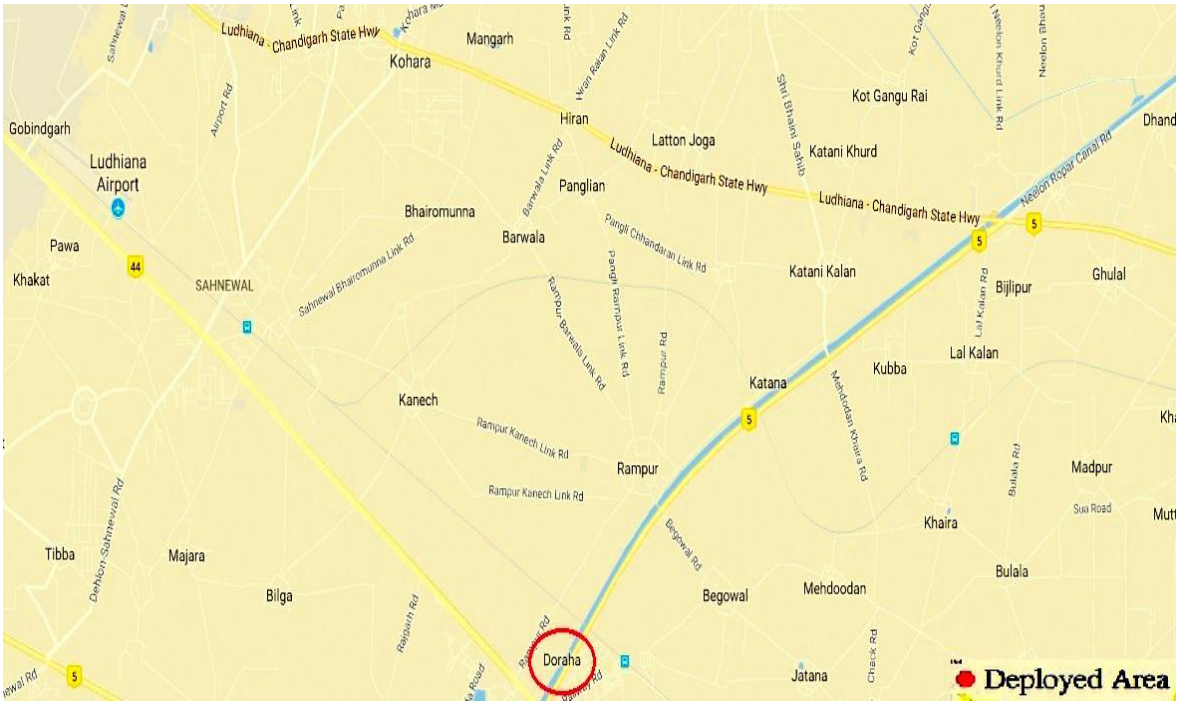

Figure 5.7: Deployment Area

manufacturing units' waste and city's domestic sewage are directly or indirectly discharged in the river at the outskirts of the city. It results into deterioration of quality of river water and should be monitored in order to take timely preventive measures.

5.3.2 Specifications Description

The various parameters of *TPT* considered in the testing are shown in Table 5.2. The S_{BoS} and S_{AS} are placed such that they stay under communication range and does not exceed 10-15 meters. The bandwidth is up to 25 *KHz*. Each data packet with the header is 532 bytes. The data value for physical parameters of water quality are shown in Table 5.3. The results are recorded for 3 months. At an instance, *TPT* is tested for 10 days. Afterwards, power cells are replaced with new batteries and is tested again.

Table 5.2: *TPT* Specifications

Specification	**Considered Value**
Bandwidth	25 KHz
Routing Protocol Implemented	DSR
Number of Sensors	11
Max. TX Distance	15 meters
Minimum Head Coverage Area	65 %
Maximum Head Coverage Area	85 %
Cell Power	2880 mAh

Table 5.3: Variables used to Estimate Water's Quality

Variables	**Prescribed Ranges**	**Calculating Method**
Electrical Conductivity (mg/l)	280-450	$EC(mg/l) = \frac{TDS\ (ppm)}{0.64}$
pH	7.0-7.9	$pH = -\log[H_3O^+]$
Temperature (°C)	20-28	$\Delta T = \frac{Q}{mc}$
Chloride (mg/l)	75-90	$NaCl + H_2O \longrightarrow Na^+ + Cl^- + H_2O$
Water Soluble Oxygen (Dissolved)	6-10	DO = Quantity of Treated Titrants

5.3.3 Measurements of Physical Parameters

The results of various physical parameters like *EC*, *pH*, Temperature, Chloride and *DO*, are observed and are discussed below.

EC is fully dependent on climate change or pollutants added. The various recorded values for *EC* are shown in graph 5.8 and Table 5.4. During the month of November (2016), *EC* lies among $350 - 423$ mg/l. This implies that there is no contamination in river water. In December (2016), *EC* is noted between $360 - 400$ (mg/l) showing the contamination to some extent due to more industrial disposal. In January (2017), *EC* ranges between $370 - 403$ (mg/l) which denotes that the river is contaminated to a major extent due to discharges of effluents from industries. This indicates a threat to river water with contamination.

Table 5.4: Electrical Conductivity (mg/l) (Nov '16, Dec '16 and Jan '17)

Days	Nov	Dec	Jan	Days	Nov	Dec	Jan	Days	Nov	Dec	Jan
1	389	372	383	12	421	399	397	23	410	400	381
2	378	374	385	13	375	391	401	24	362	394	379
3	403	388	391	14	407	389	403	25	387	399	382
4	422	362	394	15	355	385	396	26	385	390	381
5	389	370	388	16	400	391	395	27	380	392	377
6	401	368	392	17	360	389	392	28	367	400	374
7	378	379	396	18	389	381	388	29	360	398	372
8	423	374	402	19	375	387	385	30	352	394	371
9	358	381	397	20	409	392	381	31	-	387	372
10	370	379	400	21	405	394	384				
11	372	386	394	22	378	396	382				

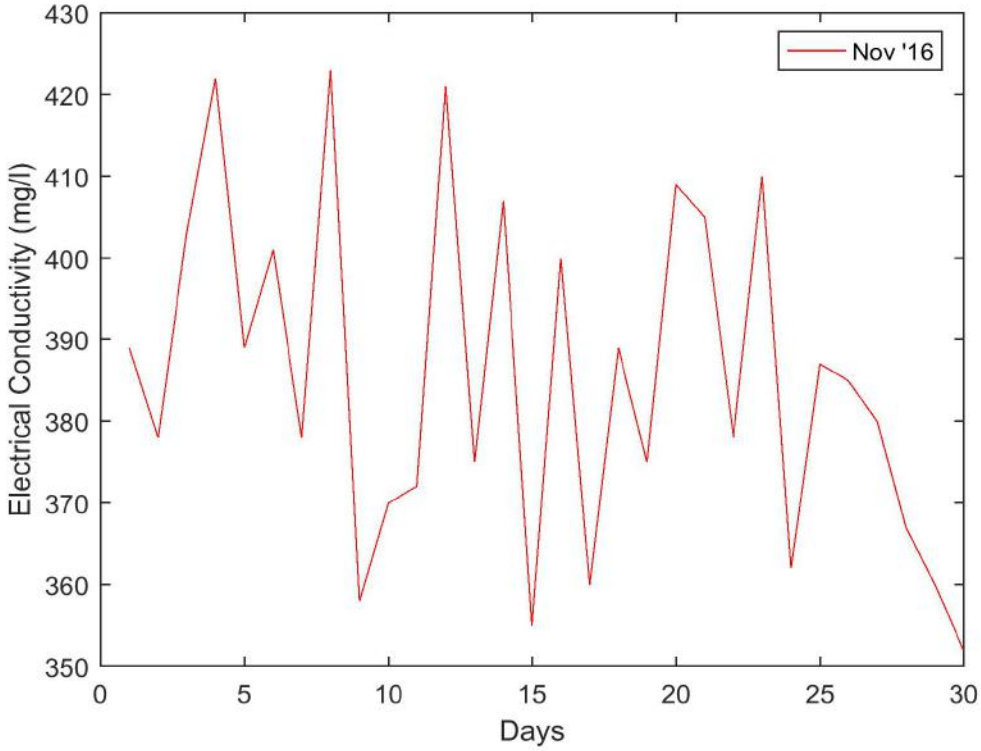

(a)

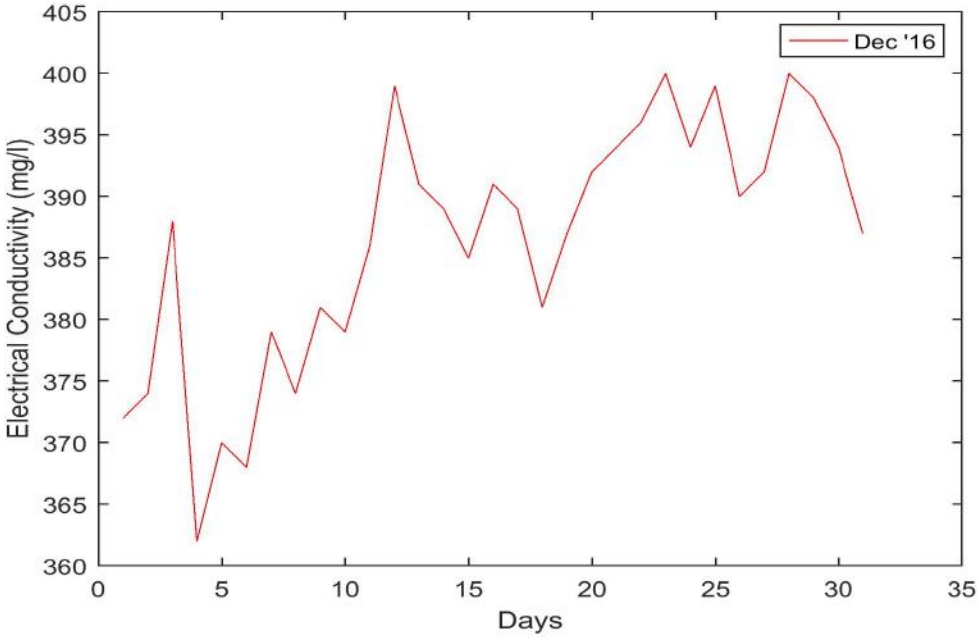

(b)

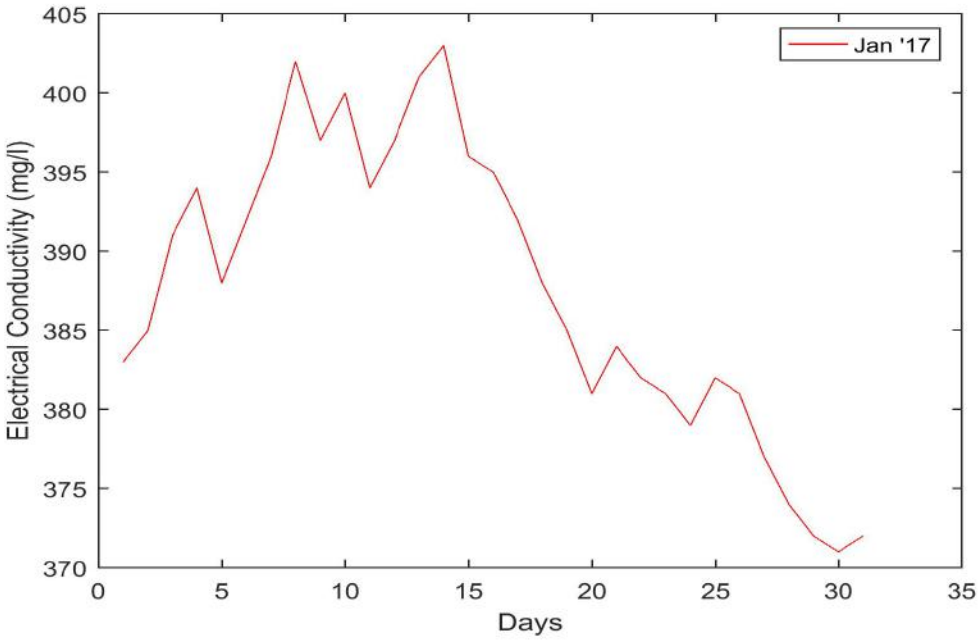

(c)

Figure 5.8: Electrical Conductivity Observations (a) Nov '16 (b) Dec '16 (c) Jan '17

pH describes the acidic or alkaline nature and it affects different organic processes. The observed data is represented in Table 5.5 and Figure 5.9. In November (2016), *pH* is varying between $7.5 - 8$ depicting that the *pH* level is under required level and is towards the lower

part of acidic nature. In December (2016), *pH* is varying from $7.6-8$ and is in the intermediate level under required aquatic conditions. In the month of January (2017), *pH* ranges maximum between $7.5-8$ and is at the highest level towards acidic nature. This shows that it would be more acidic and risk the life of flora and fauna.

Table 5.5: *pH* Data (Nov '16, Dec '16 and Jan '17)

Days	Nov	Dec	Jan	Days	Nov	Dec	Jan	Days	Nov	Dec	Jan
1	7.6	7.8	7.7	12	7.7	7.8	7.6	23	7.8	8	7.7
2	7.9	7.8	7.5	13	7.6	7.7	7.8	24	8	7.8	7.6
3	7.6	7.6	7.9	14	7.5	7.6	7.9	25	7.9	7.9	7.7
4	7.7	7.7	8	15	7.8	7.8	7.8	26	7.6	7.8	7.6
5	7.8	7.8	7.9	16	8	7.9	7.7	27	7.7	7.8	7.7
6	7.6	7.7	7.9	17	7.9	7.7	7.8	28	7.6	7.7	7.8
7	7.7	7.8	8	18	7.8	7.8	7.6	29	7.6	7.9	7.7
8	7.6	7.9	7.7	19	7.7	7.8	7.7	30	7.5	7.8	7.8
9	7.7	8	7.8	20	7.6	7.9	7.9	31	-	7.6	7.7
10	7.7	7.9	7.7	21	7.6	7.7	7.9				
11	7.8	7.9	7.8	22	7.7	7.9	7.8				

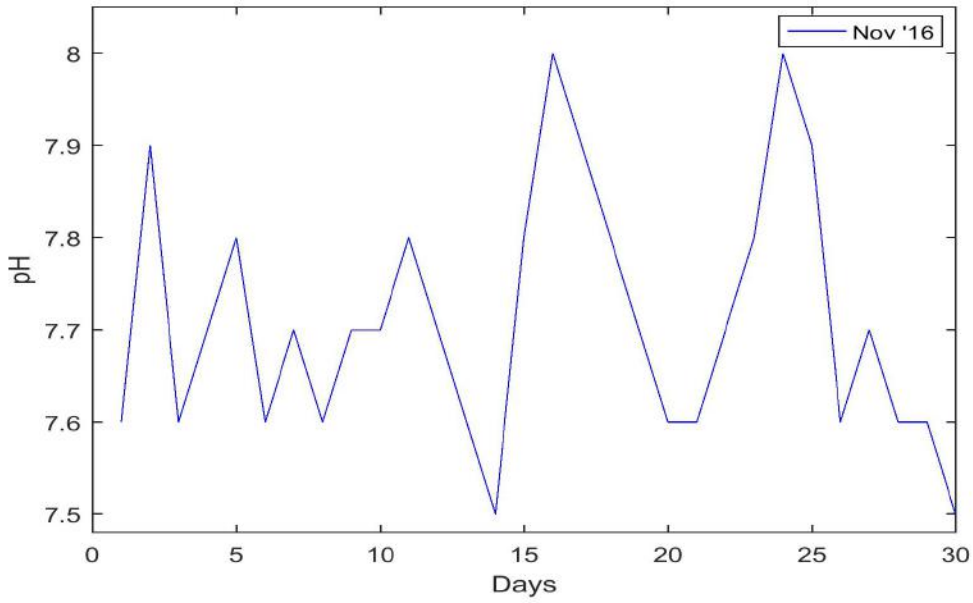

(a)

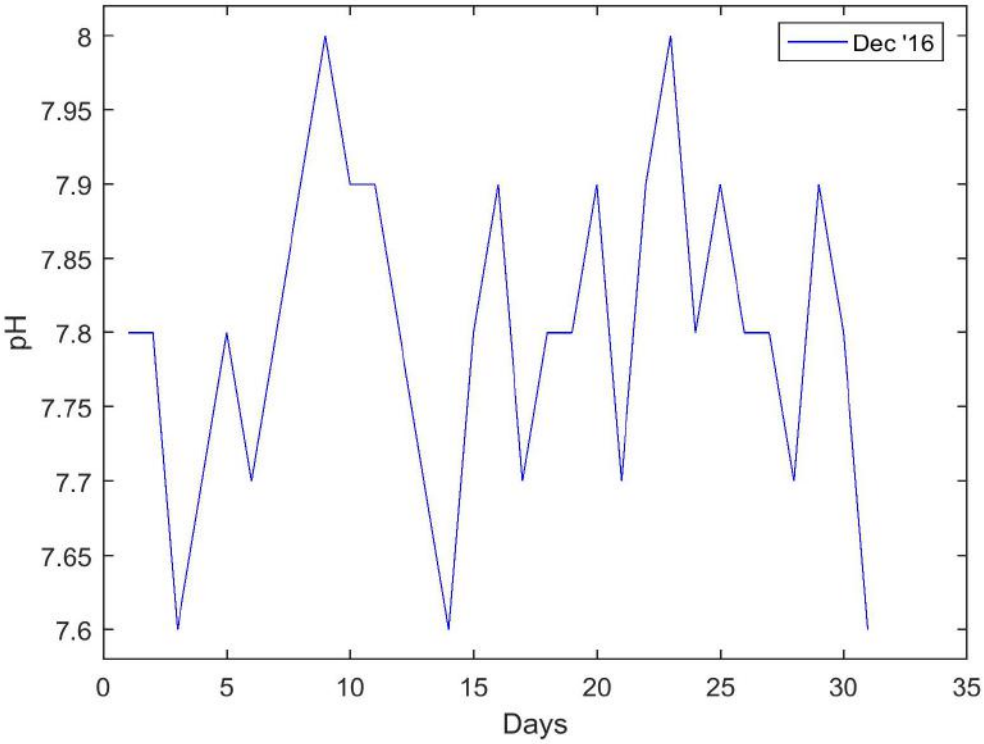

(b)

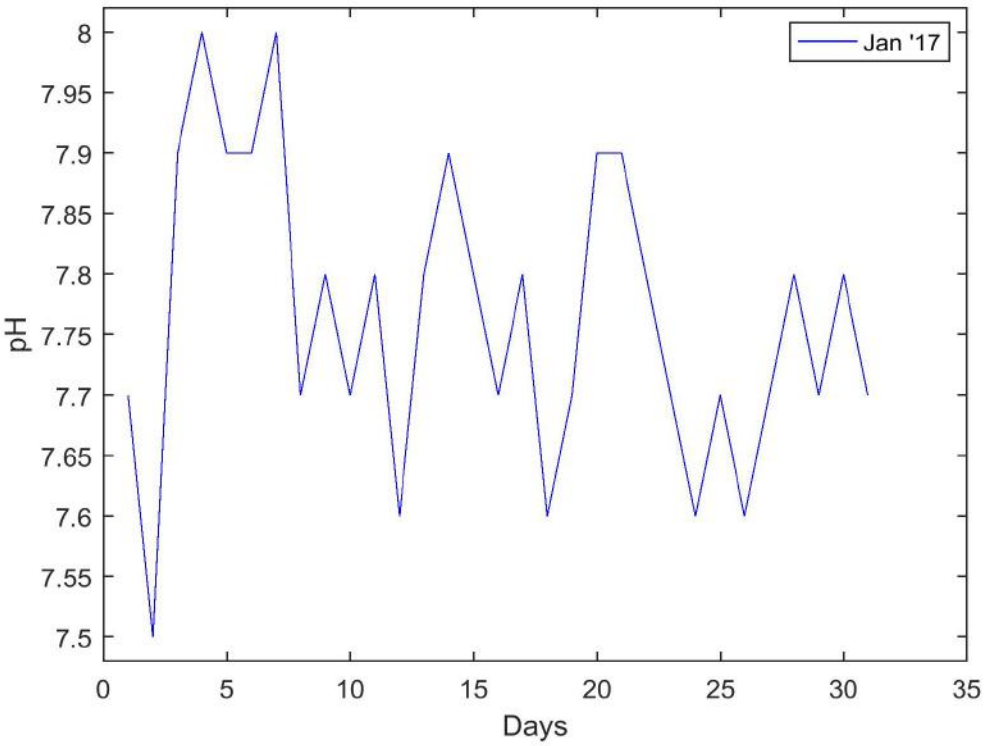

(c)

Figure 5.9: *pH* Observations (a) Nov '16 (b) Dec '16 (c) Jan '17

Temperature plays a vital role for chemical reactions underwater as its nominal range help in growth of organic beings in water. It is the measure of total amount of released or absorbed heat. The data is shown in Table 5.6 and Figure 5.10.

Table 5.6: Temperature (°C) Data (Nov '16, Dec '16 and Jan '17)

Days	Nov	Dec	Jan	Days	Nov	Dec	Jan	Days	Nov	Dec	Jan
1	22.6	27.2	28.4	12	26.4	27.5	29.4	23	26.7	27.3	29.5
2	21.1	27.3	28.3	13	26.3	27.4	29.2	24	27	27.4	29.2
3	21.4	27.4	28.2	14	27.2	27.4	29.3	25	27.1	27.7	29.3
4	22.3	27.4	28.3	15	27.1	27.3	29.2	26	26.9	28	29.1
5	25.1	27.3	28.5	16	27.2	27.5	29.5	27	27	28.2	29.2
6	27.1	27.2	28.2	17	26	27.3	29.5	28	27.1	28	29.1
7	26.5	27.3	28.5	18	26.2	27.6	29.6	29	27.2	28.1	29.3
8	26.8	27.4	28.6	19	26.4	27.5	29.4	30	27.2	28.3	29.4
9	26.2	27.2	29	20	26.4	27.6	29.3	31	-	28.4	29.2
10	26.1	27.5	29.3	21	26.5	27.7	29.1				
11	26.2	27.2	29.2	22	26.7	27.5	29.3				

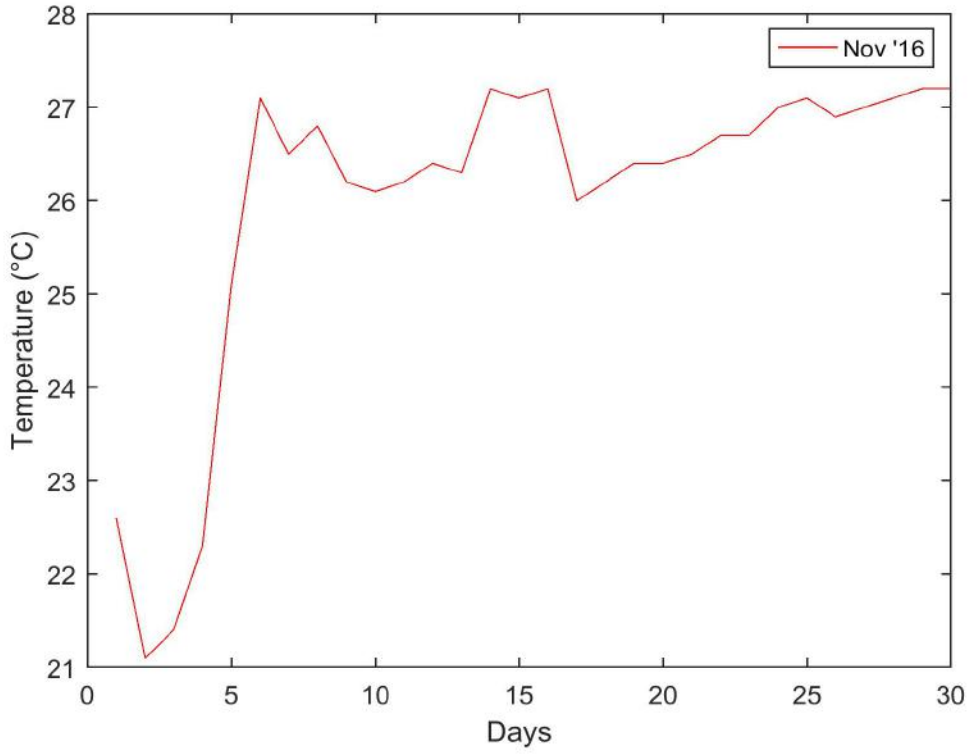

(a)

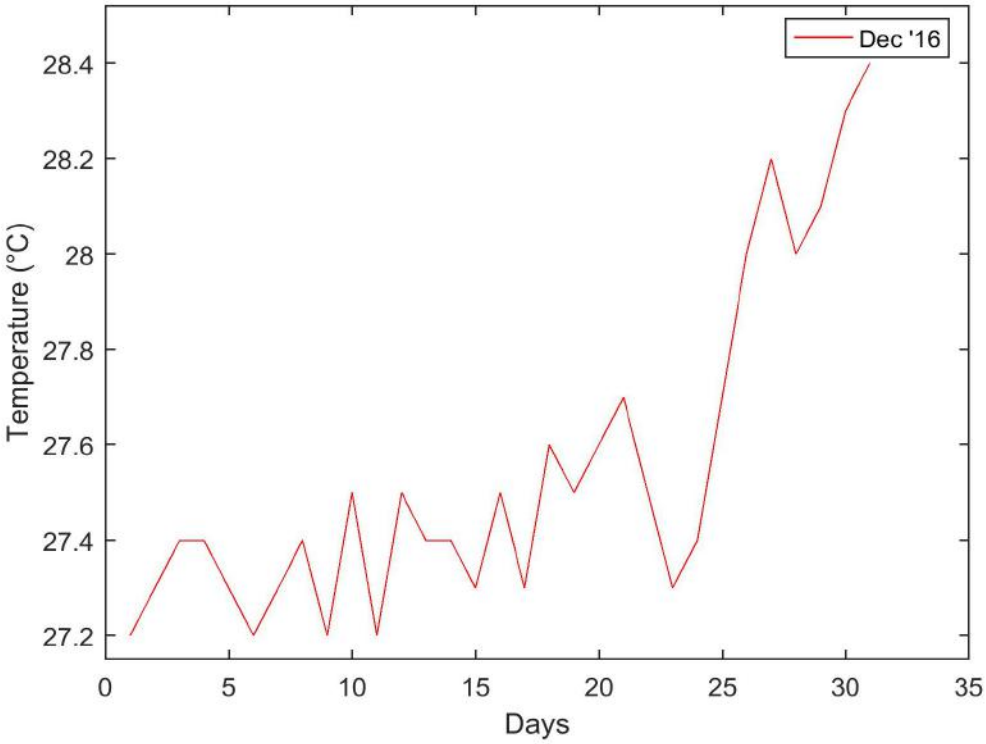

(b)

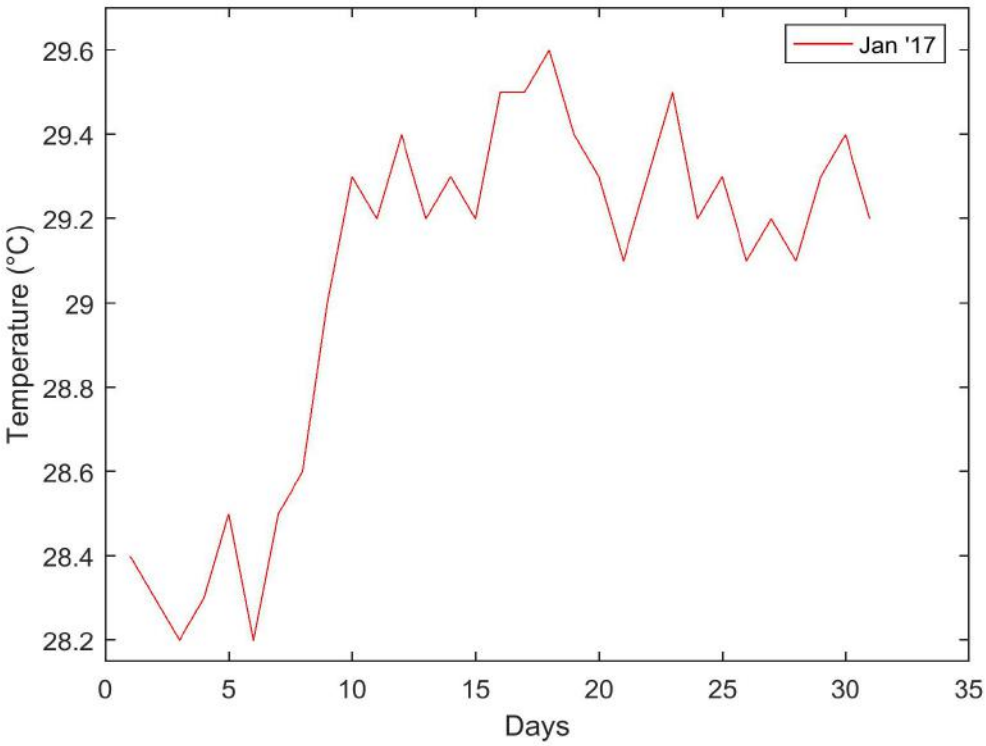

(c)

Figure 5.10: Temperature Observations (a) Nov '16 (b) Dec '16 (c) Jan '17

In November (2016), the temperature varies between $21-28$ (°C). It is the normal temperature of the river and is best suited for amphibians. In the month of December (2016), the temperature varies between $27-29$ (°C) denoting the change in temperature due to climatic change. In January (2017), it has increased range from $28-30$ (°C). This tells that the temperature affects photosynthetic process which has a negative impact on the living of flora and fauna to some extent.

Chloride is a measure of salinity in water and its high consolidation proves a risk to amphibians for its growth. The data is depicted by Table 5.7 and Figure 5.11. In November (2016), the chloride is noted between 72 mg/l $-$ 99 mg/l and is denoting the less quantity of saline water. This water is fit for domestic purposes. In December (2016), chloride has range of $74-97$ (mg/l). This shows the rise of saline level in water making it unfit for domestic use. In January (2017), chloride noted, is ranged between $81-90$ (mg/l) having normal values of salinity due to rainfall and hence, suitable for drinking.

Table 5.7: Chloride (mg/l) Data (Nov '16, Dec '16 and Jan '17)

Days	Nov	Dec	Jan	Days	Nov	Dec	Jan	Days	Nov	Dec	Jan
1	97.3	87.3	89.1	12	78.8	83.3	83.2	23	79.8	94.1	88.5
2	98.5	82.3	87.5	13	77.4	84	82.9	24	80.2	95.3	87.1
3	82.3	79.3	87.1	14	75.8	85.2	81.2	25	80.9	96.4	86.4
4	78.3	77.4	86.6	15	75.4	86.2	82.1	26	82.1	96.6	85.8
5	82.5	78	86	16	74.7	87.4	84.5	27	83	94.9	85
6	85.1	74.9	85	17	76.9	88.4	84.9	28	85.3	94.2	84.5
7	84	74.4	84.9	18	74.4	89.1	86	29	86.1	93	84.2
8	80.9	76.2	84.3	19	73.3	89.4	86.4	30	87.3	92.2	83.4
9	79.8	77.3	83.8	20	72.2	90.7	86.3	31	-	90.8	83.7
10	82.9	79.8	83.5	21	74.3	92.2	87.5				
11	82.1	80.9	83.6	22	78.4	92.6	88				

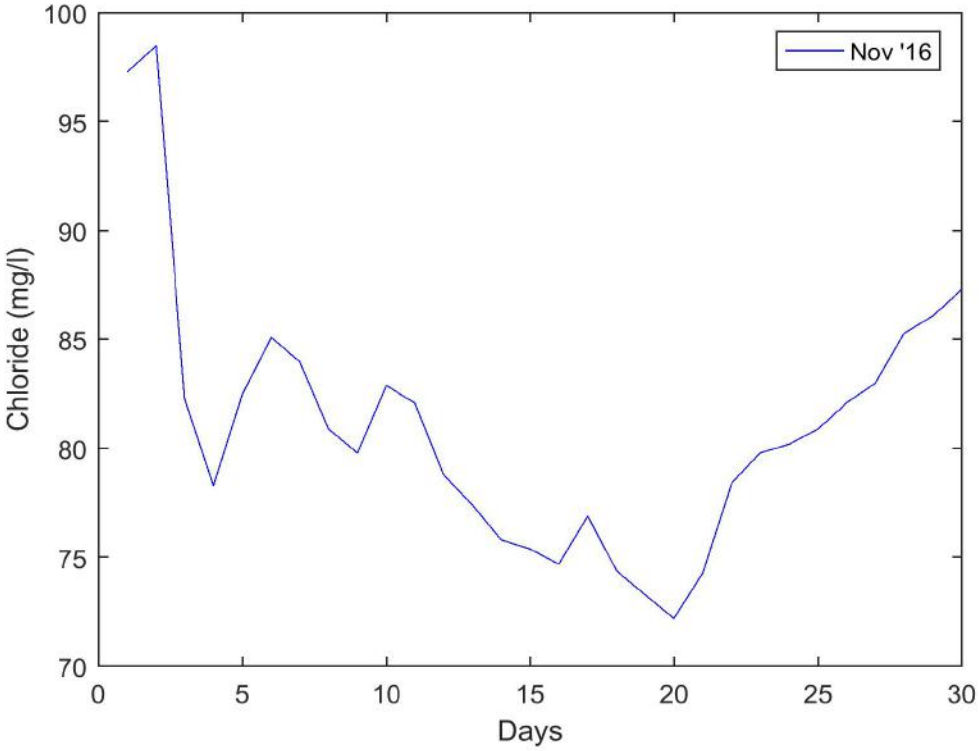
Nov '16
Chloride (mg/l)
Days
100
95
90
85
80
75
70
0
5
10
15
20
25
30

(a)

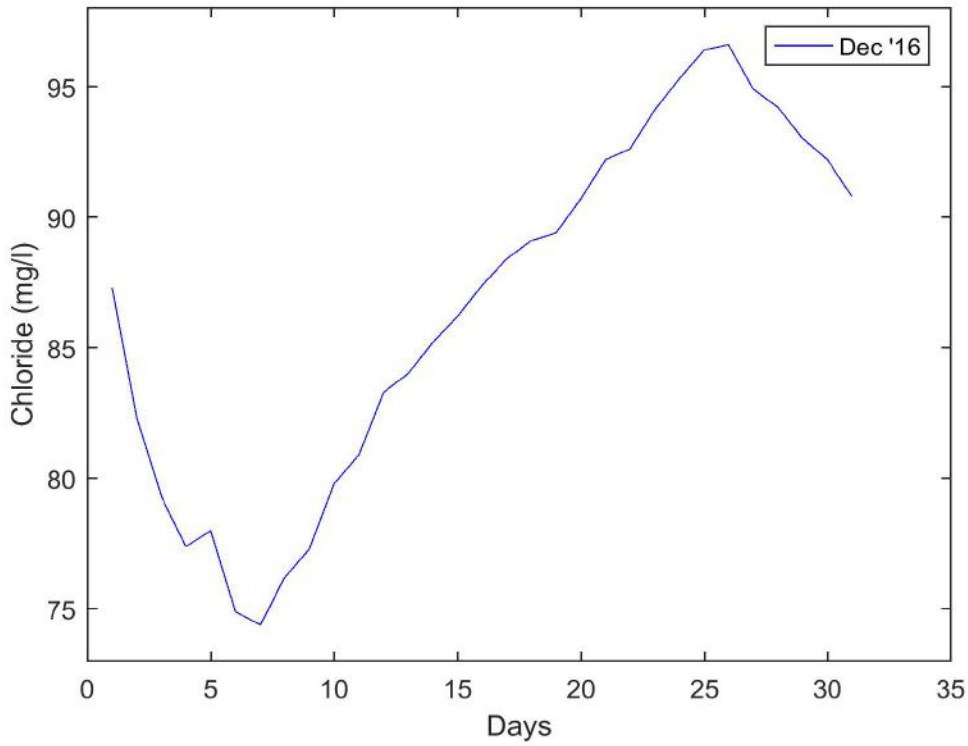
Dec '16
Chloride (mg/l)
Days
95
90
85
80
75
0
5
10
15
20
25
30
35

(b)

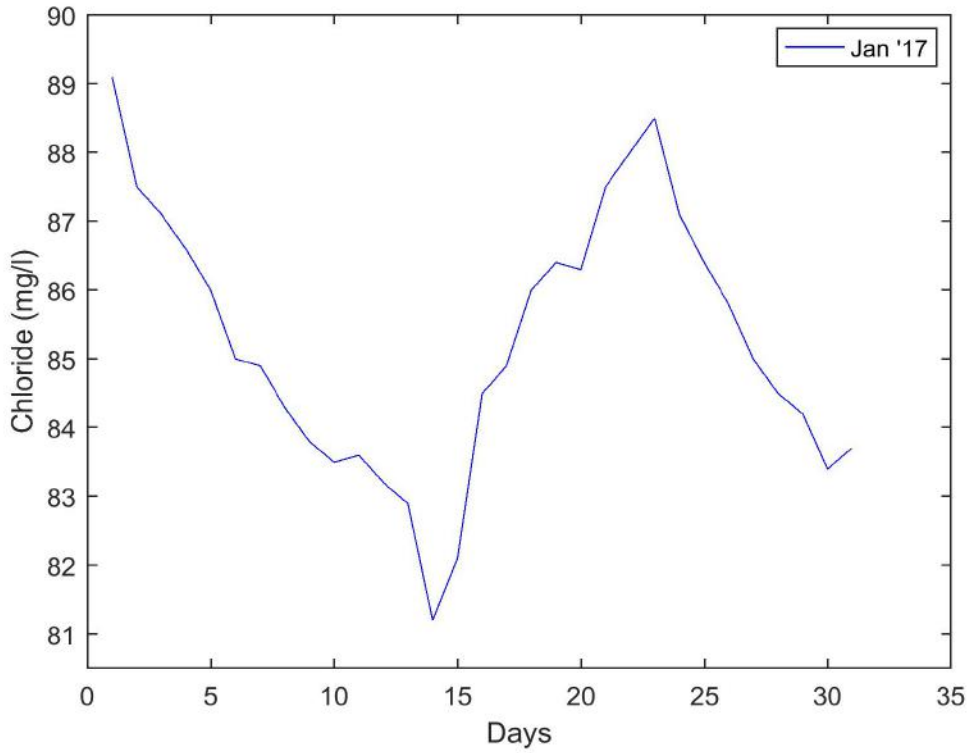

(c)

Figure 5.11: Measured Chloride Observations (a) Nov '16 (b) Dec '16 (c) Jan '17

Table 5.8: Dissolved Oxygen (mg/l) (Nov '16, Dec '16 and Jan '17)

Days	Nov	Dec	Jan	Days	Nov	Dec	Jan	Days	Nov	Dec	Jan
1	9.1	8.4	7.9	12	8.6	8.1	7.7	23	8.5	8.3	7.7
2	9.9	8.3	7.9	13	8.6	8.2	7.6	24	8.2	8.2	7.8
3	9.8	8.2	7.8	14	8.5	8	7.6	25	8.4	8.2	7.7
4	9.5	8.2	7.9	15	8.6	8.2	7.8	26	8.3	8	7.6
5	8.8	8.3	7.6	16	8.5	8	7.6	27	8.2	7.9	7.7
6	8.5	8.3	8	17	8.4	8	7.7	28	8.2	7.9	7.6
7	8.6	8.3	7.9	18	8.3	8.1	7.7	29	8.3	8	7.6
8	8.5	8.2	7.7	19	8.7	8	7.6	30	8.1	7.9	7.7
9	8.6	8.1	7.7	20	8.7	8.1	7.5	31	-	7.8	7.8
10	8.7	8.2	7.6	21	8.5	7.8	7.6				
11	8.6	8	7.7	22	8.3	7.9	7.8				

DO is the important element for respiration processes of flora and fauna. It is the water soluble oxygen that helps for phtosynthesis processes as well for aquatic plants in the absence of sunlight. The observed values are shown in Table 5.8 and Figure 5.12.

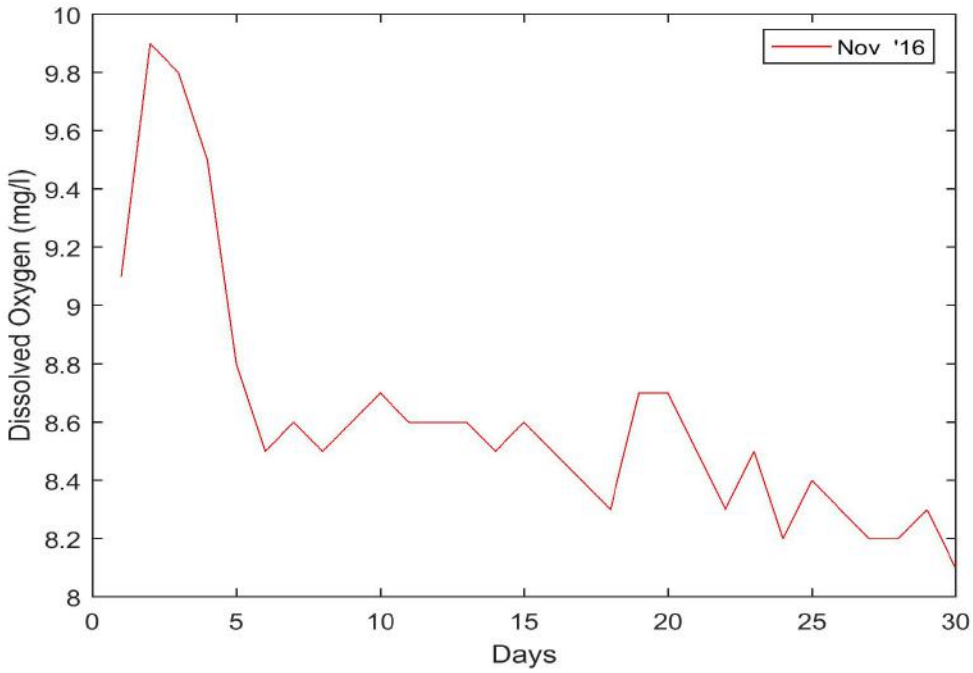

(a)

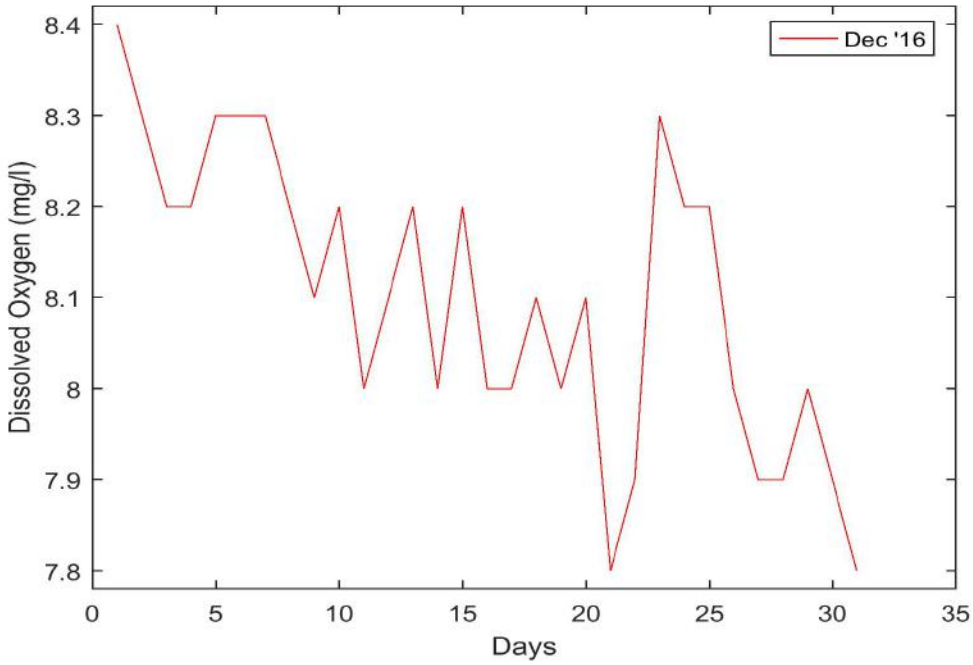

(b)

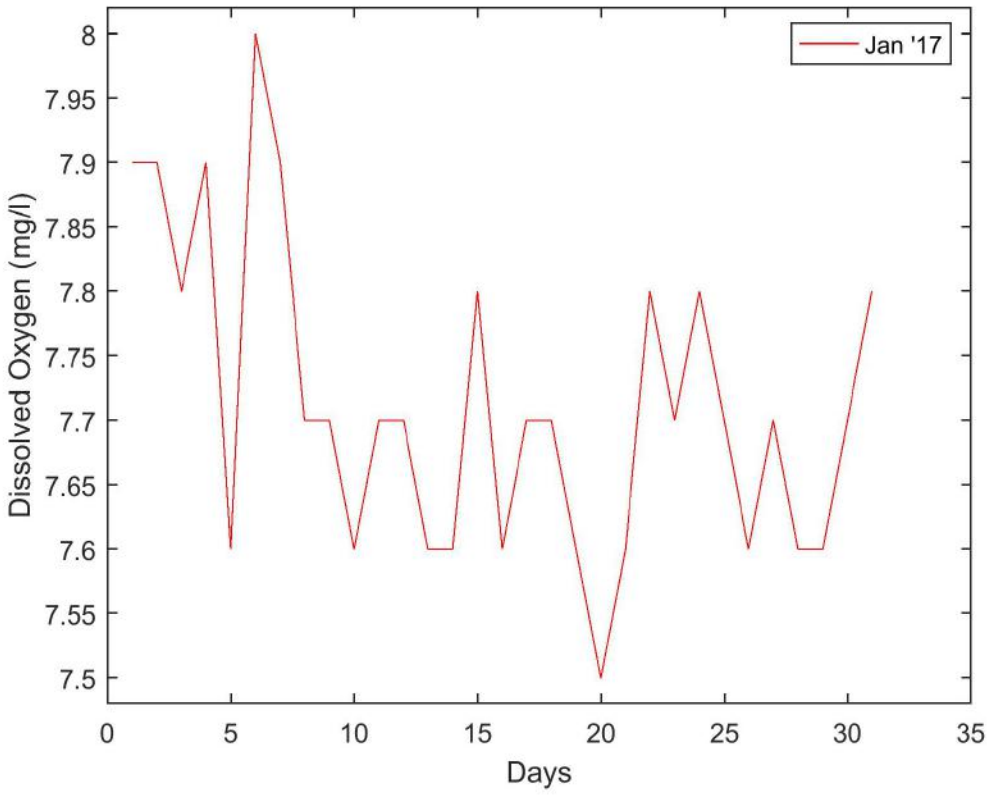

(c)

Figure 5.12: Dissolved Oxygen Observations (a) Nov '16 (b) Dec '16 (c) Jan '17

In November (2016), the *DO* is sensed between $8.1 - 9.9$ (mg/l). It is perfect solvent for amphibians. The decreased *DO* in graph is due to the addition of chemicals in river water. In December (2016), the *DO* is sensed between $7.8 - 8.4$ (mg/l). This abrupt fall in *DO* denotes the fear for living organisms in the river as it would adversely affect their lives. In the month of January (2017), *DO* thus obtained is ranged between $7.5 - 8$ (mg/l). The drastic decrease in *DO* level makes it unacceptable for growth of amphibians.

5.3.4 Comparison with Existing Sampling Technique

The existing technique of observing water quality involves sampling technique. Here, partitions (samples) of water are collected from different key locations with varying time zones manually and are further analyzed with lab equipments, which is time consuming process. Moreover, the exact percentage of chemical is not mixed for analyzing samples leading to

falsified results of varying values. Also, the equipments used are costly and need maintenance (Jindal and Sharma (2011)). In comparison, *TPT* provides on the spot measurement of physical parameters using *MPS*. Also, it helps to send gathered data to surface for deep analysis providing fast, efficient technique for analyzing realistic values. The physical parameters are analyzed on the basis of contamination using existing sampling and *TPT*. The comparison of the observed data from both techniques is described in Table 5.9 and Figure 5.13.

Table 5.9: Comparison among Water Quality Parameters

Water Quality Parameters	**Date(Month-Year)**	**Sampling Technique**	***TPT* Technique**
Conductivity (mg/l)	November 2016	427.63	385.33
	December 2016	480.45	386.48
	January 2017	499.12	387.58
pH	November 2016	7.7	7.45
	December 2016	8.1	7.54
	January 2017	7.78	7.51
Temperature (°C)	November 2016	29	26
	December 2016	28	27.55
	January 2017	27	29.05
Chloride (mg/l)	November 2016	92	81
	December 2016	94	86.57
	January 2017	89	85.25
Dissolved Oxygen (mg/l)	November 2016	7.5	8.61
	December 2016	7.9	8.1
	January 2017	7.2	7.71

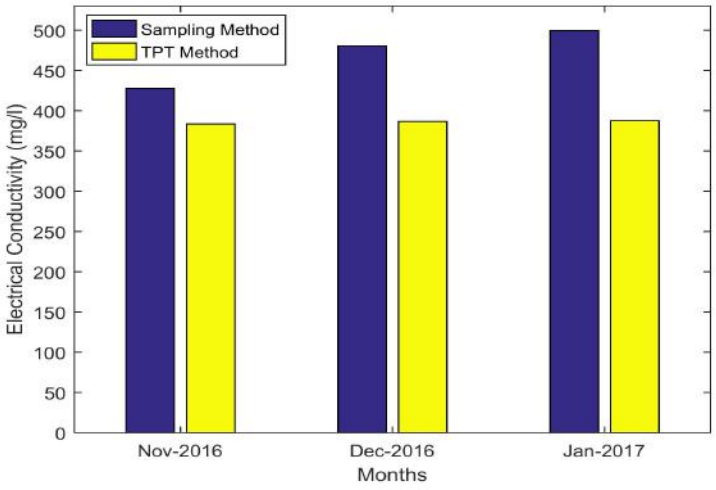
Sampling Method
TPT Method
Electrical Conductivity (mg/l)
0
50
100
150
200
250
300
350
400
450
500
Nov-2016
Dec-2016
Jan-2017
Months

(a)

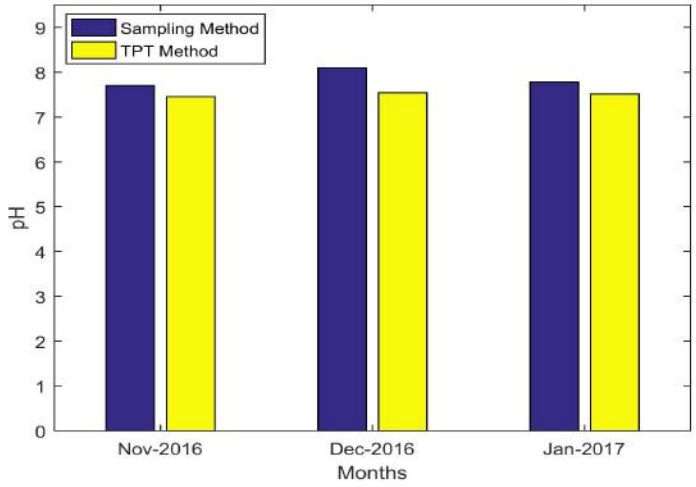
Sampling Method
TPT Method
pH
0
1
2
3
4
5
6
7
8
9
Nov-2016
Dec-2016
Jan-2017
Months

(b)

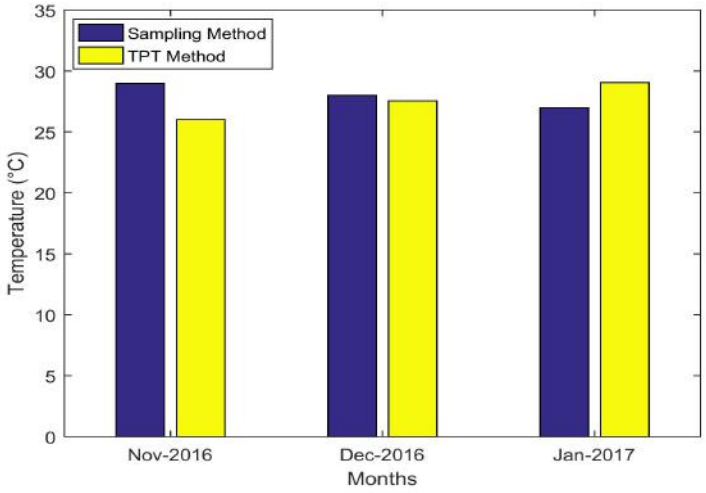
Sampling Method
TPT Method
Temperature (°C)
0
5
10
15
20
25
30
35
Nov-2016
Dec-2016
Jan-2017
Months

(c)

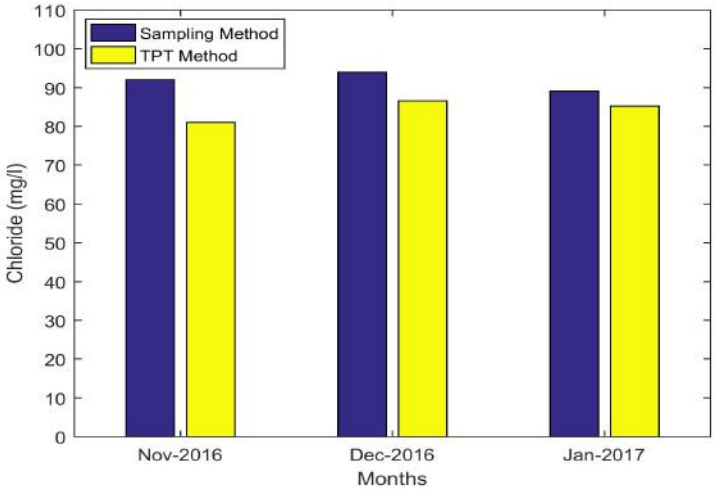

(d)

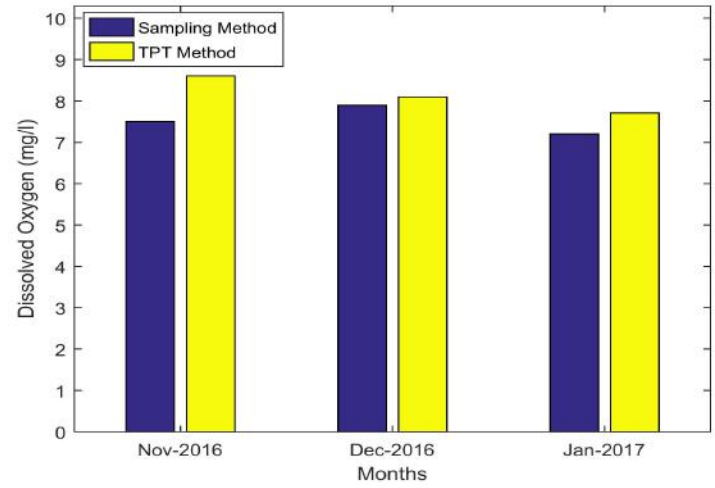

(e)

Figure 5.13: Comparison among Observed Values of Water Quality Parameters (a) *EC* (b) *pH* (c) Temperature (d) Chloride (e) *DO*

The gathered data of sampling gives alternating data values of physical parameters as compared with gathered data by *TPT*. It is due to the addition of varying amounts of effluents in water that lead to contaminate water in spite of purifying it. On the other hand, *TPT* provides descriptive results in order to have timely alarms of contaminated water with suitable preventive measurements. Therefore, it is observed that *TPT* works well and can also be used for monitoring lakes, ponds, *etc.*; to certain depth.

5.4 Conclusion

TPT is an hybrid extension to *MPST* deployment. It targets to achieve maximum coverage of deployed region considering transmission and detection ranges of *MPS*. It provides updated routing information and guarantees to deliver approximately 99 % sensed data to surface station using *DSR* protocol. It works well within the depth of 10-15 meters and provides 17.6, 5.4, 18.5, 8.76, 8.10 (in %) accurate estimation of sensing physical parameters such as conductivity, *pH*, temperature, measure of salinity (chloride) and water oxygen (dissolved), respectively, in comparison with sampling technique. Thus, it is an extensible and beneficial technique of river monitoring.

Chapter 6

Hybrid-OFDM based Panoramic Image Transmission and Refinement using Mosaicing

6.1 Introduction

The underwater through sea, oceans, rivers and lakes facilitates world with vital assets like natural resources, minerals, gas, petroleum and oil. Since, these assets promote economy of most countries, therefore, it is required to maintain and protect them. For the purpose, *UWASN* are used, which explore and extract the resources belonging to hostile environment. The applications for *UWASN* are prudent in surveillance scattering, data collection, undersea reconnaissance, pollution monitoring, reinforced navigation, tremorous monitoring, environment and pipeline monitoring. Among these applications, pipeline monitoring, being one of the important factors for economy growth; is yet to be explored. The pipeline monitoring tasks include measuring thickness of pipes, measuring velocity of oil or gas, leakages in pipes, corrosion or presence of algae blooms at joints of pipes[1].

The methodology of monitoring and finding leakages in pipes is accomplished using image sensors in *UWSN* in collaboration with various communication techniques, but they

[1]The contents are published in Jindal, H., Kasana, S. S. and Saxena, S. (2017), "Underwater pipelines panoramic image transmission and refinement using acoustic sensors", *International Journal of Wavelets, Multiresolution and Information Processing*, pp. 1850013, https://doi.org/10.1142/S0219691318500133

face limitations like time consumption, color variations, blurred data, bit or data losses. To overcome the limitations, a Panoramic Image Transmission and Refinement Technique is proposed. It uses *MPS* for image capturing, *Hybrid-OFDM* for transmitting sensed images to surface station and refines images using mosaicing. The obtained results support technique's efficiency with respect to transmission of pipeline data to surface station in short span of time. Further, the technique helps in providing better visualization of faulty regions of pipelines with complete description.

6.2 Panoramic Image Transmission and Refinement Technique

In this section, Panoramic Image Transmission and Refinement technique is discussed. It works through three phases. These phases are explained.

i. **Image Capturing Phase:** This phase deals with the image capturing using *MPS* having a camera embedded on its motherboard (*see* Figure 6.1). *MPS* is deployed tem-

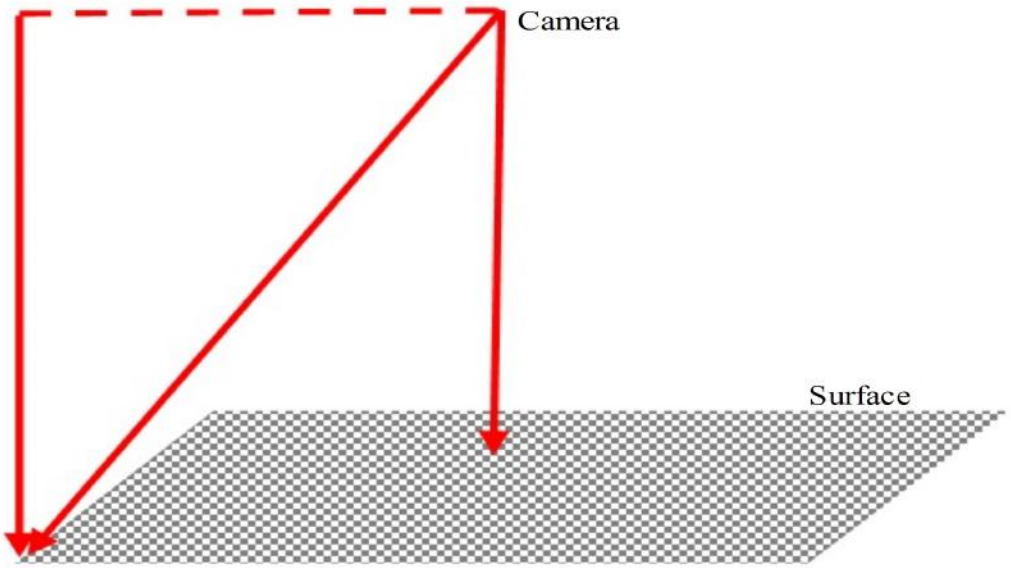

Figure 6.1: Panoramic Image Capturing Process

porarily at the joints of pipelines and is placed within a distance to communicate with surface station *via* angular acoustic waves.

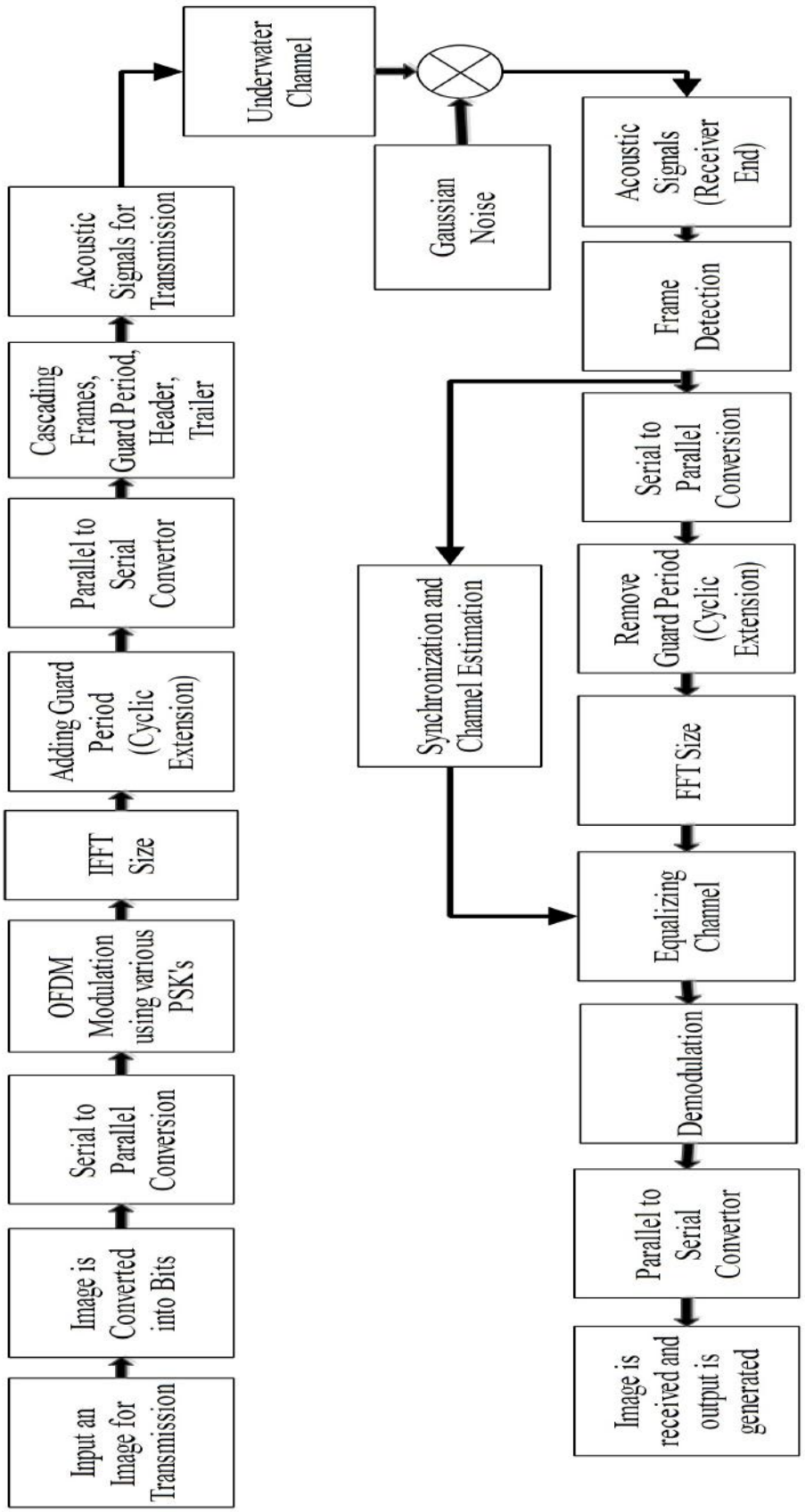

Figure 6.2: *Hybrid-OFDM*

ii. **Transmitter and Receiver Phase:** In the second phase, *Hybrid-OFDM* is proposed. It uses various modulation schemes *(PSK)* for faster transmission. It converts pixels of captured images in to bits and linked symbols. These bits are followed with guard period and *IFFT*. These bits are transmitted and received acoustically using Gaussian function. This function is used to normally distribute bits among transmitted symbols. The block diagram of *Hybrid-OFDM* is shown in Figure 6.2.

The working of *Hybrid-OFDM* is divided into two steps , *i.e.*, transmitter and receiver, explained as under.

(a) ***Hybrid-OFDM* Transmitter:** The transmission of image is processed using following steps.

- **Source:** The process begins with the input of an image which is converted in to bits.
- **Serial to Parallel Conversion:** Each linked symbol transmits 40-4000 bits, therefore, there is need for serial to parallel conversion in order to convert input image data for each symbol. The bits allocated to each symbol depend on number of sub-carriers.
- **Modulation:** The process maps bit-chunks and imaginary constellation (*IFFT* bits), using modulation schemes. The modulation helps to describe bits in symbol.
- **IFFT:** It converts symbol into time domain to allow transmission of image data.
- **Guard Period:** Guard periods are added in each symbol such that bits in one symbol is not able to interfere with each other. It eradicates problem of *ICI* by cyclically extending itself and ensuring integral number of cycles within *FFT* interval.
- **Parallel to Serial Converter:** Here, bits are converted back to serial for easier transmission.
- **Cascading:** The serial bit frames are cascaded with guard period, header and trailer to bind the data for transmission.

- **Channel:** The underwater channel is affected by noise on the receiver end which is characterized as additive Gaussian Process *(GP)*. *GP* has multivariate normal distribution and decomposes noise into a sum of low-dimensional functions. It has mean *zero* and its standard deviation (σ) is given by Eq. 6.1.

$$\sigma_{GP}(dB) = \sqrt{\frac{Variance\ of\ Acoustic\ Signal}{Noise}} \tag{6.1}$$

(b) ***Hybrid-OFDM* Receiver:** The signal is received in encoded form which is to be decoded to form original image. The steps of decoding at receiver end are described.

- **Serial to Parallel Conversion:** The received frame is rearranged into parallel block. The detected frames are forwarded to remove guard periods from them.
- **Guard Period Removal:** Here, cyclic prefixes are removed from each frame to reduce *ISI*.
- ***FFT*:** *FFT* is used to map frequency domain data from frames to bits. Therefore, amplitude and phase are estimated using *FFT*.
- **Equalizing Bits:** The equalization is provided in order to select the correct bits.
- **Demodulation:** The demodulation of text and image is done simultaneously. The demodulated text is converted into American Standard Code for Information Interchange *(ASCII)* sequence.
- **Parallel to Serial Conversion:** It separates pixels and rearrange parallel data into serial binary stream forming an output.

Thus, the processed output is a gray image at surface station.

The working of *Hybrid-OFDM* based transmission is explained in Algorithm 6.1.

Algorithm 6.1 *Hybrid-OFDM* Algorithm

Require: Image as input (B), row data (h), column data (w), bits or symbol data $(Basetx)$, total size of bits $(carrierct)$, frequency (fr), carrier of symbols $(symblcarrier)$, frame of symbols $(symblframe)$, power (pwr), length of frame $(framelen)$, data of frame $(framedata)$, modulation time $(Timetx)$, channel noise (SNR), total frame count $(numframe)$ and received image $(B1)$

//*Hybrid-OFDM* Transmission
initialize $B \longleftarrow input(image)$
for (i = 1 to m) **do**
  for (j = 1 to n) **do**
    $h = size(B,1)$ //arranging row data
    $w = size(B,2)$ //arranging column data
    $B = reshape(B',1,h \times w)$ //receiving the image with equal size of pixels in rows and columns
    $Basetx = double(B)$ //storing bits data
  end for
end for
$Basetx = Base_{convert}(Basetx)$ //converting bits data to symbol data
$carrierct = size(Basetx)$
initialize $fr = 0.25$ and $ifftsize = 8$
initialize $frguard \longleftarrow zeroes(1,fr)$
$symblcarrier = ceil(len(Basetx)/carrierct)$
if (symblcarrier $>$ symblframe) **then** //multiple-frame
  initialize $pwr \longleftarrow 0$ //power
  while (Basetx != -1) **do**
    //calculating number of symbols per frame
    calculate $framelen = min(symblframe * carrierct, Basetx)$
    calculate $framedata = Basetx(1 : framelen)$
    update $Basetx$
    $Timetx = OFDMModulate(framedata, ifftsize, carrierct, symblcarrier, Basetx)$
//selecting various OFDM techniques to send data to surface station
    $framepwr = variance(Timetx)$
  end while
  $pwr = pwr + framepwr$ //energy calculation
  print pwr, $Basetx$
end if

calculate $SNR(Timetx, Basetx)$ //channel noise
print SNR
***//Hybrid-OFDM* Receiver**
initialize $Timetx1 = Timetx'$
initialize $start = 1$, $end = Timetx1$, $data = [.]$
if $(removal(w \times h, carrierct)! = 0)$ **then**
    $B1 = carrierct - removal(w \times h, carrierct)$
end if
$numframe = ((h \times w) \times (wordsize)) / (symblframe \times carrierct)$
for (i = 1 to numframe) **do**
    $Timetx2 = Timetx1(start, end) \times (head + symblframe + 1)$
    $B1 = OFDMframe(Timetx2, symblframe, start)$ //demodulating data
end for
print $OFDMframe$, $Timetx2$
display $B1$

During transmission, the *Hybrid-OFDM* at an instance, takes an image as input in B. It calculates its pixels into rows *(h)* and columns *(w)*. The image is reshaped by re-arranging pixels into square matrix ($m \times n$). Its pixel's data is converted into bits and is stored symbols, *Basetx*. A counter is set with maximum value of size *Basetx* and is stored in total size of bits, *carrierct*. The frequency (fr) and $IFFT$ size are initialized at 0.25 and 8, respectively. A condition is checked for multiple frames, and power (*pwr*) is initialized to *zero*. The loop is described for selecting the symbol data and to put all the symbols into the frame, *i.e.*, $framedata$. The *OFDM* modulates the $framedata, IFFTsize, carrierct$ and *Basetx* into one complete set, and is stored in *Timetx*. The *Timetx* is normalized and updated in $framepwr$. With respect to modulation, total energy consumption (*pwr*) is calculated and is displayed. The channel noise (*SNR*) during transmission is also selected manually as 15 or 30 for the process. Here, the image symbol data is transmitted to surface station. The demodulation is processed to obtain the image using inverse of modulation. Demodulation removes *carrierct* from the matrix and converts symbols into bits. The conversion output is stored in $numframe$ which selects each frame of bits and modulated them to generate

an image. Finally, the demodulated image is displayed at surface station.

iii. **Refinement Phase:** In the third phase, the images received at surface station are not providing satisfactory results as these images got affected by noise while transmitting the data producing blurred or erred pixels' images. Therefore, in order to refine these images, mosaicing algorithm is proposed. Mosaicing helps to combine gathered images, and to provide the better visualization of the faulty captured regions by generating panoramic images. It involves steps of feature extraction, merging two images (stitching) and blending. These steps are described as under.

- **Feature Extraction and Registration:** For detecting key-points and locations from images, Scale Invariant Feature Transform *(SIFT)* is used. *SIFT* usually finds for stationary pixels in all presumable directions. Its operation follows four steps as construction of directions (scale) space, tracing the extrema, orientation and describing key-points. At first instance, construction of scale space is done using Gaussian filtering with changing scales. The scales are then grouped together to form output into octaves. Grouping of scales is given by Eq. 6.2.

$$Loc(L,M,\varphi) = G_f(L,M,\varphi) \times Im(L,M) \tag{6.2}$$

where, $Loc(L,M,\varphi)$ is scale space construction, $G_f(L,M,\varphi)$ is Gaussian filtering having scale 'φ' and $Im(L,M)$ is an input image. David G. Lowe proposed Difference of Gaussian function *(DoG)* (Lowe (2004)), to detect stable key-points in scale efficiently, given by Eq. 6.3.

$$\begin{aligned} DoG(L,M,\varphi) = (G_f(L,M,Z\times\varphi) - G_f(L,M,\varphi)) \\ \times Im(L,M) = Loc(L,M,Z\times\varphi) - Loc(L,M,\varphi) \end{aligned} \tag{6.3}$$

The function is used to compute adjacent Gaussian-blurred image in each octave. *DoG* has strong response along edges and key-points are identified (as local extrema) along scales. It is shown in Figure 6.3.

In key-point localization, less colored pixels and distorted edges along scales

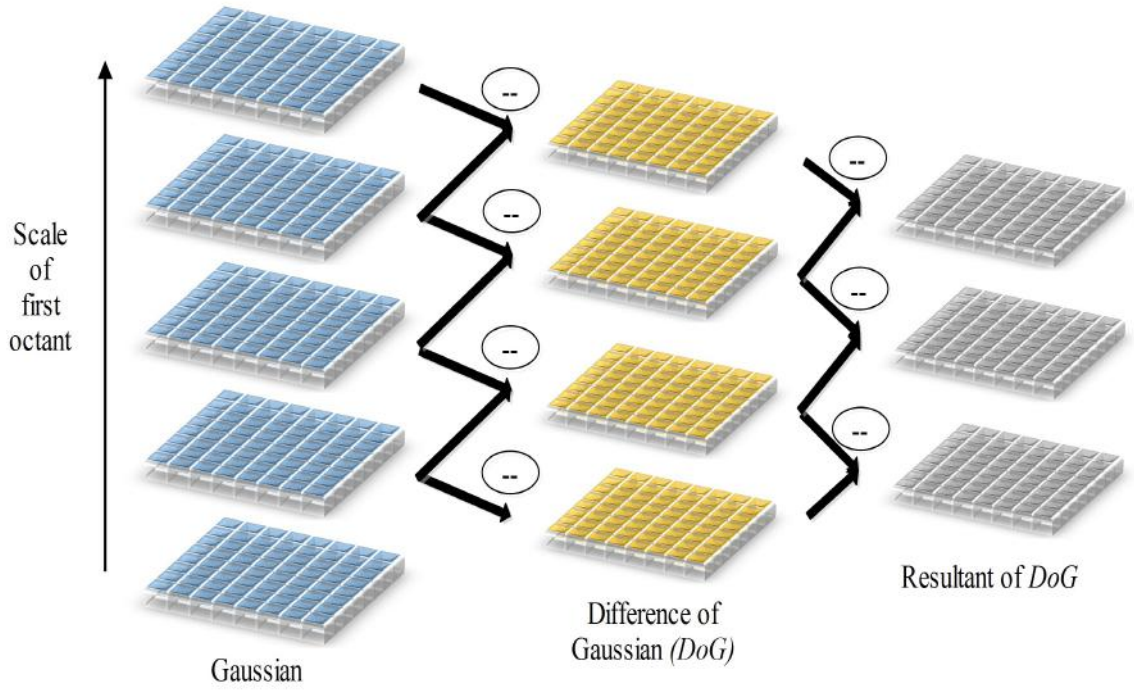

Figure 6.3: Gaussian and Difference of Gaussian *(DoG)* Construction on Scale

are eliminated. Each key-point is assigned consistent orientations to achieve invariance to image rotation. The pixel differences are used for computing the Magnitude of Gradient, $G_M(L,M)$ towards directions (scale) and its orientation, $\Theta(L,M)$, are given by Eqs. 6.4 and 6.5.

$$G_M(L,M) = \sqrt{((Loc(L+1,M) - Loc(L-1,M))^2} + \sqrt{(Loc(L,M+1) - Loc(L,M-1))^2)} \tag{6.4}$$

where, $Loc(L+1,M)$, $Loc(L-1,M)$, $Loc(L,M+1)$ and $Loc(L,M-1)$ are the direction coordinates of image, placed at center point.

$$\Theta(X,Y) = \tan^{-1}\left(\frac{Loc(L+1,M) - Loc(L-1,M)}{Loc(L,M+1) - Loc(L,M-1)}\right) \tag{6.5}$$

The combined histograms of orientation set are generated in neighbors of all key-points and thus 128×128 normalized vector is computed (describing key-points). Algorithm 6.3 describes the working of *SIFT*.

Algorithm 6.3 *SIFT Algorithm*

Require: Images as input $(A1, B1)$, scaling points $(sIm1, sIm2)$, frequency transformation $(p1, p2)$, stitched image $(Anew)$

begin
initialize $A1 \longleftarrow Image1$ //inputting an image
initialize $B1 \longleftarrow Image2$ //inputting another image
$sIm1 \longleftarrow padarray(A1)$ //stitching and scaling
$sIm2 \longleftarrow padarray(B1)$ //stitching and scaling
for (i = 1 to sIm1) **do**
  for (i = 1 to sIm1) **do**
    $p1 \longleftarrow homography(A1)$ //frequency transformation
    $p2 \longleftarrow homography(B1)$ //frequency transformation
    if $(p1 > 0$ && $p1 <= size(A1)$ && $p2 > 0$ && $p2 <= size(B1))$ **then**
      $Anew \longleftarrow stitchedImage(A1, B1)$ //combining images
    end if
  end for
end for
end

The inner process of mosaicing considers *SIFT* algorithm for stitching two images (combining). The process initiates by selecting two images and scaling them. It loops into combining two images by considering the pixels into cells (row-column matrix) of images and transform them at various frequencies. If the size of first image and second image matches and its value lies within the domain, then the process stitches the two images.

- **Feature Matching and Blending:** The features of first image are matched with second image, using the nearest neighbor in data sets of feature vectors of images. To estimate parameters of a mathematical model from a set of observed data which contains wrongful detected points, *RANSAC* algorithm is processed. It removes wrongly detected points and computes transmission parameters. The working of *RANSAC* algorithm is explained in Algorithm 6.4.

Algorithm 6.4 *RANSAC Algorithm*

Require: image $(data)$, iterations $(iter)$, minimum data values required for stitching (n), maximum number of iteration (k), threshold value (t), modeling image $(matchInd)$, number of close data points (d), output for asserting or refining the pixels $(bestfit)$, pixels without errors $(numpts)$

begin
initialize $iter = 0$, $bestfit = null$, $k = 100$, $n = 4$
while $(iter < k)$ **do**
  $S1 \longleftarrow randomize(n)$ //selecting random data value
  $matchInd \longleftarrow model(S1)$ //modeling and fitting the image
  for $((numpts$ in $matchInd)! = present)$ **do**
    if $(model(S1) == erred_{pixels})$ **then**
      $numpts \longleftarrow matchInd$ //$matchInd$ are stored in $numpts$
    else
      $matchInd = matchInd + numpts$
    end if
  end for
  if $(size(numpts) > d)$ **then** //good match is found
    if $(matchInd < threshold)$ **then**
      $m1 = combine(matchInd, numpts)$ //checking for each pixel and combining
      $bestfit = m1$
    end if
  end if
end while
display $bestfit$ //display the blended image
end

The process initiates by taking variables as iterations, $iter = 0$, output refined pixels, $bestfit = null$, total iterations, $k = 100$ and minimum data value, $n = 4$. The loop begins for $iter$ up to k which selects the random pixels from stitched images. The pixels are selected in a way to re-characterize them by refining

or modeling. The *matchInd* models the pixels of $S1$ which stores the randomize value of n. It checks the modeling for remaining pixels using the loop that analyze modeled pixels to find whether they have any erred pixels or not. The process then sums up the *matchInd* with *numpts* (pixels without error). If the produced results of pixels are more than the closed data-points d and has value less than the *threshold*, then the combined big canvas image is checked for each pixel. The final result is stored and displayed as full blended refined image.

After computation of transformation, the images are blended together. The process is known as blending. The projection of panoramic image to blend is either cylindrical or spherical surface (called as image warping). The images are warped using blending and stitched together to form a mosaic image. The process for mosaicing is described in Algorithm 6.5.

Algorithm 6.5 begins the process by selecting two images of similar size. The algorithm asks the user to select two points from each image to distinguish the similar columns of pixels from selected images. It estimates the parameter vectors and stores into Z. The process of *SIFT* is used by mosaicing to solve it linearly by constructing transformations, stitching images to produce big canvas of the image. The process is followed by *RANSAC* algorithm to blend the combined images and refining the newly generated pixels using bilinear interpolation. Finally, the mosaiced image is displayed.

The process of panoramic image mosaicing is carried out on images that are sent to surface station. The process is helpful in refining the images as well as to get big canvas that provide complete information of pipelines.

6.3 Result Analysis

This section describes the implementation of *Hybrid-OFDM* for image transmission and refinement using mosaicing. The working is described.

Algorithm 6.5 Mosaicing Algorithm

Require: Images as input (A,B), selecting points $(L1,M1,L2,M2)$, parameter vector (xp), solving $SIFT$ $(Q1)$, stitching image $(ndgrid)$, transformation (T), combine image using $RANSAC$ $(Anew,Bnew)$, big canvas image (c)

begin

initialize $A \longleftarrow Image1$ //input image

initialize $B \longleftarrow Image2$ //input image

$[h1\ w1\ d1] \longleftarrow size(A)$ //storing image size

$[h2\ w2\ d2] \longleftarrow size(B)$ //storing image size

display A, B

$[L1\ M1] \longleftarrow ginput(2,A)$ //selecting two points from user

$[L2\ M2] \longleftarrow ginput(2,B)$ //selecting two points from user

$Z \longleftarrow [L2'\ M2'; M2'\ -L2']$ //estimating parameter vectors

$xp = [L1\ M1]$

$Q1 = SIFT(Z/xp)$ //solving linearly by $SIFT$

$T = [h1\ d1\ L2; -d2\ h1\ M1]$ //constructing transformations

$ndgrid = warp(A,B,T,Q1)$ //stitching and warping image by $SIFT$

$Anew = RANSAC(A,T,ndgrid)$ //new image is combined by $RANSAC$ algorithm

$Bnew = RANSAC(B,T,ndgrid)$ //new image is combined by $RANSAC$ algorithm

for (i= 1 to 3) **do**

$c(:,:,i) = interpolate(Anew,Bnew,bilinear)$ //interpolating new points and generating big canvas

end for

display c //show the mosaiced image

end

6.3.1 *Hybrid-OFDM* based Transmission

The process of *Hybrid-OFDM* is simulated in *MATLAB* for transmitting and receiving gray scale pipeline panoramic images captured using *MPS* with specific angle at different locations. The various specifications of *Hybrid-OFDM* is shown in Table 6.1.

Table 6.1: Specifications of *Hybrid-OFDM*

S. No.	Parameters	Specifications
1	Modulation	*BPSK*, *QPSK*, 16*PSK* and 256*PSK*
2	Frequency Range	25 KHz
3	Sampling Frequency	5 KHz
4	Transmission Process	Angular
5	Coding	*DCT*
6	Symbol per Frame	8192
7	Guard Time	15 ms
8	Frequency Type	Orthogonal
9	Duration of Block	45 ms (approx.)

Captured underwater pipeline image is shown in Figure 6.4. The designated carriers, phases of modulation and after demodulating the image data are shown in Figure 6.5.

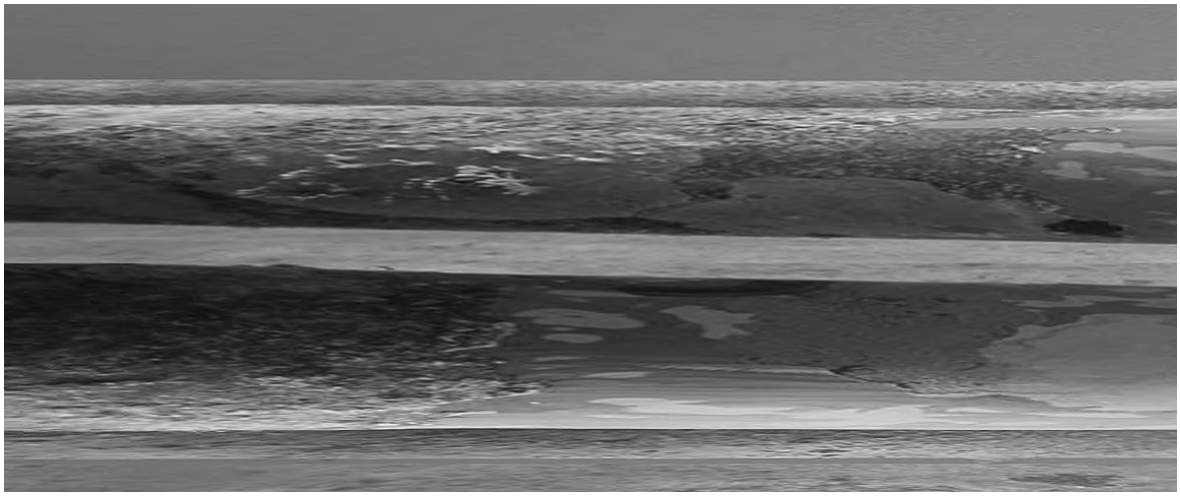

Figure 6.4: Original Image

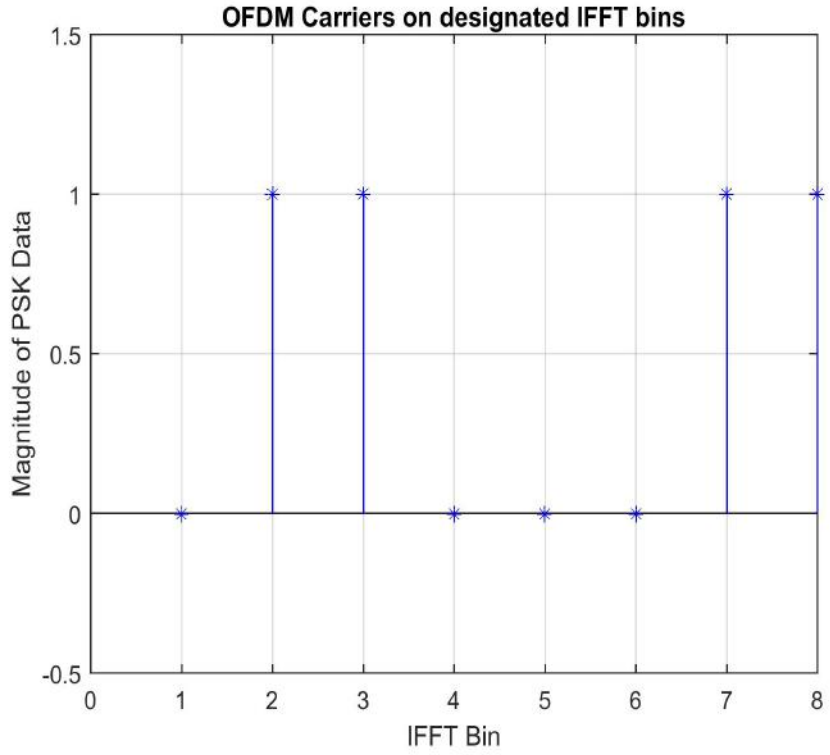

(a) Magnitude of Transmitted Modulated Data

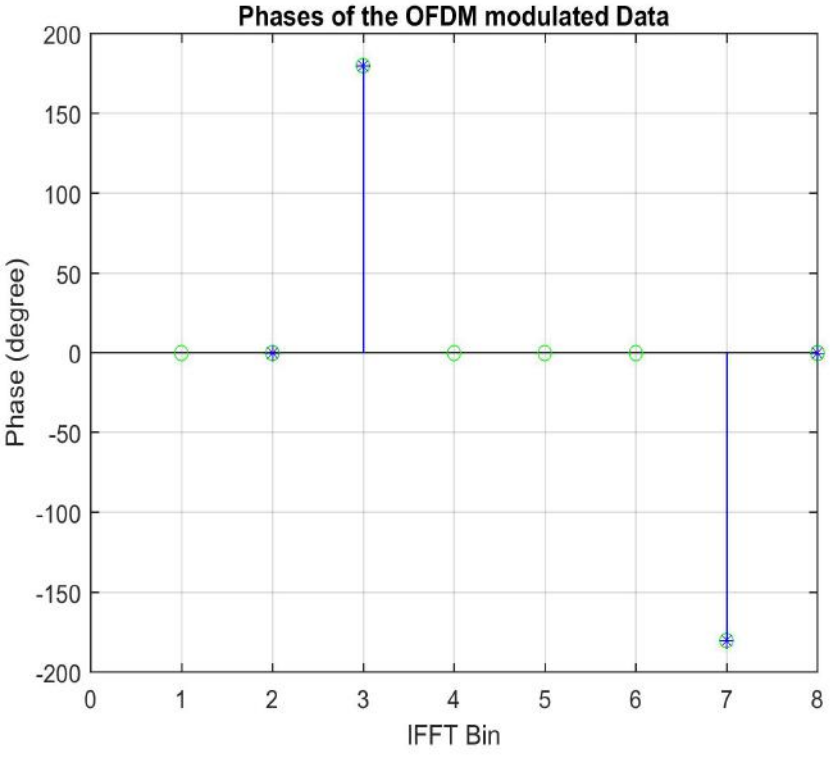

(b) Phases of Modulation on Transmission

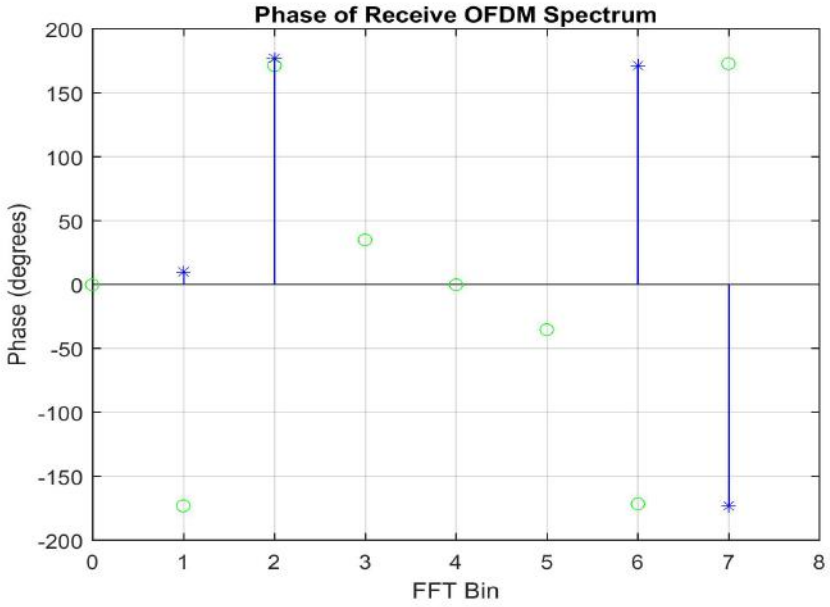

(c) Phases of Received Modulated Data

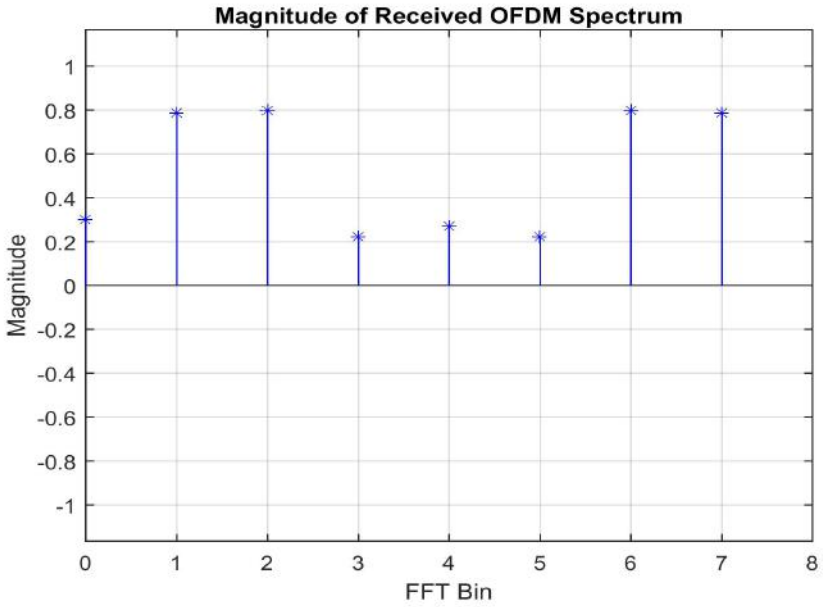

(d) Magnitude of Received Data

Figure 6.5: Output Waveforms using *BPSK* in *Hybrid-OFDM* at *SNR* = 15

Figure 6.5(a) shows the magnitude of *Hybrid-OFDM* carriers of modulated image. Figure 6.5(b) describes the phases of modulated data. Figures 6.5(c) and (d) show phases and magnitude of received image data, respectively, after transmission. The waveforms are produced using *BPSK* in *Hybrid-OFDM* at *SNR* = 15 and the output image thus received is shown in Figure 6.6.

Figure 6.6: Output Image for *BPSK* in *Hybrid-OFDM* at *SNR* = 15

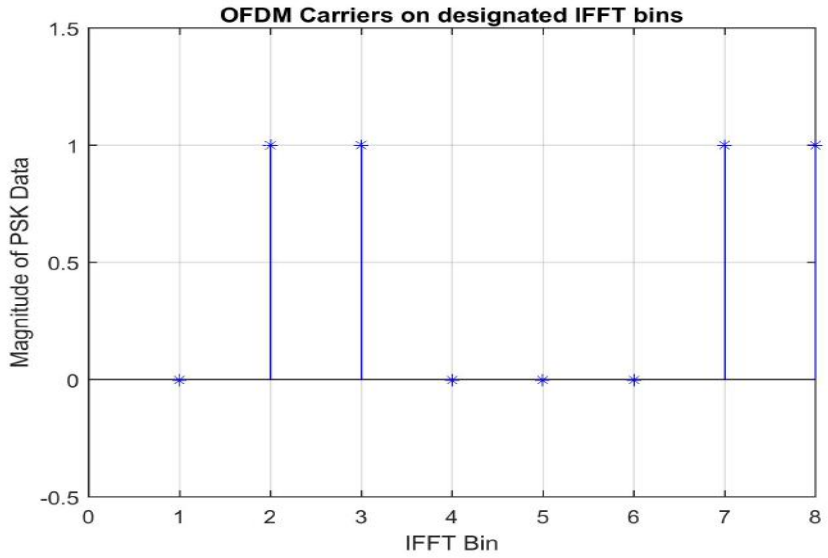

(a) Magnitude of Transmitted Modulated Data

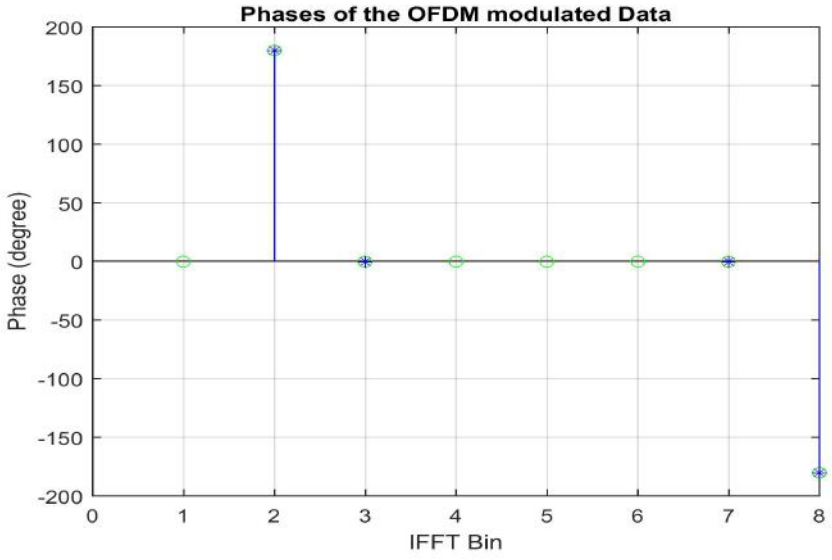

(b) Phases of Modulation on Transmission

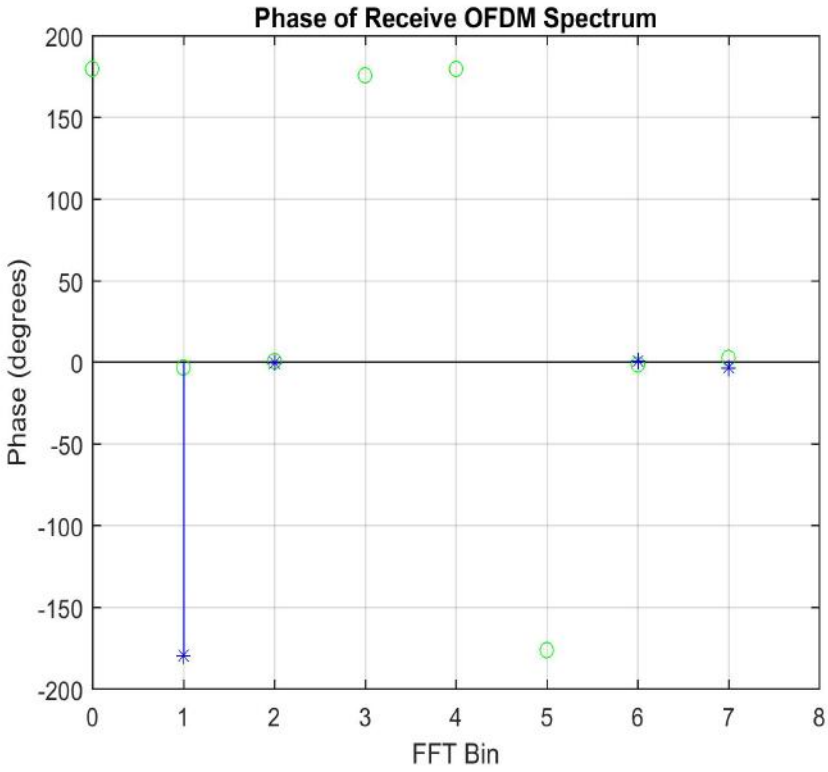

(c) Phases of Received Data

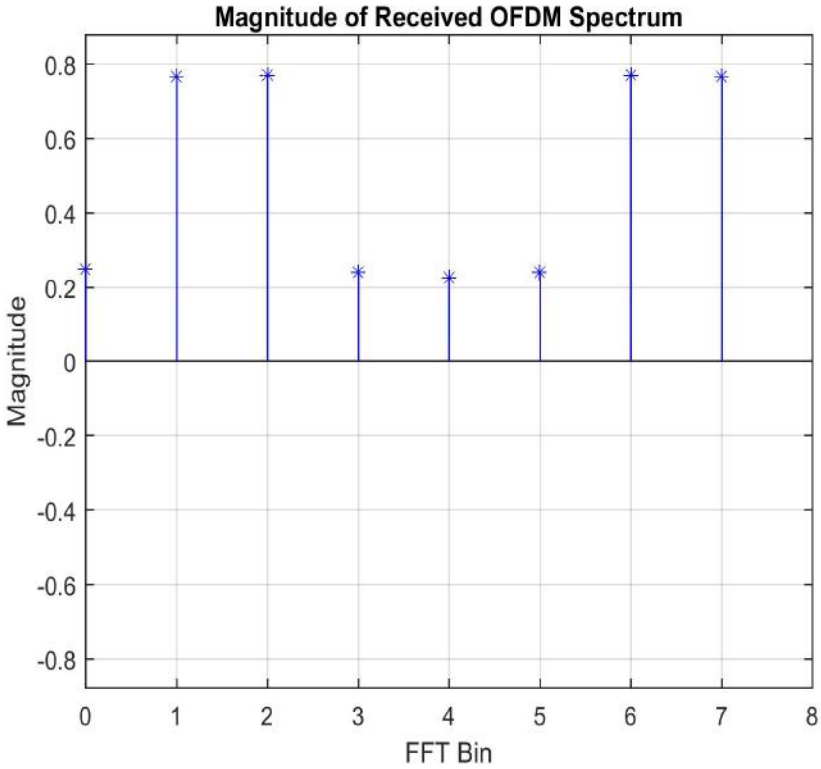

(d) Magnitude of Received Data

Figure 6.7: Output Waveforms using *BPSK* at *SNR* = 30

Figure 6.6 has bit errors and is blurred at *SNR*=15. This is due to wave noises, channel spreading in underwater. The image data has almost 19 % pixel's loss in comparison with the original image. The image data is further tested for *BPSK* at *SNR* = 30. The observed carriers are shown in Figure 6.7.

Figure 6.7(a) shows the magnitude of *Hybrid-OFDM* carriers of modulated image. Figure 6.7(b) describes the phases of modulated data. Figures 6.7(c) and (d) show phases and magnitude of received image data, respectively, after transmission. The output image thus received has 0 % bit errors at *SNR*=30 and is shown in Figure 6.8. The data loss in transmission is 0.09 %. The error of pixels of received image is only 0.08%, which is almost negligible in comparison to image transmitted at *SNR* = 15. Thus, the image is almost fully transmitted at *SNR* = 30.

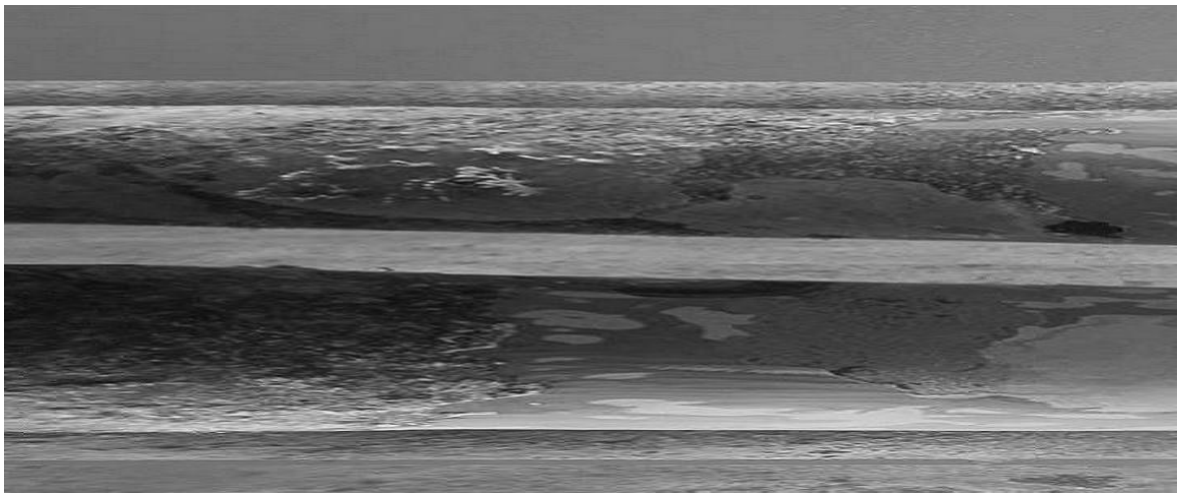

Figure 6.8: Output Image for *Hybrid-OFDM* using *BPSK* at *SNR* = 30

The captured underwater pipeline images are transmitted to surface station using *Hybrid-OFDM* channel *via* modulation schemes at *SNR* = 15 , 30. The captured images taken as input for transmission, are shown in Figure 6.9.

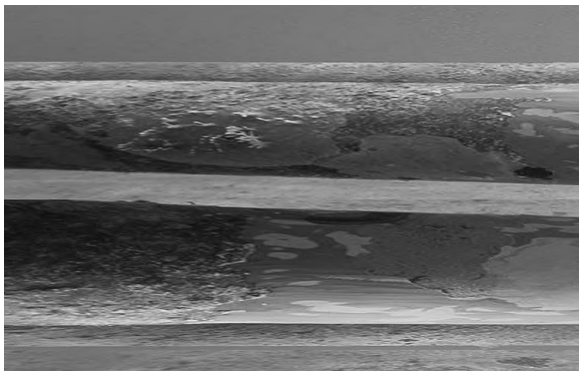

(a) Captured Rusted Pipe 1

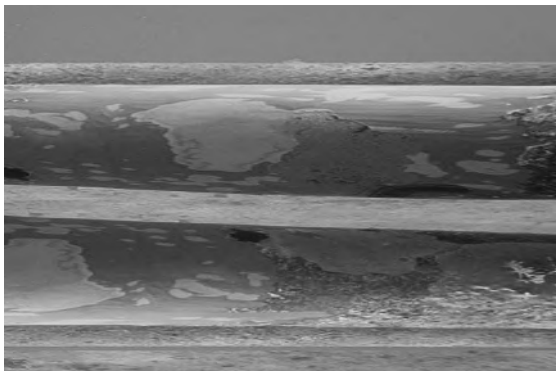

(b) Captured Rusted Pipe 2

(c) Image 1 of corroded pipe

(d) Image 2 of corroded pipe

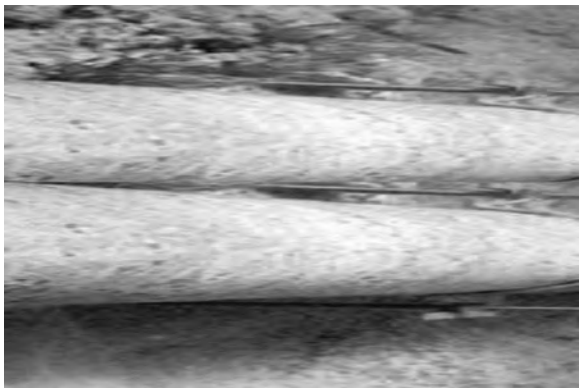

(e) Image 1 of joint in pipe

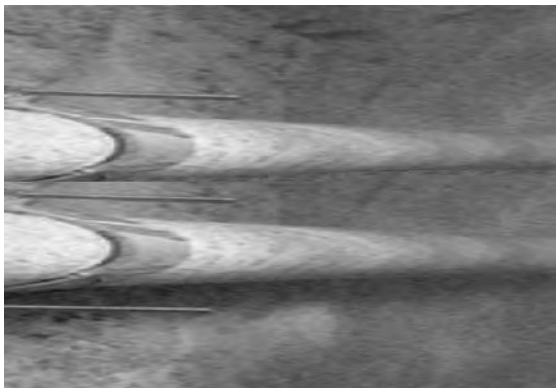

(f) Image 2 of joint in pipe

Figure 6.9: Input Images used for Data Transmission

Figures 6.9(a), (b) show the captured image of rusted pipe. Figures 6.9(c), (d) are the captured images of corroded pipe and Figures 6.9(e), (f) show the joint in the pipe captured at different angles. These images are transmitted at SNR = 15,30. The received images at surface station are shown in Table 6.2.

Table 6.2: Images Transmitted to Surface Station using *Hybrid-OFDM*

Images	**Modulation Scheme**	**SNR = 15**	**SNR = 30**
Rusted Pipe 1	BPSK	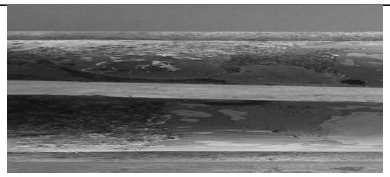	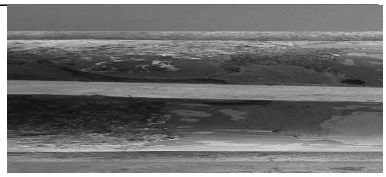
	QPSK	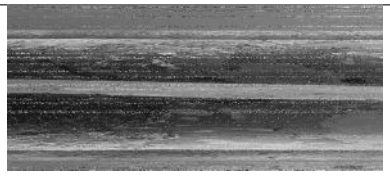	
	16PSK	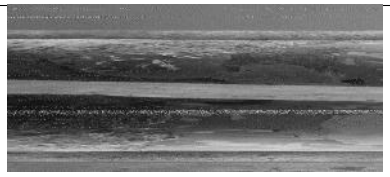	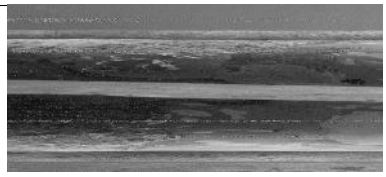
	256PSK		
Rusted Pipe 2	BPSK	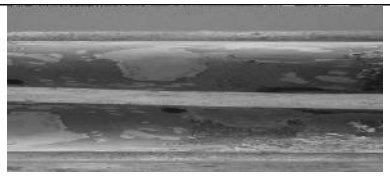	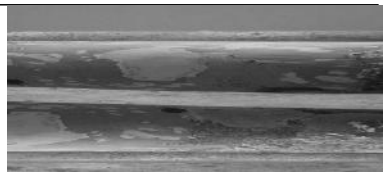
	QPSK	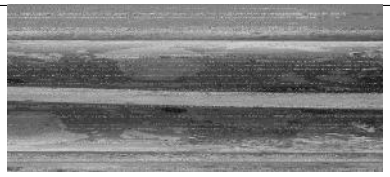	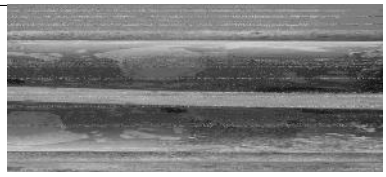
	16PSK	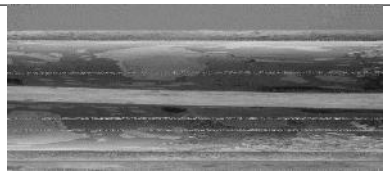	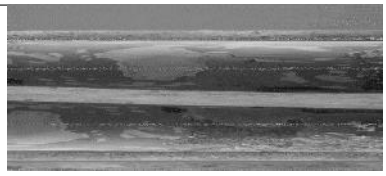
	256PSK		

Corroded Pipe 1	BPSK	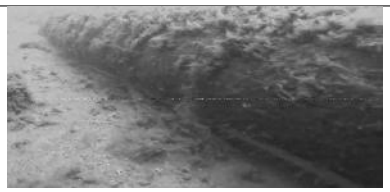	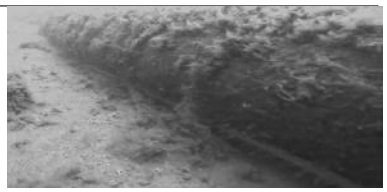
	QPSK	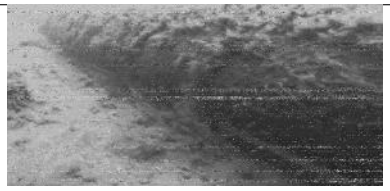	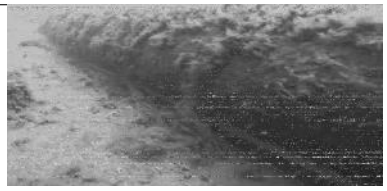
	16PSK		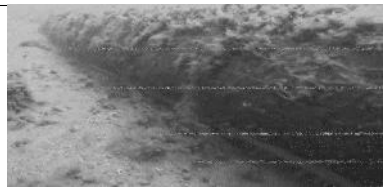
	256PSK		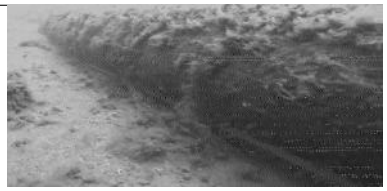
Corroded Pipe 2	BPSK		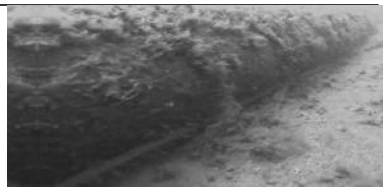
	QPSK	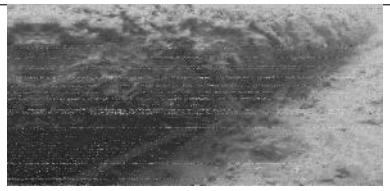	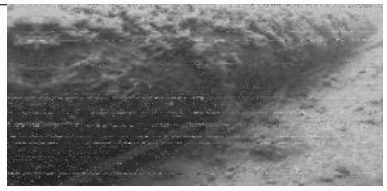
	16PSK	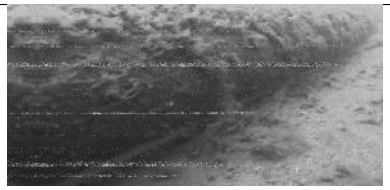	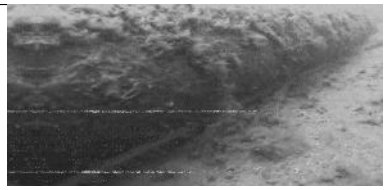
	256PSK		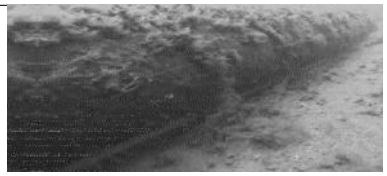

Joint in Pipe 1	BPSK	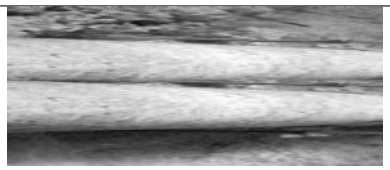	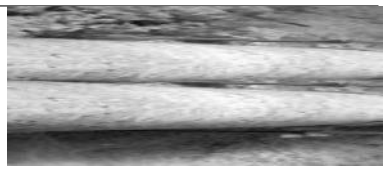
	QPSK	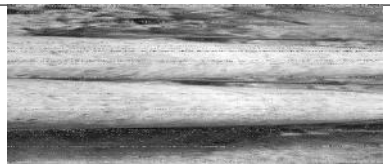	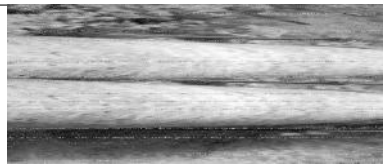
	16PSK	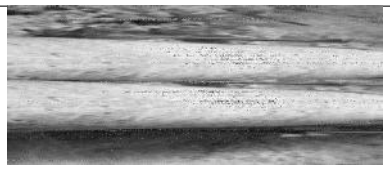	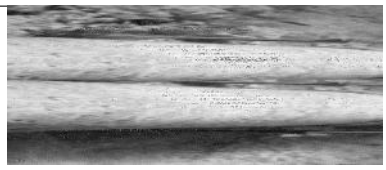
	256PSK	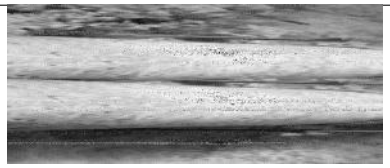	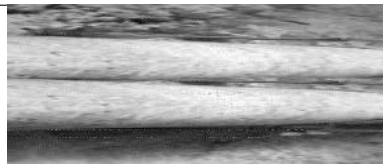
Joint in Pipe 2	BPSK	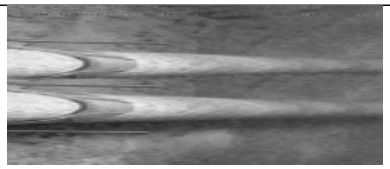	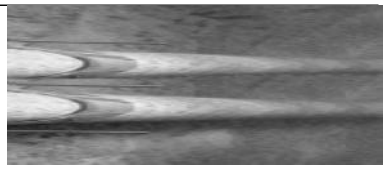
	QPSK	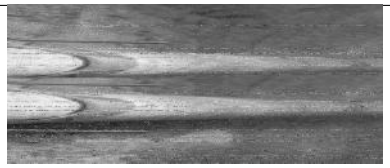	
	16PSK	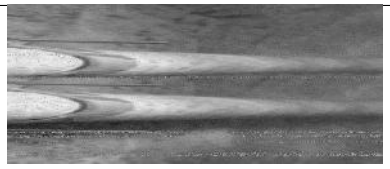	
	256PSK	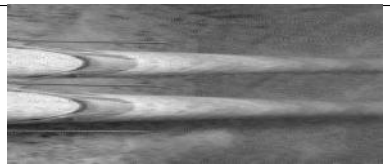	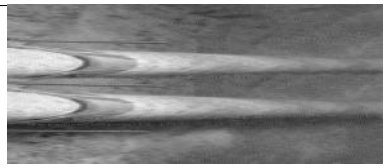

The received images have errors with loss in pixels and burst errors. These erred pixels are received at *SNR* = 15, 30 for various modulation schemes. The generated burst errors, erred pixels and additive noise *(SNR)*, on transmission are shown in Table 6.3.

Table 6.3: Bit Error Rate and Erred Pixels Received using Various *Hybrid-OFDM* Schemes

Images	Modulation Scheme	SNR = 15 (dB)			SNR = 30 (dB)		
		Bit Error Rate (%)	Erred Pixels Received (%)	Produced *SNR* (dB)	Bit Error Rate (%)	Erred Pixels Received (%)	Produced *SNR* (dB)
Rusted Pipe 1	BPSK	0.2	0.14	21.9999	0	0.09	32.7023
	QPSK	8.79	21.18	15.1485	4.51	11.16	33.8344
	16PSK	41.23	55.83	13.6158	36.09	44.10	28.5320
	256PSK	94.64	94.64	19.9688	84.65	84.65	37.2333
Rusted Pipe 2	BPSK	0.24	0.69	21.6631	0	0.08	32.1234
	QPSK	9.66	22.80	13.3310	5.43	12.96	31.6089
	16PSK	41.40	55.80	15.8739	35.90	43.37	35.1703
	256PSK	94.51	94.51	18.3422	82.59	82.60	38.3511
Corroded Pipe 1	BPSK	0.14	0.56	23.4691	0	0.06	39.7571
	QPSK	6.53	16.60	18.2819	2.97	8.22	43.5180
	16PSK	45.36	60.18	20.3362	35.41	43.42	32.2514
	256PSK	95.15	95.15	23.9719	86.14	86.15	35.0009
Corroded Pipe 2	BPSK	0.15	0.44	21.2372	0	0.08	33.3734
	QPSK	7.52	18.55	10.8547	3.68	9.60	27.0217
	16PSK	40.28	52.95	10.8591	32.02	39.33	28.3708
	256PSK	95.33	95.33	14.9398	86.54	86.54	31.9021
Joint in Pipe 1	BPSK	0.09	0.40	16.4083	0	0.08	32.0946
	QPSK	7.11	16.58	16.1721	3.76	9.23	39.1036
	16PSK	40.89	56.35	15.4502	31.85	40.04	32.7083
	256PSK	95.06	95.06	17.1297	86.72	86.72	38.8550
Joint in Pipe 2	BPSK	0.20	0.77	21.3788	0	0.08	31.9653
	QPSK	7.82	18.91	14.3669	5.59	13.35	35.7579
	16PSK	40.82	55.47	14.8874	35.28	43.28	31.9796
	256PSK	93.76	93.76	15.3823	85.67	85.67	37.9181

Table 6.3 shows the burst errors, erred pixels and produced *SNR* for received images. Each image is sent for *BPSK*, *QPSK*, *16PSK* and *256PSK* at *SNR* = 15, 30. The minimum value of errors received for Rusted Pipe 1 image is 0.09 %, which is received using *BPSK* at *SNR* = 30. Maximum error and loss in pixels are received for *256PSK* at *SNR* = 15, *i.e.*, 94.64 %. For Rusted Pipe 2 image, the minimum error noted is 0.08 % for *BPSK* at *SNR* = 30, and the maximum erred pixels received is 94.51 %, for *256PSK* at *SNR* = 15. The minimum erred pixels for Corroded Pipe 1 image is 0.08 % for *BPSK* at *SNR* = 30. Maximum loss in pixels for Corroded Pipe 1 image is observed for *256PSK* at *SNR* = 15, 30, *i.e.*, 95.15 % and 86.15 %, respectively. Corroded Pipe 2 image is observed at 0.44 %, 0.08 % errors in pixels for *BPSK* at *SNR* = 15, 30, respectively. Loss in pixels for Corroded Pipe 2 image is maximum at *SNR* = 15, 30 for *256PSK*, *i.e.*, 95.33 % and 86.54 %, respectively. Joint in Pipe 1 image is received with 0.08 % errors at *SNR* = 30 using *BPSK* and is fully recovered with no loss in pixels. It has maximum errors and loss in pixels, *i.e.*, 95.06 % and 86.72 % at *SNR* = 15, 30, respectively, for *256PSK*. The minimum value of errors and loss in pixels received for Joint in Pipe 2 image is 0 % and 0.08 %, respectively, which is achieved using *BPSK* for *SNR* = 30. The highest loss in pixels and errors in Joint in Pipe 2 image are produced by *256PSK* at *SNR* = 15, 30 having values as 93.76 % and 85.67 %, respectively. The obtained images have fluctuating *SNR* at the receiver side due to the addition of Gaussian process and thus, the images received using *QPSK*, *16PSK* and *256PSK* adhere to loss in pixels.

Thus, it is concluded that the transmissions of images are received at surface station with negligible loss in pixels using *BPSK* at *SNR* = 30. It suggests that *BPSK* provides better transmission and receiving image data, which has complete information. The technique is further combined with mosaicing process to completely analyze the affected areas.

6.3.2 Image Mosaicing

On receiving the images at surface station, it is found that the transmitted images do not provide the complete information of the affected areas. Therefore, to visualize the area in a big canvas and analyze the produced image completely for timely preventive measurements, these images are stitched and refined together using mosaicing algorithm. The gathered images at surface station by *BPSK* at *SNR* = 30 are inputted for mosiaicing and are shown in

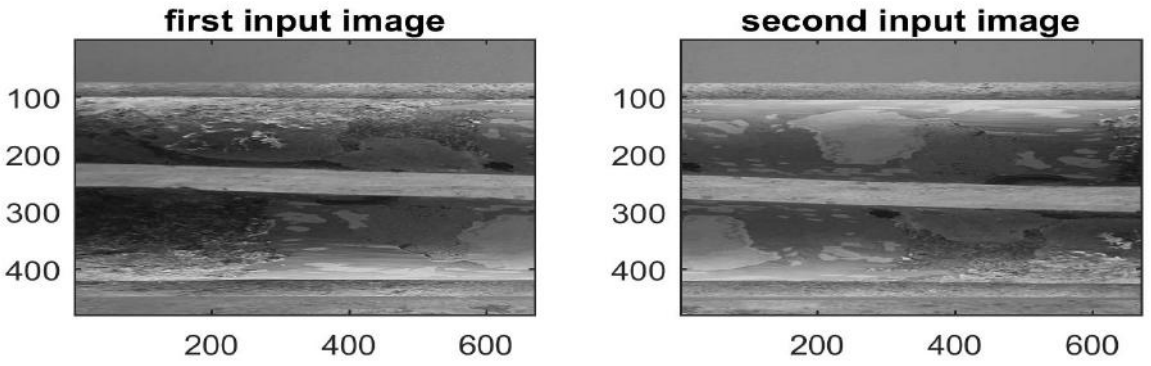

(a) Received Rusted Image of Pipe

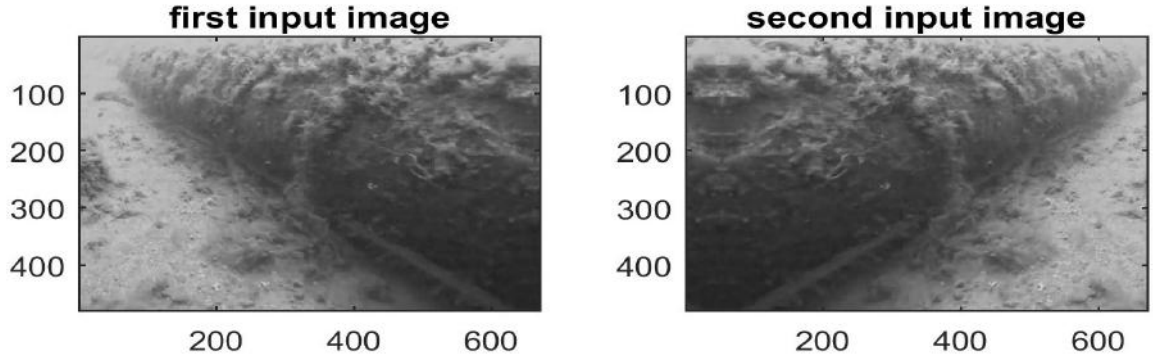

(b) Received Image of Corroded Pipe

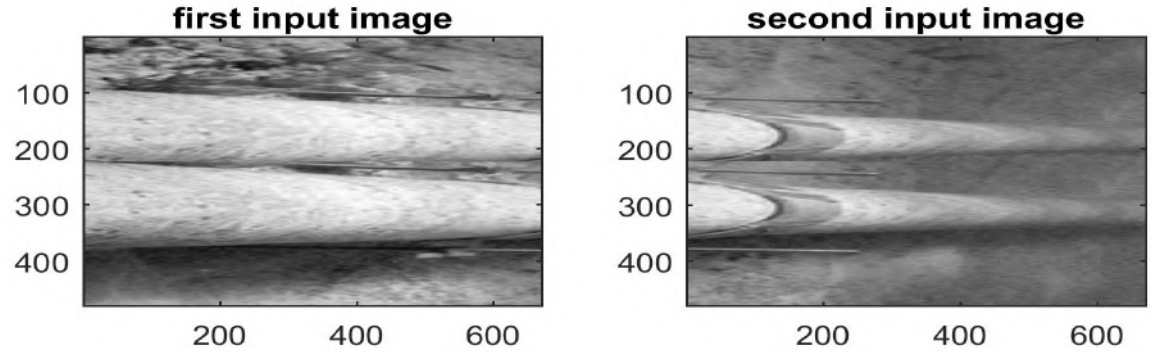

(c) Image of Joint in Pipe

Figure 6.10: Images Inputted for Mosaicing

Figure 6.10. The process considers the images and matches the pixel columns of first input image to the pixel columns of second input image. It produces the mosaiced image which has an overlapping pixel columns of both the images. Thus, it produces the big canvas of image having complete information. The outputs of mosaiced images are shown in Figure 6.11.

The mosaiced images are blended to produce panoramic images of good quality as shown

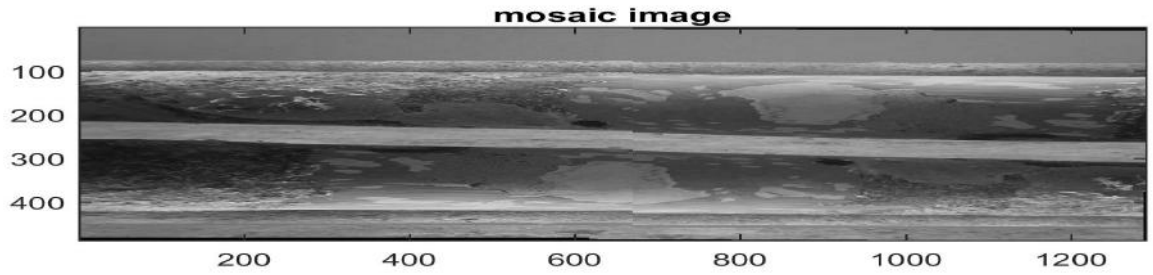

(a) Mosaiced Image of Rusted Pipe

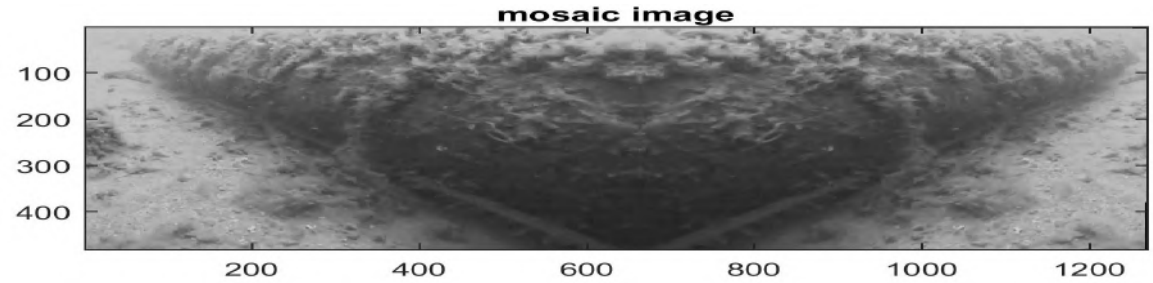

(b) Output Mosaiced Image of Corroded Pipe

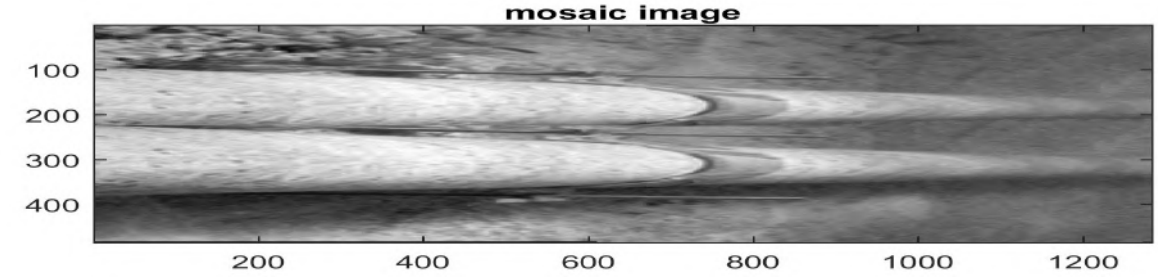

(c) Mosaiced Image of Joint in Pipe

Figure 6.11: Output Images Produced after Mosaicing

in Figure 6.12. These images are analyzed to check any leakage or corrosion in the pipe and help to rectify the joints or corroded areas to prevent leakages. Thus, the proposed technique provides good quality panoramic images.

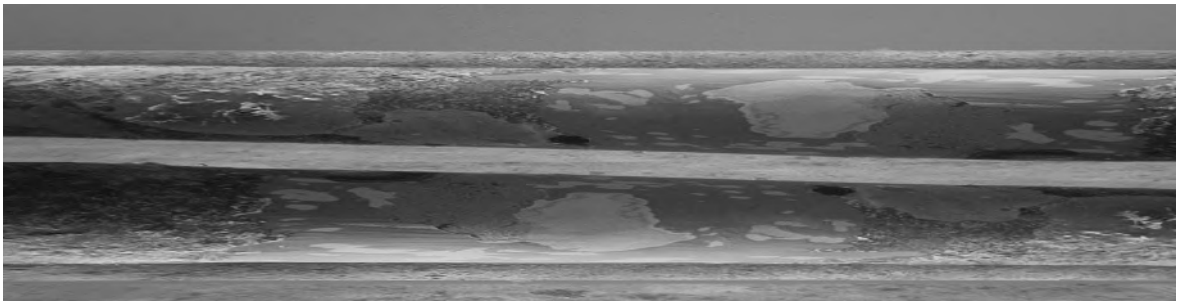

(a) Blended Image of Rusted Pipe

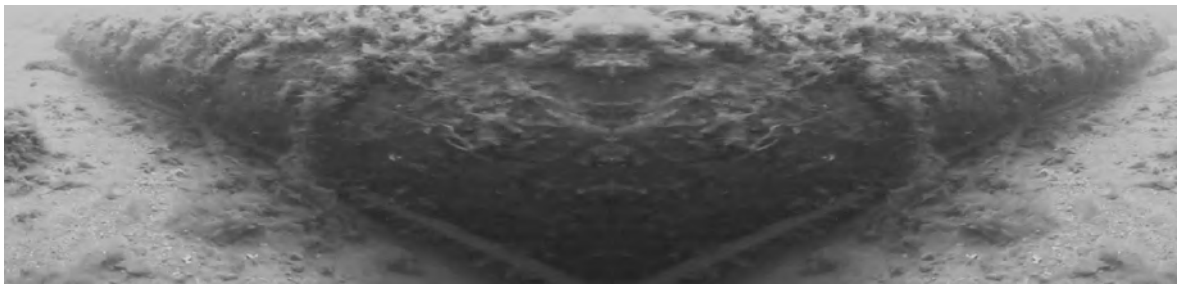

(b) Output Blended Image of Corroded Pipe

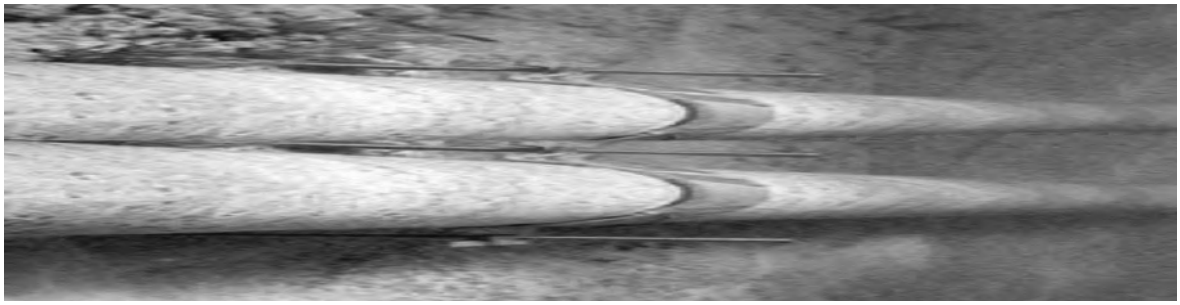

(c) Blended Image of Joint in Pipe

Figure 6.12: Output Blended Images

6.4 Conclusion

The proposed technique considers *MPS* which has a camera fabricated on chip-board and uses *Hybrid-OFDM* for image transmission. The performance of technique is evaluated on its transmission process with different modulation schemes and the transmitted image is evaluated on basis of *SNR*. The quality of images at surface station are assessed on the amount of received erred pixels which is $0.5, 19.10, 56.09, 94.74$ (%) and $0.07, 10.75, 42.25, 85.38$ (%) for *BPSK*, *QPSK*, *16PSK* and *256PSK*, respectively, at SNR = $15, 30$. It is found that the proposed technique helps to obtain quality images that are transmitted by *BPSK* without erred pixels. Furthermore, it helps in providing the big canvas image using mosaicing, in order to distinguish faults in pipelines and to take timely preventive measurements.

Chapter 7

Ridgelet based Fusion Technique for Panoramic Image Refinement

7.1 Introduction

Image mosaicing technique proposed in Chapter 5, can refine panoramic images using feature extraction, merging of two images (stitching) and blending steps. The technique is suitable to combine two or three images by considering the projection of panoramic image in either cylindrical or spherical surface. Moreover, the technique is beneficial for mosaicing images. The technique faces few challenges related to poor visibility, distortion, light scattering, noise and wavelength attenuation due to changing color with increase in depth underwater.

To address these challenges, a novel technique *namely*, *RBFT* is proposed to refine panoramic images. It combines the pixels of two or more images using fusion technique. It retains information along with contours by smoothing its edges. It maps line singularities into points *via* Radon Transform and reconstructs robust periodic images against noise. The proposed technique is validated on panoramic underwater images taken from *Bubble Vision* dataset. The obtained results support the efficiency of the proposed technique in terms of quality and visibility of the panoramic images.

7.2 Image Fusion

The image fusion is used widely for combining the properties of multiple images. It integrates the information collected from different images and produces an image with better visual quality. The process of image fusion undergoes the steps of feature extraction, classification and decision making. It has three levels as explained below.

i. **Pixel Level Image Fusion:** In this fusion, pixels of two images are combined to produce a new image using strict registration algorithms (Vijayaraj et al. (2006)). This new image provides raw data for further processing and analysis *via* feature extraction and classification. The pixel level image fusion is performed using single, multi-sensor or temporal fusion. Its main advantages are less data or pixels' loss and it contains maximum information. It has its limitations that it takes more computation time and is dependent on hardware (Ramkumar and Akansu (2004); Hui and Binbin (2009)).

ii. **Feature Level Image Fusion:** Feature level image fusion takes into account the features like shape, angle, direction, speed, depth, *etc.*, for combining the two or more images. These features are extracted from various images that are captured at same geographic area (Hui and Binbin (2009)). The combined image provides an optimal set of features that helps to analyze and view the information for optimal decision (Dawei and Fang (2007)). At this point, all the similar and existing features are deleted in order to improve reliability of the feature's information. Since the sensor alignment is less firm in comparison to pixel's level, they are distributed in nature. It is benefited in organizing real-time procedures, which further help in decision-making through the analysis process (Wang et al. (2010b)).

iii. **Decision Level Image Fusion:** The controlled decision making is performed by the decision-level image fusion where images are formulated independently (Vijayaraj et al. (2006)). The information about the output of the decision making process is further filtered through the collaboration of data received from sources, and its processing is done using various decision rules. The number of techniques exist for decision-level fusion, *e.g.*, dampster-shafer, voting system, *NN*, bayesian reasoning, cluster analysis,

entropy, fuzzy set theory, *etc*. The fusion though provides fault tolerance but is more expensive. Moreover, it has the smallest data quality and highest anti-interference capability (Hui and Binbin (2009);Dawei and Fang (2007)). The fused outcome for images with high performance and quality.

The levels of image fusion are further categorized into various techniques, *namely*, (i) arithmetic and combinations, (ii) component substitution, (iii) pyramid decomposition and (iv) wavelet transform (Mitchell (2010)). Based on these techniques, few techniques are discussed.

i. **Average based Technique:** This technique combines the features of two images. This technique produces an output image from the focused area of input images after calculating the average intensity of all corresponding pixels. Mathematically, it is given in Eq. 7.1.

$$F_{avg} = \frac{(I_{A_{ij}} + I_{B_{ij}})}{2} \tag{7.1}$$

where, F_{avg} is the fusion by average technique, $I_{A_{ij}}$ and $I_{B_{ij}}$ are the images of same location.

ii. **Maximum based Technique:** This technique selects maximum intensity of corresponding pixels from the focused area of two input images for generating highly featured image. It is computed using Eq. 7.2.

$$F_{max} = \sum_{i=0}^{k} \sum_{j=0}^{l} max\left(I_{A_{ij}}, I_{B_{ij}}\right) \tag{7.2}$$

where, F_{max} is the fusionby maximum technique.

iii. **Minimum based Technique:** Minimum based technique selects minimum intensity of corresponding pixels from the focused area of two input images to generate a fused image. Its computation formula is given in Eq. 7.3.

$$F_{min} = \sum_{i=0}^{k} \sum_{j=0}^{l} min\left(I_{A_{ij}}, I_{B_{ij}}\right) \tag{7.3}$$

where, F_{min} is the fusion by minimum technique.

iv. **Intensity-Hue-Saturation:** The *IHS* technique has faster computation capabilities for image fusion through the conversion of multi-spectral color into *IHS* color space with the axis rotation from orthogonal Red-Green-Blue *(RGB)* to the orthogonal *IHS* system. In the orthogonal *IHS* system, intensity, hue, saturation represents complete brightness of the color, dominant wavelength of the light and purity, respectively. Since, its intensity band is alike to $I_{gray-scale}$ image while performing the image fusion, *RGB* image is projected onto *IHS* color and $I_{gray-scale}$ image is used instead of the intensity band. For the fusion using *IHS*, it first considers the *RGB-IHS* conversion model, given in Eq. 7.4.

$$\begin{bmatrix} I_{intensity} \\ \upsilon_1 \\ \upsilon_2 \end{bmatrix} = \begin{bmatrix} \frac{1}{3} & \frac{1}{3} & \frac{1}{3} \\ -\frac{\sqrt{2}}{6} & -\frac{\sqrt{2}}{6} & \frac{2\sqrt{2}}{6} \\ \frac{1}{\sqrt{2}} & -\frac{1}{\sqrt{2}} & 0 \end{bmatrix} \times \begin{bmatrix} R_1 \\ G_1 \\ B_1 \end{bmatrix} \tag{7.4}$$

where $I_{intensity}$ indicates the intensity *(I)* in z-axis, υ_1 and υ_2 are intermediate variables for x and y axes in Cartesian coordinate system. The Hue *(H)* and Saturation *(S)* are represented using Eqs. 7.5, 7.6.

$$H = tan^{-1}\left(\frac{\upsilon_2}{\upsilon_1}\right) \tag{7.5}$$

and

$$S = \sqrt{\upsilon_1^2 + \upsilon_2^2} \tag{7.6}$$

The histogram matching is performed for $I_{gray-scale}$ with I component to compensate spectral differences among two images. The fusion of $I_{gray-scale}$ and *RGB* images are

obtained by reverse of *IHS* to *RGB* transformation and is given in Eq. 7.7.

$$\begin{bmatrix} R_{1_{new}} \\ G_{1_{new}} \\ B_{1_{new}} \end{bmatrix} = \begin{bmatrix} 1 & \frac{1}{\sqrt{6}} & \frac{1}{\sqrt{2}} \\ 2 & \frac{1}{\sqrt{6}} & -\frac{1}{2} \\ \frac{11}{\sqrt{2}} & -\frac{2}{\sqrt{6}} & 0 \end{bmatrix} \times \begin{bmatrix} I_{intensity} \\ \upsilon_1 \\ \upsilon_2 \end{bmatrix} \tag{7.7}$$

v. **Brovey Transform:** Based on chromaticity transform, the Brovey Transform is a numerical fusion technique which is the mathematical combination of bands of *RGB* and gray-scale images. It aims to perform fusion with the preservation of the original colors of the images and retains the spectral contributions of each pixel. It replaces the brightness of high resolution gray-scale image with original colors as shown in Eq. 7.8.

$$\begin{bmatrix} R_{1_{new}} \\ R_{2_{new}} \\ R_{3_{new}} \end{bmatrix} = \eta \times \begin{bmatrix} R_1 \\ R_2 \\ R_3 \end{bmatrix} = \frac{I_{gray-scale}}{I_o} \times \begin{bmatrix} R_1 \\ R_2 \\ R_3 \end{bmatrix} \tag{7.8}$$

where $\eta = \frac{I_{gray-scale}}{I_o}$ is the fraction of gray-scale image to the low resolution intensity. The multiplication of η and *RGB* image provides fused image with refined resolution and color in spatial domain.

vi. **Principal Component Analysis:** *PCA* calculates basic vectors for fusing two or more images using data compression techniques and is achieved by analyzing the variation in the data direction (projection). It computes the principle component using linear transformation, which contains the essential data of the image resembling the gray-scale image and replaces it. The linear transformation has derived eigen values, eigen vectors from the covariance matrix having non-diagonal elements as zero and rest are

ordered in descending order. It is given by Eq. 7.9, 7.10.

$$D_{g_m} = \begin{bmatrix} D_{k_1} & \dots & 0 \\ \vdots & \ddots & \vdots \\ 0 & \dots & D_{k_n} \end{bmatrix} \tag{7.9}$$

and

$$M_{Ev} \times C_{VM} \times M_{Ev}^{T} = D_{g_m} \tag{7.10}$$

where, M_{Ev} is matrix of eigen vectors, C_{VM} is covariance matrix and D_{g_m} is diagonal non-zero elements ordered from largest to smallest. It performs the inverse principal component transform such that new *RGB* bands with sharp quality is obtained. The *PCA* has less color distortion and affects spectral responses of the multi-spectral data.

The above discussed techniques are used for fusion of two or more images that will result into the good quality image. The resultant image has maximum information of two or more images.

7.3 Ridgelet Transform

The Ridgelet transform is computed by performing a wavelet analysis in the Radon domain. The basic description for Ridgelet Transform is describe in Chapter 3. The internal working of the transform is described below.

7.3.1 Strategies for Finite Ridgelet Transform

A basic strategy for calculating the continuous Ridgelet transform is first to compute the Radon transform *Rts* and secondly, to apply a *1D* wavelet transform to the slices $Rts(\theta,.)$. The finite wavelet decomposition, associated to a filter bank (Mallat (1989)), is easy to implement, is stable and invertible, and can be associated to a finite orthogonal representation. The discretization of the Radon transform is more difficult to achieve. The finite Radon transform is computed with a spatial strategy (summations of image pixels over a certain set of lines) or with a Fourier strategy. The steps for computation are described.

i. Compute the *2D DFT* of s.

ii. Extract Fourier coefficients along the lines L_Q going through the origin.

iii. Compute the *1D* inverse *DFT* on each line L_Q (defined for each value of the angular parameter θ).

This technique can be problematic since step (ii) is not naturally defined on finite data. Recently, some articles studied the implementation of the finite Ridgelet transform. Do (2001) have proposed an implementation technique of Ridgelet transform based on the use of the finite Radon transform. This technique achieves both invertibility (the inverse transform is stable) and non-redundancy (the associated Ridgelet transform is orthogonal). This Radon transform integrates over lines, which are defined algebraically rather than geometrically, that can be rather arbitrarily spread out over the spatial domain. This technique is not based on a geometrically faithful notion of Ridgelets and suffers from artifacts.

The Fast Slant Stack is proposed to use a scheme that substitutes the sampled values of the Fourier transform obtained on the square lattice with sampled values of s on a polar lattice (Averbuch et al. (2001)). The technique uses a pseudo polar Fourier domain. The finite pseudo polar Fourier transform of a digital image is defined by sampling the *2D* Fourier transform at the collection of pseudo polar grid points (Averbuch and Shkolnisky (2003)). The generated outcome is Ridgelet Transform based image.

7.3.2 Finite Radon Transform

Ridgelet Transform is constructed using Finite Radon Transform *(FRAT)* as it helps in transforming finite length signals. It is the summation of image pixels against set of lines defined in finite geometry (Euclidean) (Do and Vetterli (2003)). The working of *FRAT* is described. Let $M_a = 0, 1, ..., a-1$, where a is prime number and M_a is finite field, then, the *FRAT* of real function f_r on distinguished lattice M_a^2 is given in Eq. 7.11 as,

$$r_f(i,j) = FRAT_{fr}(i,j) = \frac{1}{\sqrt{a}} \times \Sigma_{(p,q)\epsilon R_{i,j}} f_r(p,q) \tag{7.11}$$

where, $R_{i,j}$ is collection of points producing line on lattice M_a^2 and $f_r(p,q)$ is input image. Specifically,

$$R_{i,j} = \{(p,q) : q = i \times p + j(mod(a)), p \epsilon M_a\} \tag{7.12}$$

and

$$R_{i,j} = \{(j,q) : q \epsilon M_a\} \tag{7.13}$$

In this domain (Eqs. 7.12, 7.13), the processing energy is saved if the mean is deducted from input image $f_r(p,q)$. To normalize $l_2 - norm$ among *FRAT*'s input or output, factor $a^{-\frac{1}{2}}$ is introduced. Line $R_{i,j}$ is represented uniquely on the plane M_a^2 by its direction i and intercept $j \epsilon M_a$. It is verified that there are $a^2 + a$ lines and each line has a points. Any two adjacent points on M_a^2 are in one line. Moreover, lines with different slopes intersect at one point. There are also a parallel lines for any slope that provide complete plane M_a^2. It is described in Eq. 7.14 suggesting that

$$\Sigma_{j=0}^{a-1} r_f(i,j) = \frac{1}{\sqrt{a}} \times \Sigma_{(p,q)\epsilon M_a} f_r(p,q) = 0 \tag{7.14}$$

It is concluded that for each direction, there is only $(a-1)$ independent *FRAT* coefficients and in direction $(a+1)$, coefficients together produce total of $(a-1)(a+1) = a^2$ independent coefficients in Radon domain. The inverse of *FRAT* is given in Eq. 7.15 as-

$$IFRAT_r(p,q) = \frac{1}{\sqrt{a}} \times \Sigma_{(i,j)\epsilon L_{p,q}} r_f(i,j) \tag{7.15}$$

where, $L_{p,q}$ set of pixels of all lines through (p,q)ϵ M_a^2. The Radon Transform and its coefficients are further used to denote points and lines in *2D* area of Ridgelet Transform (Chen et al. (2005)). The Radon Transform ($R_d(\Theta,n)$) in *2D* area is denoted in Eq. 7.16.

$$R_d(\Theta,n) = \int_{R^2} f_r \times \delta\left(y_1 cos\theta + y_2 sin\theta - n\right) dy \tag{7.16}$$

where, $f_r(y)$ is bivariate function in R^2. The Ridgelet is an application of projection *i.e.*, *1-D* wavelet transform in the slices of Radon and is given in Eq. 7.17.

$$RDT_{f_r}(x,y,\Theta) = \int_R \varphi_{x,y}(n) \times R_d(\Theta,n)dn \tag{7.17}$$

The invertible Ridgelet Transform is obtained by applying inverse of Radon and Eq. 7.17 in such a way that wavelets is applied on each ridgelet projection vector, *i.e.*, $\left\{r_f(i,j), j \epsilon M_a\right\}$ with i direction as fixed. The resultant comes out to be Finite Ridgelet Transform *(FRIT)*. The periodic wavelet is selected for periodic projection of Radon coefficients (Do and Vetterli (2003)).

Moreover, Radon is redundant and is removed using *1-D* wavelet projection on Radon, resulting into orthonormal transformation of *FRIT*. For this, assume filter banks having Z levels with low and high pass filters as E_0 and E_1, respectively. Then, the family $\left\{e_0^{(Z)}(p-2^Z \times q), e_1^{(Z)}(p-2^Z \times q)\right\}$, $q = 1,...,Z$ and $(p,q) \epsilon M_a$, is orthogonal form of wavelet. E^Z has equivalent filters at Z levels. The filter E_1 satisfies high pass condition that results into wavelet with zero mean.

For i projection of Radon Transform, the *1-D* orthogonal transformation $(v_p^{(i)}(.))$ has basis given in Eq. 7.18.

$$\left\{v_p^{(i)}(.), p \epsilon M_a, 0 \leq i \leq a\right\} \tag{7.18}$$

Then, its main function is computed using Eq. 7.19.

$$v_0^{(i)}(j) = \frac{1}{\sqrt{a}}, \forall j \epsilon M_a \tag{7.19}$$

By the condition of orthogonality, it has zero sum and this requirement is satisfied when wavelets are processed for large iterations. Thus, *FRIT* is written using Eq. 7.20 as-

$$\begin{aligned} FRIT_{f_r}(i,p) &= \left\{FRAT_{f_r}(i,.), v_p^{(i)}(.)\right\} \\ &= \sum_{j \epsilon M_a} v_p^{(i)}(j) \left(f_r, a^{-\frac{1}{2}} \times \delta_{R_{i,j}}\right) \end{aligned} \tag{7.20}$$

and basis function for *FRIT* is calculated using Eq. 7.21.

$$\rho_{i,p} = \frac{1}{\sqrt{a}} \sum_{j \epsilon M_a} v_p^{(i)}(j) \times \delta_{R_{i,j}} \tag{7.21}$$

The flowgraph of Ridgelet transform is shown in Figure 7.1. As an illustration, ridgelet is applied to sample image, the output generated at each step is shown in Figure 7.2 (Do and Vetterli (2003)).

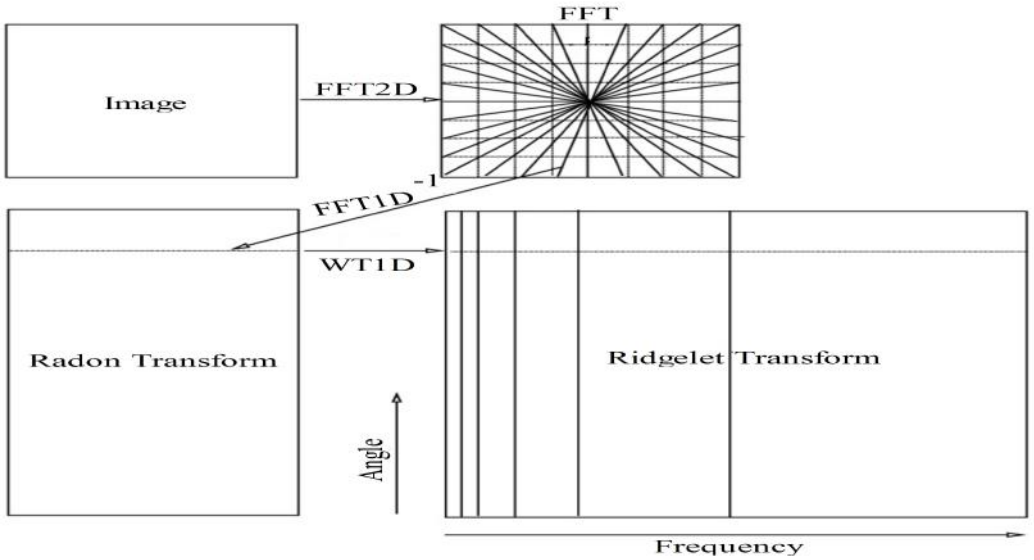

Figure 7.1: Ridgelet Transform Flow-graph

(a)

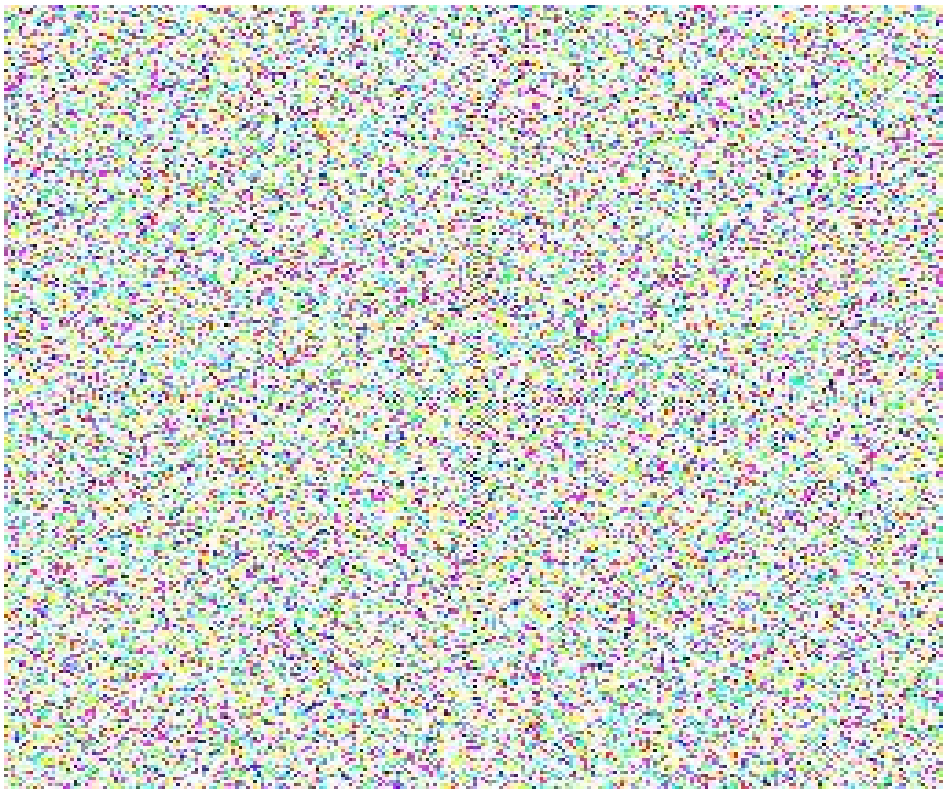

(b)

(c)

Figure 7.2: Ridgelet Transformation (a) Input Image (b)Transformed Sub-bands (c) Output Image

The Ridgelet transform is used to produce good visual quality panoramic images. the resultant images are optimal with minimized Mean Squared Error.

7.4 Ridgelet based Image Fusion Technique

The Ridgelet Transformation of input panoramic images are fused together to create a new image that contains more information and features than individual images. The fusion is applied to fuse the features of lines of two images. The advantage of fusion with ridgelets are that the ridgelets select salient points at edges against threshold and then detects the saliency of fused images' coefficients. After the process of fusion, the inverse transform is performed to get the fused and refined panoramic images. The working of Ridgelet based Fusion Technique *(RBFT)* is shown in Figure 7.3 and Algorithm 7.1.

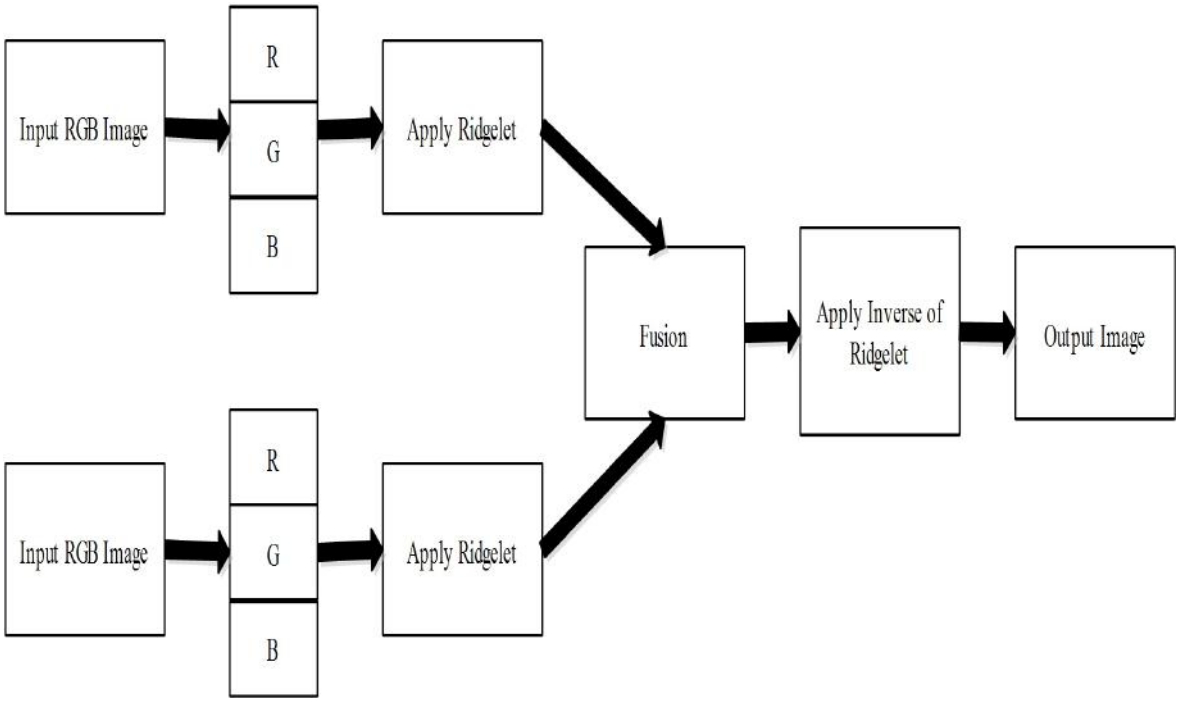

Figure 7.3: Flow of *RBFT*

Algorithm 7.1 *RBFT Algorithm*

begin

Input two images of same location, say A and B.

For each image, differentiate its coefficients into R, G, B scale

Apply ridgelet on the images as, $RT1 \longleftarrow ridgelet(A)$ and $RT2 \longleftarrow ridgelet(B)$

Initialize time $\leftarrow 0.01$

Extract features from images using hundengen i.e., $RTx1 \longleftarrow hundengen(RT1, time)$ and $RTx2 \longleftarrow hundengen(RT2, time)$

Apply fusion on extracted images, *i.e.*, $X1 \longleftarrow Fuse(RTx1, RTx2)$

Apply inverse of ridgelet to refine image, $X \longleftarrow iridgelet(X1)$

Calculate MSE,PSNR, SSIM and entropy for output images

end

Initially, it takes two images of same area and dimension as input, captured at two different timings. These images are divided into its coefficients of *R,G,B* scale. The ridgelet is applied to smooth the image along edges and the features of images are extracted. The extracted images are then fused using fusion techniques like *Average, Maximum, Minimum, IHS, Brovey* and *PCA*. The resultant of fused images are processed with inverse of ridgelet to get refined image that contain features of both input images. The output image is analyzed on the basis of performance metrics like Mean Squared Error *(MSE)*, Peak Signal to Noise Ratio *(PSNR)*, Structural Similarity Index Metrics *(SSIM)* and *Entropy*; and this analysis is discussed in the next section.

7.5 Experimental Result and Discussion

For the analysis, various panoramic images of size 900×512 are considered using *Bubble-Vision Datasets* (Hope (2001)). *DWT* and *RBFT* are applied on these images. The images are further processed using fusion techniques. The fusion techniques are independently applied on the processed images of *DWT* and *RBFT*; and further inverses of *DWT* and *RBFT* are applied to get the refined panoramic images. For the evaluations of resultant images produced by *DWT* and *RBFT*, the quality indexes are used to analyze the generated output.

The evaluation based on visual inspection does not completely justify the quality of images. Therefore, few parameters are considered for analyzing images along with visual inspection. They are explained as under:

i. ***MSE*:** It compares the difference between the input and resultant images by computing the variation of pixel values. The resultant image is equivalent to input image if value of *MSE* comes out to be zero or near to zero (Zoran (2009)). It is given by Eq. 7.22.

$$MSE = \frac{1}{k \times l} \sum_{i=1}^{k} \sum_{j=1}^{l} \left(I_{In_{i,j}} - I_{F_{i,j}} \right) \tag{7.22}$$

where $I_{In_{i,j}}$ and $I_{F_{i,j}}$ are input and resultant fused images, respectively. $k \times l$ is the size of image.

ii. ***PSNR*:** It is the ratio of maximum power of signal to the power of corrupting noise. The corrupting noise affects the fidelity of image (Naidu (2010)). It is denoted by Eq. 7.23.

$$PSNR = 10 \times log_{10} \left(\frac{255^2}{MSE} \right) \tag{7.23}$$

where, i and j are indexes of pixels in row and column. It is considered as the higher value to describe the quality of output image.

iii. ***SSIM*:** It helps to compare local patterns of intensities of pixel among input and fused image. It ranges between *-1* to *+1*. The higher value, *i.e.*, *+1* describes the similar value of input and fused resultant images (Wang et al. (2004)). It is based on computation of three components *namely*, luminance, contrast and structural. It is given by Eq. 7.24.

$$SSIM(i,j) = [lum(i,j)]^{\alpha} \times [con(i,j)]^{\beta} \times [stru(i,j)]^{\gamma} \tag{7.24}$$

where,

$$lum(i,j) = \frac{2 \times \mu_i \times \mu_j + C_1}{\mu_i^2 + \mu_j^2 + C_1} \tag{7.25}$$

$$con(i,j) = \frac{2 \times \sigma_i \times \sigma_j + C_2}{\sigma_i^2 + \sigma_j^2 + C_2} \tag{7.26}$$

$$stru(i,j) = \frac{\sigma_{ij} + C_3}{\sigma_i \times \sigma_j + C_3} \tag{7.27}$$

and, μ_i, μ_j, σ_i, σ_j, σ_{ij}, C_1, C_2, C_3 are the means, standard deviations and covariance of images, respectively. If $\alpha = \beta = \gamma = 1$, then C_1, C_2, C_3 are the regularization constants for luminance, contrast and structural, then *SSIM* is simplified as shown in Eq. 7.28.

$$SSIM(i,j) = \frac{\left(2 \times \mu_i \times \mu_j + C_1\right) \times \left(2 \times \sigma_{xy} + C_2\right)}{\left(\mu_i^2 + \mu_j^2 + C_1\right) \times \left(\sigma_i^2 + \sigma_j^2 + C_2\right)} \tag{7.28}$$

iv. **Entropy:** It measures the amount of content that is coded and stored in the resultant image using compression technique. The higher entropy value describes the rich information content (Wang and Chang (2011)). It is denoted using Eq. 7.29 as-

$$Entropy = -\sum_i I_{F_{i,j}} \times log_2(I_{F_{i,j}}) \tag{7.29}$$

where, $I_{F_{i,j}}$ is the resultant fused image.

The input images are shown in Figure 7.4.

(a) Autowrack

(b) Severance-equalised

(c) Tauchen-Straussee-Grunstich

(d) Thistlegorm-train-parts

(e) Usuario-Jaontiveros

(f) Europaeischer-Hecht

(g) RedSeaEgyptFish

(h) Wreckdiver-300

Figure 7.4: Input Images of size 900×512

The resultant fused panoramic images by *FDWT* (*DWT* with fusion) and *RBFT* are shown in Figures 7.5-7.10. It is found that *FDWT* does not decompose high frequency bands producing blurriness, distortion and aliasing in images. In comparison, *RBFT* generates images that are rich in edge preservation, color and are smooth along edges. Moreover, it decomposes high frequency parts and provide efficient images that are free from line discontinuities or straight edges (Do and Vetterli (2003)). It reconstructs robust images against noise due to threshold or quantization on *FRAT* coefficients (Chen et al. (2005)).

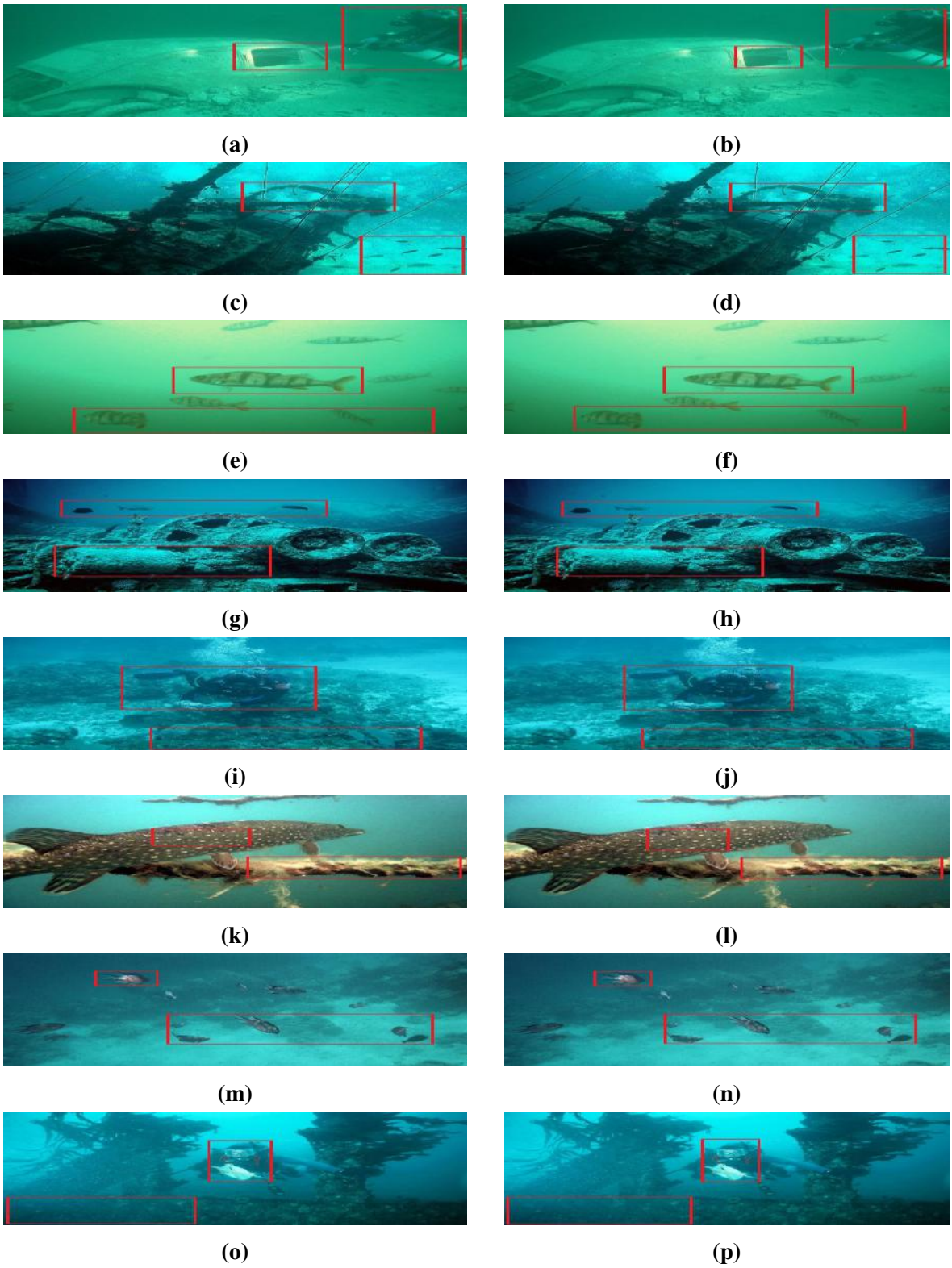

Figure 7.5: Output Images Produced using Average Fusion (a),(c),(e),(g),(i),(k),(m),(o) with *DWT* and (b),(d),(f),(h),(j),(l),(n), (p) with *RBFT*

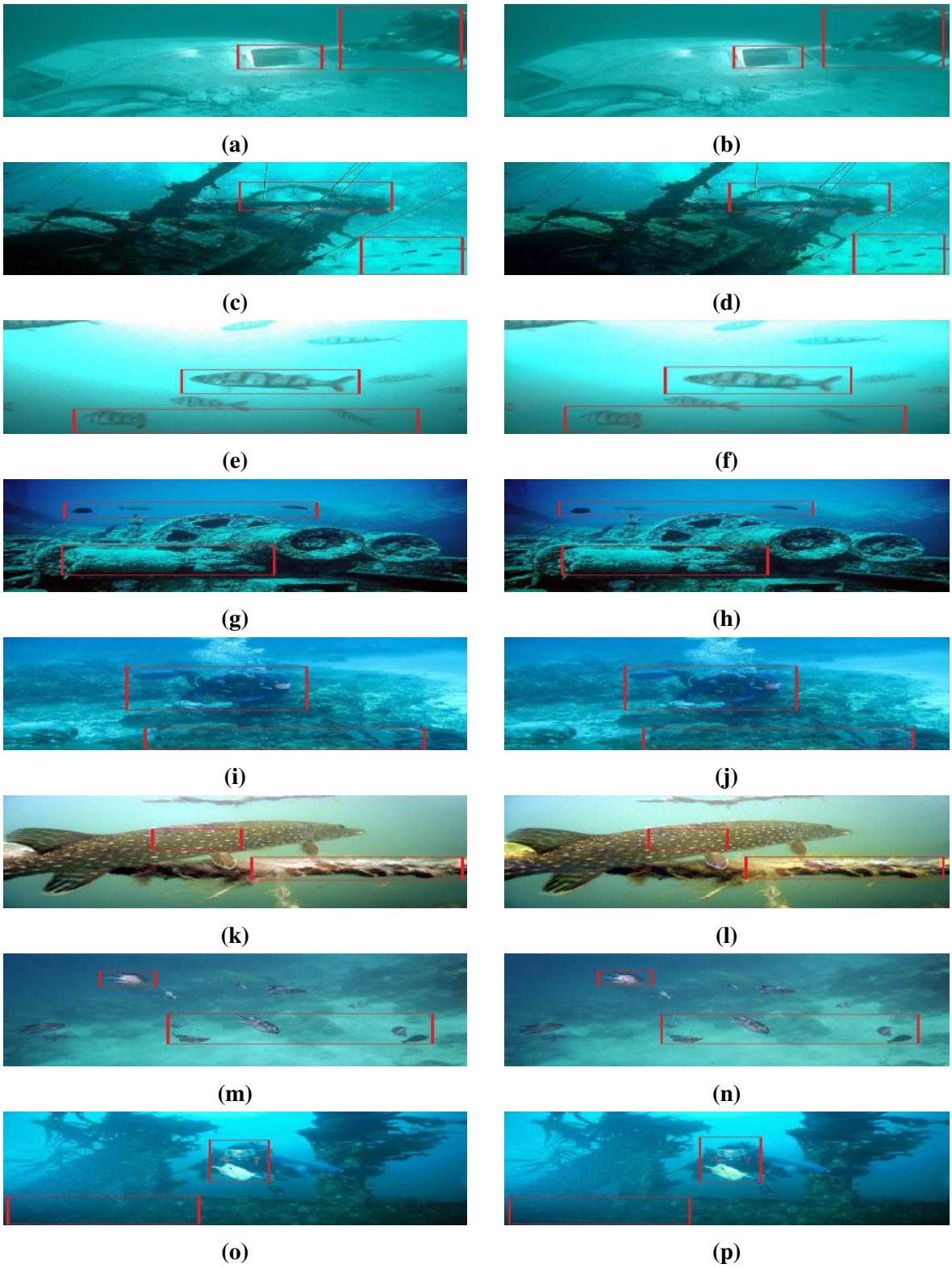

Figure 7.6: Output Images Produced using Maximum Fusion (a), (c), (e), (g), (i), (k), (m), (o) with *DWT* and (b), (d), (f), (h), (j), (l), (n), (p) with *RBFT*

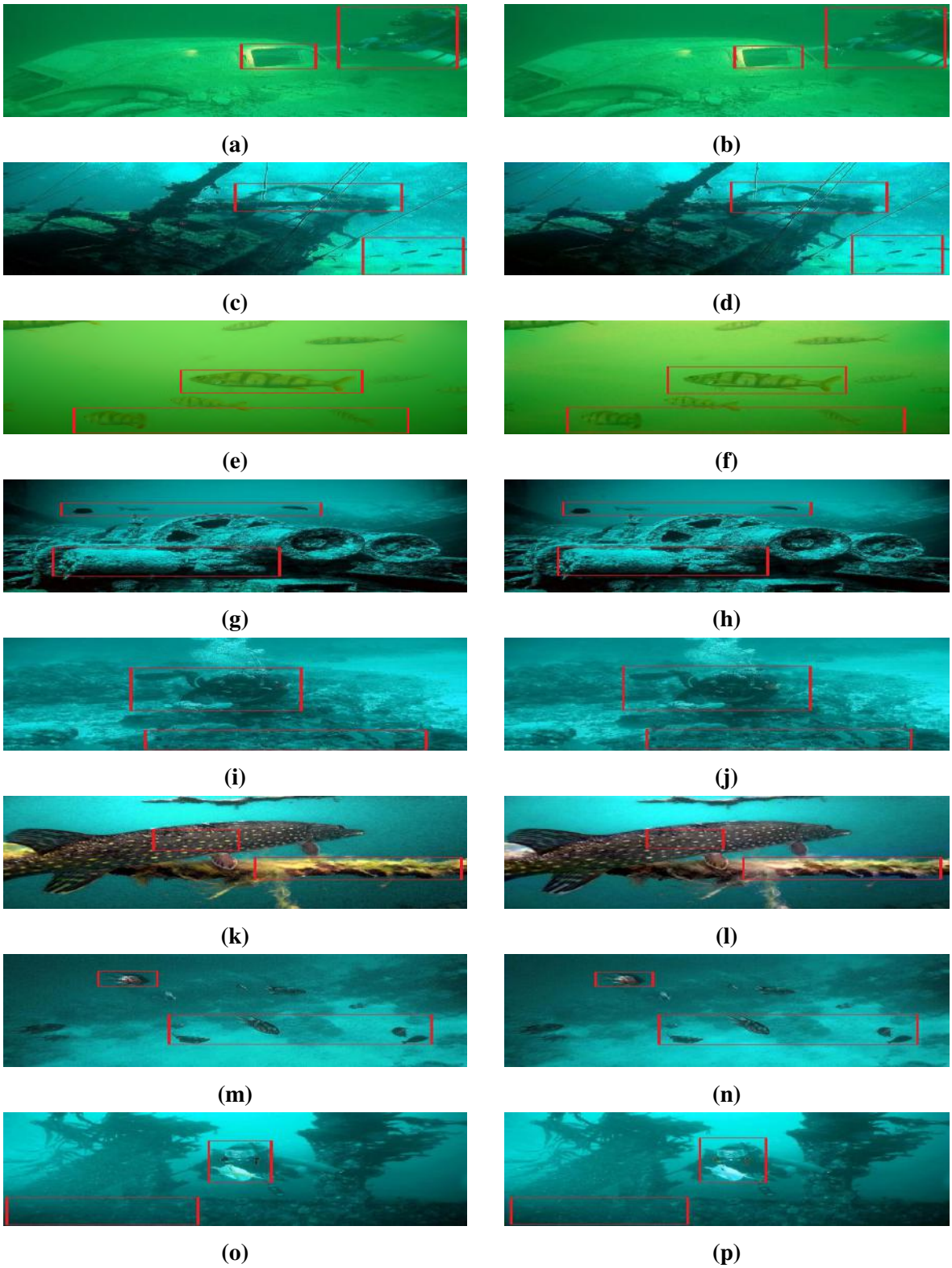

Figure 7.7: Output Images Produced using Minimum Fusion(a),(c),(e),(g),(i),(k),(m),(o) with *DWT* and (b),(d),(f),(h),(j),(l),(n), (p) with *RBFT*

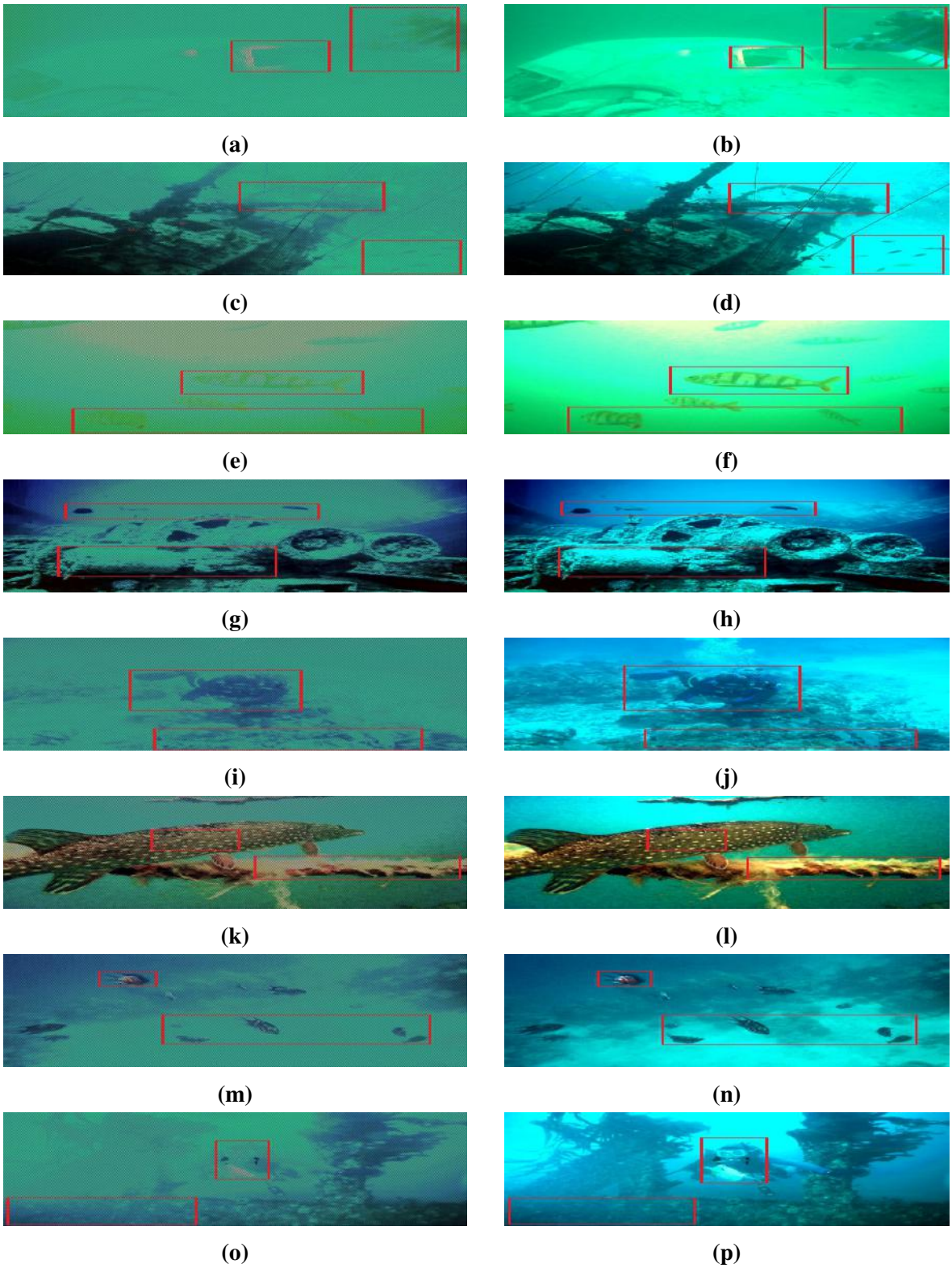

Figure 7.8: Output Images Produced using *IHS* Fusion (a), (c), (e), (g), (i), (k), (m), (o) with *DWT* and (b),(d),(f),(h),(j),(l),(n), (p) with *RBFT*

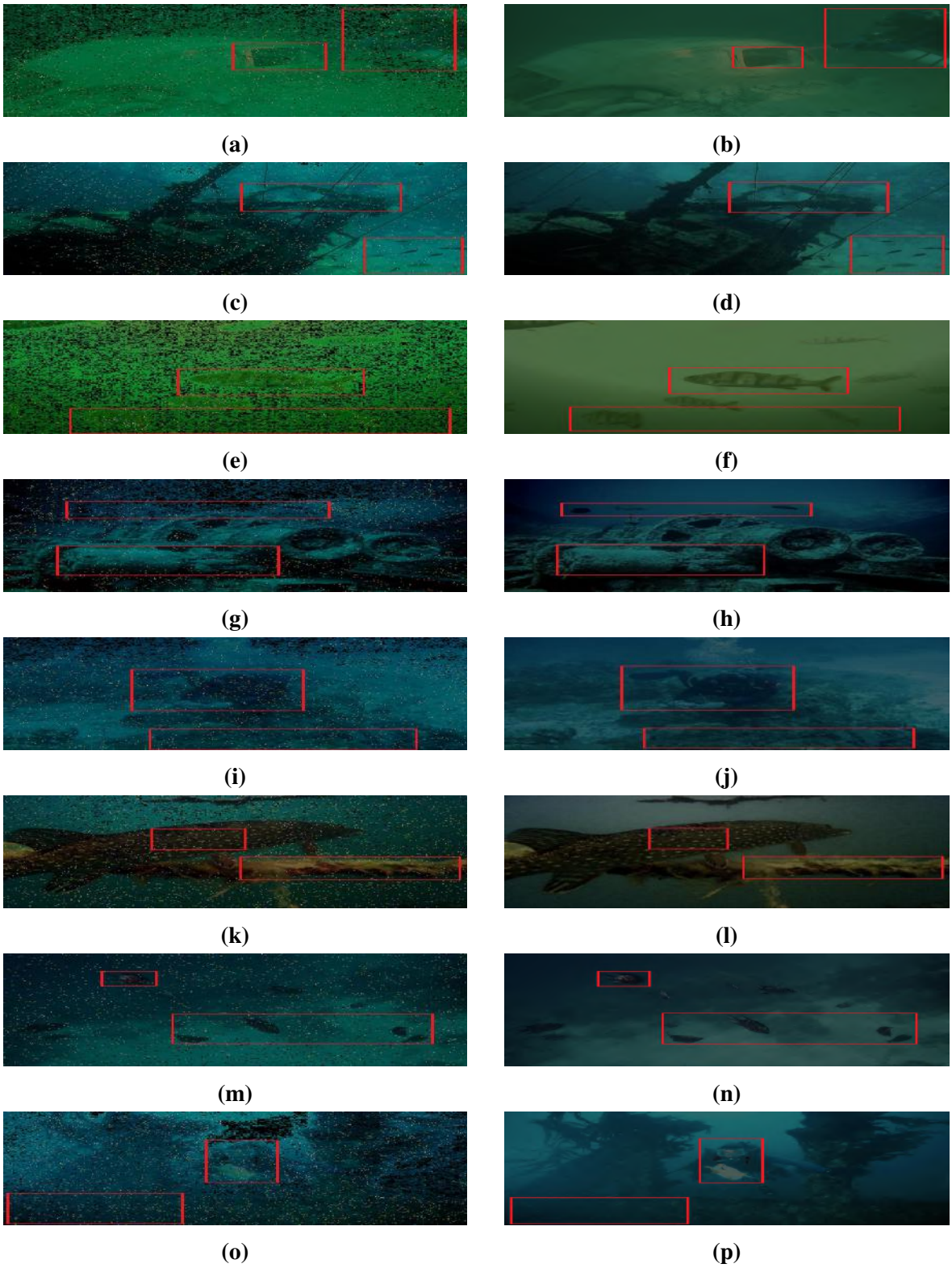

Figure 7.9: Output Images Produced using Brovey Fusion (a),(c),(e),(g),(i),(k),(m),(o) with *DWT* and (b),(d),(f),(h),(j),(l),(n), (p) with *RBFT*

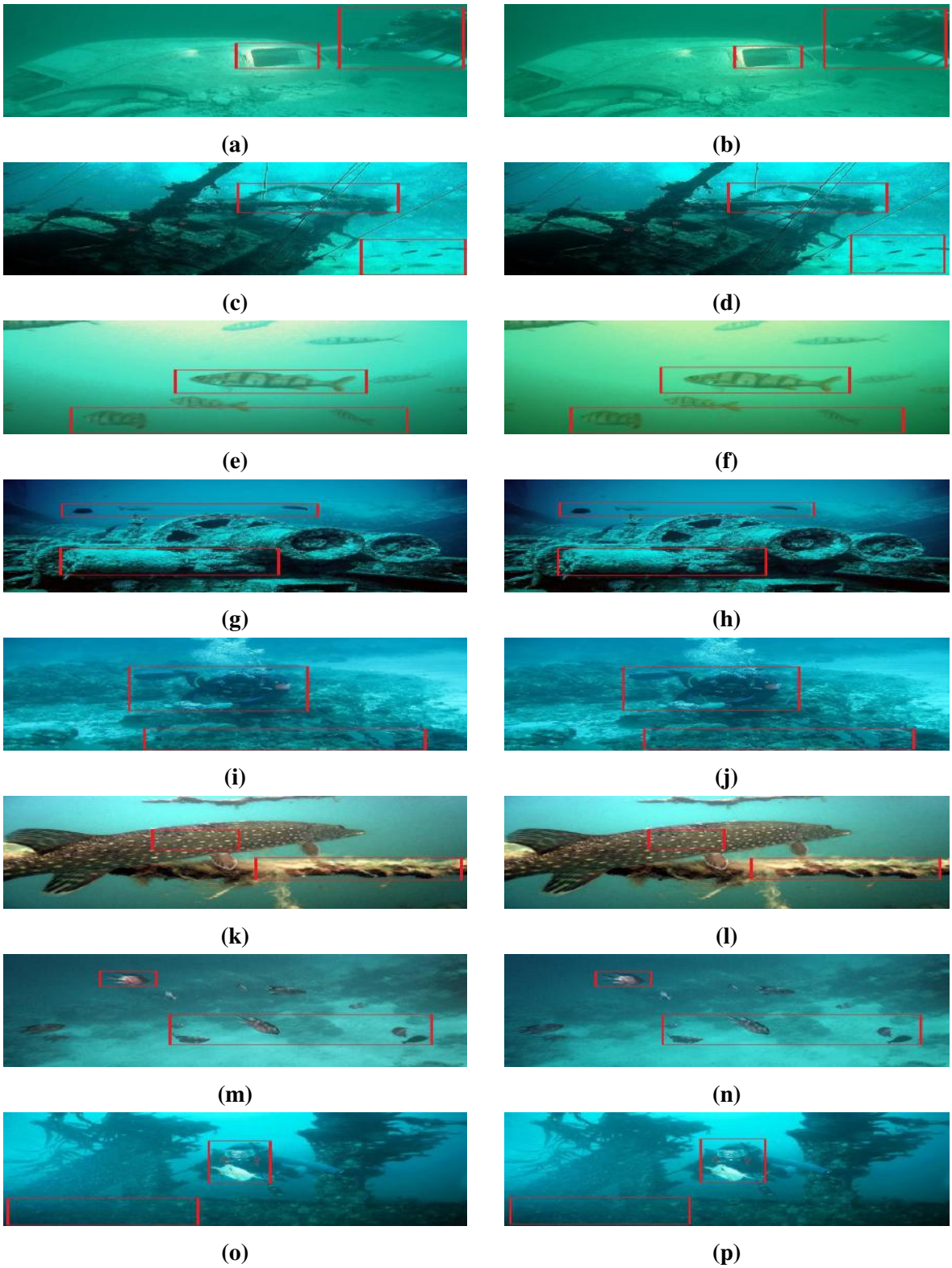

Figure 7.10: Output Images Produced using *PCA* Fusion (a),(c),(e),(g),(i),(k),(m),(o) with *DWT* and (b),(d),(f),(h),(j),(l),(n), (p) with *RBFT*

In Figures 7.5-7.10, the first column contains the output images generated by *FDWT* and second column consists of images processed by *RBFT*. Figure 7.5 is produced by *FDWT* and *RBFT* using Average fusion, Figure 7.6 by Maximum fusion and Figure 7.7 uses Minimum fusion. The output images shown in Figure 7.8 are generated by *IHS* fusion, Figure 7.9 and 7.10 by Brovey and *PCA*, respectively; processed using *FDWT* and *RBFT*.

With visual inspection, it is observed that the images generated by *FDWT* have some halo effects along the edges due to loss of pixels with some distortions and in comparison, *RBFT* does not contain these halo artifacts providing refined panoramic images. The red boxes around the edges justifies that *RBFT* provides a better view of nearby or distant objects. However, the visual inspection does not completely describe the quality of resultant images. Therefore, the quality of images are analyzed on various parameters such as *MSE*, *PSNR*, *SSIM* and *Entropy*. The analyzed values on the basis of these parameters are shown in Table 7.1.

From Table 7.1, the minimum values of *MSE* for 'Autowrack' are 0.0002 and 0.0002 whereas the maximum values are 0.0325 and 0.0067; for *FDWT* and *RBFT*, respectively. The minimum values for *PSNR* are 63.01 (*d*B) and 66.92 (*d*B); and maximum values are 84.80 (*d*B) and 84.84 (*d*B), for *FDWT* and *RBFT*, respectively. The minimum values noted for *SSIM* are 0.5814 and 0.554; maximum values are 0.9848 and 0.9853; for *FDWT* and *RBFT*, respectively. The *Entropy* for *FDWT* and *RBFT* has minimum values of 6.2406 and 6.2471; maximum values of 7.2814 and 7.3079, respectively.

For 'Severance-equalised', the minimum and maximum values for *MSE* are 0.0006 (for *FDWT*), 0.0006 (for *RBFT*); and 0.0252 (for *FDWT*), 0.0029 (for *RBFT*), respectively. The *PSNR* is noted minimum as 64.02 (*d*B) and 73.18 (*d*B); maximum as 80.33 (*d*B) and 80.30 (*d*B) for *FDWT* and *RBFT*, respectively. The observed values for *SSIM* is minimum as 0.5348 and 0.5149, maximum as 0.9832 and 0.9833, for *FDWT* and *RBFT*, respectively. The *Entropy* for *FDWT* and *RBFT* is noted minimum as 6.4072, 6.3195 and maximum as 7.4291, 7.4213, respectively.

The *MSE* for 'Tauchen-Straussee-Grunstich' has minimum values of 0.0001 and 0.0001, maximum values of 0.0845 and 0.008; for *FDWT* and *RBFT*, respectively. The observed minimum and maximum values of *PSNR* are 58.86 (*d*B) (for *FDWT*), 64.14 (*d*B) (for *RBFT*)

and 91.08 (*d*B) (for *FDWT*), 88.30 (*d*B) (for *RBFT*), respectively. The values for *SSIM* is ranged minimal as 0.303, 0.5831, and maximum as 0.9895, 0.9845; for *FDWT* and *RBFT*, respectively. The *Entropy* has minimum values of 6.5114, 5.8216 and maximum values of 7.6591, 7.6345; for *FDWT* and *RBFT*, respectively.

The minimum values of *MSE* for 'Thistlegorm-train-parts' are 0.0006 and 0.0007 whereas the maximum values are 0.025 and 0.0017; for *FDWT* and *RBFT*, respectively. The minimum values for *PSNR* are 64.14 (*d*B) and 74.97 (*d*B), and maximum values are 79.46 (*d*B) and 79.52 (*d*B), for *FDWT* and *RBFT*, respectively. The minimum values noted for *SSIM* are 0.4124 and 0.5462; maximum values are 0.976 and 0.9754; for *FDWT* and *RBFT*, respectively. The *Entropy* for *FDWT* and *RBFT* has minimum values of 6.0371 and 6.2716; maximum values of 7.4619 and 7.4339, respectively.

For 'Usuario-Jaontiveros', the minimum and maximum values for *MSE* are 0.0004 (for *FDWT*), 0.0004 (for *RBFT*); and 0.0396 (for *FDWT*), 0.0022 (for *RBFT*), respectively. The *PSNR* is noted minimum as 62.04 (*d*B) and 66.86 (*d*B); maximum as 81.18 (*d*B) and 81.17 (*d*B) for *FDWT* and *RBFT*, respectively. The observed values for *SSIM* are minimum as 0.4866 and 0.5302, maximum as 0.9953 and 0.995, for *FDWT* and *RBFT*, respectively. The *Entropy* for *FDWT* and *RBFT* is noted minimum as 6.3492, 6.5087 and maximum as 7.4845, 7.4995, respectively.

The minimum values of *MSE* for 'Europaeischer-Hecht' are 0.0003 and 0.0004 whereas the maximum values are 0.0553 and 0.0245; for *FDWT* and *RBFT*, respectively. The minimum values for *PSNR* are 55.94 (*d*B) and 56.80 (*d*B), and maximum values are 82.35 (*d*B) and 81.27 (*d*B), for *FDWT* and *RBFT*, respectively. The minimum values noted for *SSIM* are 0.3183 and 0.3084; maximum values are 0.9228 and 0.929; for *FDWT* and *RBFT*, respectively. The *Entropy* for *FDWT* and *RBFT* has minimum values of 6.4651 and 6.368; maximum values of 7.8526 and 7.8528, respectively.

Table 7.1: Comparison of Different Quality Metrics using Various Fusion Techniques

Images	Fusion Techniques	DWT				Ridgelet			
		MSE	**PSNR (*d*B)**	**SSIM**	**Entropy**	**MSE**	**PSNR (*d*B)**	**SSIM**	**Entropy**
Autowrack	Average	0.0002	83.80	0.9139	7.2009	0.0002	83.87	0.9399	7.1948
	Maximum	0.0002	84.24	0.9848	7.2814	0.0003	83.33	0.9853	7.3079
	Minimum	0.0002	84.63	0.9777	7.1215	0.0002	84.84	0.9785	7.1263
	IHS	0.0325	63.00	0.5814	6.2406	0.0012	66.92	0.9061	6.2471
	Brovey	0.0067	65.77	0.6568	6.3949	0.0067	69.85	0.554	6.2519
	PCA	0.0002	83.77	0.9608	7.2208	0.0002	83.76	0.9405	7.1956
Severance-equalised	Average	0.0006	80.18	0.9832	7.3847	0.0006	80.19	0.9833	7.3573
	Maximum	0.0006	80.04	0.9795	7.4291	0.0006	80.16	0.9727	7.4213
	Minimum	0.0006	80.33	0.9806	7.3345	0.0006	80.30	0.9753	7.3324
	IHS	0.0252	64.02	0.5348	6.892	0.0012	77.52	0.9315	6.3195
	Brovey	0.006	70.10	0.545	6.4072	0.0029	73.16	0.5149	6.6484
	PCA	0.0006	80.18	0.9831	7.3757	0.0006	80.18	0.9833	7.3704
Tauchen-Straussee-Grunstich	Average	0.0053	70.89	0.7281	7.6306	0.0053	70.92	0.7298	7.6329
	Maximum	0.0001	65.48	0.9895	7.0684	0.0001	67.49	0.9701	7.1483
	Minimum	0.0005	91.08	0.9885	7.6136	0.0001	88.29	0.9845	7.6141
	IHS	0.0845	58.86	0.303	7.1305	0.008	64.14	0.8162	7.0806
	Brovey	0.0166	65.94	0.503	6.5114	0.0021	75.00	0.5831	5.8216
	PCA	0.002	67.86	0.8899	7.6591	0.0054	70.83	0.7297	7.6345
Thistlegorm-train-parts	Average	0.0007	79.16	0.9465	7.2925	0.0007	79.15	0.9446	7.284
	Maximum	0.0007	79.46	0.976	7.4619	0.0007	79.52	0.9754	7.4339
	Minimum	0.0006	77.86	0.9746	6.9948	0.0007	77.98	0.9729	7.0327
	IHS	0.025	64.14	0.5469	6.8143	0.0012	75.61	0.9229	6.8817
	Brovey	0.008	69.12	0.4124	6.0371	0.0017	74.97	0.5462	6.2716
	PCA	0.0007	79.03	0.9485	7.2646	0.0007	79.17	0.9466	7.288

Usuario-Jaontiveros	Average	0.0004	81.18	0.9819	7.3904	0.0004	81.17	0.9814	7.3603
	Maximum	0.0005	80.77	0.9953	7.4845	0.0005	80.98	0.995	7.4995
	Minimum	0.0004	80.80	0.9947	7.185	0.0005	81.12	0.9944	7.2224
	IHS	0.0396	62.04	0.4866	6.3889	0.0016	66.86	0.9539	6.5841
	Brovey	0.0066	66.84	0.5355	6.3492	0.0022	72.33	0.5302	6.5087
	PCA	0.0004	81.14	0.9841	7.3929	0.0004	81.16	0.982	7.3805
Europaeischer-Hecht	Average	0.0057	70.33	0.8166	7.7596	0.0057	70.32	0.8177	7.7594
	Maximum	0.0003	82.35	0.9228	7.8526	0.0004	81.27	0.929	7.8528
	Minimum	0.0005	66.49	0.9146	7.7148	0.0007	66.49	0.9252	7.7404
	IHS	0.0553	57.23	0.3183	7.0488	0.0063	66.66	0.8276	7.4549
	Brovey	0.0282	55.94	0.3251	6.4651	0.0245	56.80	0.3084	6.368
	PCA	0.0057	70.56	0.8266	7.7597	0.0058	70.37	0.8156	7.7595
RedSeaEgyptFish	Average	0.0011	77.88	0.962	7.5446	0.001	77.56	0.9613	7.5448
	Maximum	0.0003	83.33	0.9926	7.6245	0.0002	83.79	0.9929	7.5686
	Minimum	0.0002	72.54	0.9957	7.221	0.0002	72.50	0.9955	7.2464
	IHS	0.032	62.89	0.459	6.5762	0.002	69.63	0.9191	6.6603
	Brovey	0.0052	61.21	0.4799	6.246	0.0039	65.29	0.4248	6.2434
	PCA	0.0009	77.23	0.9654	7.5853	0.0011	77.89	0.9621	7.5421
Wreckdiver-300	Average	0.0001	86.08	0.9865	7.0302	0.0001	86.10	0.9866	6.9859
	Maximum	0.0001	85.22	0.9967	7.1307	0.0001	85.45	0.9969	7.1194
	Minimum	0.0001	85.49	0.9973	6.863	0.0001	86.25	0.9972	6.8921
	IHS	0.0373	62.33	0.4839	6.7163	0.0003	75.22	0.9628	6.4794
	Brovey	0.0099	67.51	0.467	6.3886	0.002	73.91	0.5488	6.4416
	PCA	0.0001	86.03	0.9876	7.0077	0.0001	86.05	0.9866	7.0014

The *MSE* for 'RedSeaEgyptFish' has minimum values of 0.0002 and 0.0002, maximum values of 0.032 and 0.0039; for *FDWT* and *RBFT*, respectively. The observed minimum and maximum values of *PSNR* are 61.21 (*d*B) (for *FDWT*), 65.30 (*d*B) (for *RBFT*) and 83.33 (*d*B) (for *FDWT*), 83.80 (*d*B) (for *RBFT*), respectively. The value for *SSIM* is ranged minimal as 0.459, 0.4248, and maximum as 0.9957, 0.9955; for *FDWT* and *RBFT*, respectively. The *Entropy* has minimum values of 6.246, 6.2434 and maximum values of 7.6245, 7.5686; for *FDWT* and *RBFT*, respectively.

For 'Wreckdiver-300', the minimum and maximum values for *MSE* are 0.0001 (for *FDWT*), 0.0001 (for *RBFT*); and 0.0373 (for *FDWT*), 0.002 (for *RBFT*), respectively. The *PSNR* is noted minimum as 62.33 (*d*B) and 73.90 (*d*B); maximum as 86.08 (*d*B) and 86.25 (*d*B) for *FDWT* and *RBFT*, respectively. The observed values for *SSIM* are minimum as 0.467 and 0.5488, maximum as 0.9973 and 0.9972, for *FDWT* and *RBFT*, respectively. The *Entropy* for *FDWT* and *RBFT* is noted minimum as 6.3886, 6.4416 and maximum as 7.1307, 7.1194, respectively.

Thus, it is observed that *RBFT* has far better results as compared with *FDWT*. The *FDWT* and *RBFT* has almost similar values of quality metrics in combination with *Average*, *Maximum* and *Minimum* fusion techniques. In comparsion with *FDWT*, the *RBFT* provides refined panoramic images in terms of visual inspection and quality metrics in combination with *IHS*, *Brovey* and *PCA* fusion techniques. Thus, *RBFT* is better than *FDWT*.

The comparison among *FDWT* and *RBFT* for obtained values of quality metrics for each fusion techniques are shown in Figures 7.11 - 7.16.

Figure 7.11 show the comparison among quality metrics of various images using *FDWT* and *RBFT* in combination with Average fusion. It is observed from Figure 7.11(a) that *MSE* for *FDWT* and *RBFT* have similar values and are providing less erred pixels. Figure 7.11(b) suggests that *PSNR* for *FDWT* and *RBFT* has alike values providing good nature. Figure 7.11(c) describes the equal intensities in resultant images on the basis of *SSIM* for *FDWT* and *RBFT*, respectively. Figure 7.11(d) suggests uniform content information on the basis of *Entropy* using *FDWT* and *RBFT*.

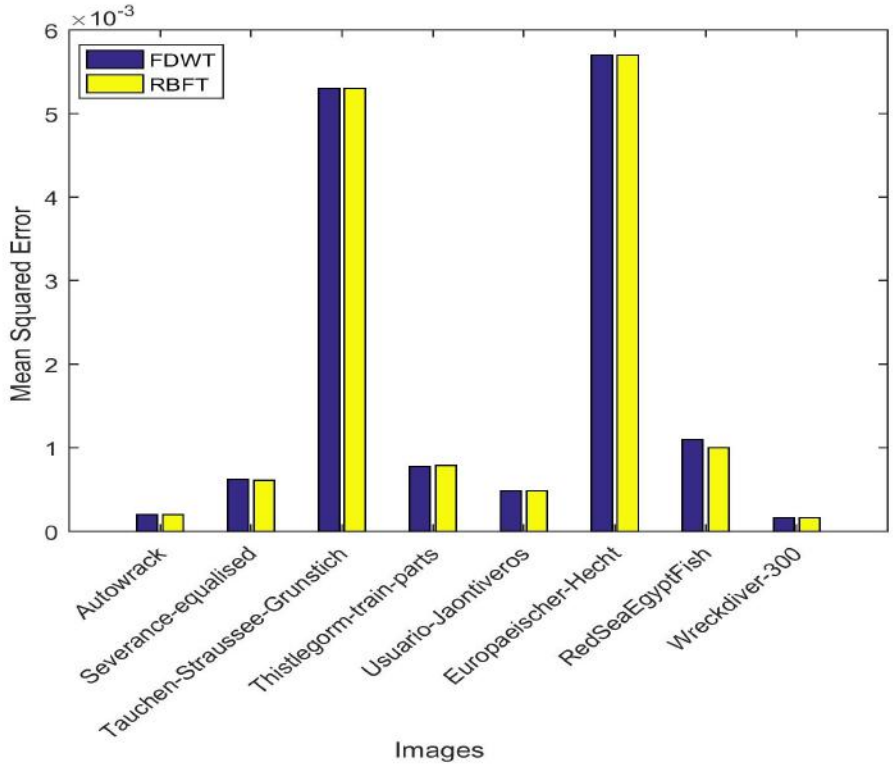
×10^-3
6
5
4
3
2
1
0
FDWT
RBFT
Mean Squared Error
Autowrack
Severance-equalised
Tauchen-Straussee-Grunstich
Thistlegorm-train-parts
Usuario-Jaontiveros
Europaeischer-Hecht
RedSeaEgyptFish
Wreckdiver-300
Images

(a)

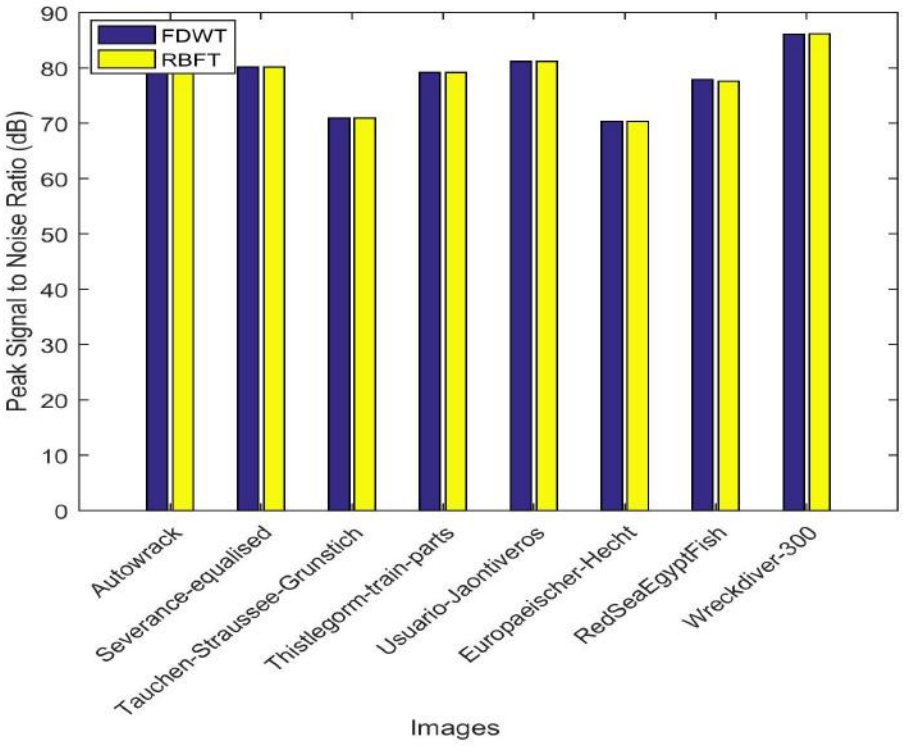
90
80
70
60
50
40
30
20
10
0
FDWT
RBFT
Peak Signal to Noise Ratio (dB)
Autowrack
Severance-equalised
Tauchen-Straussee-Grunstich
Thistlegorm-train-parts
Usuario-Jaontiveros
Europaeischer-Hecht
RedSeaEgyptFish
Wreckdiver-300
Images

(b)

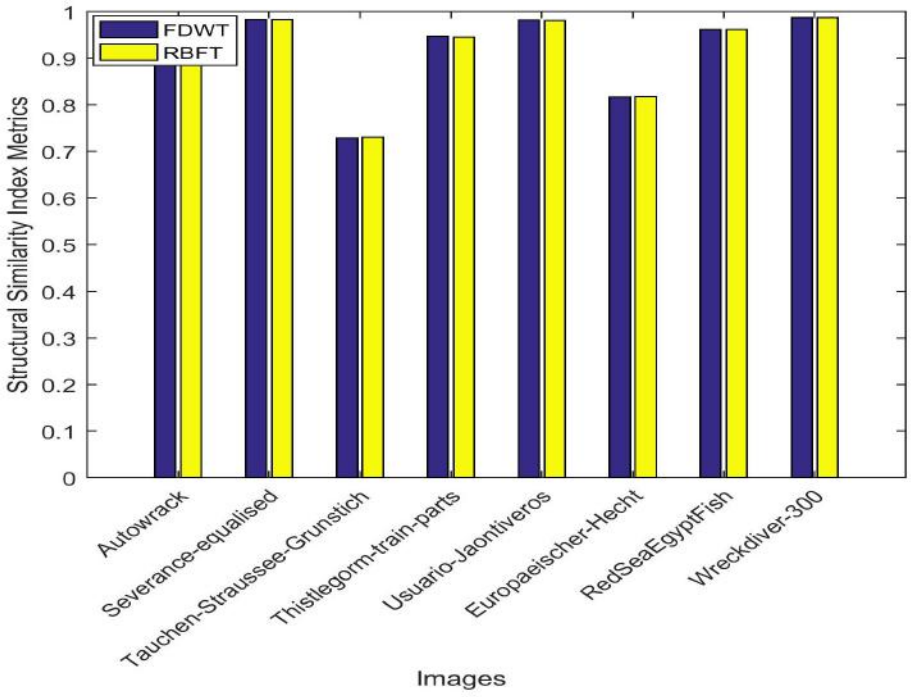

(c)

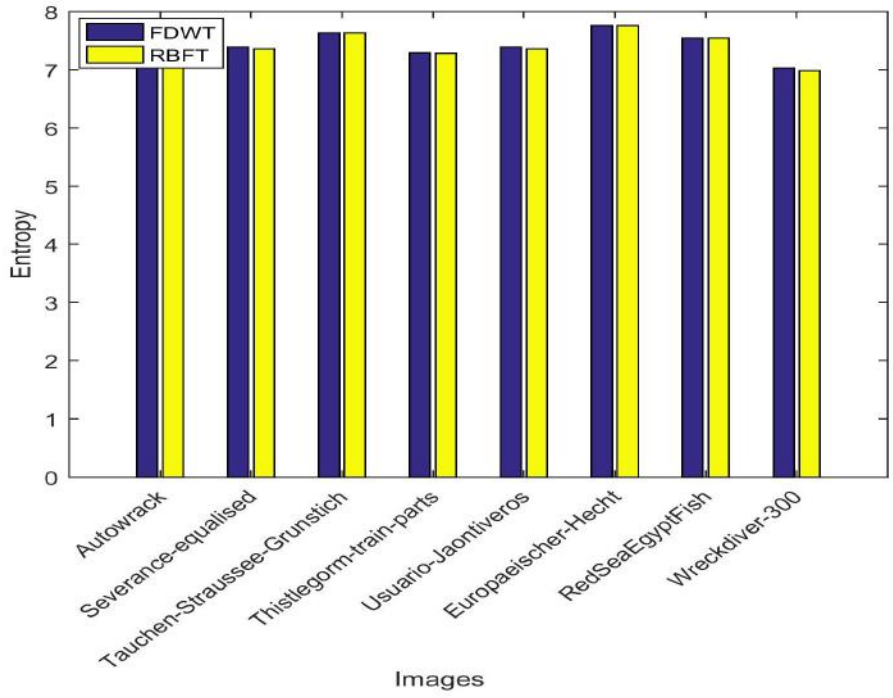

(d)

Figure 7.11: Comparison Graphs for *FDWT* and *RBFT* with Average Fusion for Metrics (a) Mean Squared Error (b) Peak Signal to Noise Ratio (c) Structural Similarity Index Metrics and (d) Entropy

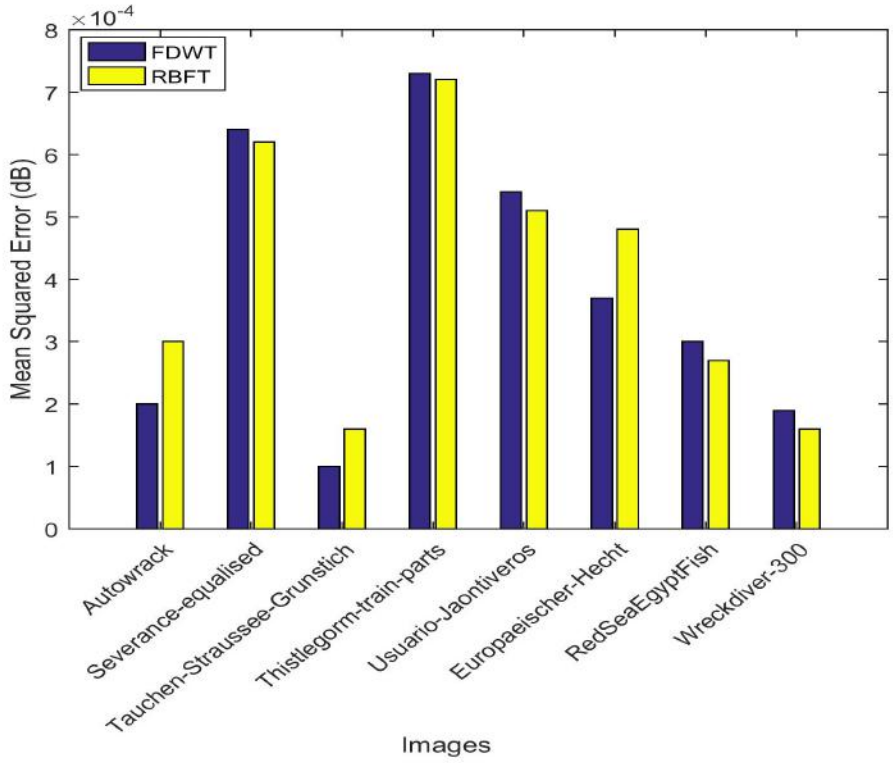
×10^-4
FDWT
RBFT
Mean Squared Error (dB)
0
1
2
3
4
5
6
7
8
Autowrack
Severance-equalised
Tauchen-Straussee-Grunstich
Thistlegorm-train-parts
Usuario-Jaontiveros
Europaeischer-Hecht
RedSeaEgyptFish
Wreckdiver-300
Images

(a)

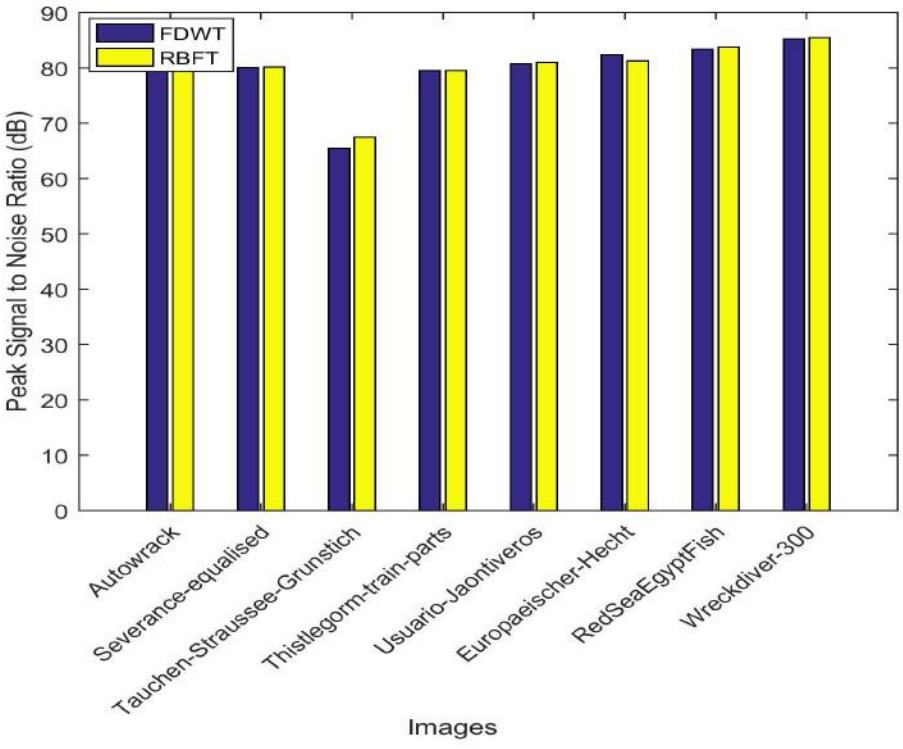
FDWT
RBFT
Peak Signal to Noise Ratio (dB)
0
10
20
30
40
50
60
70
80
90
Autowrack
Severance-equalised
Tauchen-Straussee-Grunstich
Thistlegorm-train-parts
Usuario-Jaontiveros
Europaeischer-Hecht
RedSeaEgyptFish
Wreckdiver-300
Images

(b)

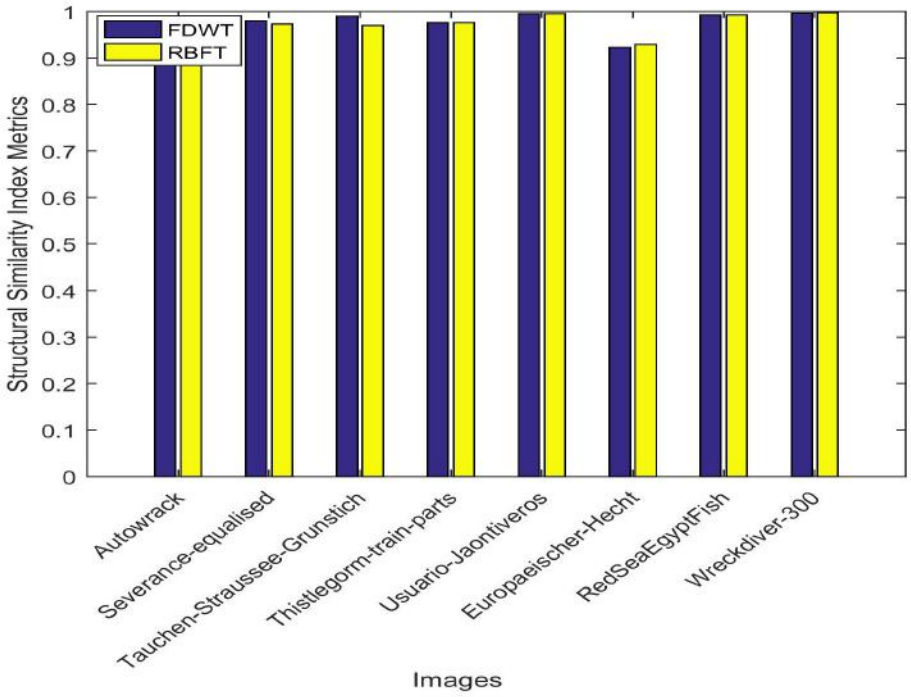

(c)

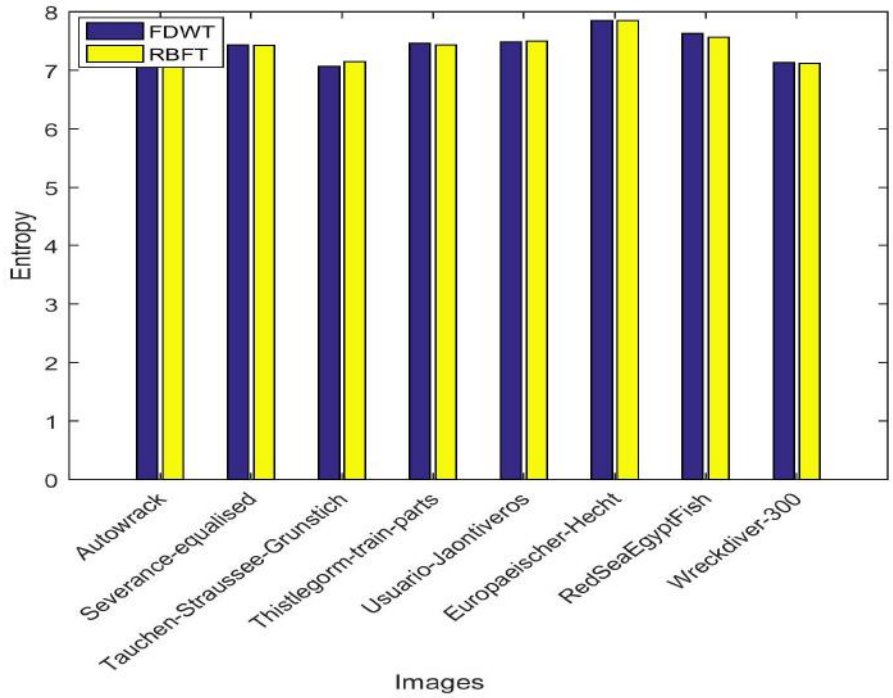

(d)

Figure 7.12: Comparison Graphs for *FDWT* and *RBFT* with Maximum Fusion for Metrics (a) Mean Squared Error (b) Peak Signal to Noise Ratio (c) Structural Similarity Index Metrics and (d) Entropy

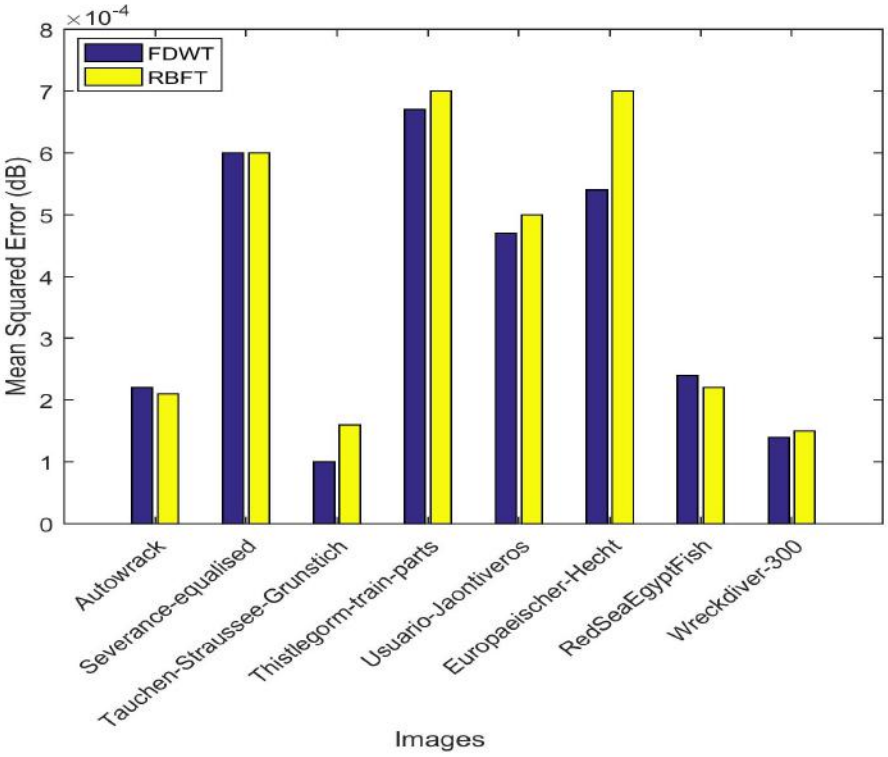
×10^-4
FDWT
RBFT
Mean Squared Error (dB)
0
1
2
3
4
5
6
7
8
Autowrack
Severance-equalised
Tauchen-Straussee-Grunstich
Thistlegorm-train-parts
Usuario-Jaontiveros
Europaeischer-Hecht
RedSeaEgyptFish
Wreckdiver-300
Images

(a)

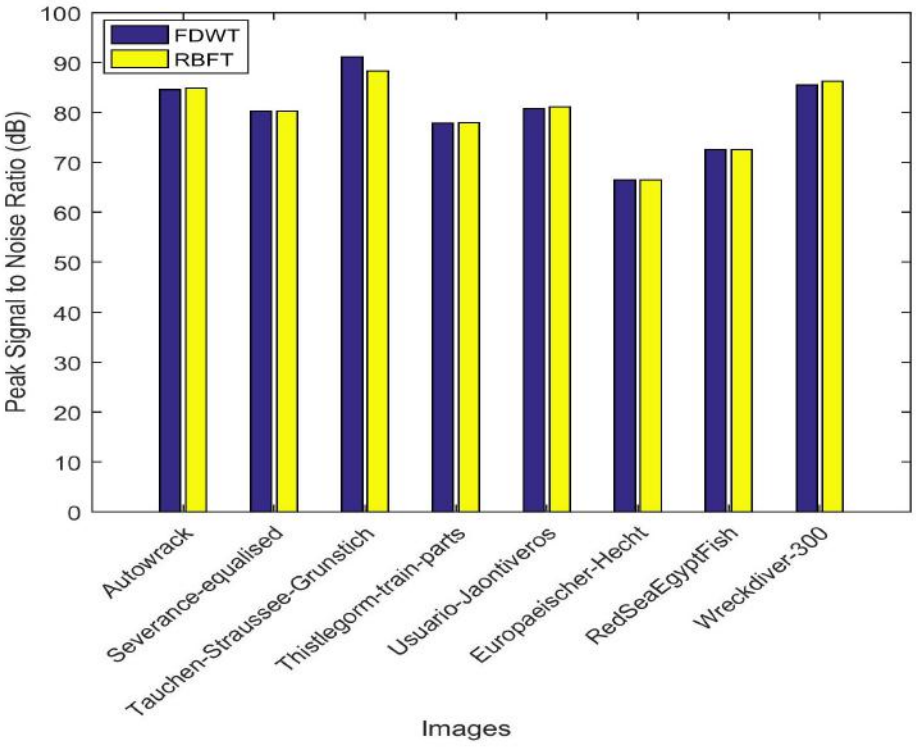
FDWT
RBFT
Peak Signal to Noise Ratio (dB)
0
10
20
30
40
50
60
70
80
90
100
Autowrack
Severance-equalised
Tauchen-Straussee-Grunstich
Thistlegorm-train-parts
Usuario-Jaontiveros
Europaeischer-Hecht
RedSeaEgyptFish
Wreckdiver-300
Images

(b)

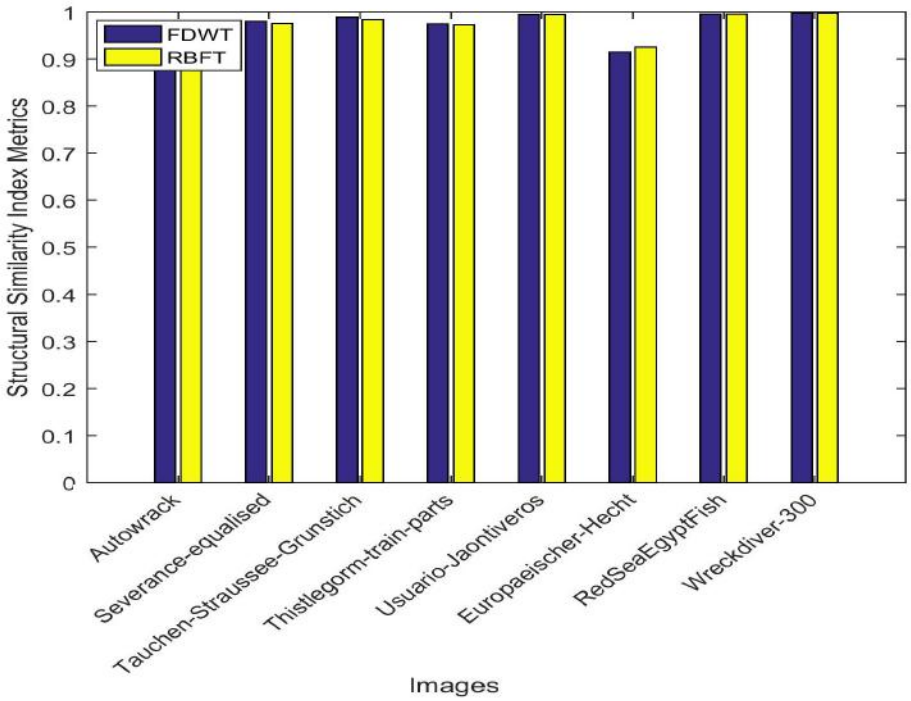

(c)

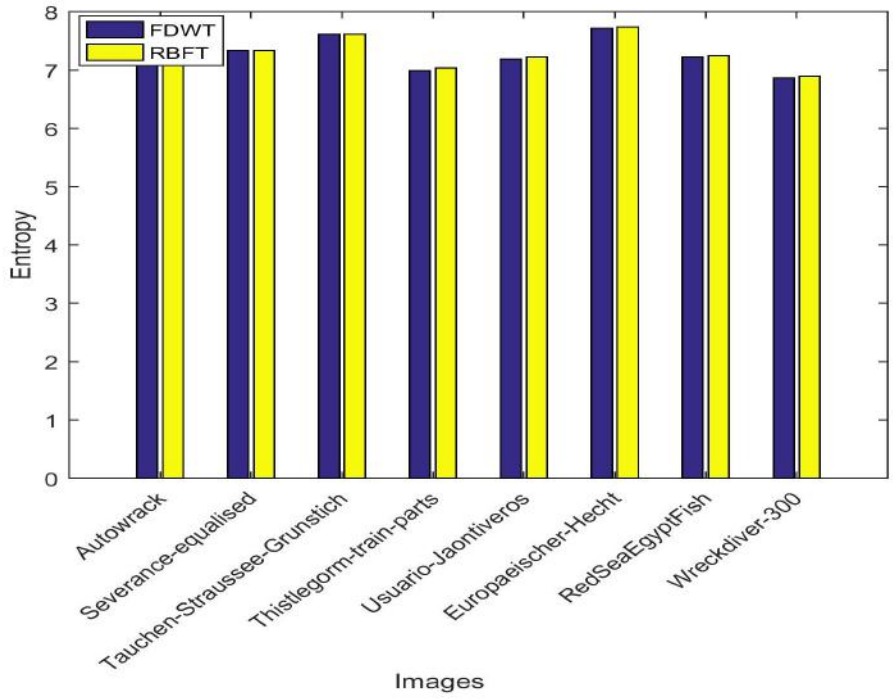

(d)

Figure 7.13: Comparison Graphs for *FDWT* and *RBFT* with Minimum Fusion for Metrics (a) Mean Squared Error (b) Peak Signal to Noise Ratio (c) Structural Similarity Index Metrics and (d) Entropy

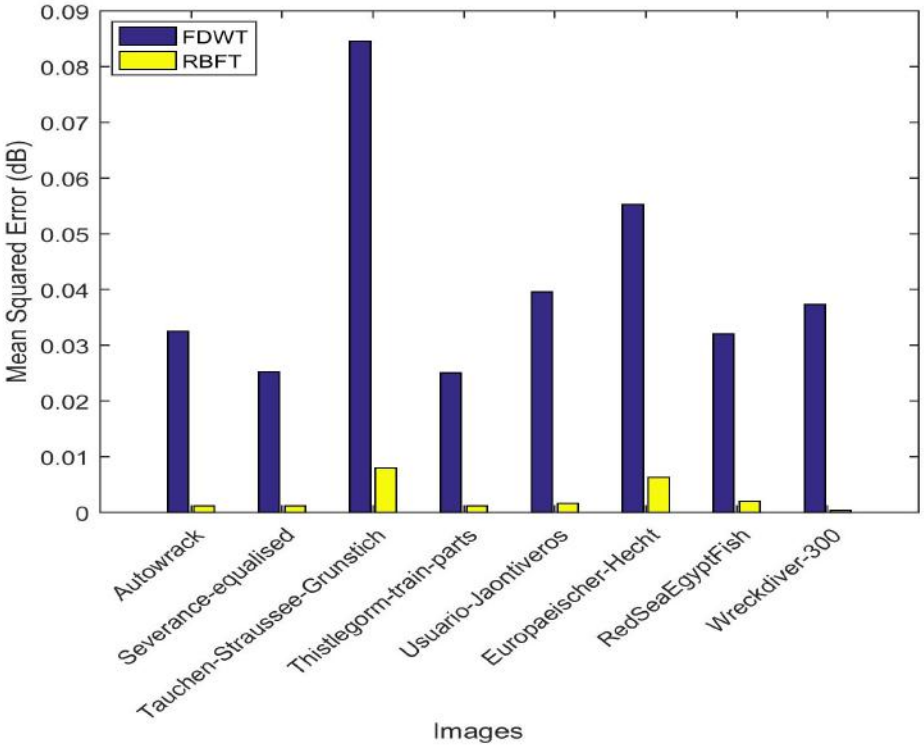
FDWT
RBFT
Mean Squared Error (dB)
0.09
0.08
0.07
0.06
0.05
0.04
0.03
0.02
0.01
0
Autowrack
Severance-equalised
Tauchen-Straussee-Grunstich
Thistlegorm-train-parts
Usuario-Jaontiveros
Europaeischer-Hecht
RedSeaEgyptFish
Wreckdiver-300
Images

(a)

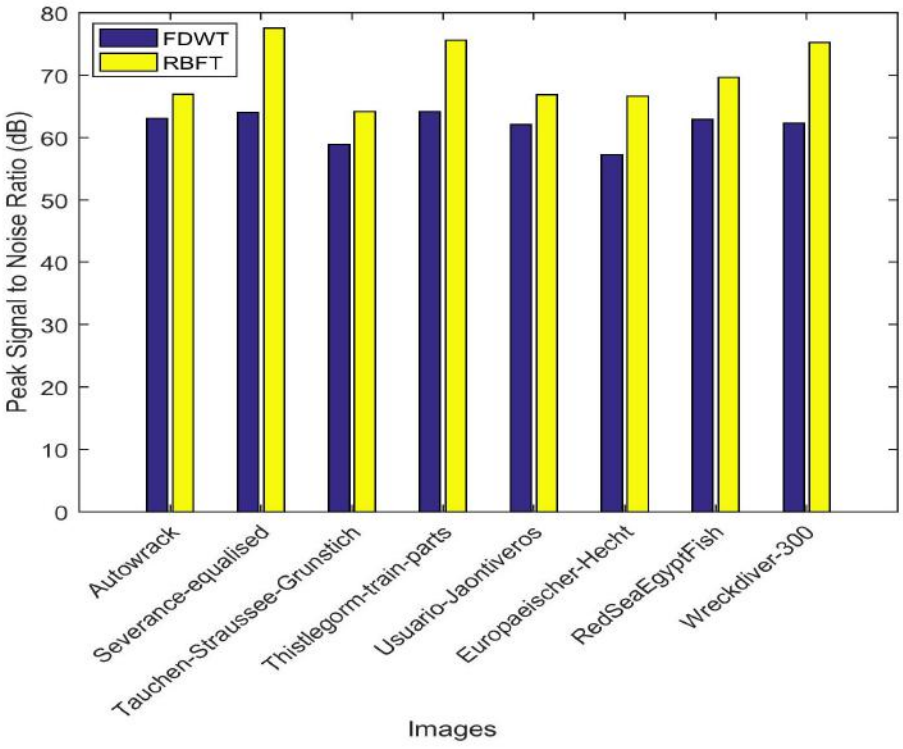
FDWT
RBFT
Peak Signal to Noise Ratio (dB)
80
70
60
50
40
30
20
10
0
Autowrack
Severance-equalised
Tauchen-Straussee-Grunstich
Thistlegorm-train-parts
Usuario-Jaontiveros
Europaeischer-Hecht
RedSeaEgyptFish
Wreckdiver-300
Images

(b)

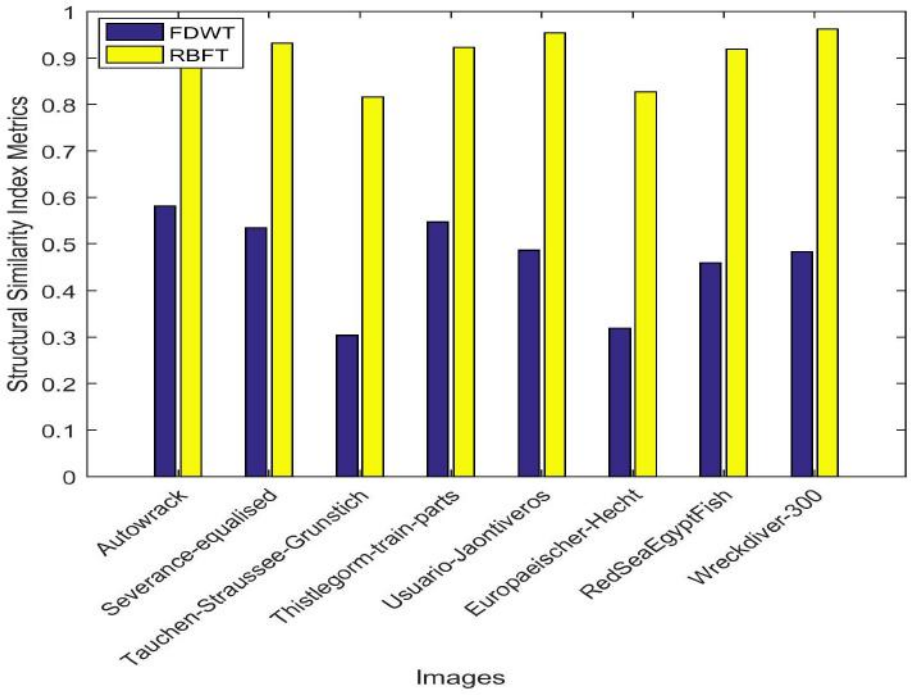

(c)

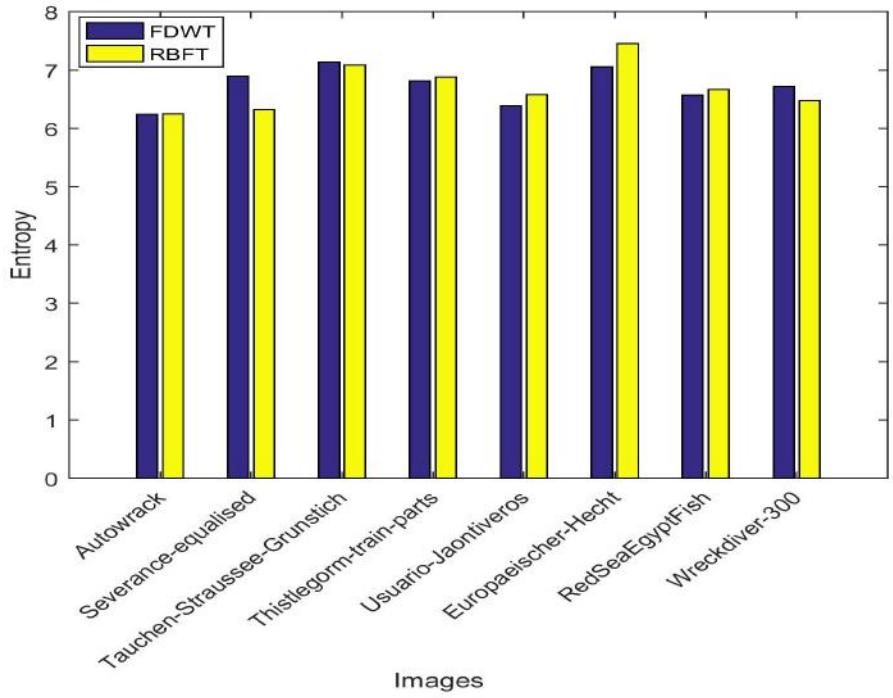

(d)

Figure 7.14: Comparison Graphs for *FDWT* and *RBFT* with *IHS* Fusion for Metrics (a) Mean Squared Error (b) Peak Signal to Noise Ratio (c) Structural Similarity Index Metrics and (d) Entropy

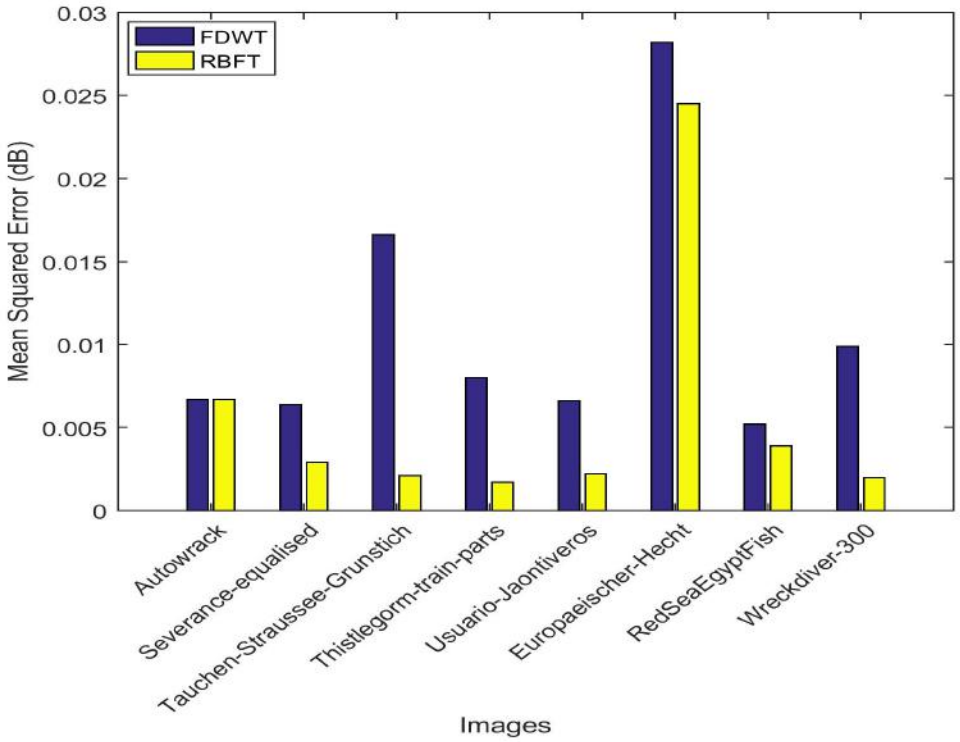
FDWT
RBFT
Mean Squared Error (dB)
0.03
0.025
0.02
0.015
0.01
0.005
0
Autowrack
Severance-equalised
Tauchen-Straussee-Grunstich
Thistlegorm-train-parts
Usuario-Jaontiveros
Europaeischer-Hecht
RedSeaEgyptFish
Wreckdiver-300
Images

(a)

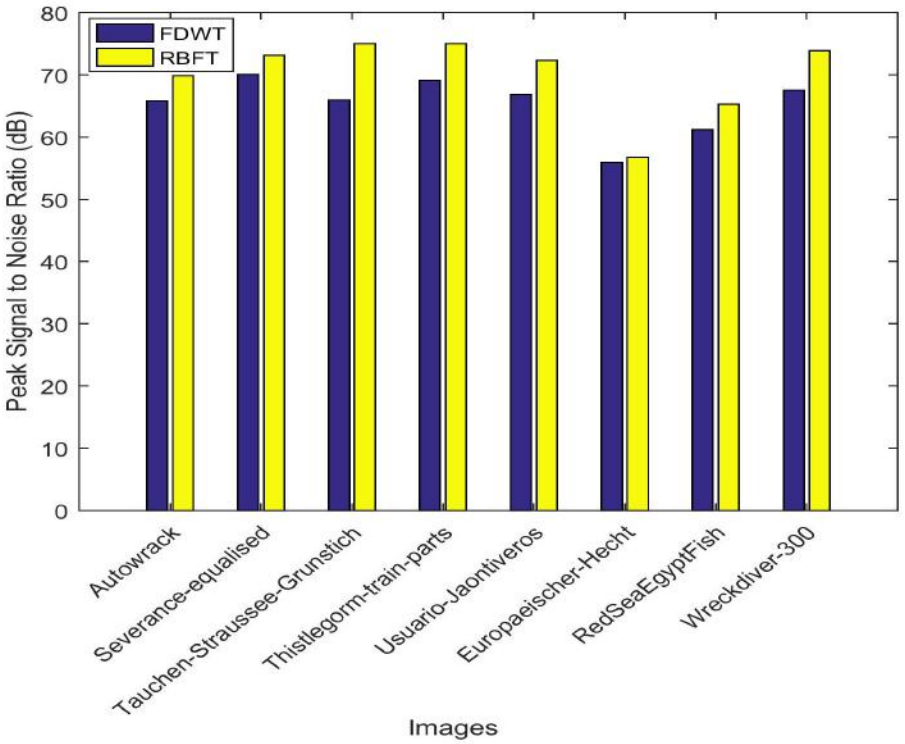
FDWT
RBFT
Peak Signal to Noise Ratio (dB)
80
70
60
50
40
30
20
10
0
Autowrack
Severance-equalised
Tauchen-Straussee-Grunstich
Thistlegorm-train-parts
Usuario-Jaontiveros
Europaeischer-Hecht
RedSeaEgyptFish
Wreckdiver-300
Images

(b)

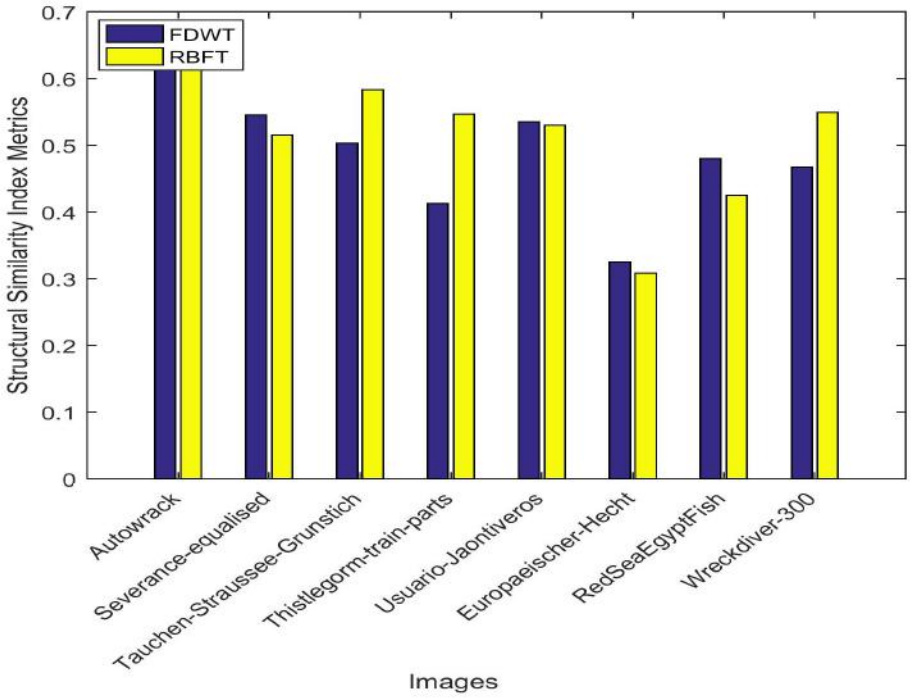

(c)

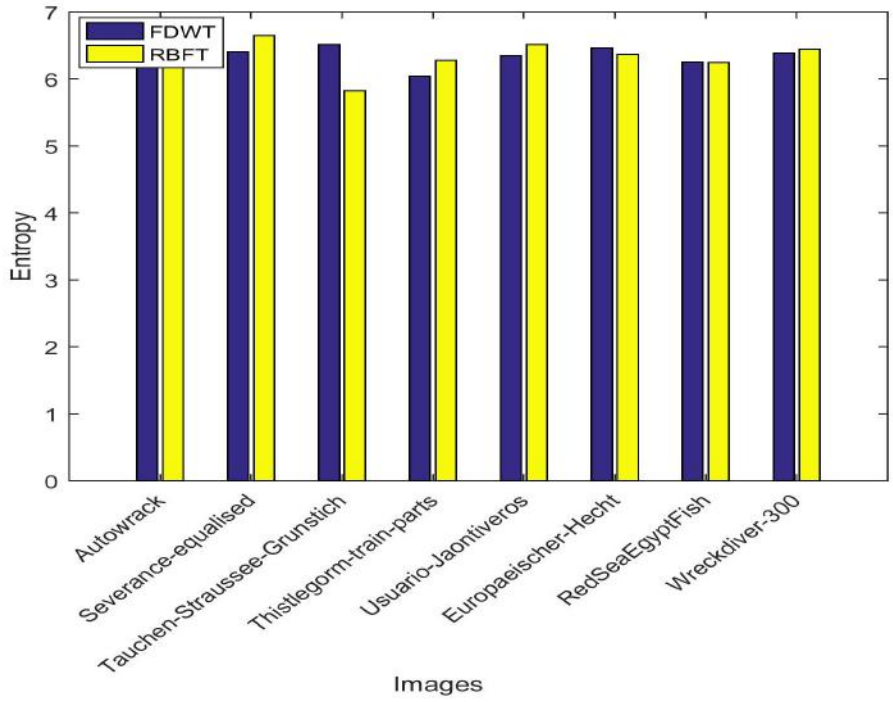

(d)

Figure 7.15: Comparison Graphs for *FDWT* and *RBFT* with Brovey Fusion for Metrics (a) Mean Squared Error (b) Peak Signal to Noise Ratio (c) Structural Similarity Index Metrics and (d) Entropy

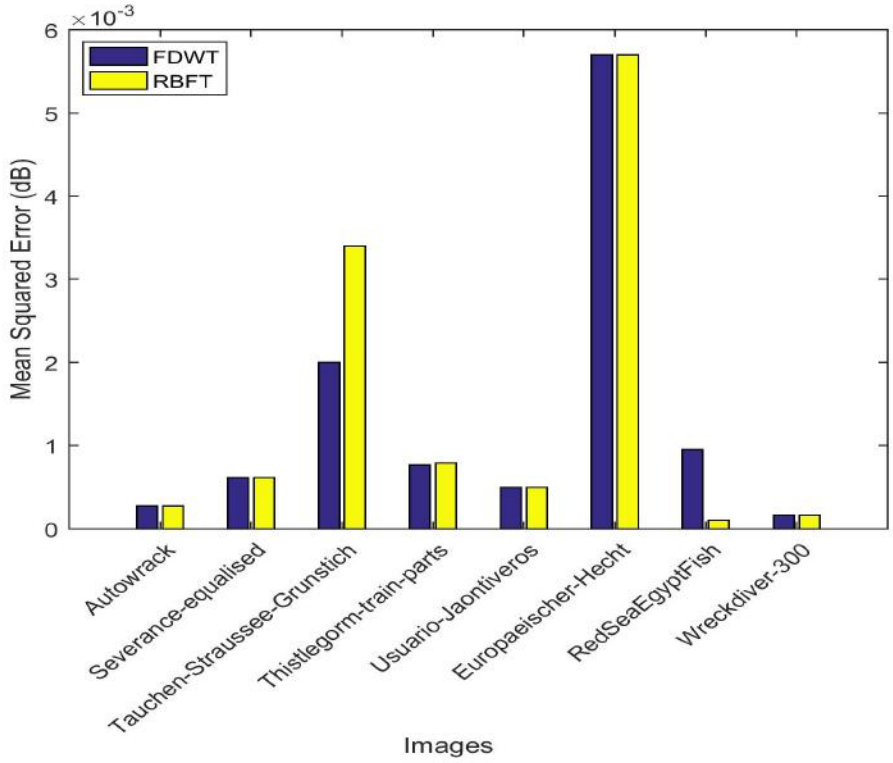
×10^-3
FDWT
RBFT
Mean Squared Error (dB)
0
1
2
3
4
5
6
Autowrack
Severance-equalised
Tauchen-Straussee-Grunstich
Thistlegorm-train-parts
Usuario-Jaontiveros
Europaeischer-Hecht
RedSeaEgyptFish
Wreckdiver-300
Images

(a)

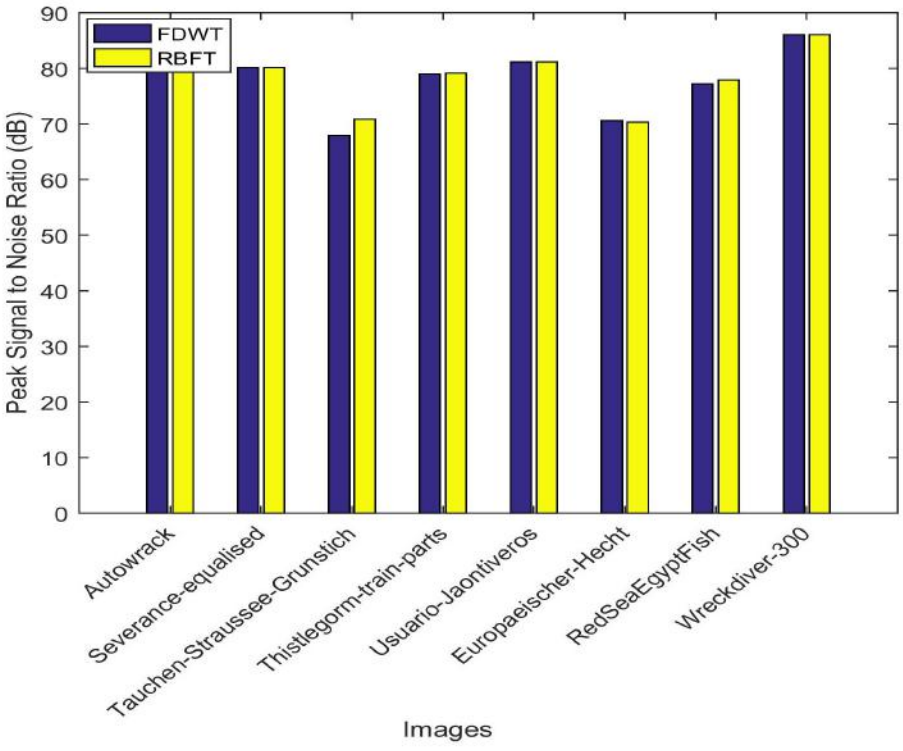
FDWT
RBFT
Peak Signal to Noise Ratio (dB)
0
10
20
30
40
50
60
70
80
90
Autowrack
Severance-equalised
Tauchen-Straussee-Grunstich
Thistlegorm-train-parts
Usuario-Jaontiveros
Europaeischer-Hecht
RedSeaEgyptFish
Wreckdiver-300
Images

(b)

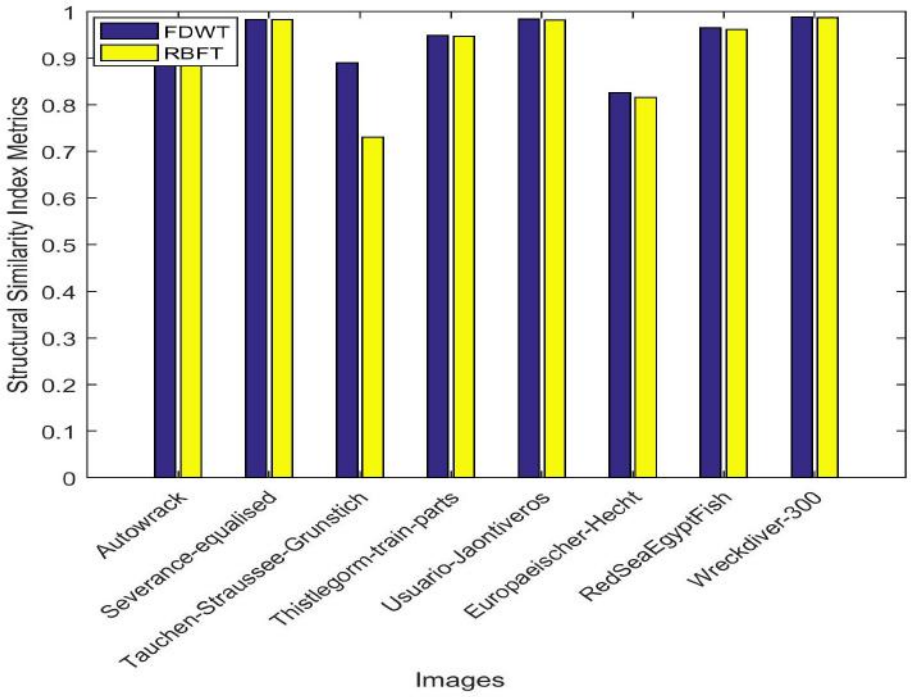

(c)

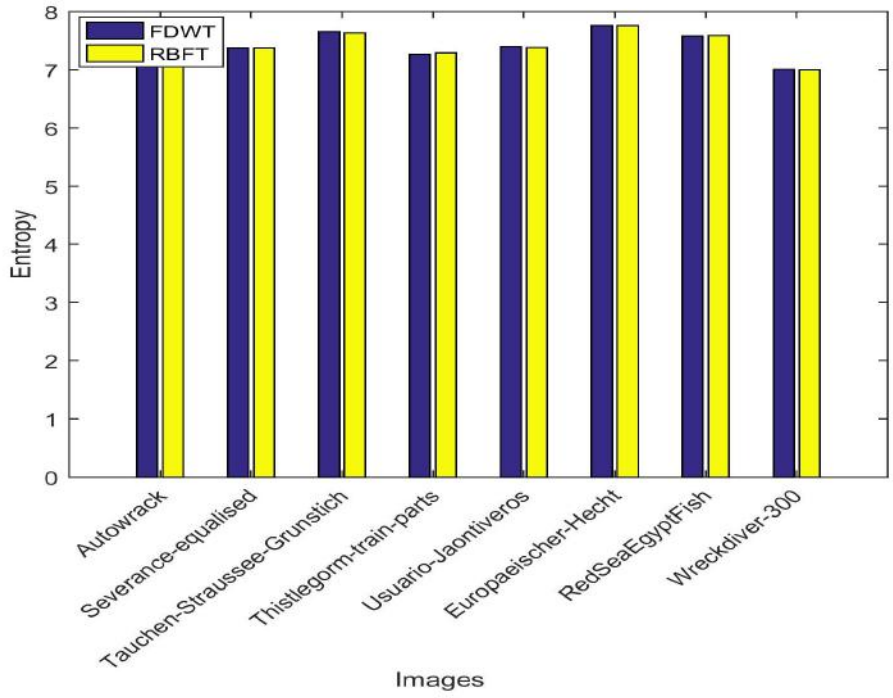

(d)

Figure 7.16: Comparison Graphs for *FDWT* and *RBFT* with *PCA* Fusion for Metrics (a) Mean Squared Error (b) Peak Signal to Noise Ratio (c) Structural Similarity Index Metrics and (d) Entropy

Figure 7.12 is produced using Maximum fusion with *FDWT* and *RBFT*. Figure 7.12(a) describes the fluctuation in *MSE* for both *FDWT* and *RBFT*. This is due to the change in colored pixels. Figure 7.12(b) shows the equivalence nature on the basis of *PSNR* for *FDWT* and *RBFT*. Figure 7.12(c) shows the *SSIM* values by both *FDWT* and *RBFT*; and is postulated that *RBFT* provides better intensities of pixels stored in images. *Entropy* values noted for *FDWT* and *RBFT* have similar content information shown in Figure 7.12(d); and is suggesting that produced images are of good quality.

The values for various quality metrics in Figure 7.13 is generated using combination of Minimum fusion with both *FDWT* and *RBFT*. From Figure 7.13(a), it is postulated that *MSE* by *RBFT* is slightly higher as compared with *MSE* by *FDWT*. It implies that the images generated by *RBFT* have more erred pixels than in *FDWT*. Figure 7.13(b) shows the equivalent values of *PSNR* by both *FDWT* and *RBFT*, respectively, suggesting the same quality for resultant images. Figure 7.13(c) describes the similar pixel's intensities of images by both techniques. Figure 7.13(d) results into better *Entropy* by *RBFT* in comparison with *FDWT*; and is postulated that the images generated by *RBFT* are rich in quality and content with few erred pixels.

Figure 7.14 describes the values for quality metrics using *IHS* fusion in combination with both *FDWT* and *RBFT*, respectively. As observed from Figure 7.14(a) the *MSE* produced by *RBFT* is negligible (< 0.01) whereas *FDWT* generates higher *MSE*. This suggests that images generated by *FDWT* contain erred pixels. Figure 7.14(b) shows the *PSNR* generated by both *FDWT* and *RBFT*. It suggests that quality of images is better in *RBFT* as compared with *FDWT*. The *SSIM* for *RBFT* has greater intensity value (equal to 1) whereas in comparison *SSIM* for *FDWT* has lesser intensity value, as suggested by Figure 7.14(c). The images generated by *RBFT* are enriched with *Entropy*, *i.e.*, content information, as compared with *FDWT* as described in Figure 7.14(d). Thus, it is found that *IHS* in combination with *RBFT* provides promising results having maximum information, negligible erred pixels and refined quality of panoramic images.

Figure 7.15 shows the comparison among various quality metrics analyzed for different images produced by *FDWT* and *RBFT* with *Brovey* fusion. Figure 7.15(a) presents the graphical notation of *MSE* observed using *FDWT* and *RBFT*. It is found that *MSE* values

in images by *RBFT* is very less as compared to images by *FDWT*. Figure 7.15(b) describes another aspect, *i.e.*, *PSNR* which suggests the refined output image generated by *RBFT* as compared with *FDWT*. Figure 7.15(c) postulates that the images are rich in pixel's intensities by *SSIM* when processed using *RBFT* and in comparison, there is loss of pixel by *FDWT*. Figure 7.15(d) theorizes the content information as observed through *Entropy* using *FDWT* and *RBFT*. It is concluded that resultant images produced by *RBFT* has more information with less pixel losses as compared to *FDWT*.

Figure 7.16 illustrates the quality metrics observed for *FDWT* and *RBFT* using *PCA* fusion. Figure 7.16(a) suggest the equivalent nature of erred pixels in both *FDWT* and *RBFT*. Figure 7.16(b) describes the slight increase in *PSNR* values by *RBFT* in comparison with *FDWT*. Figure 7.16(c) shows the *SSIM* values providing the pixel's intensities of image produced by *FDWT* and *RBFT*; and authorizes that resultant images have equal intensities by both techniques. Figure 7.16(d) describes the content information by *Entropy* values and is suggesting that *RBFT* in comparison with *FDWT* provide images having high quality data and has better visualization.

From the above analysis, it is concluded that *RBFT* in combination with *IHS*, *Brovey* and *PCA* fusion techniques, provide better quality panoramic images; as compared to *FDWT*. Moreover, the resultant images are enriched with content, pixel intensities and minimal erred pixels. They have better visual inspection, and *RBFT* retains pixels around the edges. Even, *RBFT* helps to refine panoramic images for studying the minutest information and smooth them by color approximations *via* fusion techniques. Thus, *RBFT* is better than *FDWT* for refining panoramic images.

7.6 Comparison with Existing Techniques

It is necessary to validate the results by comparing the suggested technique with existing techniques and to describe the relative degree of improvement. Having a pragmatic approach towards values obtained for quality metrics such as *MSE*, *PSNR*, *SSIM* and *Entropy* for individual images, by applying *RBFT*; and thus similar values are obtained by applying existing techniques of image refinement *namely*, Dark Channel Prior *(DCP)* (He et al. (2011)),

Contrast Limited Adaptive Histogram Equalization *(CLAHE)* (Yadav et al. (2014)), Guided Image Filtering (He et al. (2013)) and Discrete Wavelet Transform *(DWT)* (Andreopoulos and van der Schaar (2008)). The Table 7.2 and Figure 7.17 describe the difference among values for quality metrics thus obtained.

Table 7.2: Comparison with Existing Techniques

Images	**Techniques**	**Quality Metrics**			
		MSE	**PSNR**	**SSIM**	**Entropy**
Autowrack	*DCP*	0.0004	82.02	0.7535	6.9014
	CLAHE	0.0425	61.85	0.0409	7.1531
	Guided Filtering	0.0003	82.64	0.9153	7.1309
	DWT	0.0003	82.54	0.9105	7.0955
	RBFT	0.0002	83.76	0.9405	7.1956
Severance-equalised	*DCP*	0.0005	79.10	0.9829	7.3336
	CLAHE	0.0037	72.48	0.0808	7.3579
	Guided Filtering	0.0014	79.05	0.9768	7.3419
	DWT	0.0007	79.39	0.9564	7.1804
	RBFT	0.0006	80.18	0.9833	7.3704
Usuario-Jaontiveros	*DCP*	0.0003	80.95	0.9398	7.1789
	CLAHE	0.0245	64.24	0.0016	7.3006
	Guided Filtering	0.0012	79.06	0.9717	7.3578
	DWT	0.0005	80.54	0.9722	7.3425
	RBFT	0.0004	81.16	0.982	7.3805

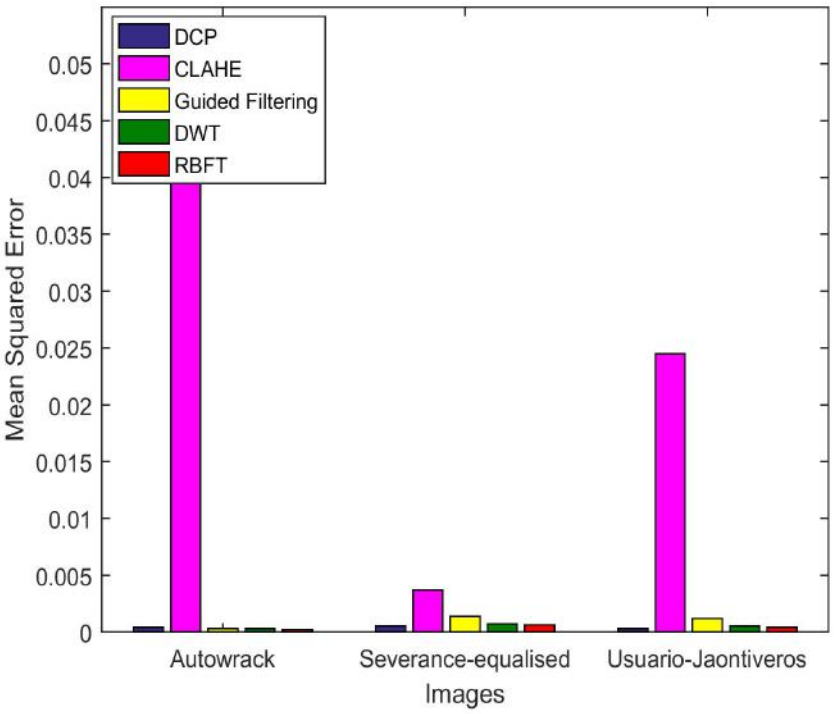
DCP
CLAHE
Guided Filtering
DWT
RBFT
Mean Squared Error
0.05
0.045
0.04
0.035
0.03
0.025
0.02
0.015
0.01
0.005
0
Autowrack
Severance-equalised
Usuario-Jaontiveros
Images

(a)

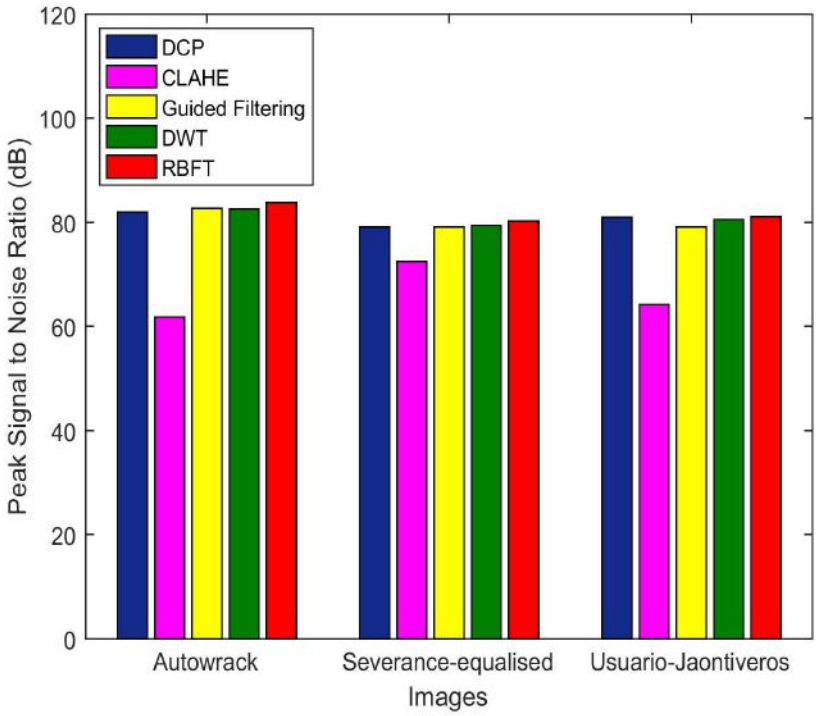
DCP
CLAHE
Guided Filtering
DWT
RBFT
Peak Signal to Noise Ratio (dB)
120
100
80
60
40
20
0
Autowrack
Severance-equalised
Usuario-Jaontiveros
Images

(b)

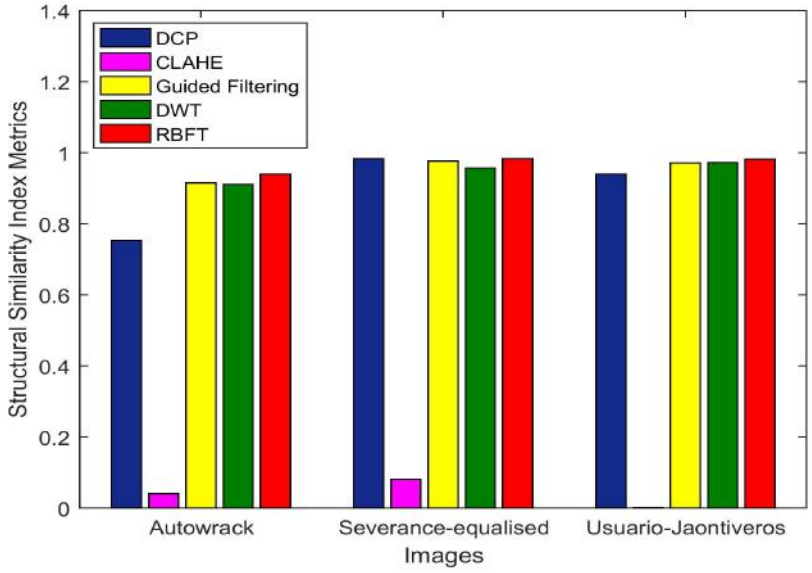

(c)

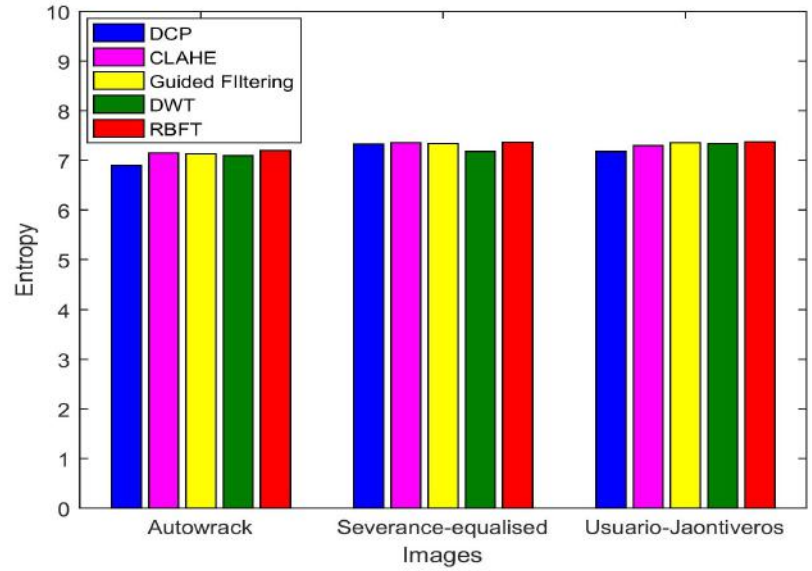

(d)

Figure 7.17: Comparison with Existing Techniques for Metrics (a) Mean Squared Error (b) Peak Signal to Noise Ratio (c) Structural Similarity Index Metrics and (d) Entropy

It is observed from Figure 7.17 that *RBFT* produces quality panoramic images as compared with existing techniques of image refinement. It provides resultant images with minimal erred pixels, *i.e.*, equivalent to zero (as observed from Figure 7.17(a)), higher *PSNR* (shown in Figure 7.17(b)), maximum pixel intensities (*see* Figure 7.17(c)) and retain the content information by combining two images of the same area (shown in Figure 7.17(d)).

The resultant images produced by existing and proposed techniques are shown in Figures 7.18-7.20.

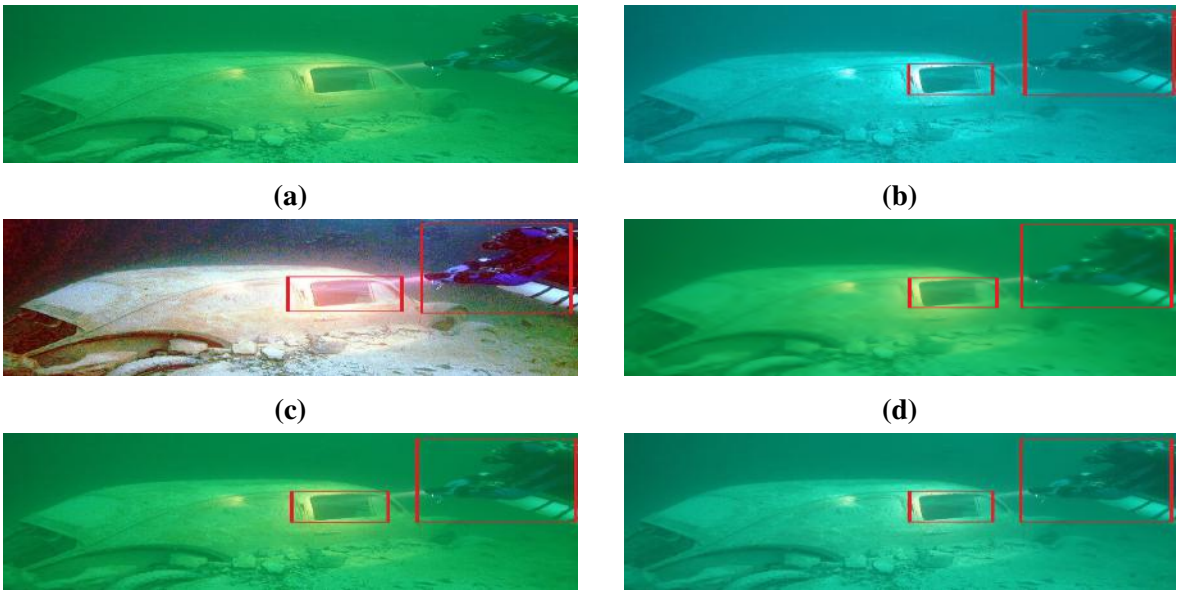

(a) **(b)** **(c)** **(d)** **(e)** **(f)**

Figure 7.18: Results of Autowrack (a) Input Image (b) *DCP* (c) *CLAHE* (d) *Guided Filtering* (e) *DWT* (f) *RBFT*

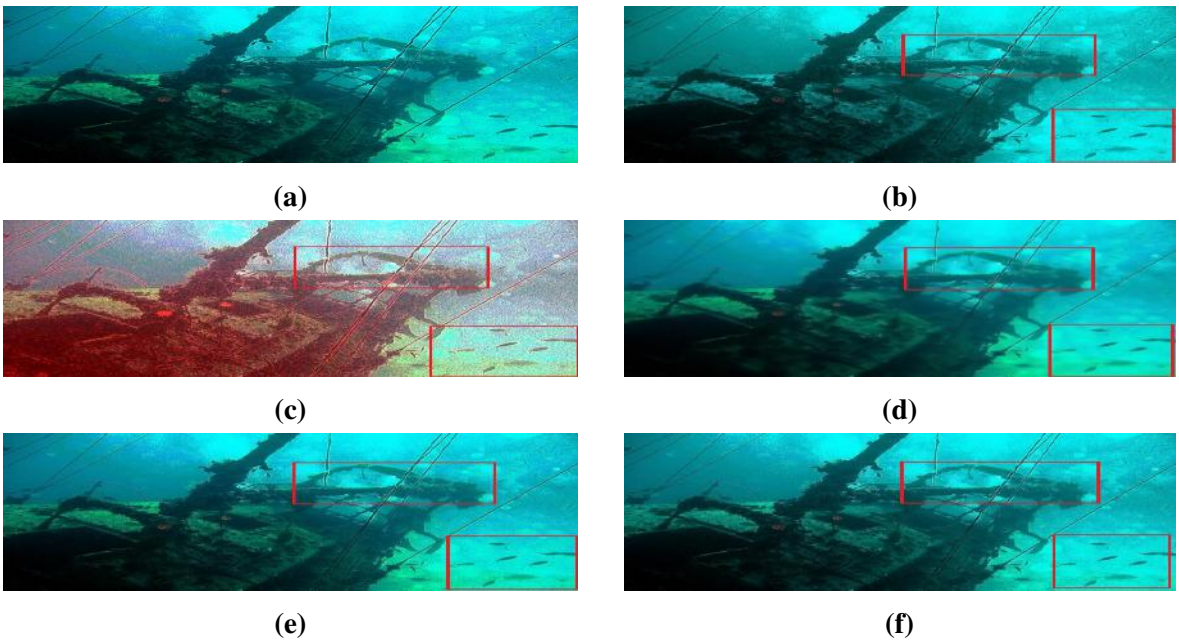

(a) **(b)** **(c)** **(d)** **(e)** **(f)**

Figure 7.19: Results of Severance-equalised (a) Input Image (b) *DCP* (c) *CLAHE* (d) *Guided Filtering* (e) *DWT* (f) *RBFT*

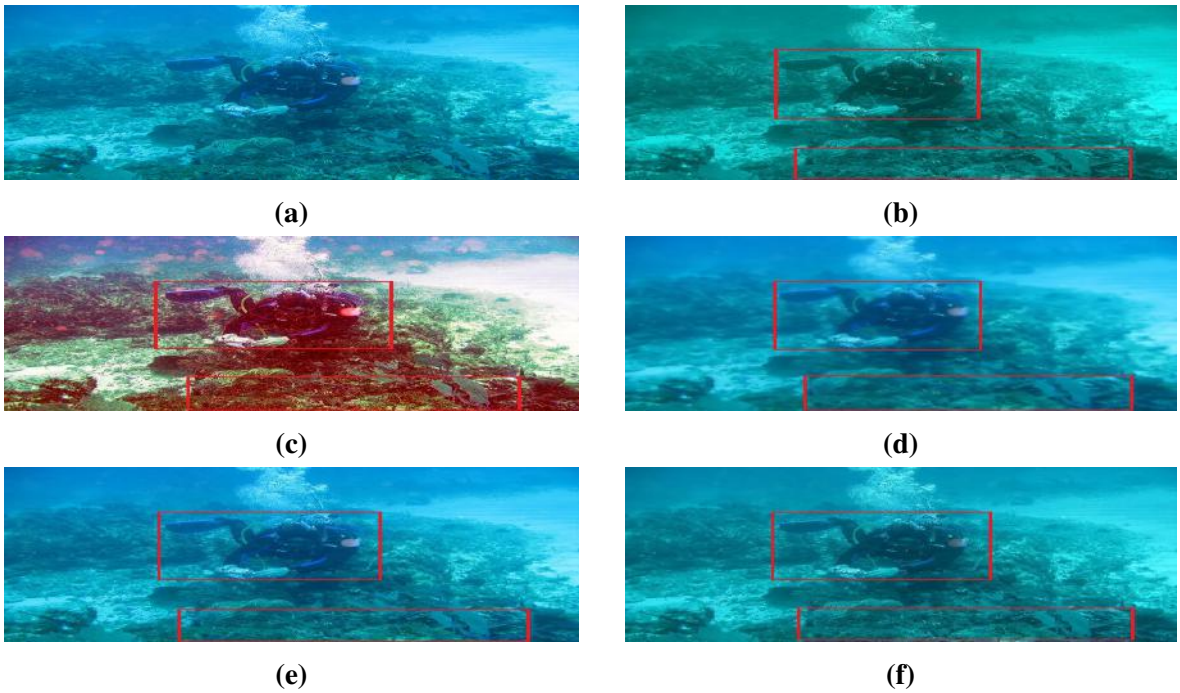

Figure 7.20: Results of Usuario-Jaontiveros (a) Input Image (b) *DCP* (c) *CLAHE* (d) *Guided Filtering* (e) *DWT* (f) *RBFT*

Figures 7.18-7.20 show the resultant panoramic images produced by *DCP*, *CLAHE*, *Guided Filtering*, *DWT* and proposed *RBFT*. It is found that *DCP* helps in removing the haze artifacts from images but adheres to the problem of color distortion. *CLAHE* improves the contrast of resultant images but intensities of most of the pixels got lost and thus, does not retain the content stored in images. *Guided Filtering* improves the quality by removing the problem of *DCP*, *i.e.*, color distortion but provide images with blurriness and erred pixels along edges. *DWT* helps in producing refined images by removing errors through high and loss pass filters but faces the problem of aliasing and does not retain pixel's intensity along edges. In comparison with existing techniques, *RBFT* provides better refined panoramic images with minimal loss of pixels and retains maximum content information with greater pixel intensities.

7.7 Conclusion

RBFT helps in refining underwater panoramic images. It filters and smooth the pixels along edges; and these pixels are fused to improve contrast of the resultant image producing good

quality and refined panoramic images. In comparison with state-of-the-art techniques, it is found that *RBFT* provides approximately *18.5 %* less *MSE*, as an average. This implies that produced images has less erred pixels. With respect to *PSNR*, *RBFT* provides high quality resultant panoramic images which is upto an average of *10.8 %*. It is observed that *RBFT* generates approximately *14.3 %* higher average *SSIM* for resultant panoramic images, suggesting that images have higher intensity values. It is found that *RBFT* provide upto 10.1 % average higher entropy values for resultant panoramic images. It suggests that the images are enriched with content information. Also, *RBFT* helps in viewing distant objects and reconstructing smooth image. It enhances the visualization quality of images and is a better technique for panoramic image refinement.

Chapter 8

Conclusion and Future Scope

8.1 Conclusion

UWASN has enabled broad range of To deal with real world applications like monitoring, pollution, habitat prevention, *etc.*, various deployment strategies are adopted using *UWASN*. It is realized that the dynamic deployment of sensors has lead to falsification in sensing data and covered area. This is due to sensors' communication range and water constraints like path loss, ambient noise, Doppler effect and propagation delay. Moreover, the image transmission and refinement need more attention in harsh environments. Therefore keeping all these aspects in view, this thesis intends to propose an *MPS*, an energy efficient network topology, a communication technique for image transmission and techniques for refining panoramic images.

A *MPS* is designed to sense physical parameters of river water. It is used in *MPST* that presents a monitoring technique for data gathering and forwarding. The topology is tested to justify its contributions, *i.e.*, (i) it channelizes the frequency upto *25 KHz* to reduce acoustic path loss, (ii) it minimizes energy consumption due to single hop communication and is sustainable *via* sleep-awake schema, and (iii) it procures cost effective technique using *ToA* based localization and communication algorithm. *MPST* provides 11.1, 5.20, 5.19, 8.69, 6.4 (in %) more accurate measurements for physical parameters such as *EC*, *pH*, temperature, chloride and *DO*, respectively, in comparison with sampling technique. It is concluded that devised topology helps the user to regularly monitoring of river water.

TPT performs efficient monitoring of river water's quality by analyzing physical parameters and uses sleep wake-up scheme to maximize utilization of battery. It outperforms well under *DSR* protocol as it helps in updating routing information and sending approximately 99 % packets to surface station. It provides 17.6, 5.4, 18.5, 8.76, 8.10 (in %) accurate estimation of sensing physical parameters such as conductivity, *pH*, temperature, measure of salinity (chloride) and water oxygen (dissolved), respectively, in comparison with sampling technique. It helps in stimulating timely preventive measures for river water's maintenance.

Hybrid-OFDM uses modulation schemes such as *BPSK*, *QPSK*, *16PSK* and *256PSK* for transmitting images to surface station. The proposed technique helps to obtain quality images transmitted by *BPSK* without any error. It uses mosaicing algorithm to produce big canvas of gathered images and to visualize wider area providing complete information of targeted region.

RBFT efficiently preserves the pixel's intensities along edges and refine panoramic images using fusion techniques such as Average, Maximum, Minimum, *IHS*, Brovey and *PCA*. The visual quality of images are enhanced significantly by *IHS*, Brovey and *PCA* fusion techniques. *RBFT* helps to analyze minutest information stored in it. It provides approximately 18.5 %, 10.8 %, 14.3 % and 10.1 % averaged efficient quality in terms of metrics *MSE*, *PSNR*, *SSIM* and *Entropy*, respectively. *RBFT* produces better quality panoramic images with high pixel intensities, high content information and minimal erred pixels. It efficiently refines the panoramic images.

8.2 Future Scope

In future, *MPST* and *TPT* topologies can be extended globally covering more geographical area. These topologies can be tested for random and distributed deployment of *MPS*. The topologies can be deployed for underwater oil refinery monitoring, exploration and data gathering processes. Distributed protocols should be devised to reduce the activity of sensor when its battery is depleting without compromising on network operation. For delay-sensitive applications such as long term monitoring, there is a need to develop algorithms to provide strict latency bounds and to handle loss of connectivity without provoking imme-

diate retransmissions. Various algorithms and protocols should be devised that detect and deal with disconnections due to failures, unforeseen mobility of sensors, or battery depletion. Fault tolerant techniques should be developed to minimize impact of loss in distributed environment. Low-complexity acoustic techniques to solve the underwater localization problem with limited energy expenditure for measuring errors need to be investigated. There is need of new flow control strategies to tackle the high delay and delay variance of the control messages sent back by the surface station. The performance of *MPS* can be improved by incorporating diffusing elements into the path which would reduce the sensitivity of the measurement. By equalizing the modulation scheme *(PSK)*, *BER* can potentially be lowered. *Hybrid-OFDM* can be improved to accept input source data in a word size than bits. The panoramic image refinement technique can be extended with respect to capturing colored image as color varies with depth of water. *RBFT* can be used for complex panoramic images where edges are mainly along curves. It will help to utilize a quad-tree division of images into suitable block where *RBFT* can be applied to each block.

Bibliography

Ainslie, M. A. and McColm, J. G. (1998). A Simplified Formula for Viscous and Chemical Absorption in Sea Water. *The Journal of the Acoustical Society of America*, 103(3), pp. 1671–1672.

Akan, O. B. and Akyildiz, I. F. (2005). Event-to-Sink Reliable Transport in Wireless Sensor Networks. *IEEE/ACM Transactions on Networking*, 13(5), pp. 1003–1016.

Akkaya, K. and Newell, A. (2009). Self-deployment of Sensors for Maximized Coverage in Underwater Acoustic Sensor Networks. *Computer Communications*, 32(7-10), pp. 1233–1244.

Akyildiz, I. F. (2007). Underwater Acoustic Sensor Networks. *Broadband Wireless Networking Laboratory, Georgia Institute of Technology, http://bwn.ece.gatech.edu/UWASN/*.

Akyildiz, I. F., Melodia, T., and Chowdhury, K. R. (2007). A Survey on Wireless Multimedia Sensor Networks. *Computer Networks*, 51(4), pp. 921–960.

Akyildiz, I. F., Melodia, T., and Chowdhury, K. R. (2008). Wireless Multimedia Sensor Networks: Applications and testbeds. *Proceedings of the IEEE*, 96(10), pp. 1588–1605.

Akyildiz, I. F., Su, W., Sankarasubramaniam, Y., and Cayirci, E. (2002). Wireless Sensor Networks: A Survey. *Computer Networks*, 38(4), pp. 393–422.

Al-Radaei, S. A. M. and Mishra, R. (2013). Multi-agent Paradigm for Semantic Web Service in E-learning System. *International Journal of Agent Technologies and Systems*, 5(4), pp. 20–43.

Alajeely, M., Doss, R., and Ahmad, A. (2017). Routing Protocols in Opportunistic Networks–A Survey. *IETE Technical Review*, pp. 1–19.

Alam, S. M. N. and Haas, Z. J. (2015). Coverage and Connectivity in Three-dimensional Networks with Random Node Deployment. *Ad Hoc Networks*, 34: pp. 157 – 169.

Allebach, J. and Wong, P. W. (1996). Edge-Directed Interpolation. in Proceedings of IEEE International Conference on Image Processing, 3, pp. 707–710.

Alsaghier, H. and Mishra, S. (2014). QOS based Performance Analysis of EAODV Protocol in Overlay Network. *International Journal of Computer Applications*, 94(9), pp. 1–14.

Ammari, H. M. and Das, S. (2010). A Study of k-coverage and Measures of Connectivity in 3D Wireless Sensor Networks. *IEEE Transactions on Computers*, 59(2), pp. 243–257.

Ancuti, C., Ancuti, C. O., Haber, T., and Bekaert, P. (2012). Enhancing Underwater Images and Videos by Fusion. in Proceedings of IEEE Conference on Computer Vision and Pattern Recognition, pp. 81–88.

Andreopoulos, Y. and van der Schaar, M. (2008). Incremental Refinement of Computation for the Discrete Wavelet Transform. *IEEE Transactions on Signal Processing*, 56(1), pp. 140–157.

Angove, P., Grady, M. O., Hayes, J., Flynn, B. O., Hare, G. M. P. O., and Diamond, D. (2011). A Mobile Gateway for Remote Interaction with Wireless Sensor Networks. *IEEE Sensors Journal*, 11(12), pp. 3309–3310.

Ansar, M. and VR, V. K. (2014). Performance Evaluation of Image Fusion Algorithms for Underwater Images-A Study based on PCA and DWT. *International Journal of Image, Graphics and Signal Processing*, 6(12), pp. 65–69.

Antoniadis, A. and Fan, J. (2001). Regularization of Wavelet Approximations. *Journal of the American Statistical Association*, 96(455), pp. 939–967.

Aslam, N. and Robertson, W. (2010). Distributed Coverage and Connectivity in Three Dimensional Wireless Sensor Networks. in Proceedings of the 6^{th} International Conference on Wireless Communications and Mobile Computing, pp. 1141–1145.

Averbuch, A., Coifman, R., Donoho, D., Israeli, M., and Walden, J. (2001). Fast Slant Stack: A Notion of Radon Transform for Data in a Cartesian Grid which is Rapidly Computible, Algebraically Exact, Geometrically Faithful and Invertible. *SIAM Scientific Computing*, pp. 1–40.

Averbuch, A. and Shkolnisky, Y. (2003). 3D Fourier based Discrete Radon Transform. *Applied and Computational Harmonic Analysis*, 15(1), pp. 33–69.

Azzari, P., Di Stefano, L., and Mattoccia, S. (2008). An Evaluation Methodology for Image Mosaicing Algorithms. in Proceedings of International Conference on Advanced Concepts for Intelligent Vision Systems, pp. 89–100.

Bai, X., Zhang, C., Xuan, D., and Jia, W. (2009). Full-Coverage and k-Connectivity (k=14,6) Three Dimensional Networks. in Proceedings of IEEE Conference on Computer Communications, pp. 388–396.

Ballari, D., Wachowicz, M., and Callejo, M. A. M. (2009). Metadata Behind the Interoperability of Wireless Sensor Networks. *Sensors*, 9(5), pp. 36–35.

Banik, B., Alfonso, L., Torres, A., Mynett, A., Cristo, C. D., and Leopardi, A. (2015). Optimal Placement of Water Quality Monitoring Stations in Sewer Systems: An Information Theory Approach. *Procedia Engineering*, 119, pp. 1308 – 1317.

Banzi, M. and Shiloh, M. (2014). Getting Started with Arduino: The Open Source Electronics Prototyping Platform. *Maker Media, Inc.*.

Baruch, O. and Anderson, J. (2007). Securing Pipelines requires Planning and Equipment. *Pipeline and Gas Journal*, 234(3), pp. 3–8.

Basagni, S., Carosi, A., Melachrinoudis, E., Petrioli, C., and Wang, Z. M. (2008). Controlled Sink Mobility for Prolonging Wireless Sensor Networks Lifetime. *Wireless Networks*, 14(6), pp. 831–858.

Behie, S. W., Fryer, R., Ashby, M., Al Emadi, H., Al Rahbi, A., Laczko, L., et al. (2008). Managing Risks During the Transition of Dolphin Energy Project from Construction to Full Operations. in Proceedings of SPE Middle East Heath, Safety, Security, and Environment Conference and Exhibition, pp. 1–8.

Behrens, A., Guski, M., Stehle, T., Gross, S., and Aach, T. (2010). Intensity based Multi-Scale Blending for Panoramic Images in Fluorescence Endoscopy. in Proceedings of IEEE International Symposium on Biomedical Imaging: From Nano to Macro, pp. 1305–1308.

Belan, S. and Yuzhakov, S. (2013). Machine Vision System based on the Parallel Shift Technology and Multiple Image Analysis. *Computer and Information Science*, 6(4), pp. 115–121.

Bellingham, J. (2003). Second Field Test for the AOSN Program. *Monterey Bay, http://www3.mbari.org/aosn/MontereyBay2003/MontereyBay2003Default.htm*.

Berry, P. A., Smith, R. G., and Benveniste, J. (2012). Envisat Altimetry for River and Lakes Monitoring. in Proceedings of IEEE International Conference on Geoscience and Remote Sensing Symposium, pp. 1844–1847.

Bevilacqua, A. and Azzari, P. (2007). A Fast and Reliable Image Mosaicing Technique with Application to Wide Area Motion Detection. in Proceedings of International Conference Image Analysis and Recognition, pp. 501–512.

Bhavana, V. and Krishnappa, H. (2015). Multi-Modality Medical Image Fusion using Discrete Wavelet Transform. *Procedia Computer Science*, 70, pp. 625–631.

Bisht, A. K., Kumar, B., Mishra, S., and Hussain, A. (2011). Simulation based Analysis of Position based Routing Protocols in Vehicular Ad Hoc Networks. in Proceedings of International Conference on Advanced Computing, Communication and Networks, pp. 750–757.

Black, M. J., Sapiro, G., Marimont, D. H., and Heeger, D. (1998). Robust Anisotropic Diffusion. *IEEE Transactions on Image Processing*, 7(3), pp. 421–432.

Brekhovskikh, L. M. and Lysanov, Y. P. (2003). *Fundamentals of Ocean Acoustics*. Springer-Verlag New York.

Bruggen, B. V. D. and Braeken, L. (2006). The Challenge of Zero Discharge: from Water Balance to Regeneration. *Desalination*, 188(3), pp. 177 – 183.

Bruneo, D., Distefano, S., Longo, F., Puliafito, A., and Scarpa, M. (2010). Reliability Assessment of Wireless Sensor Nodes with Non-Linear Battery Discharge. in Proceedings of International Conference on Federation for Information Processing Wireless Days, pp. 1–5.

Candes, E. J. (1998). *Ridgelets: Theory and Applications*. PhD Thesis, Stanford University Stanford.

Capel, D. (2004). Image Mosaicing. *Image Mosaicing and Super-Resolution*, pp. 47–79. Springer.

Catipovic, J. A. (1990). Performance Limitations in Underwater Acoustic Telemetry. *IEEE Journal of Oceanic Engineering*, 15(3), pp. 205–216.

Chadda, S., Kaur, N., and Thakur, R. (2012). Zooming Techniques for Digital Images: A Survey. *International Journal of Computer Science and Technology*, 3(1), pp. 519–523.

Chaitanya, D. E., Sridevi, C. V., and Rao, G. S. B. (2011). Path Loss Analysis of Underwater Communication Systems. in Proceedings of IEEE Students' Technology Symposium, pp. 65–70.

Chambolle, A., De Vore, R. A., Lee, N.-Y., and Lucier, B. J. (1998). Nonlinear Wavelet Image Processing: Variational Problems, Compression, and Noise Removal through Wavelet Shrinkage. *IEEE Transactions on Image Processing*, 7(3), pp. 319–335.

Chandrasekhar, V., Seah, W. K., Choo, Y. S., and Ee, H. V. (2006). Localization in Underwater Sensor Networks: Survey and Challenges. in Proceedings of ACM International Workshop on Underwater Networks, pp. 33–40.

Chapman, S. J. (2015). MATLAB Programming for Engineers. *Nelson Education*.

Charbonnier, P., Blanc-Feraud, L., Aubert, G., and Barlaud, M. (1997). Deterministic Edge-Preserving Regularization in Computed Imaging. *IEEE Transactions on Image Processing*, 6(2), pp. 298–311.

Chen, T., Zhang, J., and Zhang, Y. (2005). Remote Sensing Image Fusion based on Ridgelet Transform. in Proceedings of IEEE International Conference on Geoscience and Remote Sensing Symposium, 2, pp. 1150–1153.

Chiang, J. Y. and Chen, Y.-C. (2012). Underwater Image Enhancement by Wavelength Compensation and Dehazing. *IEEE Transactions on Image Processing*, 21(4), pp. 1756–1769.

Choi, K.-S. and Ko, S.-J. (2009). Fast Content-Aware Image Resizing Scheme in the Compressed Domain. *IEEE Transactions on Consumer Electronics*, 55(3), pp. 5–18.

Chow, K.-Y., Lui, K.-S., and Lam, E. Y. (2007). Efficient Selective Image Transmission in Visual Sensor Networks. in Proceedings of IEEE 65^{th} Vehicular Technology Conference, pp. 1–5.

Chryssostomidis, C. (1991). AUV Laboratory at MIT Sea Grant. *https://auvlab.mit.edu/*.

Chung, W.-Y. and Yoo, J.-H. (2015). Remote Water Quality Monitoring in Wide Area. *Sensors and Actuators B: Chemical*, 217, pp. 51–57.

Climent, S., Capella, J. V., Meratnia, N., and Serrano, J. J. (2012). Underwater Sensor Networks: A New Energy Efficient and Robust Architecture. *Sensors*, 12(1), pp. 704–731.

Dai, R. and Akyildiz, I. F. (2009). A Spatial Correlation Model for Visual Information in Wireless Multimedia Sensor Networks. *IEEE Transactions on Multimedia*, 11(6), pp. 1148–1159.

Dawei, Z. and Fang, Z. (2007). A New Improved Hierarchical Model of Image Fusion. in Proceedings of IEEE 8^{th} International Conference on Electronic Measurement and Instruments, 2, pp. 853 – 857.

Dengwen, Z. (2010). An Edge-Directed Bi-Cubic Interpolation Algorithm. in Proceedings of IEEE 3^{rd} International Congress on Image and Signal Processing, 3, pp. 1186–1189.

Diamond, D., Coyle, S., Scarmagnani, S., and Hayes, J. (2008a). Wireless Sensor Networks and Chemo-/Biosensing. *Chemical Reviews*, 108(2), pp. 652–679.

Diamond, D., Lau, K. T., Brady, S., and Cleary, J. (2008b). Integration of Analytical Measurements and Wireless Communications Current Issues and Future Strategies. *Talanta*, 75(3), pp. 606 – 612.

Ding, W., Tang, L., and Ji, S. (2016). Optimizing Routing based on Congestion Control for Wireless Sensor Networks. *Wireless Networks*, 22(3), pp. 915–925.

Do, M. N. (2001). *Directional Multi-resolution Image Representations*. PhD Thesis.

Do, M. N. and Vetterli, M. (2003). The Finite Ridgelet Transform for Image Representation. *IEEE Transactions on Image Processing*, 12(1), pp. 16–28.

Donoho, D. L. and Johnstone, J. M. (1994). Ideal Spatial Adaptation by Wavelet Shrinkage. *Biometrika*, 81(3), pp. 425–455.

Doss, R., Jennings, A., and Shenoy, N. (2006). Prediction based Location Aided Routing for Mobile Ad Hoc Networks. *International Journal of Pervasive Computing and Communications*, 2(2), pp. 91–102.

Durand, F. and Dorsey, J. (2002). Fast Bilateral Filtering for the Display of High-Dynamic-Range Images. in Proceedings of ACM Transactions on Graphics, 21, pp. 257–266.

Dutta, S., Sarma, D., and Nath, P. (2015). Ground and River Water Quality Monitoring using a Smartphone-based pH Sensor. *AIP Advances*, 5(5), pp. 05–15.

Fall, K. Delay-Tolerant Networking Research. *https://irtf.org/concluded/dtnrg*.

Farbman, Z., Fattal, R., Lischinski, D., and Szeliski, R. (2008). Edge-Preserving Decompositions for Multi-Scale Tone and Detail Manipulation. in Proceedings of ACM Transactions on Graphics, 27(3), pp. 67–71.

Fattal, R. (2008). Single Image Dehazing. in Proceedings of ACM Transactions on Graphics, 27(3), pp. 72–79.

Fiorelli, E., Leonard, N. E., Bhatta, P., Paley, D. A., Bachmayer, R., and Fratantoni, D. M. (2006). Multi-AUV Control and Adaptive Sampling in Monterey Bay. *IEEE Journal of Oceanic Engineering*, 31(4), pp. 935–948.

Foley, J., van Dam, A., Feiner, S., and Hughes, J. (2013). Clipping Lines. in *Computer Graphics (3rd edition)*. Tata McGraw Hill-New Delhi.

Fonseca, M. S. P., Munaretto, A., Mendes, C., and Chaouchi, H. (2015). A Resource Management Framework for 802.11 Wireless Access Networks. *Wireless Networks*, 21(6), pp. 1891–1898.

Foo, K., Atkins, P., Collins, T., Morley, C., and Davies, J. (2004). A Routing and Channel-Access Approach for An Ad Hoc Underwater Acoustic Network. in Proceedings of IEEE Marine Technology Society/Techno-Ocean'04, 2, pp. 789–795.

Fortuna, C., Oniga, P., Padrah, Z., Mohorcic, M., and Moraru, A. (2012). Metadata Management for The Web of Things: A Practical Perspective. in Proceedings of the Third International Workshop on the Web of Things, pp. 401–406.

Freitag, L., Stojanovic, M., Singh, S., and Johnson, M. (2001). Analysis of Channel Effects on Direct-Sequence and Frequency-Hopped Spread-Spectrum Acoustic Communication. *IEEE Journal of Oceanic Engineering*, 26(4), pp. 586–593.

Gao, G. and Jia, K. (2007). A New Image Mosaics Algorithm based on Feature Points Matching. in Proceedings of IEEE Second International Conference on Innovative Computing, Information and Control, pp. 471–471.

Gao, R., Song, J.-P., and Tai, X.-C. (2009). Image Zooming Algorithm based on Partial Differential Equations Technique. *International Journal of Numerical Analysis and Modeling*, 6(2), pp. 284–292.

Ge, F. and Wang, Y. (2016). Energy Efficient Networks for Monitoring Water Quality in Subterranean Rivers. *Sustainability*, 8(6), pp. 526–532.

Geng, N., He, D., and Song, Y. (2012). Camera Image Mosaicing based on An Optimized SURF Algorithm. *Indonesian Journal of Electrical Engineering and Computer Science*, 10(8), pp. 2183–2193.

Ghannam, S. and Abbott, A. L. (2013). Cross Correlation Versus Mutual Information for Image Mosaicing. *International Journal of Advanced Computer Science and Applications*, 20(3), pp. 21–27.

Ghosh, D., Park, S., Kaabouch, N., and Semke, W. (2012). Quantitative Evaluation of Image Mosaicing in Multiple Scene Categories. in Proceedings of IEEE International Conference on Electro/Information Technology, pp. 1–6.

Giuseppe, A., Marco, C., Mario, D. F., and Andrea, P. (2009). Energy Conservation in Wireless Sensor Networks: A Survey. *Ad Hoc Networks*, 7(3), pp. 537–568.

Glasgow, H. B., Burkholder, J. M., Reed, R. E., Lewitus, A. J., and Kleinman, J. E. (2004). Real-Time Remote Monitoring of Water Quality: A Review of Current Applications, and Advancements in Sensor, Telemetry, and Computing Technologies. *Journal of Experimental Marine Biology and Ecology*, 300(1-2), pp. 409–448.

Glegg, S. Ocean engineering at Florida Atlantic University. *http://www.ome.fau.edu/labs-centers/*.

Glegg, S., Pirie, R., and LaVigne, A. (2000). A Study of Ambient Noise in Shallow Water. *Florida Atlantic University Technical Report*, pp. 1–28.

Grady, L. (2006). Random Walks for Image Segmentation. *IEEE Transactions on Pattern Analysis and Machine Intelligence*, 28(11), pp. 1768–1783.

Guariglia, E. (2016). Entropy and Fractal Antennas. *Entropy*, 18(3), pp. 84–90.

Guariglia, E. (2017). Spectral Analysis of the Weierstrass-Mandelbrot Function. in Proceedings of Second International Multidisciplinary Conference on Computer and Energy Science, pp. 1–6.

Guariglia, E. and Silvestrov, S. (2017). *Fractional-Wavelet Analysis of Positive definite Distributions and Wavelets on D'(C)*. Springer International Publishing, Cham.

Guo, Z., Hong, F., Feng, H., Chen, P., Yang, X., and Jiang, M. (2008). OceanSense: Sensor Network of Real-Time Ocean Environmental Data Observation and its Development Platform. in Proceedings of the Third ACM International Workshop on UnderWater Networks, pp. 101–105.

Hajizadeh, M., Helfroush, M. S., and Tashk, A. (2009). Improvement of Image Zooming using Least Directional Differences based on Linear and Cubic Interpolation. in Proceedings of Second International Conference on Computer, Control and Communication, pp. 1–6.

He, C., Liu, Q., Li, H., and Wang, H. (2010). Multimodal Medical Image Fusion based on IHS and PCA. *Procedia Engineering*, 7, pp. 280–285.

He, K., Sun, J., and Tang, X. (2011). Single Image Haze Removal using Dark Channel Prior. *IEEE Transactions on Pattern Analysis and Machine Intelligence*, 33(12), pp. 2341–2353.

He, K., Sun, J., and Tang, X. (2013). Guided Image Filtering. *IEEE Transactions on Pattern Analysis and Machine Intelligence*, 35(6), pp. 1397–1409.

Heidemann, J., Stojanovic, M., and Zorzi, M. (2011). Underwater Sensor Networks: Applications, Advances and Challenges. *Philosophical Transactions of the Royal Society of London A: Mathematical, Physical and Engineering Sciences*, 370(1958), pp. 158–175.

Heiskala, J. and Terry, J. (2001). *OFDM Wireless LANs: A Theoretical and Practical Guide*. Sams, Indianapolis, IN, USA.

Hong, S.-H., Wang, L., Truong, T.-K., Lin, T.-C., and Wang, L.-J. (2013). Novel Approaches to The Parametric Cubic-Spline Interpolation. *IEEE Transactions on Image Processing*, 22(3), pp. 1233–1241.

Hope, N. (2001). Bubble Vision Underwater Images and Videos. http://bubblevision.com/underwater-videos/index.htm. Accessed: 2017-06-02.

Horng, M., Chen, Y., Chu, S., Pan, J., and Liao, B. (2010). Chapter. An Extensible Particles Swarm Optimization for Energy-Effective Cluster Management of Underwater Sensor Networks, pp. 109–116. Berlin, Heidelberg.

Hou, W., Gray, D. J., Weidemann, A. D., Fournier, G. R., and Forand, J. (2007). Automated Underwater Image Restoration and Retrieval of Related Optical Properties. in Proceedings of IEEE International Conference on Geoscience and Remote Sensing Symposium, pp. 1889–1892.

Huang, C.-J., Chen, Y.-J., Chen, I.-F., Hu, K.-W., Liao, J.-J., and Yang, D.-X. (2008). A Clustering Head Selection Algorithm for Underwater Sensor networks. in Proceedings of Second International Conference on Future Generation Communication and Networking, pp. 21–24.

Huang, C.-J., Wang, Y.-W., Shen, H.-Y., Hu, K.-W., Hsu, P.-A., and Chang, T.-Y. (2009). A Direction-Sensitive Routing Protocol for Underwater Wireless Sensor Networks. in Proceedings of the 22^{nd} International Conference on Industrial, Engineering and Other Applications of Applied Intelligent Systems: Next-Generation Applied Intelligence, pp. 419–428.

Hui, T. and Binbin, W. (2009). Discussion and Analyze on Image Fusion Technology. in Proceedings of Second International Conference on Machine Vision, pp. 246–250.

Hung, K.-W. and Siu, W.-C. (2012). Fast Image Interpolation using The Bilateral Filter. *IET Image Processing*, 6(7), pp. 877–890.

Ingram, M. A. and Acosta, G. (2000). OFDM Simulation using MATLAB.

Iqbal, K., Abdul Salam, R., Osman, M., Talib, A. Z., et al. (2007). Underwater Image Enhancement using An Integrated Color Model. *IAENG International Journal of Computer Science*, 32(2), pp. 239–244.

Isabona, J. and Srivastava, V. M. (2017). Coverage and Link Quality Trends in Suburban Mobile Broadband HSPA Network Environments. *Wireless Personal Communications*, 95(4), pp. 3955–3968.

Isbitiren, G. and Akan, O. B. (2011). Three-Dimensional Underwater Target Tracking with Acoustic Sensor Networks. *IEEE Transactions on Vehicular Technology*, 60(8), pp. 3897–3906.

Isik, M. T. and Akan, O. B. (2009). A Three Dimensional Localization Algorithm for Underwater Acoustic Sensor Networks. *IEEE Transactions on Wireless Communications*, 8(9), pp. 4457–4463.

Islam, S., Balasubramaniam, S., Goyal, P., Sati, M., and Goyal, N. (2017). A Domain Specific Language for Clustering. in Proceedings of International Conference on Distributed Computing and Internet Technology, pp. 231–234.

Issariyakul, T. and Hossain, E. (2012). Introduction to Network Simulator 2 (NS2). *Introduction to Network Simulator NS2*, pp. 21–40.

Jain, D. K., Saxena, G., and Singh, V. K. (2012). Image Mosaicing using Corner Techniques. in Proceedings of International Conference on Communication Systems and Network Technologies, pp. 79–84.

Jassim, F. A. (2013). Image Inpainting by Kriging Interpolation Technique. *Computer Vision and Pattern Recognition*, 3(5), pp. 91–96.

Jeong, B. G., Kim, H. S., Kim, S. C., and Eom, I. K. (2008). Edge-Adaptive Demosaicking for Reducing Artifact along Line Edge. in Proceedings of International Congress on Image and Signal Processing, 3, pp. 316–319.

Jindal, H., Kasana, S. S., and Saxena, S. (2017a). Underwater Pipelines Panoramic Image Transmission and Refinement using Acoustic Sensors. *International Journal of Wavelets, Multiresolution and Information Processing*, pp. 1850013.

Jindal, H., Saxena, S., and Kasana, S. S. (2017b). Sewage Water Quality Monitoring Framework using Multi-Parametric Sensors. *Wireless Personal Communications*, 97(1), pp. 881–913.

Jindal, H., Saxena, S., and Kasana, S. S. (2017c). A Sustainable Multi-Parametric Sensors Network Topology for River Water Quality Monitoring. *Wireless Networks*, https://doi.org/10.1007/s11276-017-1532-z.

Jindal, H., Saxena, S., and Kasana, S. S. (2017d). Triangular Pyramidal Topology to Measure Temporal and Spatial Variations in Shallow River Water using Ad-Hoc Sensors Network *Ad Hoc & Sensor Wireless Networks*, 39(1-4), pp. 1–35.

Jindal, H., Saxena, S., and Singh, S. (2014). Challenges and Issues in Underwater Acoustics Sensor Networks: A Review. in Proceedings of IEEE International Conference on Parallel, Distributed and Grid Computing, pp. 251–255.

Jindal, R. and Sharma, C. (2011). Studies on Water Quality of Sutlej River Around Ludhiana with Reference to Physicochemical Parameters. *Environmental monitoring and assessment*, 174(1-4), pp. 417–425.

John Carpenter House, J. C. S. (2007). Pipeline Guerrillas. *Offshore Technology*.

Joshi, H. (2013). Khomlalsinha, Novel Techniques Image Mosaicing based on Image Fusion using Harris and SURF. in Proceedings of International Conference on Computer Science and Information Technology, pp. 15–22.

Joyce, C. (2006). Underwater Pipeline Damage Underestimated in Gulf. *All Things Considered*.

Jurdak, R., Lopes, C. V., and Baldi, P. (2004). Battery Lifetime Estimation and Optimization for Underwater Sensor Networks. *IEEE Sensor Network Operations*, 2006, pp. 397–420.

Kamenar, E., Zelenika, S., Blažević, D., Maćešić, S., Gregov, G., Marković, K., and Glažar, V. (2016). Harvesting of River Flow Energy for Wireless Sensor Network Technology. *Microsystem Technologies*, 22(7), pp. 1557–1574.

Kang, P. and Ma, H. (2011). An Automatic Airborne Image Mosaicing Method based on The SIFT Feature Matching. in Proceedings of International Conference on Multimedia Technology, pp. 155–159.

Karvonen, H., Suhonen, J., Petjjrvi, J., Hmlinen, M., Hnnikinen, M., and Pouttu, A. (2014). Hierarchical Architecture for Multi-Technology Wireless Sensor Networks for Critical Infrastructure Protection. *Wireless Personal Communications*, 76(2), pp. 209–229.

Kass, M. and Solomon, J. (2010). Smoothed Local Histogram Filters. in Proceedings of ACM Transactions on Graphics, 29, pp. 100–112.

Khalfallah, Z., Fajjariy, I., Aitsaadiz, N., Langar, R., and Pujolle, G. (2013). A New WSN Deployment Algorithm for Water Pollution Monitoring in Amazon Rainforest Rivers. in Proceedings of IEEE Global Communications Conference, pp. 267–273.

Kilfoyle, D. B. and Baggeroer, A. B. (2000). The State of The Art in Underwater Acoustic Telemetry. *IEEE Journal of Oceanic Engineering*, 25(1), pp. 4–27.

Kim, H., Cha, Y., and Kim, S. (2011). Curvature Interpolation Method for Image Zooming. *IEEE Transactions on Image Processing*, 20(7), pp. 1895–1903.

Kim, J., Lim, J. S., Friedman, J., Lee, U., Vieira, L., Rosso, D., Gerla, M., and Srivastava, M. B. (2009). SewerSnort: A Drifting Sensor for In-Situ Sewer Gas Monitoring. in Proceedings of IEEE Sixth Annual Conference on Sensor, Mesh and Ad Hoc Communications and Networks, pp. 1–9.

King, P., Venkatesan, R., and Li, C. (2010). Modeling a Shallow Water Acoustic Communication Channel using Environmental Data for Seafloor Sensor Networks. *Wireless Communications and Mobile Computing*, 10(11), pp. 1521–1532.

Kocak, D. M., Dalgleish, F. R., Caimi, F. M., and Schechner, Y. Y. (2008). A Focus on Recent Developments and Trends in Underwater Imaging. *Marine Technology Society Journal*, 42(1), pp. 52–67.

Kumari, S., Maheshwari, A., Goyal, P., and Goyal, N. (2015). Parallel Framework for Efficient K-Means Clustering. in Proceedings of the Eighth Annual ACM India Conference, pp. 63–71.

Lakshman, H., Lim, W.-Q., Schwarz, H., Marpe, D., Kutyniok, G., and Wiegand, T. (2013). Image Interpolation using Shearlet based Sparsity Priors. in Proceedings of IEEE 20^{th} International Conference on Image Processing, pp. 655–659.

Lakshman, H., Lim, W.-Q., Schwarz, H., Marpe, D., Kutyniok, G., and Wiegand, T. (2015). Image Interpolation using Shearlet based Iterative Refinement. *Signal Processing: Image Communication*, 36, pp. 83–94.

Lebart, K., Smith, C., Trucco, E., and Lane, D. M. (2003). Automatic Indexing of Underwater Survey Video: Algorithm and Benchmarking Method. *IEEE Journal of Oceanic Engineering*, 28(4), pp. 673–686.

Lee, D.-U., Kim, H., Rahimi, M., Estrin, D., and Villasenor, J. D. (2009). Energy-Efficient Image Compression for Resource-Constrained Platforms. *IEEE Transactions on Image Processing*, 18(9), pp. 2100–2113.

Lee, E.-J., Yoo, G.-Y., Jeong, Y., Kim, K.-U., Park, J.-H., and Oh, N.-H. (2015). Comparison of UV–VIS and FDOM Sensors for In Situ Monitoring of Stream DOC Concentrations. *Biogeosciences*, 12(10), pp. 3109–3118.

Lee, H., Tessens, L., Morbee, M., Aghajan, H., and Philips, W. (2008a). Sub-Optimal Camera Selection in Practical Vision Networks through Shape Approximation. in Proceedings of International Conference on Advanced Concepts for Intelligent Vision Systems, pp. 266–277.

Lee, H.-H., Hong, S.-T., Shin, G.-W., and Kim, H.-I. (2012). Propagation Analysis of Wireless Mesh Network for Real-Time Monitoring Around the Four Major Rivers in South Korea. in Proceedings of International Symposium on Communications and Information Technologies, pp. 428–433.

Lee, K. H., Yu, C. H., Choi, J. W., and Seo, Y. B. (2008b). TOA based Sensor Localization in Underwater Wireless Sensor Networks. in Proceedings of IEEE Society of Instrument and Control Engineers Annual Conference, pp. 1357–1361.

Levin, A., Lischinski, D., and Weiss, Y. (2004a). Colorization using Optimization. in Proceedings of ACM Transactions on Graphics, 23, pp. 689–694.

Levin, A., Zomet, A., Peleg, S., and Weiss, Y. (2004b). Seamless Image Stitching in The Gradient Domain. in Proceedings of European Conference on Computer Vision, pp. 377–389.

Li, J., Xin, M., and Jin, J. (2011). An Evolutionary Approach for Gray-Level Image Zooming. in Proceedings of IEEE NASA/ESA Conference on Adaptive Hardware and Systems, pp. 383–389.

Li, J., Zhang, Y., Chen, Y., Nagaraja, K., Li, S., and Raychaudhuri, D. (2013). A Mobile Phone based WSN Infrastructure for IOT over Future Internet Architecture. in Proceedings of IEEE International Conference on Green Computing and Communications and IEEE Internet of Things and IEEE Cyber, Physical and Social Computing, pp. 426–433.

Li, S., Kang, X., Fang, L., Hu, J., and Yin, H. (2017). Pixel-Level Image Fusion: A Survey of The State of the Art. *Information Fusion*, 33, pp. 100–112.

Li, X. and Orchard, M. T. (2001). New Edge-Directed Interpolation. *IEEE Transactions on Image Processing*, 10(10), pp. 1521–1527.

Li, X. Y., Wan, P. J., and Wang, Y. (2001). Power Efficient and Sparse Spanner for Wireless Ad Hoc Networks. in Proceedings of Tenth International Conference on Computer Communications and Networks, pp. 564–567.

Li, Y. and Osher, S. (2009). A New Median Formula with Applications to PDE based Denoising. *Communications in Mathematical Sciences*, 7(3), pp. 741–753.

Li, Y., Wang, Y., Huang, W., and Zhang, Z. (2008). Automatic Image Stitching using SIFT. in Proceedings of International Conference on Audio, Language and Image Processing, pp. 568–571.

Litwin, L. and Pugel, M. (2001). The Principles of OFDM. *RF Signal Processing*, 2, pp. 30–48.

Liu, H. and Wei, Z. (2010). An Edge-Adaptive Structure Tensor Kernel Regression for Image Interpolation. in Proceedings of Second International Conference on Future Computer and Communication, 2, pp. 672–681.

Lloret, J. (2013). Underwater Sensor Nodes and Networks. *Sensors*, 13(9), pp. 11782–11796.

Lowe, D. G. (2004). Distinctive Image Features from Scale-Invariant Keypoints. *International Journal of Computer Vision*, 60(2), pp. 91–110.

Lukin, A. (2008). High-Quality Spatial Interpolation of Interlaced Video. *Laboratory of Mathematical Methods of Image Processing, Computer Vision and Graphics*, pp. 301–307.

Lukin, A., Krylov, A. S., and Nasonov, A. (2006). Image Interpolation by Super-Resolution. in Proceedings of International Conference on GraphiCon, 2006, pp. 239–242.

Luque-Nieto, M.-A., Moreno-Roldán, J.-M., Poncela, J., and Otero, P. (2016). Optimal Fair Scheduling in S-TDMA Sensor Networks for Monitoring River Plumes. *Journal of Sensors*, 2016(2), pp. 343–351.

Mallat, S. and Zhong, S. (1992). Characterization of Signals from Multiscale Edges. *IEEE Transactions on Pattern Analysis and Machine Intelligence*, 14(7), pp. 710–732.

Mallat, S. G. (1989). A Theory for Multiresolution Signal Decomposition: The Wavelet Representation. *IEEE Transactions on Pattern Analysis and Machine Intelligence*, 11(7), pp. 674–693.

Mitchell, H. B. (2010). *Image Fusion: Theories, Techniques and Applications*. Springer Science & Business Media.

Mittal, R. C. and Kumar, S. (2006). Numerical Study of Fisher's Equation by Wavelet Galerkin Method. *International Journal of Computer Mathematics*, 83(3), pp. 287–298.

Mohamed, N., Jawhar, I., Al-Jaroodi, J., and Zhang, L. (2011). Sensor Network Architectures for Monitoring Underwater Pipelines. *Sensors*, 11(11), pp. 107–118.

Morón, M. J., Luque, R., and Casilari, E. (2014). On the Capability of Smartphones to Perform as Communication Gateways in Medical Wireless Personal Area Networks. *Sensors*, 14(1), pp. 575–581.

Mrázek, P., Weickert, J., and Steidl, G. (2003). Correspondences between Wavelet Shrinkage and Non-Linear Diffusion. in Proceedings of International Conference on Scale-Space Theories in Computer Vision, pp. 101–116.

Mueller, N., Lu, Y. M., and Do, M. N. (2007). Image Interpolation using Multiscale Geometric Representations. in Proceedings of SPIE Computational Imaging, 6498, pp. 1–11.

Naidu, V. (2010). Discrete Cosine Transform-based Image Fusion. *Defence Science Journal*, 60(1), pp. 48–61.

Naik, S. S. and Nene, M. J. (2012). Realization of 3D Underwater Wireless Sensor Networks and Influence of Ocean Parameters on Node Location Estimation. *International Journal of Wireless & Mobile Networks*, 4(2), pp. 135–144.

Nassiraei, A. A. F., Kawamura, Y., Ahrary, A., Mikuriya, Y., and Ishii, K. (2007). Concept and Design of a Fully Autonomous Sewer Pipe Inspection Mobile Robot "KANTARO". in Proceedings of IEEE International Conference on Robotics and Automation, pp. 136–143.

Nemra, A. and Aouf, N. (2009). Robust Invariant Automatic Image Mosaicing and Super Resolution for UAV Mapping. in Proceedings of Sixth International Symposium on Mechatronics and its Applications, pp. 1–7.

Norman, M. L. (2010). SDSC Storage Resource Broker. *University of California, San Diego, http://www.sdsc.edu/about_sdsc/index.html*.

O'Connor, E., Smeaton, A. F., and O'Connor, N. E. (2011). A Multi-Modal Event Detection System for River and Coastal Marine Monitoring Applications. in Proceedings of IEEE Oceanic Engineering Society, pp. 1–10.

O'Connor, E., Smeaton, A. F., O'Connor, N. E., and Regan, F. (2012). A Neural Network Approach to Smarter Sensor Networks for Water Quality Monitoring. *Sensors*, 12(4), pp. 4605–4632.

Olivier, R. and Hanqiang, C. (2012). Nearest Neighbor Value Interpolation. *International Journal of Advanced Computer Science and Applications*, 3(4), pp. 6–12.

Orumwense, E. F., Afullo, T. J., and Srivastava, V. M. (2016). Cognitive Radio Networks: A Social Network Perspective. in Proceedings of International Conference on Advances in Nature and Biologically Inspired Computing, pp. 441–450.

Ouyang, B., Dalgleish, F., Caimi, F., Vuorenkoski, A., Giddings, T., and Shirron, J. (2012). Image Enhancement for Underwater Pulsed Laser Line Scan Imaging System. in Proceedings of SPIE Ocean Sensing and Monitoring, 8372, pp. 83–92.

PadmaPriya, S. (2015). An Unidentified Position-based Capable Routing Protocol in Mobile Ad Hoc Networks. *International Journal*, 5(6), pp. 17–25.

Pandey, A. and Pati, U. C. (2013). A Novel Technique for Non-Overlapping Image Mosaicing based on Pyramid Method. in Proceedings of IEEE Annual India Conference, pp. 1–6.

Park, S., Ghosh, D., Kaabouch, N., Fevig, R. A., and Semke, W. (2012). Hierarchical Multi-Level Image Mosaicing for Autonomous Navigation of UAV. in Proceedings of SPIE Intelligent Robots and Computer Vision XXIX: Algorithms and Techniques, 830116, pp. 65–77.

Patel, V. and Mistree, K. (2013). A Review on Different Image Interpolation Techniques for Image Enhancement. *International Journal of Emerging Technology and Advanced Engineering*, 3(12), pp. 129–133.

Pellerin, B. A., Stauffer, B. A., Young, D. A., Sullivan, D. J., Bricker, S. B., Walbridge, M. R., Clyde, G. A., and Shaw, D. M. (2016). Emerging Tools for Continuous Nutrient Monitoring Networks: Sensors Advancing Science and Water Resources Protection. *Journal of the American Water Resources Association*, 52(4), pp. 993–1008.

Perona, P. and Malik, J. (1990). Scale-Space and Edge Detection using Anisotropic Diffusion. *IEEE Transactions on Pattern Analysis and Machine Intelligence*, 12(7), pp. 629–639.

Petschnigg, G., Szeliski, R., Agrawala, M., Cohen, M., Hoppe, H., and Toyama, K. (2004). Digital Photography with Flash and No-Flash Image Pairs. in Proceedings of ACM Transactions on Graphics, 23, pp. 664–672.

Pokorny, J. (2006). Database Architectures: Current Trends and Their Relationships to Environmental Data Management. *Environmental Modelling and Software*, 21(11), pp. 1579 – 1586.

Pompili, D. and Akyildiz, I. F. (2009). Overview of Networking Protocols for Underwater Wireless Communications. *IEEE Communications Magazine*, 47(1), pp. 97–102.

Pompili, D., Melodia, T., Akyildiz, I. F., et al. (2006). A Resilient Routing Algorithm for Long-Term Applications in Underwater Sensor Networks. in Proceedings of Mediterranean Ad Hoc Networking Workshop, pp. 1–8.

Preisig, J. (2007). Acoustic Propagation Considerations for Underwater Acoustic Communications Network Development. *ACM SIGMOBILE Mobile Computing and Communications Review*, 11(4), pp. 2–10.

Proakis, J. G., Sozer, E. M., Rice, J. A., and Stojanovic, M. (2001). Shallow Water Acoustic Networks. *IEEE Communications Magazine*, 39(11), pp. 114–119.

Prodan, R., Iosup, A., and Bologa, C. (2014). Comparison of Static and Dynamic Resource Allocations for Massively Multiplayer Online Games on Unreliable Resources. in Proceedings of European Conference on Parallel Processing, pp. 299–310.

Puchyova, J., Kochlan, M., and Hodon, M. (2013). Development of Special Smartphone-based Body Area Network: Energy Requirements. in Proceedings of IEEE Federated Conference on Computer Science and Information Systems, pp. 895–900.

Quazi, A. and Konrad, W. (1982). Underwater Acoustic Communications. *IEEE Communications Magazine*, 20(2), pp. 24–30.

Ramanath, R., Snyder, W. E., Bilbro, G. L., and Sander, W. A. (2002). Demosaicking Methods for Bayer Color Arrays. *Journal of Electronic imaging*, 11(3), pp. 306–315.

Ramkumar, M. and Akansu, A. N. (2004). On the Design of Data Hiding Methods Robust to Lossy Compression. *IEEE Transactions on Multimedia*, 6(6), pp. 947–951.

Rawat, P., Singh, K. D., Chaouchi, H., and Bonnin, J. M. (2014). Wireless Sensor Networks: A Survey on Recent Developments and Potential Synergies. *The Journal of Supercomputing*, 68(1), pp. 1–48.

Remimol, A. M. and Sekar, K. (2014). A Method of DWT with Bi-Cubic Interpolation for Image Scaling. *International Journal of Computer Science Engineering*, 3(2), pp. 131–135.

Rong, W., Chen, H., Liu, J., Xu, Y., and Haeusler, R. (2009). Mosaicing of Microscope Images based on SURF. in Proceedings of IEEE 24^{th} International Conference on Image and Vision Computing, pp. 271–275.

Roy, R., Pal, M., and Gulati, T. (2013). Zooming Digital Images using Interpolation Techniques. *International Journal of Application or Innovation in Engineering & Management*, 2(4), pp. 34–45.

Rudin, L. I., Osher, S., and Fatemi, E. (1992). Non-linear Total Variation based Noise Removal Algorithms. *Physica D: nonlinear phenomena*, 60(1-4), pp. 259–268.

Sahu, V. and Sahu, D. (2014). Image Fusion using Wavelet Transform: A Review. *Global Journal of Computer Science and Technology*, 14(5), pp. 21–28.

Schechner, Y. Y. and Averbuch, Y. Regularized Image Recovery in Scattering Media. *IEEE Transactions on Pattern Analysis and Machine Intelligence*, 29(9), pp. 1655–1660.

Schettini, R. and Corchs, S. (2010). Underwater Image Processing: State of the Art of Restoration and Image Enhancement Methods. *EURASIP Journal on Advances in Signal Processing*, 746052(1), pp. 1–15.

Sehgal, A., David, C., and Schonwalder, J. (2011). Energy Consumption Analysis of Underwater Acoustic Sensor Networks. in Proceedings of IEEE Oceanic Engineering Society, pp. 1–6.

Shaban, M., Urban, B., Saadi, A. E., and Faisal, M. (2010). Detection and Mapping of Water Pollution Variation in the Nile Delta using Multivariate Clustering and {GIS} Techniques. *Journal of Environmental Management*, 91(8), pp. 1785 – 1793.

Sharma, A. and Swami, P. D. (2013). Redundant Wavelet Transform based Image Super Resolution. *International Journal of Engineering Research and Applications*, 3(4), pp. 2055–2062.

Singh, S., Shakya, R. and Singh, Y. (2015). Localization Techniques in Wireless Sensor Networks. *International Journal of Computer Science and Information Technologies*, 6(1), pp. 844–850.

Sinha, A., Kumar, M., Jaiswal, A., and Saxena, R. (2014). Performance Analysis of High Resolution Images using Interpolation Techniques in Multimedia Communication System. *Signal & Image Processing*, 5(2), pp. 39–45.

Skarbovik, E. and Roseth, R. (2015). Use of Sensor Data for Turbidity, pH and Conductivity as An Alternative to Conventional Water Quality Monitoring in Four Norwegian Case Studies. *Acta Agriculturae Scandinavica, Section B– Soil & Plant Science*, 65(1), pp. 63–73.

Sklar, B. (2001). *Digital Communications*, 2. Prentice Hall Upper Saddle River.

Smith, S. M. and Brady, J. M. (1997). SUSANA New Approach to Low Level Image Processing. *International Journal of Computer Vision*, 23(1), pp. 45–78.

Solberg, L., Gjertveit, E., et al. (2007). Constructing the World's Longest Subsea Pipeline, Langeled Gas Export. in Offshore Technology Conference. pp. 51–62.

Sozer, E. M., Stojanovic, M., and Proakis, J. G. (2000). Underwater Acoustic Networks. *IEEE Journal of Oceanic Engineering*, 25(1), pp. 72–83.

Steidl, G. and Weickert, J. (2002). Relations between Soft Wavelet Shrinkage and Total Variation Denoising. in Proceedings of International Conference on Joint Pattern Recognition Symposium, pp. 198–205.

Steidl, G., Weickert, J., Brox, T., Mrázek, P., and Welk, M. (2004). On the Equivalence of Soft Wavelet Shrinkage, Total Variation Diffusion, Total Variation Regularization, and Sides. *SIAM Journal on Numerical Analysis*, 42(2), pp. 686–713.

Suri, A., Iyengar, S., and Cho, E. (2006). Ecoinformatics using Wireless Sensor Networks: An Overview. *Ecological Informatics*, 1(3), pp. 287 – 293.

Szeliski, R. (2006). Image Alignment and Stitching: A Tutorial. *Foundations and Trends in Computer Graphics and Vision*, 2(1), pp. 1–104.

Szeliski, R., Uyttendaele, M., and Steedly, D. (2011). Fast Poisson Blending using Multi-Splines. in Proceedings of IEEE International Conference on Computational Photography, pp. 1–8.

Tam, W. S., Kok, C. W., and Siu, W. C. (2010). Modified Edge-Directed Interpolation for Images. *Journal of Electronic imaging*, 19(1), pp. 013011–013011.

Thorp, W. H. (1967). Analytic Description of The Low-Frequency Attenuation Coefficient. *Acoustical Society of America Journal*, 42, pp. 270–281.

Tomasi, C. and Manduchi, R. (1998). Bilateral Filtering for Gray and Color Images. in Proceedings of IEEE Sixth International Conference on Computer Vision, pp. 839–846.

Tran, L., Mertins, A., and Wysocki, T. A. (2007). Quasi-Orthogonal Space-Time-Frequency Codes in MB-OFDM UWB Communications. *Computer & Electronics Engineering Faculty Publications*, pp. 39–47.

Treibitz, T. and Schechner, Y. Y. (2012). Turbid Scene Enhancement using Multi-Directional Illumination Fusion. *IEEE Transactions on Image Processing*, 21(11), pp. 4662–4667.

Tripathi, S. and Mishra, R. Two Phase Integrated Rule based Model (TPC-IRBM) for Clustering of Gene Expression Data of CA1 Region of Rat Hippocampus. *International Journal of Computer Applications*, 84(6), pp. 15–23.

Tseng, Y.-C., Hsu, P.-H., and Chang, T.-S. (2011). A 124 MPixels/s VLSI Design for Histogram-based Joint Bilateral Filtering. *IEEE Transactions on Image Processing*, 20(11), pp. 3231–3241.

Tu, Y. and Chen, H. (1999). Design of Oil Pipeline Leak Detection and Communication System based on Optical Fiber Technology. in Proceedings of SPIE Optical Systems Design and Production, 3737, pp. 584–592.

Ueyama, J., Hughes, D., Man, K. L., Guan, S.-U., Matthys, N., Horré, W., Michiels, S., Huygens, C., and Joosen, W. (2010). Applying A Multi-Paradigm Approach to Implementing Wireless Sensor Network based River Monitoring. in Proceedings of First ACIS International Symposium on Cryptography and Network Security, Data Mining and Knowledge Discovery, E-Commerce & Its Applications and Embedded Systems, pp. 187–191.

Urick, R. J. (1967). *Principles of Underwater Sound for Engineers*. Tata McGraw-Hill Education.

Vassev, E., Hinchey, M., and Nixon, P. (2010). Developing Intelligent Sensor Networks: A Technological Convergence Approach. in Proceedings of ICSE Workshop on Software Engineering for Sensor Network Applications, pp. 66–71.

Velasquez-Villada, C. and Donoso, Y. (2016). Delay/Disruption Tolerant Network-based Message Forwarding for a River Pollution Monitoring Wireless Sensor Network Application. *Sensors*, 16(4), pp. 436–445.

Vieira, R. G., Da Cunha, A. M., and de Camargo, A. P. (2015). An Energy Management Method of Sensor Nodes for Environmental Monitoring in Amazonian Basin. *Wireless Networks*, 21(3), pp. 793–807.

Vijayaraj, V., Younan, N., and O'Hara, C. (2006). Concepts of Image Fusion in Remote Sensing Applications. in Proceedings of IEEE International Conference on Geoscience and Remote Sensing Symposium, pp. 3798–3801.

Vivet, M., Peleg, S., and Binefa, X. (2011). Real-Time Stereo Mosaicing using Feature Tracking. in Proceedings of IEEE International Symposium on Multimedia, pp. 577–582.

Wang, J., Li, Z., and Zhang, M. (2010a). Two New Proposed Image Zooming Methods. in Proceedings of IEEE Sixth International Conference on Wireless Communications Networking and Mobile Computing, pp. 1–4.

Wang, M. and Blu, T. (2010). Generalized YUV Interpolation of CFA Images. in Proceedings of IEEE 17^{th} International Conference on Image Processing, pp. 1909–1912.

Wang, P., Li, C., and Zheng, J. (2007). Distributed Minimum-Cost Clustering Protocol for Underwater Sensor Networks (UWSN)s. in Proceedings of IEEE International Conference on Communications, pp. 3510–3515.

Wang, W. and Chang, F. (2011). A Multi-Focus Image Fusion method based on Laplacian Pyramid. *Journal of Computers*, 6(12), pp. 2559–2566.

Wang, X.-f. and Ling, H.-f. (2010). An Edge-Adaptive Interpolation Algorithm for Super-Resolution Reconstruction. in Proceedings of IEEE International Conference on Multimedia Information Networking and Security, pp. 81–84.

Wang, Y. (2008). chapter Topology Control for Wireless Sensor Networks *Wireless Sensor Networks and Applications*, pp. 113–147. Springer US, Boston, MA.

Wang, Y., Yang, J., Yin, W., and Zhang, Y. (2008). A New Alternating Minimization Algorithm for Total Variation Image Reconstruction. *SIAM Journal on Imaging Sciences*, 1(3), pp. 248–272.

Wang, Z., Bovik, A. C., Sheikh, H. R., and Simoncelli, E. P. (2004). Image Quality Assessment: From Error Visibility to Structural Similarity. *IEEE Transactions on Image Processing*, 13(4), pp. 600–612.

Wang, Z., Tie, Y., and Liu, Y. (2010b). Design and Implementation of Image Fusion System. in Proceedings of IEEE International Conference on Computer Application and System Modeling, 10, pp. 140–143.

Watfa, M. K. and Commuri, S. (2006a). The 3-Dimensional Wireless Sensor Network Coverage Problem. in Proceedings of IEEE International Conference on Networking, Sensing and Control, pp. 856–861.

Watfa, M. K. and Commuri, S. (2006b). Optimal 3-Dimensional Sensor Deployment Strategy. in Proceedings of IEEE Third Consumer Communications and Networking Conference, 2, pp. 892–896.

Wenz, G. M. (1962). Acoustic Ambient Noise in the Ocean: Spectra and Sources. *The Journal of the Acoustical Society of America*, 34(12), pp. 1936–1956.

Wong, C.-S. and Siu, W.-C. (2010). Adaptive Directional Window Selection for Edge-Directed Interpolation. in Proceedings of IEEE 19^{th} International Conference on Computer Communications and Networks, pp. 1–6.

Wu, H. and Abouzeid, A. A. (2006). Error Resilient Image Transport in Wireless Sensor Networks. *Computer Networks*, 50(15), pp. 2873–2887.

Wu, L., Riihijarvi, J., and Mahonen, P. (2007). A Modular Wireless Sensor Network Gateway Design. in Proceedings of Second International Conference on Communications and Networking in China, pp. 882–886.

Xiao, Y. (2009). *Underwater Acoustic Sensor Networks*. Auerbach Publications, Boston, MA, USA, 1 Edition.

Xie, G. G. and Gibson, J. H. (2001). A Network Layer Protocol for UANs to Address Propagation Delay Induced Performance Limitations. in Proceedings of MTS/IEEE Oceans Conference-An Ocean Odyssey, 4, pp. 2087–2094.

Xiong, H., Zhang, D., Wang, L., and Chaouchi, H. (2015). Emc^3: Energy-Efficient Data Transfer in Mobile Crowd Sensing under Full Coverage Constraint. *IEEE Transactions on Mobile Computing*, 14(7), pp. 1355–1368.

Xiong, Y. (2009). Eliminating Ghosting Artifacts for Panoramic Images. in Proceedings of IEEE 11^{th} International Symposium on Multimedia, pp. 432–437.

Xiong, Y. and Turkowski, K. (1998). Registration, Calibration and Blending in Creating High Quality Panoramas. in Proceedings of IEEE Fourth Workshop on Applications of Computer Vision, pp. 69–74.

Yadav, G., Maheshwari, S., and Agarwal, A. (2014). Contrast Limited Adaptive Histogram Equalization based Enhancement for Real Time Video System. in Proceedings of IEEE International Conference on Advances in Computing, Communications and Informatics, pp. 2392–2397.

Yadav, S. and Yadav, R. S. (2016). A Review on Energy Efficient Protocols in Wireless Sensor Networks. *Wireless Networks*, 22(1), pp. 335–350.

Yamashita, A., Fujii, M., and Kaneko, T. (2007). Color Registration of Underwater Images for Underwater Sensing with Consideration of Light Attenuation. in Proceedings of IEEE International Conference on Robotics and Automation, pp. 4570–4575.

Yang, J., Zhang, C., Li, X., Huang, Y., Fu, S., and Acevedo, M. F. (2010a). Integration of Wireless Sensor Networks in Environmental Monitoring Cyber Infrastructure. *Wireless Networks*, 16(4), pp. 1091–1108.

Yang, L., Wu, X., Zhai, J., and Li, H. (2011). A Research of Feature-based Image Mosaic Algorithm. in Proceedings of IEEE Fourth International Congress on Image and Signal Processing, 2, pp. 846–849.

Yang, W., Nan, J., and Sun, D. (2008). An Online Water Quality Monitoring and Management System Developed for The Liming River Basin in Daqing, China. *Journal of environmental management*, 88(2), pp. 318325.

Yang, Y., Park, D. S., Huang, S., and Rao, N. (2010b). Medical Image Fusion via An Effective Wavelet-based Approach. *EURASIP Journal on Advances in Signal Processing*, 2010(1), pp. 79–91.

Yao, L. (2008). Image Mosaic based On SIFT and Deformation Propagation. in Proceedings of IEEE International Symposium on Knowledge Acquisition and Modeling Workshop, pp. 848–851.

Yaroslavsky, L. P. (2012). *Digital Picture Processing: An Introduction*, 9. Springer Science & Business Media.

Yuh, J. and West, M. (2001). Underwater Robotics. *Advanced Robotics*, 15(5), pp. 609–639.

Zennaro, M. and Bagula, A. (2009). Design of A Flexible and Reliable Gateway to Collect Sensor Data in Intermittent Power Environments. in Proceedings of IEEE International Conference on Computer Communications and Networks, pp. 1–6.

Zhang, C., Bai, X., Teng, J., Xuan, D., and Jia, W. (2010). Constructing Low-Connectivity and Full-Coverage Three Dimensional Sensor Networks. *IEEE Journal on Selected Areas in Communications*, 28(7), pp. 984–993.

Zhang, J., Ma, S., Zhang, Y., and Zhao, D. (2009). Fast and Effective Interpolation using Median Filter. in Proceedings of Pacific-Rim Conference on Multimedia, pp. 1174–1184.

Zhu, J. and Ren, M. (2014). Image Mosaic Method Based on SIFT Features of Line Segment. *Computational and Mathematical Methods in Medicine*, 2014(3), pp. 1–11.

Zoran, L. F. (2009). Quality Evaluation of Multiresolution Remote Sensing Images Fusion. *UPB Scientific Bulletin, Series C*, 71, pp. 38–52.

Zorzi, M., Casari, P., Baldo, N., and Harris, A. F. (2008). Energy-Efficient Routing Schemes for Underwater Acoustic Networks. *IEEE Journal on Selected Areas in Communications*, 26(9), pp. 1754–1766.

List of Publications

SCI Journals

1. Himanshu Jindal, Sharad Saxena and Singara Singh Kasana, "A Sustainable Multi-parametric Sensors Network Topology for River Water Quality Monitoring", *Wireless Networks*, pp. 1-25, 2017. DOI: 10.1007/s11276-017-1532-z. SCI, SCIE Indexed (IF:1.584)

2. Himanshu Jindal, Sharad Saxena and Singara Singh Kasana, "Sewage Water Quality Monitoring Framework using Multi-parametric Sensors", *Wireless Personal Communications*, Vol. 97, No. 1, pp. 881-913, 2017. SCIE Indexed (IF:0.951)

3. Himanshu Jindal, Sharad Saxena and Singara Singh Kasana, "Triangular Pyramidal Topology to Measure Temporal and Spatial Variations in Shallow River Water using Ad-hoc Sensors Network", *Ad Hoc and Sensor Wireless Networks*, Old City Publishing, Vol. 39, No. 1-4, pp. 1-35, 2017. SCIE Indexed (IF:1.034)

4. Himanshu Jindal, Singara Singh Kasana and Sharad Saxena, "Underwater Pipelines Panoramic Image Transmission and Refinement using Acoustic Sensors" *International Journal of Wavelets, Multiresolution and Information Processing*, World Scientific, 2017. DOI: https://doi.org/10.1142/S0219691318500133 SCIE Indexed (IF:0.6)

5. Himanshu Jindal, Singara Singh Kasana and Sharad Saxena, "Ridgelet based Fusion Technique for Panoramic Underwater Image Refinement" *Multimedia Tools and Applications*, 2018. SCIE Indexed (IF:1.541) **(Communicated)**

Conferences

6. Himanshu Jindal, Sharad Saxena and Singara Singh, "Challenges and Issues in Underwater Acoustics Sensor Networks: a review", in: Proceedings of *IEEE International Conference on Parallel, Distributed and Grid Computing*, pp. 251-255, December, 2014, Solan, India.

7. Himanshu Jindal, Singara Singh Kasana and Sharad Saxena, "A Novel Image Zooming Technique using Wavelet Coefficients", in: Proceedings of *International Conference on Recent Cognizance in Wireless Communication and Image Processing*, pp. 1-7, January, 2016, Jaipur, India.